In presenting this dissertation/thesis as a partial fulfilment of the requirements for an advanced degree from Emory University, I agree that the Library of the University shall make it available for inspection and circulation in accordance with its regulations, governing materials of this type. I agree that permission to copy from, or to publish, this thesis/dissertation may be granted by the professor under whose direction it was written, or, in his/her absence, by the Dean of the Graduate School when such copying or publication is solely for scholarly purposes and does not involve potential financial gain. It is understood that any copying from, or publication of, this thesis/dissertation which involves potential financial gain will not be allowed without written permission.

_____

Yan Liang

Energetic Contribution of Amyloid Self-assembly

By
Yan Liang
Doctor of Philosophy
in
Chemistry

_____
Dr. David G. Lynn
Adviser

_____
Dr. Keith M. Berland
Committee Member

_____
Dr. Tianquan Lian
Committee Member

_____
Dr. Stefan Lutz
Committee Member

Accepted:

_____
Lisa A. Tedesco, Ph.D.
Dean of the Graduate School

_____
Date

Energetic Contribution of Amyloid Self-assembly

By

Yan Liang

B.S., Beijing Normal University, 1999
M.S., Beijing Normal University, 2002

Adviser: David G. Lynn, Ph.D.

An Abstract of

A dissertation submitted to the Faculty of the Graduate

School of Emory University in partial fulfillment

of the requirements for the degree of

Doctor of Philosophy

in

Chemistry

2009

Abstract

Energetic Contribution of Amyloid Self-assembly

By

Yan Liang

Controlling pathways that distinguish protein folding from misfolding is critical to viability as highlighted by the nearly 40 protein misfolding diseases. The correlated interactions between amino acid side chains and the backbone have been implicated in protein β-structural assembly and stability, yet the relative contributions have been difficult to evaluate directly. In this dissertation, the central core sequence of the Aβ peptide associated with Alzheimer's disease, Aβ(16-22), was developed as an experimental system for evaluating these interactions. Factors which contribute to the hydrophobic core interactions, such as side chain cross-strand pairing along the β-sheet surface, buried solvent accessible surface area in forming an amyloid structure, and the side chain conformational entropy, were shown to determine the characteristic amyloid cross-β structure. The assembly of the Aβ(16-22) model system indicates that a desolvation step occurs during amyloid nucleation. By direct real-time imaging, peptides that give rise to amyloid assemblies undergo hydrophobic collapse to large micron size aggregates which maintain the properties of molten globules. Further, the amyloid growth is nucleated within these dynamic unstructured aggregates; and once the nuclei are formed, the amyloid assembly grows via monomer addition to the highly ordered amyloid ends. These results provide a direct real-time observation of amyloid assemblies, and suggest that therapeutic intervention should focus on cell type-specific surfaces able to template the nucleation of cytotoxic amyloid. In addition, taking advantage of the amyloid cross-β scaffold, a pigment array has been constructed within a paracrystalline amyloid nanotube and Förster energy transfer along the nanotube surface has been demonstrated to self-assembled acceptor dyes, which promises the potential application of using amyloid structures to generate light harvesting antenna.

Energetic Contribution of Amyloid Self-assembly

By

Yan Liang

B.S., Beijing Normal University, 1999
M.S., Beijing Normal University, 2002

Adviser: David G. Lynn, Ph.D.

A dissertation submitted to the Faculty of the Graduate

School of Emory University in partial fulfillment

of the requirements for the degree of

Doctor of Philosophy

in

Chemistry

2009

ACKNOWLEDGEMENTS

I wish to first thank my advisor Dr. David Lynn for the support and encouragement he has given me during my graduate career. I appreciate Dave's patience for his understanding regarding his students and allowing them to learn through their own pursuits and mistakes. He allows the most freedom and best opportunity a student can get. Without his support, I cannot imagine where I would be standing today. I also wish to thank Dr. Keith Berland for his support through collaboration since my 3rd year, which provided great opportunities in my graduate studies. From Keith, I have learned many fluorescence concepts and techniques, which have broadened my view in my academic pursuits. I thank my committee members, Dr. Stephan Lutz and Dr. Tianquan Lian, supervising me over the years. I deeply thank Dr. Virginia Shadron from graduate school services, for her constant support and encouragement, in addition to her many valuable suggestions for life.

I wish to thank Dr. P. Thiyagarajan and Dr. Sai Venkatesh Pingali, at Argonne national laboratory's (ANL) Intense Pulsed Neutron Source for their support and challenge in our two-year project at Argonne Advanced Photon Source (APS). Thanks to Dr. Jim Snyder and Ashutosh Jogalekar in the molecular modeling project. Thanks to Hong Yi and Jeannette V. Taylor at the Robert P. Apkarian Integrated Electron Microscopy Core at Emory for TEM and cryo-HRSEM support. Thanks to Dr. Anil Mehta for his help in my solid-state NMR experiments. Thanks to W. Seth Childers for his help with electron diffraction experiments. Thanks to Peng Guo at Dr. Berland's lab for the help in running the fluorescence lifetime experiment.

Thanks to Dr. Kun Lu and Dr. Jijun Dong for the help they offered when I started my project. Thanks to Dr. Suzette Pabit, Dr. Jianrong Wu, and Neil Anthony for the instrumentation support and friendship when I worked in Dr. Berland's lab. Thanks to all the biophysical journal club members for their encouragement in sharing science, essentially Dr. Kurt Warncke, Dr. Ivan Rasnik, Dr. Vincent Huynh, and Dr. Laura Finzi. I had great time in your club. I sincerely thank all of the past and present members of the Lynn group and Berland group.

And finally, thanks to my family for supporting my ambitions and being champions for my success.

TABLE OF CONTENTS

LIST OF FIGURES

LIST OF TABLES

LIST OF ABBREVIATIONS

2D	two Dimension
A555	Alexa 555
A633	Alexa 633
Å	Angstrom
Aβ	Amyloid β peptide
AD	Alzheimer's Disease
AFM	Atomic Force Microscopy
CD	Circular Dichroism
CNT	Carbon NanoTubes
CP	Cross-Polarization
Cryo-SEM	Cryo-etch Scanning Electron Microscopy
CSA	Chemical Shielding Anisotropy
DQF	Double Quantum Filtered
DRAWS	Dipolar Recoupling with A Windowless Sequence
FCS	Fluorescence Correlation Spectroscopy
Fmoc	FlourenylMethOxyCarbonyl
FRAP	Fluorescence Recovery After Photobleaching
FRET	Förster Resonance Energy Transfer
FTIR	Fourier Transform Infrared Raman spectroscopy
IE-FTIR	Isotope-Edited Fourier Transform Infrared Raman spectroscopy

HPLC	High-Performance Liquid Chromatograph
kcal/mol	kilocalories per mole
kV	kiloVolt
LNT	Lipid NanoTubes
MALDI-TOF	Matrix Assisted Laser Desorption Ionization - Time Of Flight mass spectrometry
MAS	Magic Angle Spinning
MD	Molecular Dynamics
min	minute
ml	mili-liter
mM	milli-Molar
μm	micrometer
μM	micro-Molar
MQ-NMR	Multiple Quantum NMR
MRME	Molar Residue Mean Ellipticity
nm	nanometer
NMM	4-MethylMorpholine
PME	Particle-Mesh Ewald
PNT	Peptide NanoTubes
Rh	Rhodamine
RMSD	Root Mean Square Deviation
SASA	Surface Accessible Surface Area
SAXS	Small Angle X-ray Scattering

SHG	Second Harmonic Generation
SPC	Simple Point Charge
SSNMR	Solid State NMR
TDC	Transition Dipolar Coupling
TCSPC	Time-Correlated Single-Photon-Counting
TEM	Transmission Electron Microscopy
TFA	TriFluoroAcid
WAXS	Wide Angle X-ray Scattering

* All amino acids were abbreviated according to the standard three-letter or one-letter codes.

CHAPTER 1

MECHANISM OF AMYLOID SELF-ASSEMBLY AND AMYLOID STRUCTURAL FUNCTIONALITY: GENERAL INTRODUCTION

Protein Misfolding and Amyloidosis

Protein misfolding and aggregation into amyloid have been implicated in a growing number of diseases, including Alzheimer's, Parkinson's, Huntington's and prion's diseases (Buxbaum 2003, Bossy-Wetzel 2004). Although the proteins involved exhibit diverse sequences and structural properties, the formed amyloid all contain the characteristic cross β pattern, in which β-sheets are laminated through side chain interactions. Because amyloid-forming proteins do not have sequence and structural similarity, amyloid was proposed to be the generic feature of the protein main chains, for they all have the same backbones (Dobson, 2003). However, like protein folding, many factors, such as pH (Lu 2003), temperature (Arora 2004), and solvent (Dzwolak 2005),

can affect amyloid formation. Also, globular proteins contain all kinds of sequences, form all kinds of globular structures with different functions, but their 2nd structures are limited to β-sheet, α-helix, and β-turn. Therefore, claiming amyloid-formation as the generic feature of the protein main chains may not be meaningful, and may be misleading in amyloid mechanism studies. Most likely, protein amyloid formation is the result of specific protein interactions, although it is mostly abnormal in the living systems and can cause diseases. Therefore, to unveil the mechanism of protein amyloid formation, knowledge of protein folding should play an important role.

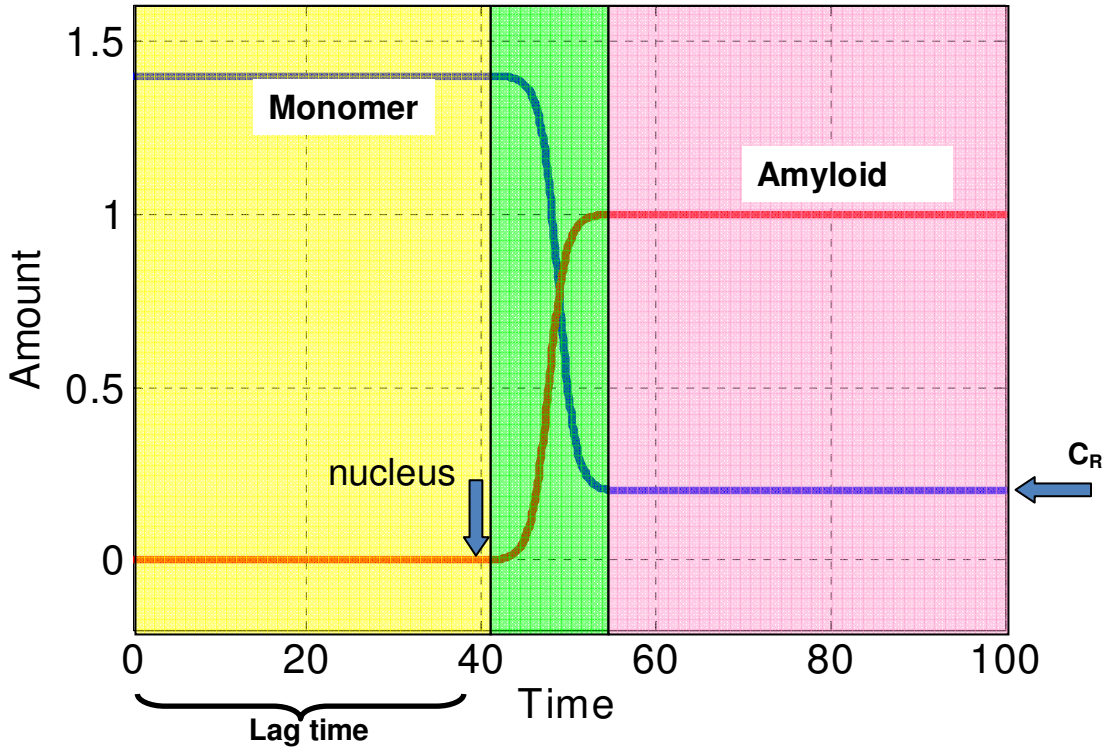

Figure 1.1. Kinetic curve of amyloid assembly

An idealized kinetic curve of amyloid assembly at the concentration exceeding the critical concentration (C_R). There are three stages in amyloid assembly, nucleation (yellow), elongation (green), and steady-state (purple). The protein stays soluble during the lag time. (Harper 1997)

Amyloid *in vitro* studies indicate amyloid assembly is a nucleation-dependent process (Wogulis 2005, Wetzel 2006, Quijano 2007, Congdon 2008), which involves a slow nucleation phase in which ordered nuclei are formed through a series of unfavorable association steps; a growth phase in which nuclei rapidly grow and elongate to form larger amyloid fibers; and a steady-state phase in which the resulting fibers and the monomers maintain an equilibrium (Harper 1997). The ideal kinetic curve of Aβ fibril formation has a sigmoid shape as shown in Figure 1.1.. In addition, amyloid formation *in vitro* has been observed to be concentration-dependent. In Figure 1.1., C_R is the critical concentration for amyloid formation, below which the protein or peptide does not assemble at all. At a concentration above C_R, the peptide or protein undergoes a lag phase before the nuclei are formed, (Come 1993, Auer 2007), which is resulted from time consuming kinetic barriers. It is not clear what these kinetic barriers are, which contributes the complication to understand the amyloid mechanism, and cause C_R is difficult to determine. Also because of the non-unified intermediates at the early stage of amyloid assembly, and the lack of standard determination of amyloid at the early stage, the results about amyloid assembly mechanism are usually inconsistent. For example, the estimation of amyloid β (Aβ) C_R is in the broad range of 6-40μM in physiological pH (Sengupta 2003). In Figure 1.1., the lag time is defined as a period of time in which the peptide or protein is supersaturated before the amyloid starts to form. During lag phase, amyloid fibrillar nuclei are proposed to build up with slow rates presumably due to the unfavorable association steps. The transition from pre-nucleus species to nuclei is difficult to detect, and a convincing and defined nucleic structure has not been revealed.

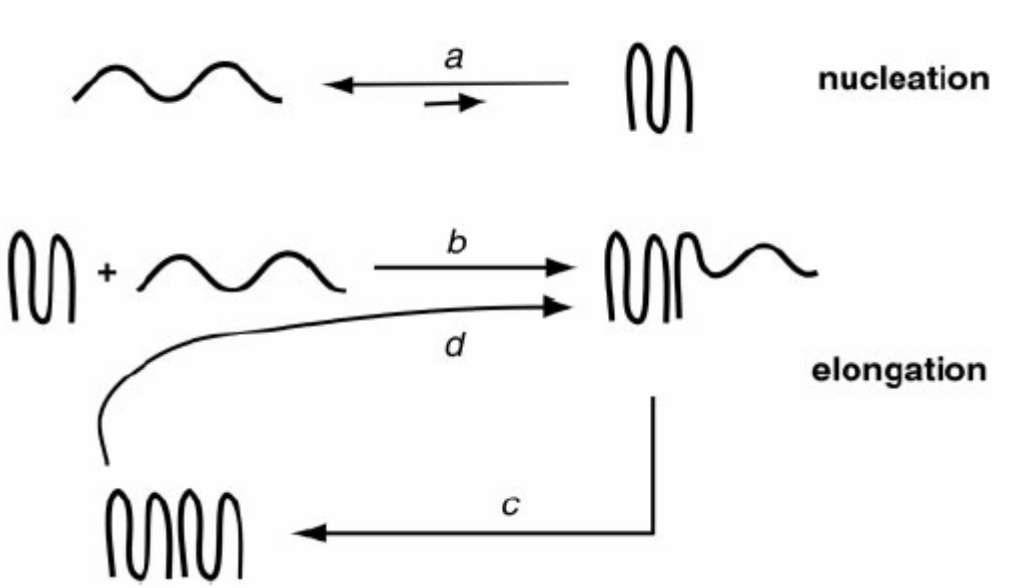

Figure 1.2. A model of poly(Gln) self-assembly: nucleation and elongation.

(Step a) represents the nucleation with an unfavorable transition from random coiled state to a compact state corresponding to the nucleus. In elongation, (Step b) is the initial binding of the nucleus to an extended monomer; (Step c) is a consolidation of the structure which generates a new binding site for the monomer. The resulted dimeric species further binds to another monomer for elongation. (Chen 2002)

Traditional techniques in kinetic and thermodynamic studies of protein folding were applied in amyloid assembly *in vitro* studies. For example, circular dichroism (CD) can monitor the conformal transition of proteins or peptides from their non-amyloid native or random coil state to amyloid β-sheet state (Juszczyk 2005). To disrupt amyloid structure by adding protein "denature" reagents, or adjusting the temperature or pH, amyloid disassembly can be followed (Kiuchi 2002). In addition, amyloid can bind to Congo Red positively with green characteristic birefringence, which has been used as a marker of amyloid formation in many amyloid kinetic studies (Elghetany 1989). These

methods have exacted the kinetic and thermodynamic parameters of amyloid aggregation with similar standards as globular protein folding. In a polyglutamine peptide model (Chen 2002), following the well-accepted 3-stage amyloid aggregation: nucleation, elongation and steady-state equilibrium, the nuclei are considered to be the least stable species; therefore, the nucleation can be affected by the rapid exchange rate between the nuclei and the ground-state monomers, and the rate constant of nucleic elongation (Figure 1.2.). Based on this model (Chen 2002), the mathematical relationship is

$$\Delta = \frac{1}{2} k_+^{\,2} K_{n^*} c^{(n^*+2)} t^2$$

Here, Δ is the amount of monomer converted to aggregate at time t, which depends on the monomer concentration, c; the critical nucleus or the number of monomers that come together to form the nucleus, n*; the nucleation equilibrium constant, K_{n^*}, describing the pre-equilibrium between the bulk monomer pool and the nuclei,; and the second-order elongation rate constant, k_+, which is assumed to be identical for reactions of both the nuclei and early aggregates for simplicity. By following the aggregation process of samples in a serial monomer concentrations, the number of monomers that come together to form the nucleus n* can be determined.

Because amyloid fibril formation is nucleation-dependent, the elongation rate can be determined in the presence of exogenous seeds (which are usually fibril fragments) (Schilling 2006). The model of amyloid elongation was proposed to be a multiple-step process including monomer addition to the fibril ends and protofibril-protofibril association (Figure 1.3.). An Aβ(1-40) protofibril growth study revealed the elongation only appeared at the fibril ends, and proceeded without changes in the original number of

fibril ends (Nichols 2002). This result favors the monomer addition model. Single-molecule fluorescence imaging of the propagation of amyloidogenic yeast prion Sup35 also suggested amyloid growth occurs by monomer addition (Collins 2004). However, the protofibril fusion model may well co-exist because of the appearance of protofibrils as subunits of mature fibrils (Poirier 2002).

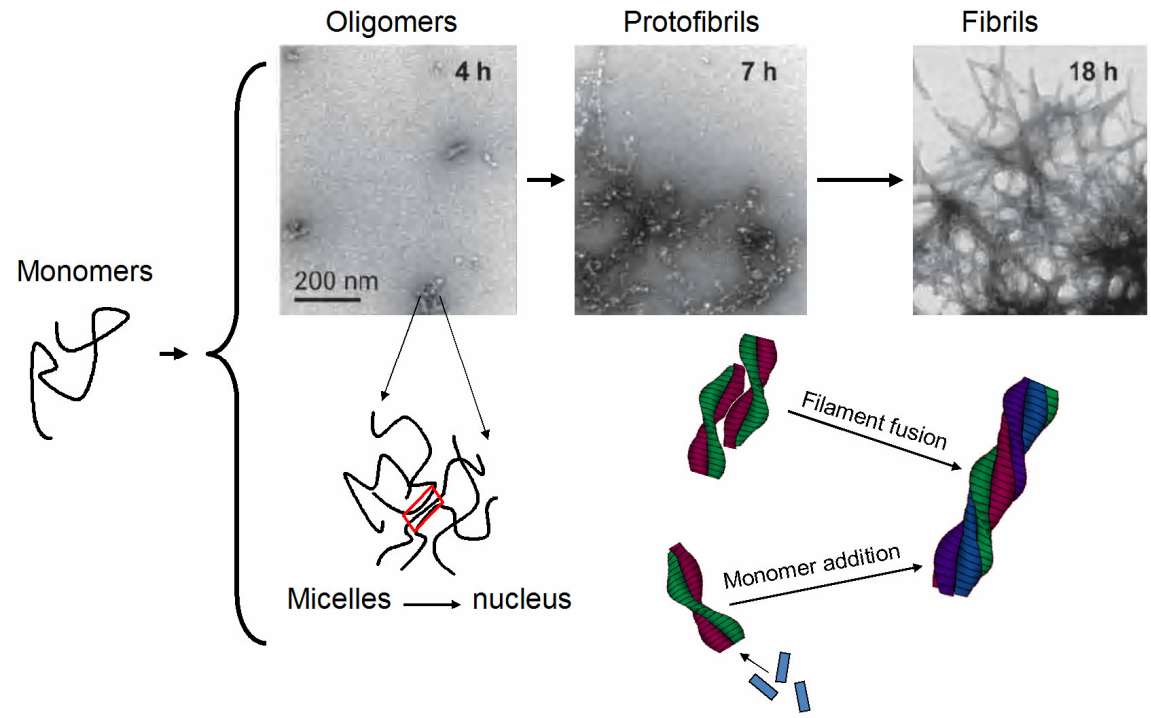

Figure 1.3. Proposed pathways of amyloid assembly.

The TEM images were adopted from Habicht 2007. The observed particle-like species were proposed to be "micelles", which induce the nucleation. Protofibril fusion and monomer addition to the nuclei are proposed to be possible steps in elongation.

Pathways of Amyloid Self-assembly

To understand the mechanism of amyloid assembly, determining the associations of peptides or proteins, and intermediate pathways, during the nucleation phase is a critical task. In microscopic imaging, such as AFM and TEM, particle-like species were observed as in Figure 1.3. (Harper 1997, Stine 2003, Habicht 2007). It has been proposed that these particles are peptide or protein oligomers. Strikingly, there is evidence that these oligomers are more toxic than the mature amyloid fibrils in pathological models, and therefore viewed as the primary pathological species in neurodegenerative diseases (Kayed 2003, Carrotta 2006). Because oligomers are usually clarified as pre-amyloid species, the question of the connection between the oligomers and mature amyloid fibrils is raised. Are amyloid oligomeric intermediates in the pathway to fibril formation? If the oligomers are off pathway, but they are the primary pathological species, what are the roles of amyloid fibril deposits in neurodegeneration? Extensive debates exist around this topic, but the role of amyloid oligomers on amyloid fibril formation remains elusive. A study of small molecular inhibitors of Aβ(1-42) aggregation identified compounds that can block oligomerization while having no effect on inhibiting fibrillization, which indicated amyloid β oligomerization is not an obligatory step toward fibrillization (Necula 2007). Ultimately the peptides in these oligomers will form fibrils, and no evidence indicates fibrillization is limited to a single pathway. These inhibition results support amyloid β oligomerization and fibrillization are independent. Some peptides form amyloid fibrils, but do not appear to form oligomers. For example, a monomeric variant of transthyretin (M-TTR) was found to nucleate with monomers (Hurshman, 2004), and a kinetic model of simple polyglutamine peptides suggested the critical nuclei

are monomers (Wetzel, 2006). These results support oligomerization may not be necessary in nucleation.

On the pathways of amyloid formation, besides oligomers and mature fibrils, protofibrils (filaments) have also been identified as intermediates. Protofibrils were suggested to be kinetically-trapped and semi-flexible species from oligomer fusion, and were formed from non-nucleation-dependent pathway (Modler 2003, Gosal, 2005, Kaylor, 2005). Therefore, oligomers and protofibers may be both off pathway, and do not contribute to the nucleation-dependent growth of the rigid long-straight amyloid fibrils. Oligomerization in amyloid assembly has attracted great attention, especially when oligomers were indicated to be more toxic than amyloid fibrils. Also, in an assembled system, it is easy to think the monomer assembly starts from small (oligomers) to big (fibrils). However, evidence has shown that oligomerization can be varied and some systems even do not form oligomers at all. This should suggest oligomerization is not the characteristic feature shared by every amyloid-formation peptides. Well then, what is the true feature of amyloid fibrillization, from nucleation to elongation?

Using circular dichroism (CD) only random coil signals appear during the lag-time period of a peptide self-assembly (Lu 2003), indicating no confirmed protein structures. Lomakin et al have proposed that Aβ peptide micelles are procurers of nuclei formation, as they accumulate peptide monomers (Lomakin 1996, Lomakin 1997). This is somehow relevant to the particle-species observation during lag phase. However, a micelle is defined as an aggregate of surfactant molecules dispersed in a liquid colloid. Using “micelle” to describe peptide aggregates can be partially misleading because the peptide sequences are much more functionally complex than surfactant head and tail

groups. It is true that amyloid-formation peptides can be typically amphiphilic, i.e. their sequences can be split into hydrophobic and hydrophilic regions. Indeed, the so called critical micelle concentration (CMC) of Aβ(1-40) can be obtained by the analysis of solution surface tension (Sabate 2005). Still, because the peptide amphiphilic sequence is not like the simple separation of the surfactant head and tail, but contains multiple hydrophobic and hydrophilic regions, the peptide aggregates may be hard to be described by "CMC". In addition, micelles have the specific shape with hydrophilic heads exposing to the surrounding solvent and the hydrophobic tails buried in the center. Most likely, the amphiphilic peptides tend to bury the hydrophobic region inside and expose the hydrophilic counterpart to the solvent. With more complicated monomer sequences, the peptide aggregates may involve more molecular interactions than surfactant micelles. The hydrophobic and hydrophilic separation in protein folding is usually called hydrophobic collapse. In amyloid assembly, instead of one protein hydrophobic collapse and folds, an amount of peptides or proteins collapse and assemble. Indeed, relevant to protein folding, the conformational change model was proposed, in which peptides or proteins undergo a partially unfolded process to increase the β-sheet component, and drive the association of more monomers to form amyloid fibrils (Uversky 2004, Laidman 2006). This model requires the protein to be partially unfolded. How the conformational change takes place in amyloid-formation proteins, and whether other monomers contribute to the partially unfolded nucleus is unknown. In addition, the partially unfolded state can not be accessed by small amyloid-formation peptides, which usually sample a wide range of random-coil structures.

Therefore, there has not been conclusive amyloid assembly pathway which is shared by all the amyloid formation peptides. Amyloid assemblies all share the characteristic cross-β structure. To form this structural scaffold, some fundamental molecular association pathways may be shared during amyloid formation. Identifying factors which determine these molecular associations may be the key to unveil the amyloid mechanism.

Structural Characterization of Amyloid

Amyloid structures display characteristic cross-β patterns, in which β-sheets are laminated through side chain interactions. The cross-β patterns can be detected by X-ray diffraction and electronic diffraction (Figure 1.4.) (Blake 1996, Sunde 1997, Sikorski 2003). Because amyloid fibrils are usually large assemblies and they are not crystalline, the traditional structural analysis, such as solution NMR and X-ray crystallography are not useful in determining amyloid structures. Solid-state NMR and isotope-edited FTIR are not limited by these constructions and amyloid β-sheet orientation and registry can be determined. Among amyloid-forming peptides, both parallel and antiparallel arrangements are observed. The parallel arrangement is usually formed by longer sequences in the order of 7-10 amino acids (Lakdawala 2002). When Aβ peptide is truncated, the β-sheets in their amyloid fibers can switch to antiparallel. Aβ(1-40) forms parallel β-sheet (Tycko 2003, Tycko 2004), the truncated Aβ(10-35) also forms parallel β-sheet (Benzinger 1998), but truncation to Aβ(16-22) creates antiparallel β-sheets (Mehta 2008). However, peptides that are short can also populate the parallel β-sheet in amyloid assemblies, such as GNNQQNY (Sawaya, 2007), HHQALVFFA ([2]Dong 2006)

and NFGAIL (Melquiond, 2007). Although the propensity for a peptide sequence to adopt parallel or antiparallel orientation in amyloid assemblies relies mainly on the properties of the sequence (Wouters 1995, Santiveri 2004), the determining factors remain unclear. The two possible β-strand orientations, the parallel and antiparallel, are equally distributed in globular proteins, and there is no direct evidence showing one is more favorable than the other (Gailer 1997, Scheiner 2006). The resulted β-structure is determined by the thermodynamic stability of the overall structure (Gellman 1998, Zhao 2006). Amyloid assemblies contain continued β network. The amyloid assembly models suggest the early nucleation may initiate from simple β-sheet formation (Nguyen 2004, Urbanc 2004, Hwang 2004, Ikebe 2007, Jang 2008). Identifying the factors which contribute to the β-structures may be important in unveiling the amyloid nucleation.

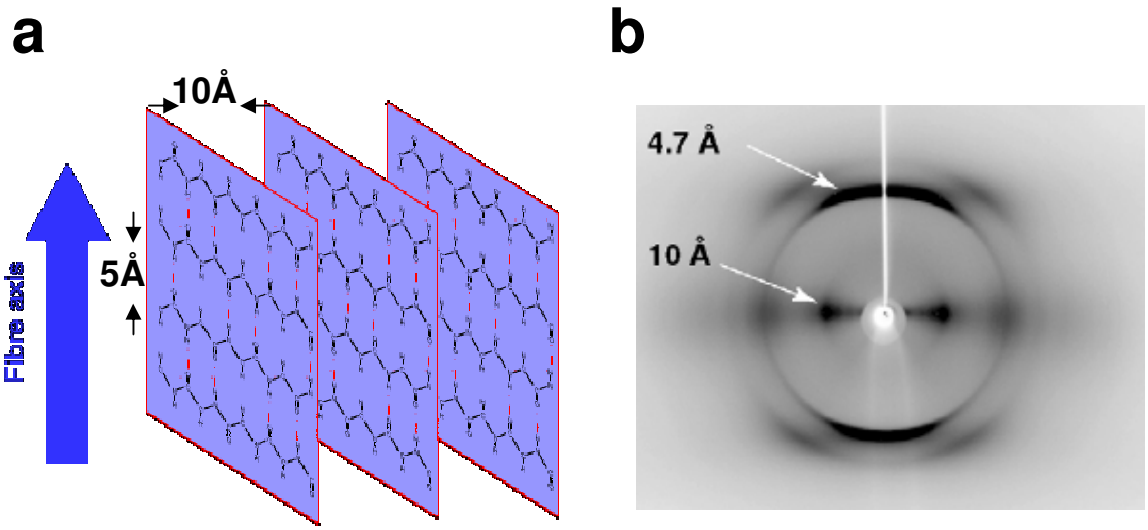

Figure 1.4. The cross-β structure of amyloid.

(a) β-sheet laminants with ~10Å apart. The H-bonding (~5Å) dimension is on the amyloid fiber axis

(b) X-ray diffraction pattern of H-bonding (~5Å) and lamination (~10Å) (Makin 2006)

The amyloid cross-β pattern features β-sheet lamination, or so-called sheet-sheet stacking. Although the sheet-sheet stacking is mainly through the side chain interactions, the backbone H-bonding can determine the side chain distribution on the β-sheet surface. For example, Aβ(16-22) forms fibers with the antiparallel in-register β-sheet in a neutral water acetonitrile solution (v:v 3:2). Under the acidic condition (0.1% TFA), the peptide forms tubes with the antiparallel one-residue shifted β-sheet (Lu 2003). The reason of the morphology change is because the antiparallel one-residue-shifted β-sheet has same side chain distribution on both sides of the β-sheet, which induces more sheets stacking, from 4-6 sheets in fibers to over 100 sheets in tubes (Mehta 2008). The general rules for the propensity of amyloid formation remain elusive. What is most accepted for the intrinsic β-aggregation propensity is still sequence-dependent (Fernandez-Escamilla 2004, Yoon 2004, Trovato 2006), and the conditions for amyloid aggregation are important, as supported by recent examples of native non-amyloid related proteins can form amyloid in adjusted conditions (Fandrich 2001, Pavlov 2002). Therefore, factors which determine the polypeptide sequence associations may be the key to address the amyloid formation mechanism.

Amyloid Nanomaterial Fabrication and Application

Synthetic peptide nanotubes (PNT) constructed through highly ordered non-covalent bonds contain unique structural and functional properties. Relative to carbon nanotubes (CNT) (Iijima 1991, Iijima 1993) and lipid nanotubes (LNT) (Nakashima 1985, Yager 1985), these peptide-based hollow cylindrical structures have attracted diverse bionanotechnological applications (Gao 2005) (Figure 1.5.). For example, by bioengineering, peptide nanotubes can mimic tissue structures (Holmes 2000). Because of the complication of polypeptide assembly, generating robust procedures to produce homogeneous PNT remains a challenge in material science. The first PNT was synthesized in 1990s through the ring stacking of cyclic D, L-peptides (Ghadiri 1993). The cyclic D, L-peptides can maintain the ring-shape conformation, and stack through extensive antiparallel backbone H-bonding. The diameters of these PNT can be adjusted by the size of the peptide ring. However, this method can only synthesize limited diameter PNT to keep a stable ring structure of cyclic D, L-peptides (Khazanovich 1994). By generating a helical pitch, PNT can be synthesized through the self-assembly of extended amyloid peptides (Lu 2003, [1]Dong 2006). This makes it possible to generate more diverse diameter tubes. The curvature of nanotubes (Ding 2003), which is adjusted by the tube diameters, can be used in PNT electronic and mechanical applications. If the helical pitch of PNT is well understood and controlled, the generation of a large range of tube diameters will be beneficial.

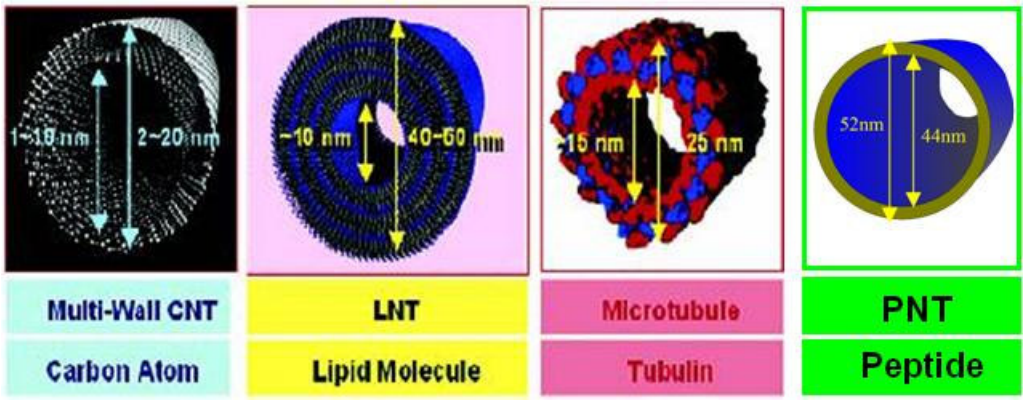

Figure 1.5. Peptide nanotubes (PNT)

Comparing with other representative nanotubes (Shimizu 2005). The tube dimensions are labeled for comparison.

Amyloid has characteristic cross-β structural pattern, which shows specific X-ray diffraction patterns, β-sheet CD signature, and Congo Red dye binding. If a PNT is amyloid, many amyloid properties can be useful in PNT fabrication and structural determination. For example, amyloid formation is nucleation dependent, which usually exhibits as seeding effect or co-assembly. The co-assembled amyloid systems are beneficial because they can take advantage of the existing well-determined amyloid structures, and co-assemble new peptides with functional groups or other valuable modifications. The β-backbone H-bonding is easier to control comparing with lipid tail interactions in LNTs, and the amino acid chemical capacity in PNTs is much broader than CNTs. Better understanding of amyloid assembly and the factors which contribute to the final assembly is critical in fabricating novel amyloid PNT nanomaterials.

Summary

Determining the amyloid assembly mechanism and factors which contribute to amyloid formation is the ultimate goal. The amyloid assembly propensity possibly inheres in the polypeptide sequences. The challenge is to build up promising model systems which can address the critical rules determining polypeptide chain associations. Aβ(16-22), containing the central hydrophobic core of amyloid β peptide, can form amyloid with robust procedures and defined structures. The hydrophobic core has been identified being important in Aβ peptide self-assembly, and possibly possesses critical structural association in the assembly process. Using Aβ(16-22) as a mode system, I am going to address the following questions:

1. What factors can affect amyloid backbone conformation?
2. What are the key structural elements of amyloid nucleus?
3. What are the pathways of amyloid assembly?
4. What is the factor determining the amyloid tube diameter?
5. What are the amyloid nanotube application potentials?

CHAPTER 2

CROSS-STRAND PAIRING AND AMYLOID ASSEMBLY

INTRODUCTION

The α- and β-secondary protein structure elements each contribute significantly, but very differently, to polymer folding and stability. In contrast to α-structures where the relative contributions of individual amino acid propensities within the helix can be estimated (Wojcik 1990, Lyu 1990, O'Neil 1990, Padmanabhan 1990, Horovitz 1992, Blaber 1993), the longer range tertiary interactions that contribute significantly to β-sheet stability remain difficult to predict (Chou 1974, Minor 1994, Kim 1993). An initial survey of 253 known globular protein structures from the Brookhaven protein data base found that pairwise distributions of amino acids in antiparallel β-sheets are not random (Wouters 1995). When viewed along two antiparallel strands (Scheme 1.1.), the amino acid backbone atoms can be either directly hydrogen bonded (H-bonded site) or not

bonded (non-H-bonded site), and such cross-strand pairing interactions, which could be stabilizing or destabilizing (Hutchinson 1998, Zaremba 1999), appear to contribute significantly to β-sheet structure.

Recent studies from Koide, et al. have featured an in-depth analysis of the outer surface protein A (OspA) from *Borrelia burgdorferi*, a protein that contains a single sheet connecting two globular domains (Yan 2007, Makabe 2006, Makabe 2007). A series of mutants generated by alanine scanning did not correlate with experimental β-sheet propensity scales, statistical β-sheet propensity scales, or cross-strand pairwise interactions (Yan 2007). Instead, the free energy of the assembly of this single β-sheet solvated on both surfaces was most strongly correlated with the buried non-polar surface area of the assembly. This difference in the energetic factors that contribute most to the assembly of isolated β-sheets and those within globular proteins may well be relevant to the early steps in amyloid assembly and β-sheet nucleation.

Amyloid can be an all β-peptide assembly and is implicated in more than four dozen disorders including Alzheimer's, Huntington's, and the prion diseases. These fibrous aggregates, which assemble through nucleation dependent kinetics (Harper 1997, Westermark 2005, Wetzel 2006), form a characteristic cross-β spine where peptide strands are arrayed perpendicular to the long fiber axis (Blake 1996, Sunde 1997, Sikorski 2003). The resulting three-dimensional arrangement produces characteristic orthogonal X-ray diffraction reflections at ~5Å and ~10Å, generally assigned to the spacing between individual strands within a β-sheet and the packing of neighboring sheets as laminates. Although amyloid may well be accessible to all α-amino acid polypeptides (Dobson 2003, Uversky 2004, Dobson 2004), surprisingly little is known

about the growth mechanism or the molecular structure of the species responsible for disease etiology (Dobson 2003). Current models suggest the β assembly of amyloid originate from simple sheets as early nucleation events (Nguyen 2004, Urbanc 2004, Hwang 2004, Ikebe 2007, Jang 2008), and this early structure is propagated to create the final assembly.

Scheme 1.1. One residue shift in a three-strand antiparallel β-sheet

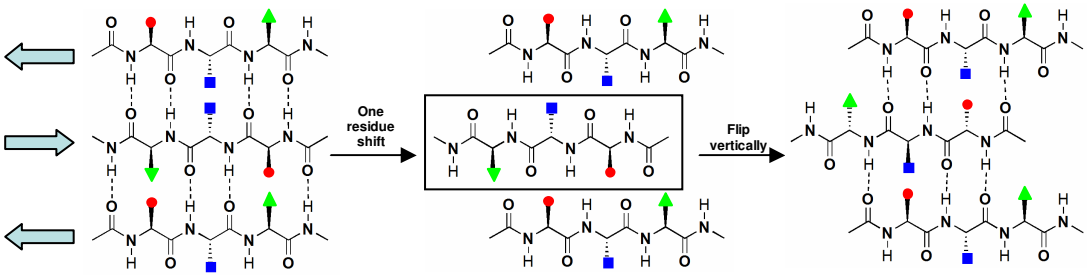

The seven-residue peptide that constitutes the central core of the Aβ peptide of Alzheimer's disease, Ac-KLVFFAE-NH_2 or Aβ(16-22), presents several valuable and simplifying elements helpful in exploring amyloid assembly. First, Aβ(16-22) is one of the smallest peptides able to form amyloid, and unlike most amyloid fibrils, the assemblies of Aβ(16-22) are soluble and readily analyzed spectroscopically. Second, a simple change in strand registry (Scheme 1.1.) is amplified by a switch from amyloid fibers to nanotube morphologies (Lu 2003, Mehta 2008). And finally, Aβ(16-22) contains complementary charged residues at each terminus and a single β-branched residue at V18. We now report the development of experimental and computational models of Aβ(16-22) to evaluate contributions to β-sheet assembly in this simple model peptide. We provide evidence that cross-strand pairwise interactions contribute significantly to Aβ(16-22) assembly and that there must exist steps early in the process prior to β-sheet

assembly that facilitate peptide desolvation. These results reveal the subtle differences that may regulate morphologically important misfolding assemblies in disease (Mehta 2008) and bring into focus the specific early steps of the nucleation-dependent mechanism for their assembly.

MATERIALS AND METHODS

Peptide Synthesis and Purification

Aβ(16-22) and its V18 congeners were synthesized using standard FMOC peptide synthesis protocols on an Applied Biosystems ABI431 peptide synthesizer. The resulting peptides were cleaved from the resin using a solution of TFA/thioanisole/ehtanedithiol /anisole (90/5/3/2 v/v), precipitated from the cleavage solution using excess ice-cold diethyl ether, and washed repeatedly with ice-cold diethyl ether. Reverse phase HPLC (Water Delta 600) with a linear gradient of acetonitrile and water (0.1% TFA) was used for peptide purification. The molecular weight of each peptide was verified by MALDI mass spectroscopy. Peptides containing F19 [1-^{13}C] labels were synthesized as described using [1-^{13}C]-phenylalanine and also confirmed by MALDI mass spectroscopy.

Tube and Fiber Assembly

The nanotubes and fibers were prepared under two conditions in an attempt to exploit the protonation states of the terminal Lys and Glu side chains. Under the first "acidic" condition, purified Aβ (16-22) and its V18 congeners were dissolved respectively in 40% acetonitrile/water with 0.1% TFA to a final concentration of 2.0mM. The peptide solution was allowed to self-assemble and mature at room temperature for 2 weeks. Under the second "neutral" conditions, purified Aβ (16-22) and its V18 congeners

were dissolved respectively in 40% acetonitrile/water to a final concentration of 2.0mM. Because peptides are purified in an acetonitrile/water gradient containing 0.1% TFA, a solution of 0.1M NaOH in 40% acetonitrile/water solution was added to give a 0.1mM NaOH final concentration and peptide assembly was allowed to mature at room temperature for 2 weeks.

Transmission Electron Microscopy (TEM)

Aliquots (20 μl) of a 2mM solution of Aβ(16-22) or the structural congeners were applied to TEM grids (Formvar/carbon film coated 200 mesh, Electron Microscopy Sciences, Hatfield, PA) and allowed to adsorb for 1 min. Excess peptide solution was wicked off with filter paper before 10 μl of 5% uranyl acetate (Sigma-Aldrich) was added for 3 min to stain the sample. Again, excess fluid was wicked off with filter paper and the grid was dried under house vacuum overnight. Each micrograph was recorded on a Hitachi H-7500 transmission electron microscope instrument with a tungsten emission filament at an accelerating voltage of 75 kV. Negatives were scanned at 1800 dpi on Microtek ArtixScan 1800f scanner. (Microtek Lab, Inc., Carson, CA).

Small Angle X-ray Scattering (SAXS)

SAXS was carried out at Sector 12-ID with the Advanced Photon Source (APS) at Argonne National Laboratory using 12 keV X-rays and a Mar CCD with a sample-to-detector distance of 2m. To reduce radiation damage, the sample solutions were allowed to flow through a 1.5 mm quartz capillary using a Hamilton syringe pump. SAXS intensity $I(Q)$ for a dilute system of scattering particles can be described by equation 1,

$$I(Q) = I_0 n(\Delta\rho)^2 V^2 P(Q) + I_b \qquad (1)$$

where I_0 is an instrument constant, n, the number density of the particles, $\Delta\rho$, the difference in electron density between particles and solvent (contrast), V, the volume of the particles, I_b, the flat background intensity and $P(Q)$, the particle form factor (Lu 2003). Q is the momentum transfer given by $Q = (4\pi/\lambda)\sin(\theta/2)$, where λ is the X-ray wavelength and θ is the scattering angle.

Scattering curves with no oscillations, but with a power law of -1 in the low Q region, were interpreted using a modified Guinier analysis for rod-like particles (fibers) by plotting $\ln[Q \bullet I(Q)]$ versus Q^2. From the slope of a fit to a linear Q^2 region at $0.4 < Q_{max} \bullet R_c < 1.0$ in the modified Guinier plot the cross-sectional radius of gyration of the fiber, R_c (corresponding Radius $R = \sqrt{2} \bullet R_c$), can be derived using R_c^2 = -2•slope. Scattering data exhibiting a power law of -2 in the lower Q are interpreted using a modified Guinier analysis for sheet-like particles by plotting $\ln[Q^2 \bullet I(Q)]$ versus Q^2. The slope from a fit to the linear Q^2 region at $Q \bullet R_t < 0.85$ was used to determine the thickness factor of the sheet, R_t (corresponding thickness $T = \sqrt{12} \bullet R_t$) using R_i^2 = -slope.

Scattering curves with oscillations were fit to a hollow circular cylinder (nanotube) model by substituting for $P(Q)$ in Eq. 1 with the following form factor expression:

$$P(Q) = \int_0^1 \left(\frac{1}{1-(R_2/R_1)^2} \right)^2 \left[\frac{2J_1\left(QR_1\left(1-x^2\right)^{0.5}\right)}{QR_1\left(1-x^2\right)^{0.5}} - \right.$$

$$\left. (R_2/R_1)^2 \frac{2J_1\left(QR_2\left(1-x^2\right)^{0.5}\right)}{QR_2\left(1-x^2\right)^{0.5}} \right]^2 \left(\frac{\sin(QLx/2)}{QLx/2} \right)^2 dx \quad (2)$$

where R_1 is the outer radius, R_2, the inner radius, L, the cylinder length and $J_1(x)$ is the Bessel function of the first order. Although the peak positions and amplitudes agree well between the measured SAXS data and the fits using Eq. 2, they do not match very well at the minima due to factors such as instrument resolution, presence of smaller aggregates under equilibrium, roughness along the surfaces of the nanotubes, orientation disorder, etc. We like to point out that the slight disagreement in the amplitudes at the minima will not alter the precision of the structural parameters and conclusions.

Wide Angle X-ray Scattering (WAXS)

Powder samples in 1.5mm diameter quartz capillary tubes were measured at the APS facility using 18 keV X-rays and a smaple-to-detector distance of 0.4m. From the diffraction peaks the repeat distance $d = (2\pi/Q)$ were derived. Intense, sharp and narrow reflections imply high degree of repetition order while the weaker and broad peaks indicate smaller crystallite size with fewer repetitions or the presence of disorder in the crystallinity.

Isotope-Edited Fourier Transform Infrared Spectroscopy (IE-FTIR)

A 500 µL solution of mature tubes or fibers were spun down at 16,100 x g for 30 min and the pellet was frozen at -80^{o}C and lyophilized. The lyophilized sample was mixed with dehydrated KBr crystals at a ratio of 1:10 (w/w), pressed into a KBr/peptide pellet, and analyzed on a MAGNA-IR 560, E.S.P. instrument operated at 2 cm^{-1} resolution.

Molecular Modeling

Six copies of the seven residue Ac-KLVFFAE-NH_2 peptide were combined twice graphically in Maestro v8.0 (Schrodinger) (Spoel 2003) to produce two versions of the

six-strand antiparallel β-sheet with full hydrogen bonding as depicted in Scheme 1.1.. The strands were organized either as in-register β-sheets corresponding to fibers or as one-residue-shifted nanotubes. Five copies of the identical sheets were then stacked atop one another to provide five homogeneous laminates. To prepare for subsequent molecular dynamics simulations, the laminates were relieved of unfavorable torsions and steric contacts by energy minimization using the Truncated Newton Conjugate Gradient method and the GBSA/Water continuum solvation model. The relaxed peptide laminates were then enclosed in a truncated octahedral box and surrounded by 30,000-60,000 SPC water molecules in GROMACS v3.3. For peptides with positive charges, chloride ions were added to make the system neutral. The systems were prepared for MD simulations by performing initial energy minimizations on the aggregates for 10 ps using a steepest descent algorithm followed by solvent equilibration for 20 ps. Unrestrained MD was subsequently carried out for 2 ns at 300K with a 2 fs time step using the OPLS 2005 force field. The resulting trajectories were viewed with VMD, and RMSD plots were generated using the xmgrace routine in GROMACS. Lipophilic potentials were mapped onto Connolly surfaces generated in the MOLCAD surface viewer with sphere radius of 1.4Å in SYBYL 7.2 (SYBYL 7.3).

RESULTS

Assembly Morphology

Conditions for the homogeneous assembly of Aβ(16-22), Ac-KLVFFAE-NH_2, into fibrils and nanotubes have been described (Lu 2003, Mehta 2008), and here two conditions are used. When the peptide was dissolved in 40% acetonitrile/water with 0.1%

TFA, where both the K16 and E22 side chains are predicted to be protonated and maintain a single positive charge at the *N*-terminus (acidic condition), the peptide assembles into homogeneous nanotubes. Under the same conditions but containing 0.1mM NaOH instead of TFA to ionize the Glu sidechain (neutral conditions), Aβ(16-22) is expected to carry a positive charge at the *N*-terminus and a negative charge at the *C*-terminus. Under these conditions the peptide assembles as homogeneous fibrils (Mehta 2008). The two morphologies are reversible and interconvert with changes in the assembly conditions, but probably through disassembly as they contain a shift in peptide strand registry (Mehta 2008); antiparallel in-register for fibrils and antiparallel one residue shifted for nanotubes. It has been suggested that the stability of the pairwise K-E salt bridge contributes to the registry of the fibers and is weakened under the more acidic conditions (Mehta 2008).

The contribution of cross-strand pairing complementarity to sheet registry was further evaluated by replacing the only β-branched residue V18 in Aβ(16-22) with a series amino acids that varied in side chain steric demand. For example, when the 18^{th} position differed by no more than a single CH_2 from valine, e.g., Abu, Leu, norL and norV, only fibers formed under the acidic conditions (Figure 2.1.). However, the β-branched amino acids Ile and terL directed nanotube assembly, and the most sterically demanding terL congener directed nanotube assemble even under neutral conditions (Figure 2.1.d and Figure 2.2.f).

Figure 2.1. TEM of self-assembled structures

(a) Aβ(16-22) nanotubes assembled under acidic conditions

(b) Aβ(16-22) fibers assembled under neutral conditions

(c) Nanotubes or fibers formed by Aβ(16-22) V18 congeners under acidic conditions, scale=100nm. Inset: the side chain structure of the residue substituted at the 18^{th} position.

(d) Nanotubes or fibers formed by Aβ(16-22) V18 congeners under acidic conditions, scale=100nm.

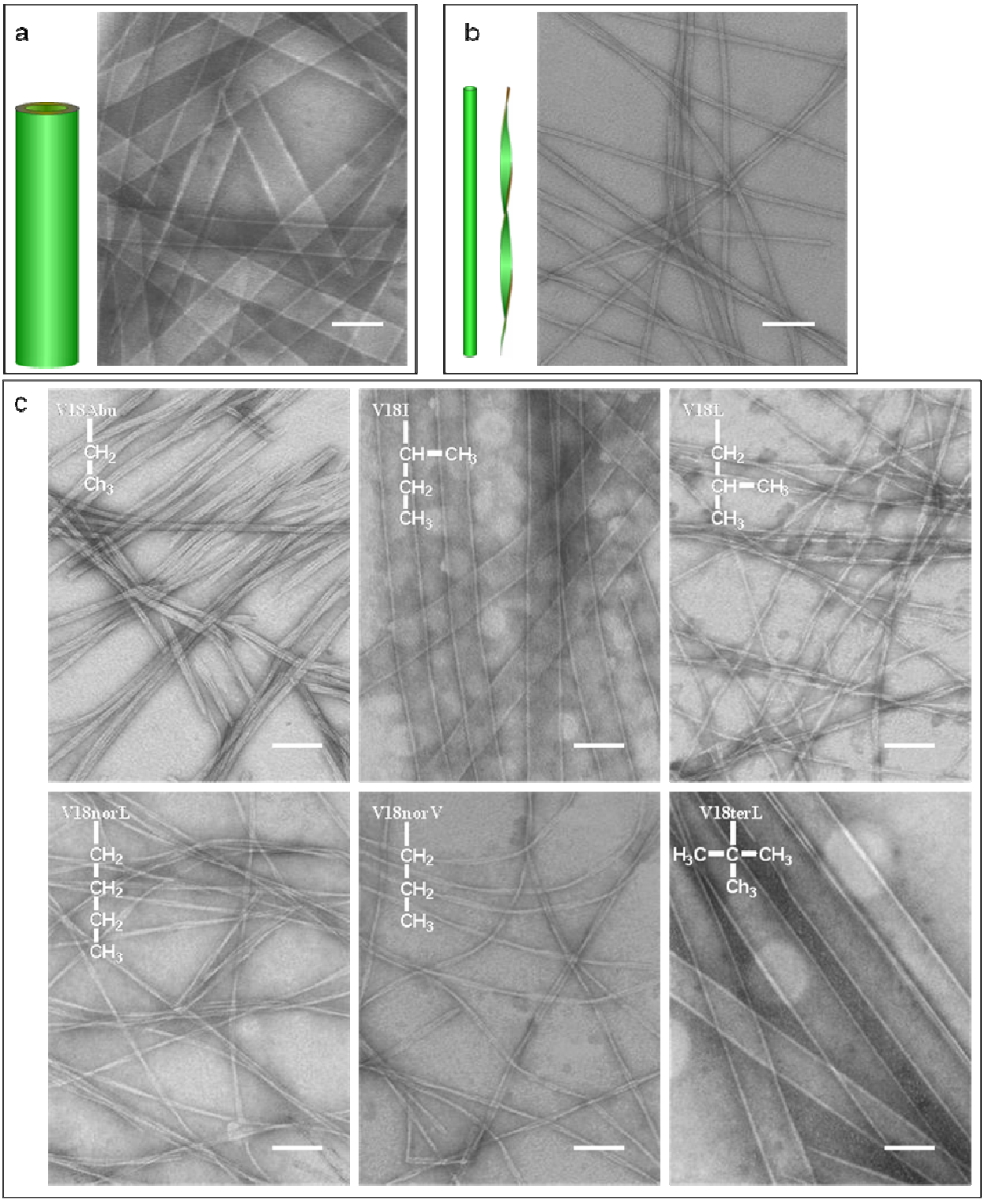
a
b
c
V18Abu
V18I
V18L
V18norL
V18norV
V18terL

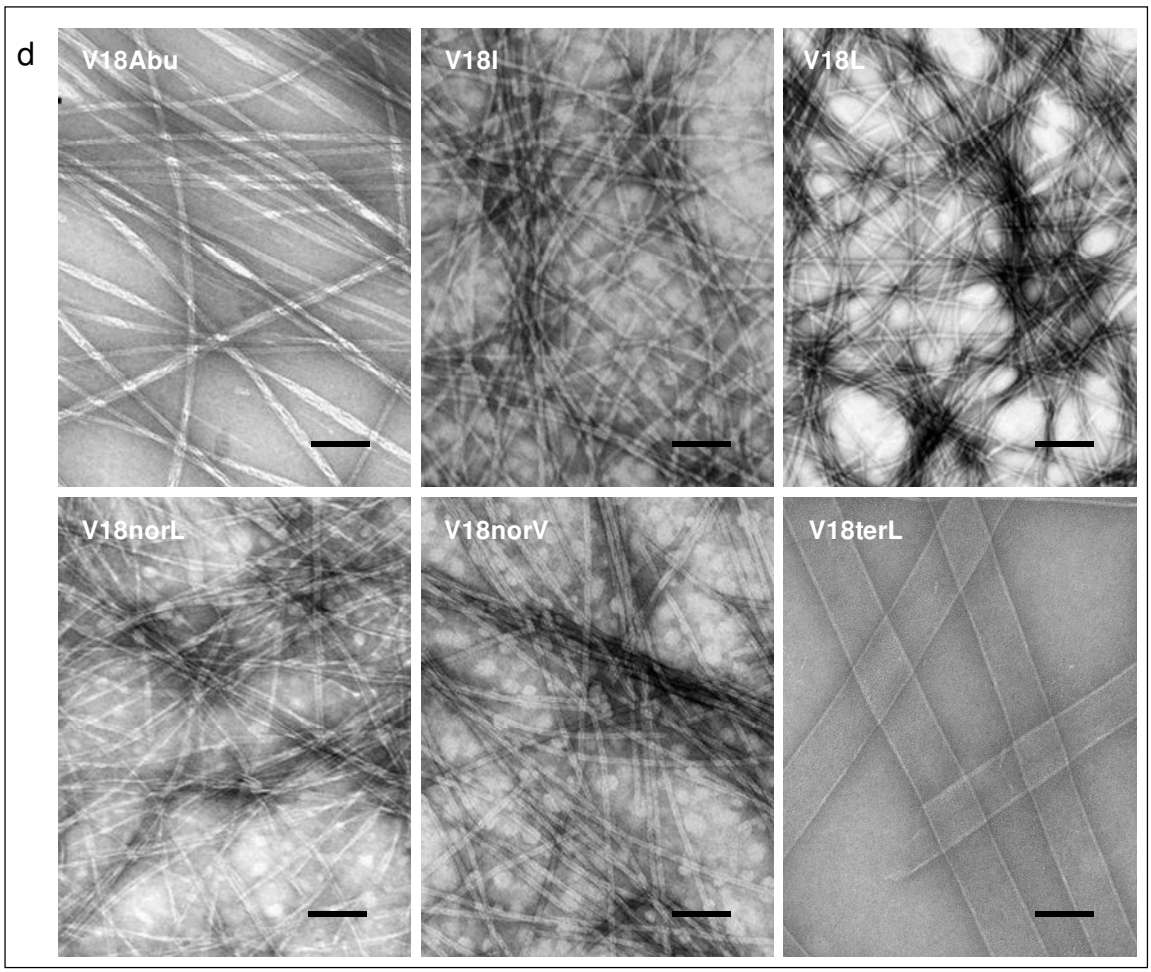

The fiber and nanotube morphologies are readily differentiated in solution by the pronounced oscillations that originate from the differential X-ray reflections of the inner and outer walls of the hollow nanotubes (Lu 2003). In contrast, fibers exhibit a Q^{-1} power-law in the low Q region that can be analyzed by a modified Guinier fit with a rod-like or sheet-like form factor. As shown in Figure 1.2., the fibers have similar diameters, ranging from 8 to 16nm (Table 2.1.), or about 3-6 times smaller than the 52 ± 8nm nanotubes (shell thickness ~4nm) of V18I and V18terL congeners. The V18terL peptide forms nanotubes that maintain identical cross-sectional area under both neutral and acidic conditions (Figure 2.2.f), and the attenuated amplitude in neutral conditions is consistent

with a lower nanotube concentration. Wide-angle X-ray scattering (WAXS) confirmed the characteristic cross-β amyloid pattern (Figure 2.3. and Table 2.1.). The 4.7Å reflection is sharp and strong for all the assemblies, whereas the 10Å band is specifically characteristic of the nanotubes (Figure 2.3.a) and consistent with a larger number of laminates for these structures (Lu 2003, Mehta 2008, Dong 2006).

Table 2.1. Structural Parameters from the SAXS of solutions and WAXS of powders of fibers and nanotubes formed by Aβ(16-22) and its V18 congeners under neutral and acidic conditions.

Peptides	Solution SAXS			Powder Diffraction	
	Fibers (Å)	Tubes (Å)		Distance correlations (Å)	
	Outer Radius	Outer Radius	Shell Thickness	Inter-Strand	Inter-Sheet
Acidic condition					
Aβ(16-22)	**-**	**263.7 ± 2.0**	**39.0 ± 1.0**	**4.72**	**9.9**
V18I	**-**	**223.7 ± 1.1**	**34.0 ± 1.0**	**4.71**	**10.1**
V18terL	**-**	**301.6 ± 5.0**	**38.0 ± 1.0**	**4.71**	**10.1**
V18Abu	87.3 ± 0.3	-	-	4.63	*10.0*
V18L	39.67 ± 0.03	-	-	4.64	*10.4*
V18norL	36.73 ± 0.07	-	-	4.64	-
V18norV	62.7 ± 0.1	-	-	4.67	*10.4*
Neutral condition					
Aβ(16-22)	**59.0 ± 0.2**	**-**	**-**	**4.70**	***9.9***
V18I	**49.5 ± 0.1**	**-**	**-**	**4.69**	***10.3***
V18terL	**-**	**282 ± 11**	**39.0 ± 1.0**	**4.76**	**10.2**
V18Abu	56.0 ± 0.1	-	-	4.68	*11.2*
V18L	60.6 ± 0.1	-	-	4.71	*10.6*
V18norL	45.2 ± 0.1	-	-	4.68	-
V18norV	44.6 ± 0.1	-	-	4.67	*11.5*

Bold face: Aβ(16-22) and β-branched V18 congeners; *Italics face: Weak and broad inter-sheet correlation peak*

Figure 2.2. SAXS of V18 congeners

(a) SAXS of fibers assembled under acidic conditions: V18Abu(□, black), V18L(△, green), V18norL(▽, cyan), and V18norV(○, blue)

(b) Modified Guinier analysis of fibers assembled under acidic conditions with sheet-like forms (fit in red): V18Abu (□, black), and V18norV (○, blue)

(c) Modified Guinier analysis of fibers assembled assembled under acidic conditions with rod-like forms (fit in red): V18L (△, green), and V18norL (▽, cyan)

(d) SAXS scattering of tubes under acidic conditions, and their shell core circular cylinder fitting (in red): Aβ(16-22) (■, black), V18I (▲, green), and V18terL (▲, blue)

(e) Modified Guinier analysis of fibers assembled under neutral conditions with rod-like forms (fit in red): Aβ(16-22) (■, black), V18I(▼, green), V18Abu(□, black), V18L(△, green), V18norL(▽, cyan), and V18norV(○, blue)

(f) SAXS scattering of V18terL tubes, and their shell core circular cylinder fitting (in red): formed under acidic (▲, blue) and neutral conditions (●, blue).

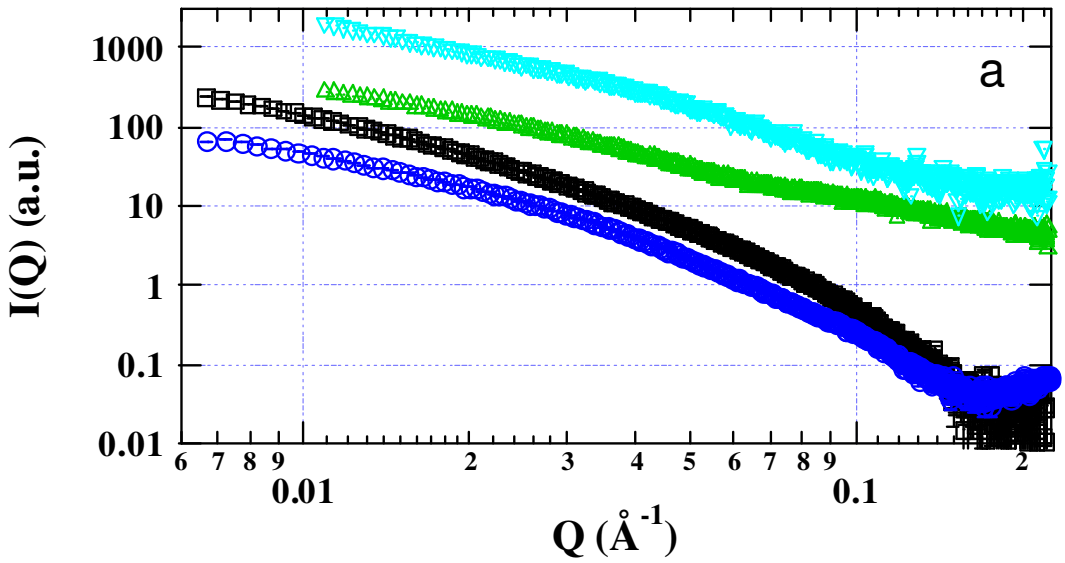
a
I(Q) (a.u.)
1000
100
10
1
0.1
0.01
6 7 8 9
0.01
2 3 4 5 6 7 8 9
0.1
2
Q (Å-1)

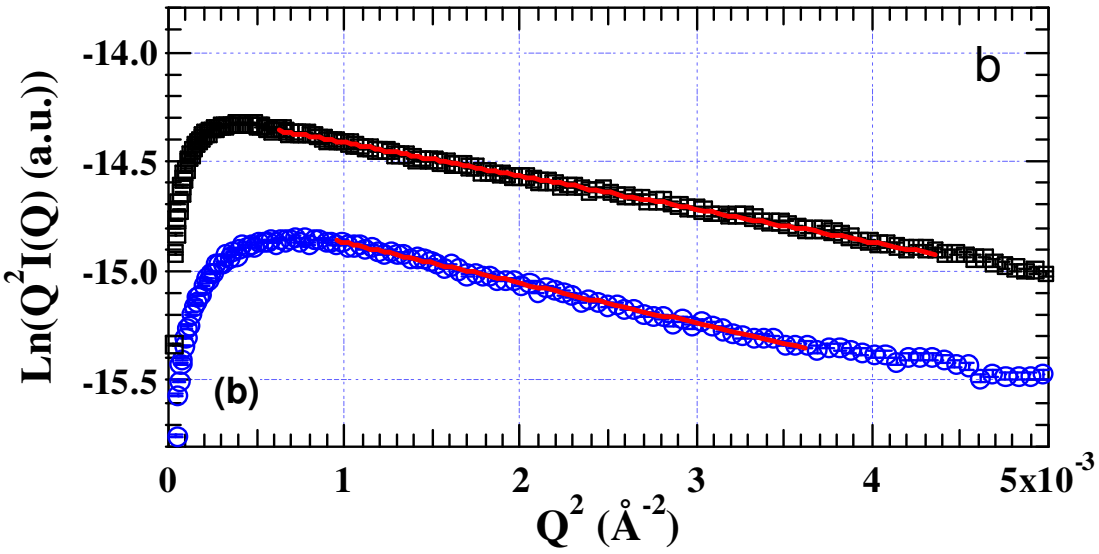
b
Ln(Q2I(Q) (a.u.))
-14.0
-14.5
-15.0
-15.5
(b)
0
1
2
3
4
5x10-3
Q2 (Å-2)

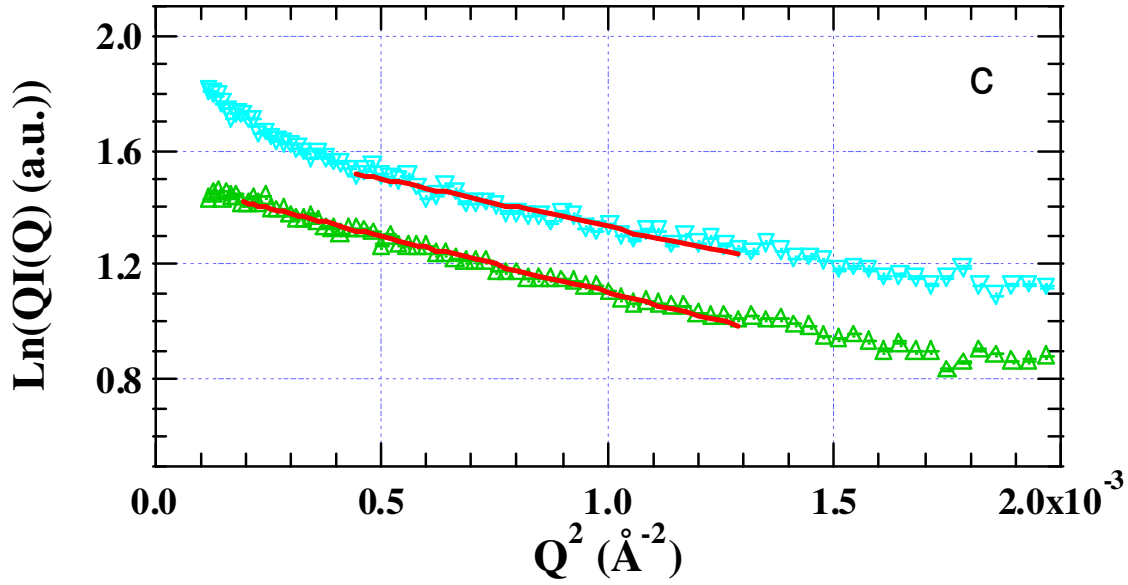
c
Ln(QI(Q) (a.u.))
2.0
1.6
1.2
0.8
0.0
0.5
1.0
1.5
2.0x10-3
Q2 (Å-2)

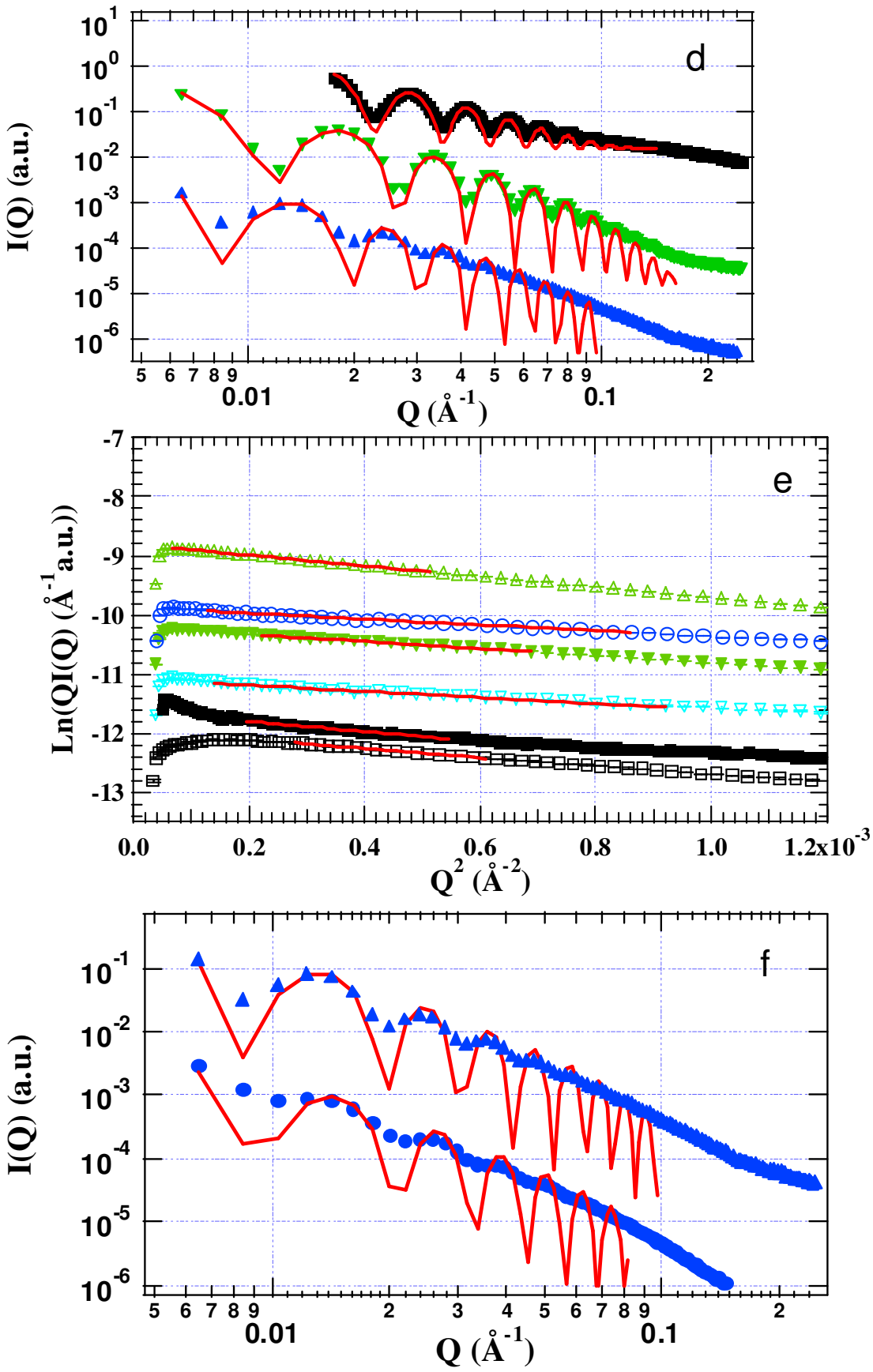
d
I(Q) (a.u.)
Q (Å^{-1})
e
Ln(QI(Q) (Å^{-1}a.u.))
Q^2 (Å^{-2})
f
I(Q) (a.u.)
Q (Å^{-1})

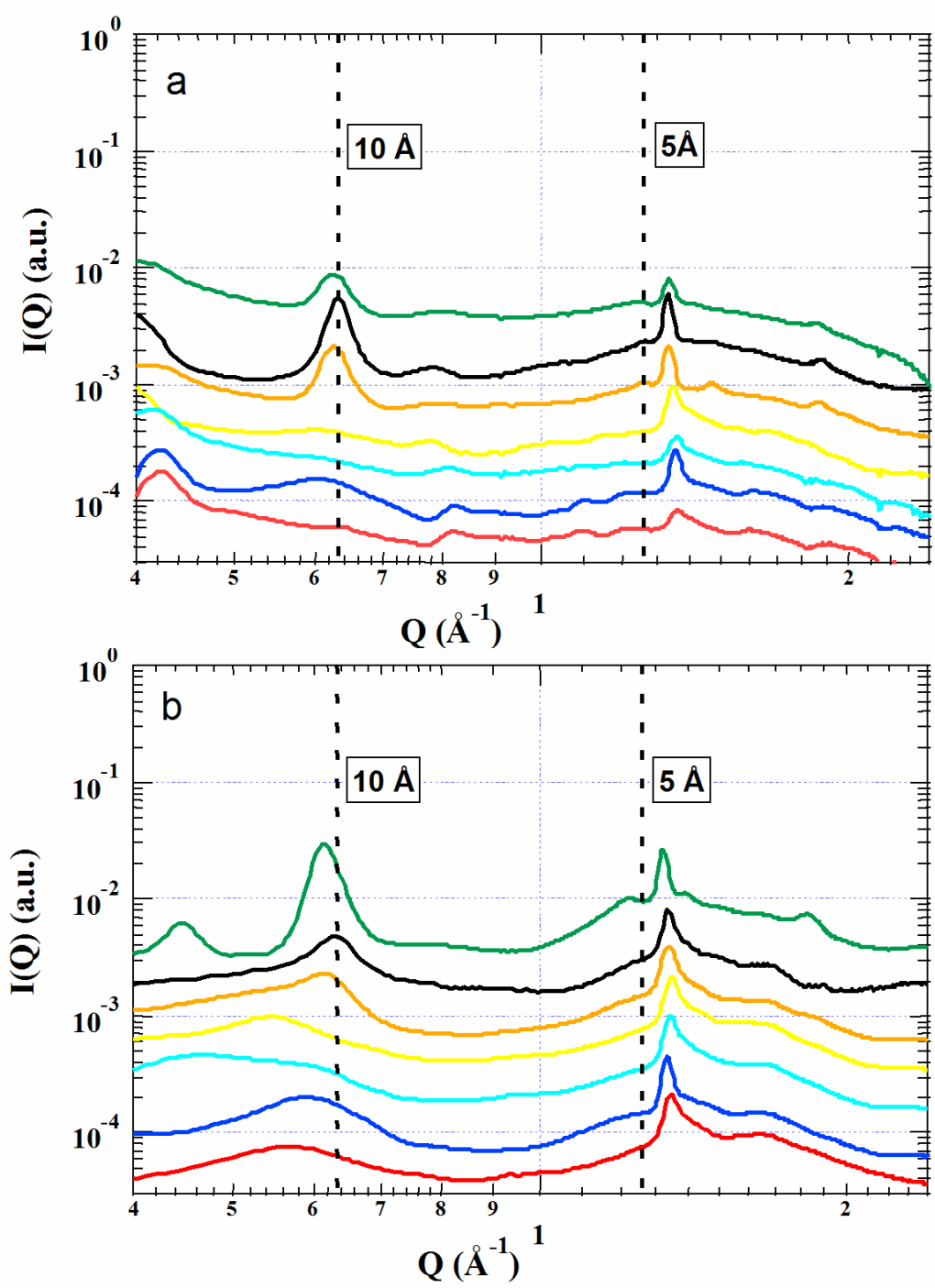

Figure 2.3. Inter-stand and inter-sheet WAXS of V18 congeners

V18terL (green), Aβ(16-22) (black), V18I (orange), V18norV (yellow), V18norL (cyan), V18L (blue), and V18Abu (red) assembled under (a) acidic or (b) neutral conditions.

Table 2.2. ^{12}C and ^{13}C amide I band shifts in IE-FTIR of fibers and nanotubes formed by Aβ(16-22) and its V18 congeners under neutral and acidic conditions.

Peptides	^{12}C shift (cm^{-1})	^{13}C shift (cm^{-1})	The split between ^{12}C and ^{13}C (cm^{-1})
Acidic condition			
Aβ(16-22)	**13**	**29**	**42**
V18I	**12**	**28**	**40**
V18terL	**14**	**29**	**43**
V18Abu	7	20	27
V18L	8	24	32
V18norL	7	22	29
V18norV	7	21	28
Neutral condition			
Aβ(16-22)	**8**	**21**	**29**
V18I	**9**	**23**	**32**
V18terL	**14**	**28**	**42**
V18Abu	6	18	24
V18L	9	22	31
V18norL	7	22	29
V18norV	7	20	27

Bold face: Aβ(16-22) and β-branched V18 congeners.

Strand Registry

To better visualize the impact of a one-residue shift in β-sheet registry on each face of the β-sheet, they are color coded in Figure 2.5.c. The side chains of K, V, F(20) and E (green bar) alternate with the side chains L, F(19), and A (purple bar) along each face of the register-shifted nanotube β-sheets. In contrast, the in-register sheets isolate K-V-F(20)-E side chains and L-F(19)-A side chains to opposite faces, giving polar and non-polar β-sheet surfaces.

Strand registry of the antiparallel β-sheets of Aβ(16-22) fibers (Antzutkin 2002) and nanotubes (Mehta 2008) display a range of spectroscopic signatures. Within these Aβ(16-22) congeners, the characteristic β-sheet amide I infrared stretch centered at $1627cm^{-1}$ and the higher energy but weaker shoulder at $1694cm^{-1}$ proved to be most diagnostic of antiparallel sheets (Mehta 2008, Elliott 1950, Halverson 1991), independent

of strand registry (Figure 2.4.). In addition, isotope-edited FTIR (IE-FTIR) reported on β-sheet strand registry (Kubelka 2001, Hiramatsu 2005, Paul 2005, Petty 2005, Decatur 2006) because a β-sheet sequence containing a single ^{13}C carbonyl substitution splits the amide I band into distinct transitions corresponding to the ^{12}C and ^{13}C components at higher and lower energy, respectively. This splitting arises from the mass-dependent vibrational frequency that limits coupling between the ^{12}C and ^{13}C carbonyls along the sheet (Mehta 2008, Kubelka 2001, Hiramatsu 2005, Paul 2005, Petty 2005, Decatur 2006). When ^{13}C carbonyls are aligned and positioned closely within adjacent sheets, transition dipole coupling (TDC) contributes significantly to both the stretching frequency and band separation. For example, Aβ(16-22) nanotubes contain one-residue shifted antiparallel β-sheets where the carbonyls of F19 are aligned along the center of the β-sheet and the band splitting is 42 cm^{-1} (Figure 2.5.b, carbonyl in red). In contrast, the fibrils display in-register antiparallel β-sheets where the F19 carbonyls are cross-aligned and the band splitting is 29 cm^{-1} (Figure 2.5.e).

Under acidic conditions, both V18I and V18terL nanotubes have ^{12}C / ^{13}C band splits of 40 and 42cm^{-1} respectively, similar to the 42cm^{-1} for the Aβ(16-22) nanotubes (Figure 2.5.a and Table 2.2.). The non-β-branched congener fibers have ^{12}C and ^{13}C band splits in a range of 27-32cm^{-1}; V18Abu (27cm^{-1}), V18L (32cm^{-1}), V18norL (29cm^{-1}), and V18norV (28cm^{-1}) (Figure 2.5.a and Table 2.2.), reflecting the Aβ(16-22) fibers value of 29cm^{-1}. The V18terL nanotubes under neutral conditions also have a ^{12}C / ^{13}C band split of 42cm^{-1}, consistent with the one-residue shifted registry (Figure 2.5.d and Table 2.2.), whereas all other V18 congeners under neutral assembly conditions have ^{12}C / ^{13}C amide I bands separated by 24~32cm^{-1}, assigned as in register backbone arrays. Therefore,

within the V18 congener β-sheets, one-residue shifted strands are present in the nanotube morphologies and in-register assemblies are present in fibers, just as in native Aβ(16-22).

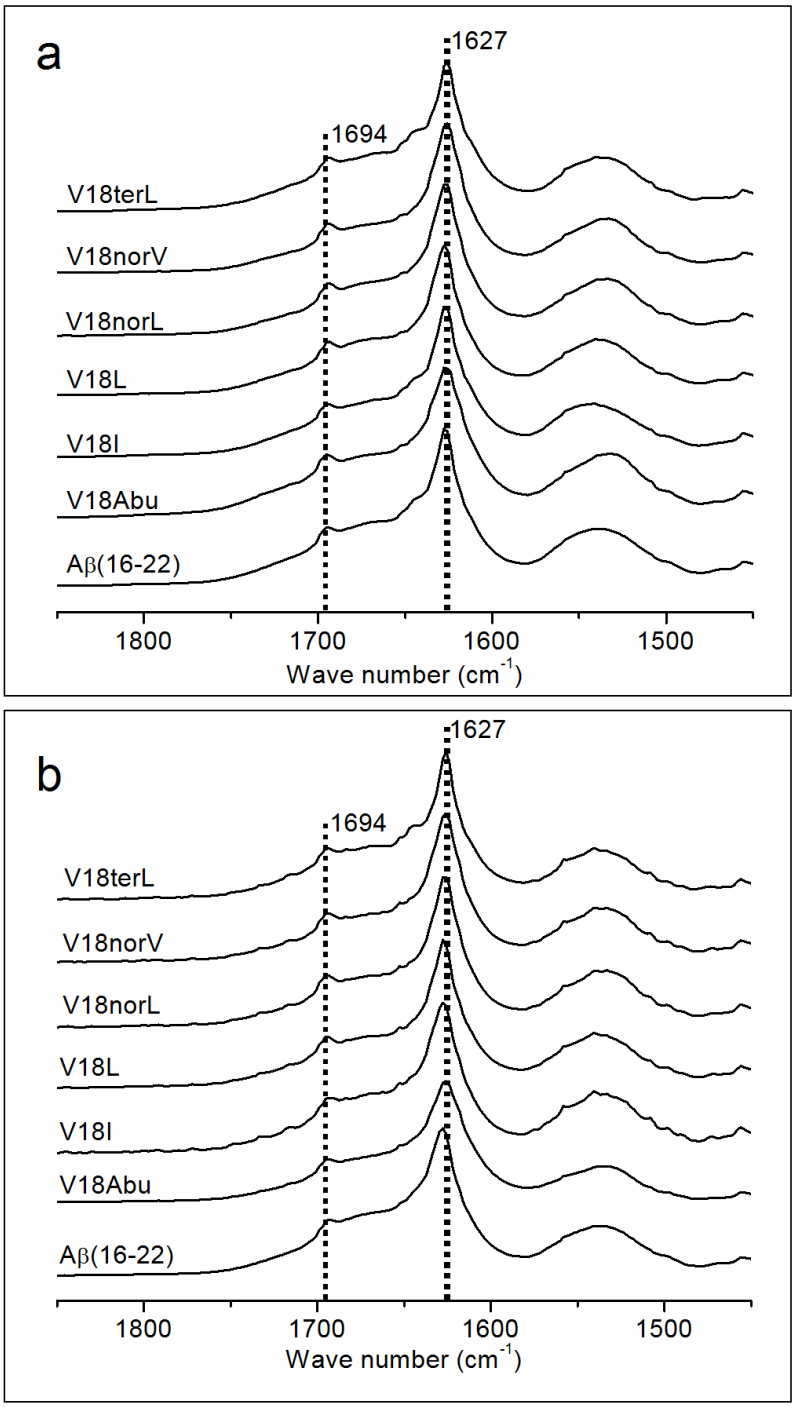

Figure 2.4. FTIR amide I band of V18 congeners self-assembled under (a) acidic conditions, and (b) neutral conditions.

Figure 2.5. IE-FTIR of V18 congeners

(a) ^{12}C / ^{13}C amide I absorbance under acidic conditions

(b) Antiparallel one-residue-shifted β-sheet of Aβ(16-22) with F19 carbonyl in red

(c) Side chain distribution of the antiparallel one-residue-shifted Aβ(16-22) β-sheet, K-V-F(20)-E in green and L-F(19)-A in pink

(d) ^{12}C / ^{13}C amide I absorbance under neutral conditions

(e) Antiparallel in-register β-sheet of Aβ(16-22), with F19 carbonyl in red

(f) Side chain distribution of the antiparallel in-register Aβ(16-22) β-sheet, K-V-F(20)-E in green and L-F(19)-A in pink.

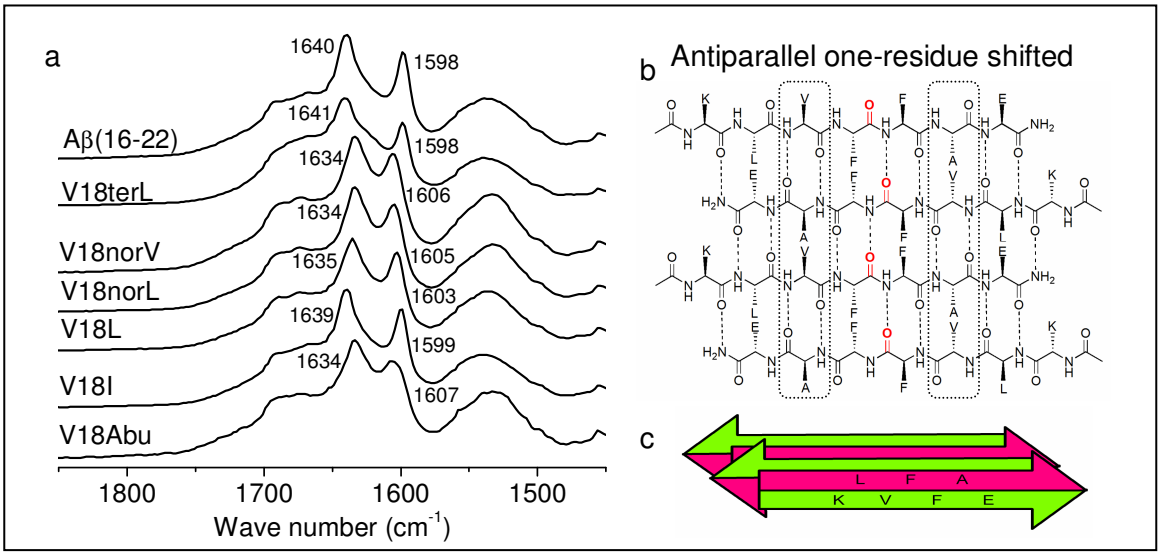
a
1640
1598
Aβ(16-22)
1641
1598
V18terL
1634
1606
V18norV
1634
1605
V18norL
1635
1603
V18L
1639
1599
V18I
1634
1607
V18Abu
1800
1700
1600
1500
Wave number (cm-1)
b
Antiparallel one-residue shifted
c
L F A
K V F E

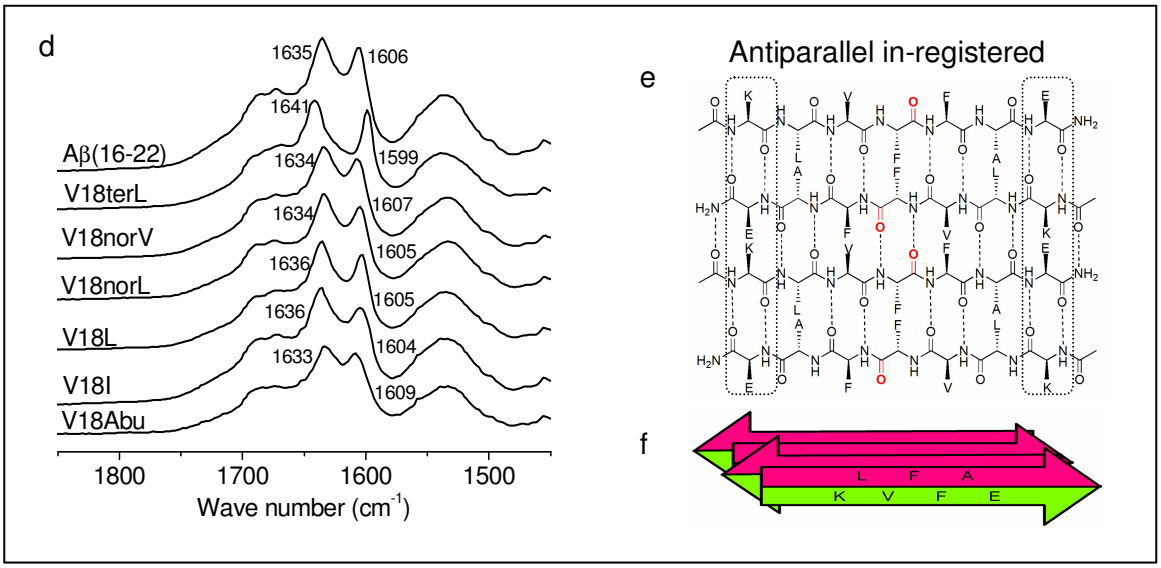
d
1635
1606
Aβ(16-22)
1641
1599
V18terL
1634
1607
V18norV
1634
1605
V18norL
1636
1605
V18L
1636
1604
V18I
1633
1609
V18Abu
1800
1700
1600
1500
Wave number (cm-1)
e
Antiparallel in-registered
f
L F A
K V F E

Molecular Modeling

To approximate side-chain arrangements, the structural features of the 6-strand, 5-sheet Aβ(16-22) arrays were captured by averaging over the last 20 ps of the trajectories of molecular dynamics (MD) simulations. Lipophilic surfaces were generated in Sybyl for the central ß-sheet; namely the third strand in each of the laminates. Figure 2.6. displays this averaged property for the top and bottom surfaces of the one-residue shifted and in-register β-sheets. For the one-residue shifted sheet, both surfaces appear very similar. In contrast, the in-register β-sheet surfaces differ significantly in their lipophilic characteristics. Furthermore, Lys-Glu cross-strand electrostatic interactions are abundant between adjacent peptides within the in-register β-sheets (Figure 2.7.), suggesting an important contribution to the in-register β-sheet stability. This feature is absent in the one-residue shifted sheet models because Lys and Glu in the adjacent strands are positioned on opposite sides of each sheet (Figure 2.6. and Figure 2.8.). Hydrogen bonding between the polar Lys and Glu residues is precluded within the β-sheets. Therefore, the modeling predicts the Lys-Glu salt-bridges under neutral conditions could indeed contribute substantial electrostatic stabilization to the in-register β-sheet integrity.

Since energetic differences resulting from changing nonpolar amino acid side chains to β-branched ones are assumed to be largely steric, these differences were probed using molecular mechanics. Especially in the absence of explicit solvent, force fields overemphasize electrostatic interaction energies (Lakdawala 2001). On the other hand, they are well parameterized to reproduce steric energies. To minimize the role played by side-chain electrostatic interactions that might lead to energetic overstabilization and to estimate the steric contribution of cross-strand pairing to the stability of β-sheet

assemblies, the Lys and Glu residues in each peptide strand were replaced with alanine and the relative energies estimated with energy minimization (Table 2.3.). For each peptide, the central 3-strand β-sheets were compared, either in-register or one-residue-shifted antiparallel registry, and the structures minimized with both OPLS 2005 and AMBER 94. When expressed as ΔΔE ($\Delta E_{\text{one residue-shifted}} - \Delta E_{\text{in-register}}$), the in-register arrangement, which contains one additional H-bond, is lower in energy in each case. However, with β-branched residues at 18, the energy difference is reduced significantly (Table 3), consistent with the β-branched residue at 18 preferring the one-residue-shifted registry. For example, the peptide with the non-β-branched Leu at 18 has the largest absolute ΔΔE, about 4 kcal/mol. With the β-branched residue, Val or Ile, the ΔΔEs are reduced to 2.5 kcal/mol, and with terL, the ΔΔE is further reduced to 0.5 kcal/mol. These results are consistent with the experimental observation that peptides with β-branched residues at 18 significantly favor a one-residue-shifted registry, and support side-chain packing along the sheet face as a significant contributor to β-sheet assembly and amyloid nucleation.

To determine the hydrophobic surface burial between non-β-branched and β-branched amino acid side chains within the Aβ(16-22) V18 congeners, their 3-strand antiparallel in-register or one-residue-shifted β-sheets were compared (Table 2.4.). For each peptide, the buried surface area was calculated by subtracting the solvent accessible surface area (SASA) value in the β-sheet from its corresponding value in the random coil (Yan 2007, Lesser 1990). The Val, Ile or Leu congeners did not differ significantly in the mean fraction buried, f, which is an intrinsic measurement of the hydrophobicity (Lesser 1990). More significantly, the peptides with Leu or Ile at 18 have the same number of

atoms, and their difference in buried surface area upon forming the β-sheet is less than 1% in both in-register and one-residue-shifted β-sheets.

Table 2.3. Energy difference between in-register and one-residue-shifted registries of Aβ(16-22) and its V18 congeners.

Peptides	OPLS_2005 (kcal/mol)	AMBER94(kcal/mol)
Ac-AL**V**FFAA-NH_2	2.27	2.43
Ac-AL**I**FFAA-NH_2	2.79	3.24
Ac-AL-**terL**-FFAA-NH_2	0.61	0.44
Ac-AL**L**FFAA-NH_2	3.93	5.42

Notes: 1. For each peptide, the simulation is done with 3-strands of either antiparallel in-register and antiparallel one-residue-shifted β-sheets. 2. The energy difference is calculated as $\Delta\Delta E=\Delta E_{\text{one-residue-shifted}} - \Delta E_{\text{in-register}}$ for each peptide in each force field.

Table 2.4. Buried surface area of Aβ(16-22) and its V18 congeners.

	Ac-AL**V**FFAA-NH_2	Ac-AL**I**FFAA-NH_2	Ac-AL**L**FFAA-NH_2
A^0_T	3990.3	4039.8	4076.1
$A^0_{B\text{-}B}$	1378.2	1362.6	1375.8
$A^0_{S\text{-}C}$	2612.1	2677.2	2700.3
Antiparallel One-residue-shifted β-sheet			
A_T	1076.1	1107.6	1147
A_{phi}	583.4	583.6	593.3
A_{pho}	492.8	524	553.7
ΔA_T	2914.2	2932.2	2929.1
ΔA_{phi}	794.8	779.0	782.5
ΔA_{pho}	2119.3	2153.2	2146.6
Antiparallel in-register β-sheet			
A_T	1131.7	1100.6	1099.7
A_{phi}	527.9	545.5	539.4
A_{pho}	603.8	555.1	560.3
ΔA_T	2858.6	2939.2	2976.4
ΔA_{phi}	850.3	817.1	836.4
ΔA_{pho}	2008.3	2122.1	2140.0
Comparison ($\Delta\Delta A=\Delta A_{\text{one-residue-shifted}} - \Delta A_{\text{in-register}}$)			
$\Delta\Delta A_{phi}$	-55.5	-38.1	-53.9
$\Delta\Delta A_{pho}$	111	31.1	6.6

Notes: For each peptide, the simulation is done with 3-strand β-sheet. The unit is $Å^2$. $\mathbf{A^0_T}$ is the total surface area by adding the solvent accessible surface area (SASA) of all seven residues in each peptide, and multiplied by 3 since this is a 3-strand β-sheet. SASA value is from Lesser 1990. $\mathbf{A^0_{S\text{-}C}}$ is the total SASA of the side chains. In our case, all the side chains are all aliphatic or aromatic, which is defined as the hydrophobic surface area. $\mathbf{A^0_{B\text{-}B}}$ is the total SASA of the backbone, defined as hydrophilic area. Because our peptide are capped at the both termini, the surface values of CH3, C=O are used as those in Ala, and the surface value of NH_2 is used as that in Lys. The "$\mathbf{A_{phi}}$" and "$\mathbf{A_{pho}}$" are hydrophilic and hydrophobic surface area of each 3-strand β-sheet calculated from *Maestro*. They are viewed as the hydrophilic or hydrophobic SASA in the folded state. $\mathbf{\Delta A_{phi}= A^0_{B\text{-}B} - A_{phi}}$, $\mathbf{\Delta A_{pho}= A^0_{S\text{-}C} - A_{pho}}$ (*Lesser 1990*).

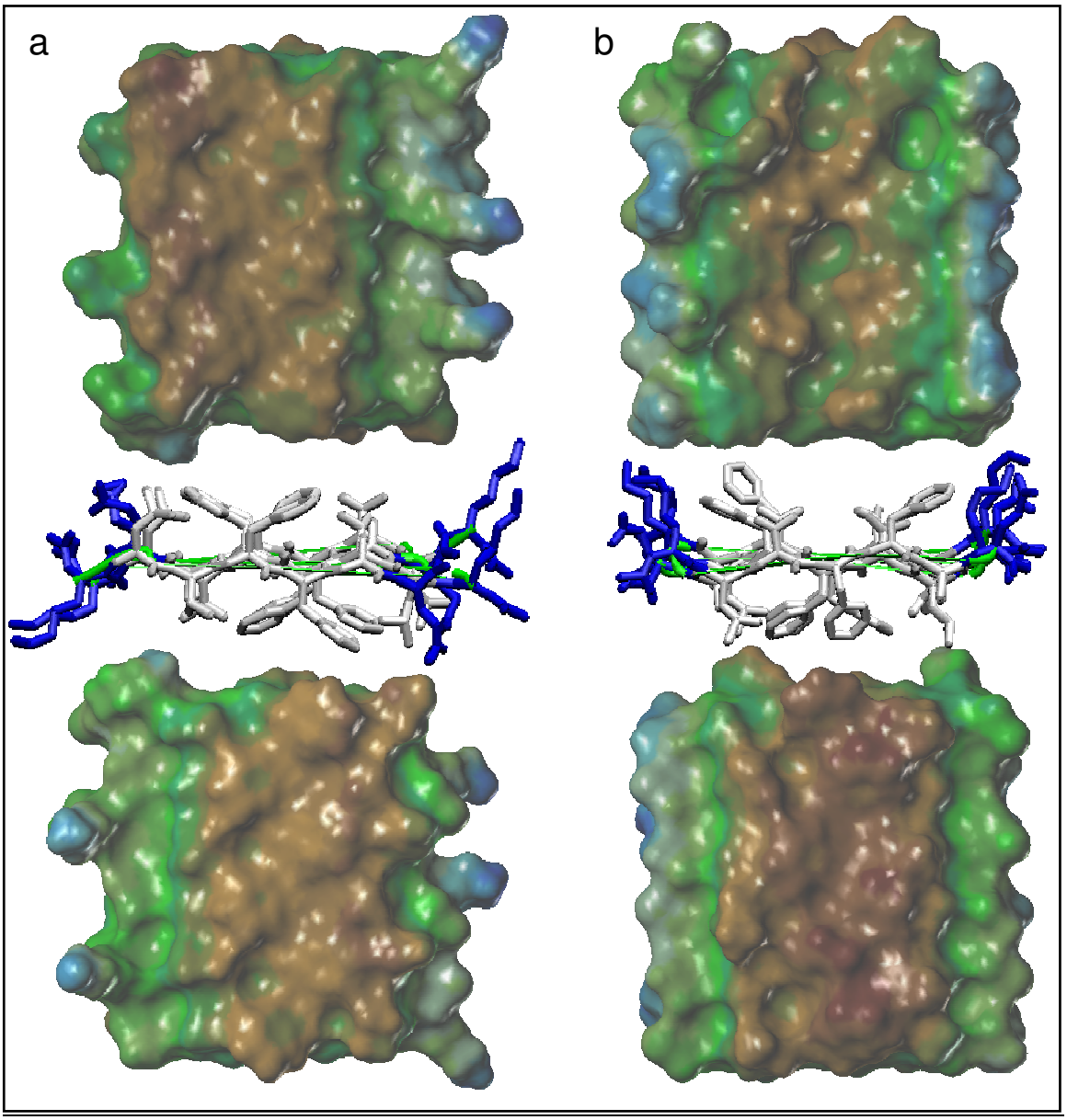

Figure 2.6. Surface lipophilicity

(a) Aβ(16-22) antiparallel one-residue-shifted β-sheet

(b) Aβ(16-22) antiparallel in-register β-sheet. Color scale of lipophilicity: brown more hydrophbobic to blue more hydrophilic. Color of four-strand β-sheet building: backbone is green, Lys and Glu are blue, and hydrophobic residues are white.

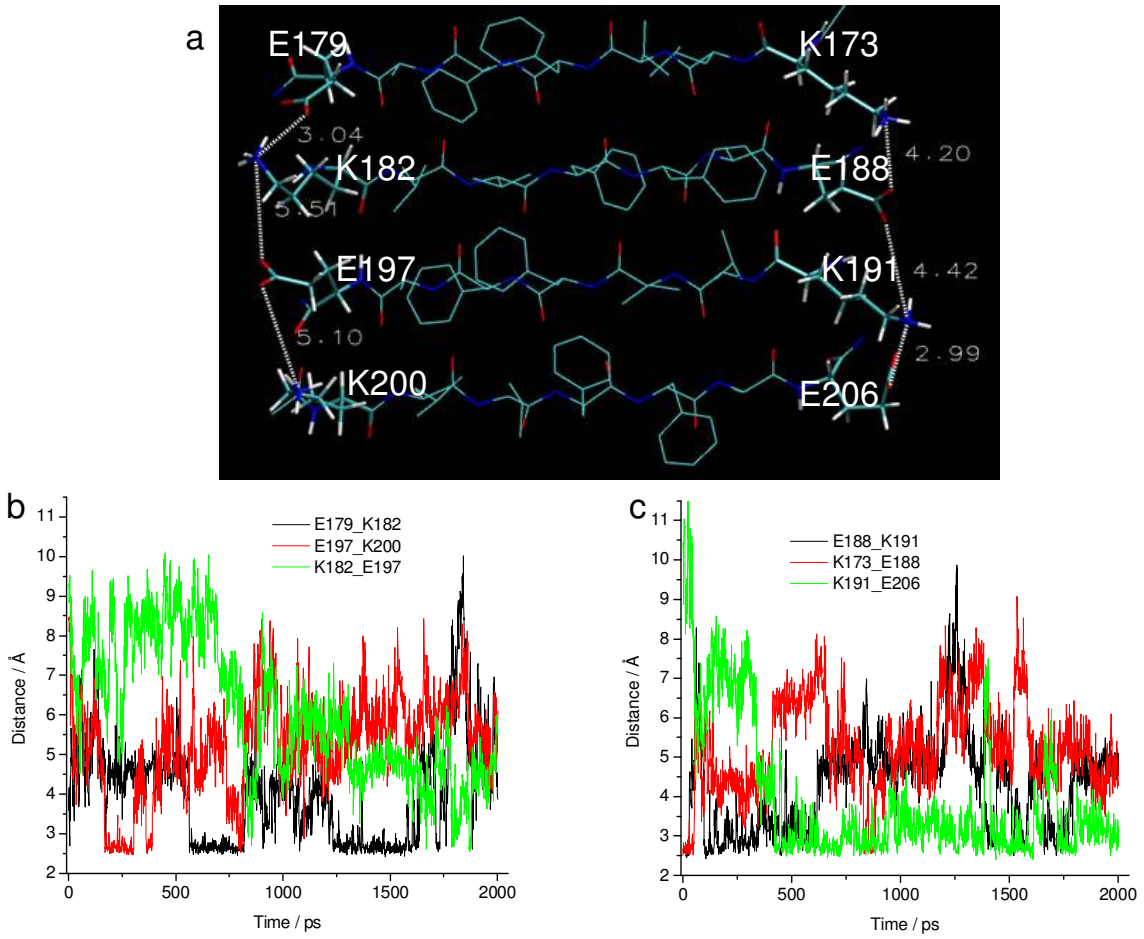

Figure 2.7. Side chain distance variation of Lys-Glu pairs (ladders) in the in-register Aβ(16-22) β-sheet over a 2ns MD simulation

The center four strands in the middle sheet of the in-register six-strand-five-sheet system are exhibited as the example. The side chain distance is measured between the N of Lys side chain and the O of Glu side chain.

(a) A snapshot of the center four strands with Lys and Glu labeled

(b) The side chain distance variation of Lys-Glu pairs on the left corresponding to (a)

(c) The side chain distance variation of Lys-Glu pairs on the right corresponding to (a)

Salt bridge side chain hydrogen bonding is observed between Lys and Glu of adjacent strands within the in-register β-sheet (with ~3Å N-O distance). Moreover, residues forming side chain salt bridges can switch their hydrogen bonding pairs.

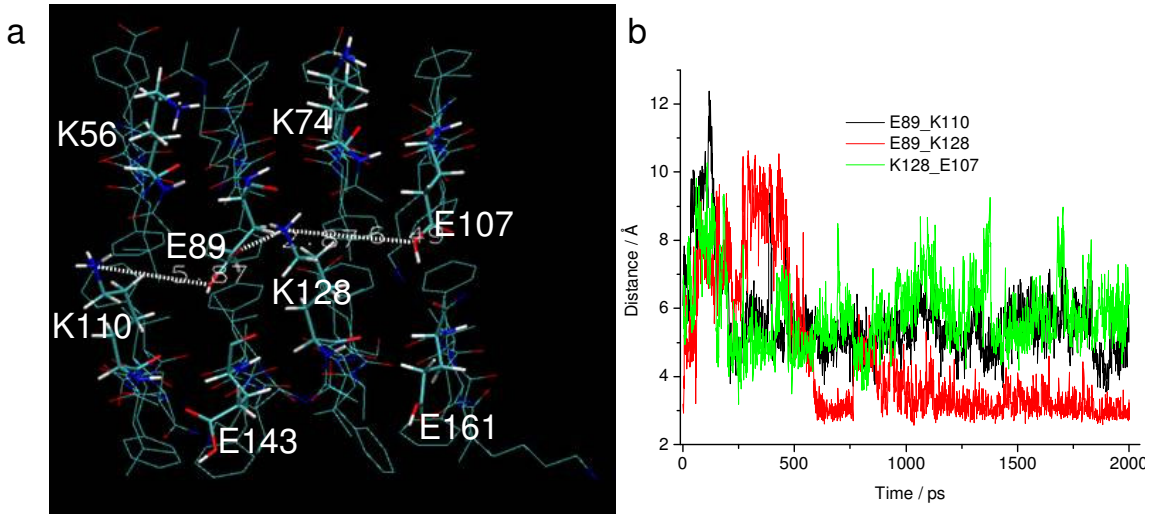

Figure 2.8. Side chain distance variation of Lys and Glu from two adjacent one-residue shifted Aβ(16-22) β-sheets over the 2ns MD simulation

The center two β-sheets of one-residue-shifted six-strand-five-sheet system are shown as the example. The side chain distance is measured between the N of Lys side chain and the O of Glu side chain.

(a) A snapshot of two adjacent four-strand one-residue-shifted β-sheets viewed from the peptide terminal side with Lys and Glu labeled

(b) Side chain distance variation of Lys and Glu. The Lys-Glu side chain hydrogen bonding (with ~3Å N-O distance) occurs between adjacent one-residue-shifted β-sheets

DISCUSSION

The assembly of secondary structural elements is of critical importance in protein folding, and both experimental evidence (Smith 1995) and bioinformatic analyses (Wouters 1995, Hutchinson 1998) have implicated cross-strand pairing as a contributor to β-sheet assembly and stability in globular proteins. However, recent evidence suggests that formation of a single isolated β-sheet might be regulated by hydrophobic surface burial events that dominate other β-sheet propensity measures (Yan 2007). This difference suggests that the early steps in protein misfolding, events that have been debated for many years (Harper 1997, Westermark 2005, Wetzel 2006), could be structurally probed in amyloid. Accordingly, we sought to use the simple core segment from the Alzherimer's disease peptide Aβ to investigate early β-sheet nucleation during assembly.

Our modeling results suggest that small energy differences underlie β-sheet peptide registry, and yet these differences can be sufficient to lead to the exclusive formation of a single sheet morphology, manifested as either amyloid nanotubes or fibrils in Ac-KLVFFAE-NH_2, Aβ(16-22). The Lys and Glu residues at the N- and C-termini of Aβ(16-22) are positioned as cross-strand pairs that could stabilize antiparallel β-sheets through side-chain salt bridges (Wouters 1995, Hutchinson 1998, Yan 2007). Indeed, MD simulations support extended pairwise K-E ladders or networks (Kumar 2002) formed along the β-sheet surface that stabilize the in-register antiparallel β-sheets formed in Aβ(16-22) fibers. However, the magnitude of the K-E ladder stabilization is expected to depend on the desolvation penalties and the required loss of side chain entropy (Kumar 2002, Hendsch 1994, Honig 1995) that make these assemblies so challenging to model.

Nevertheless, the protonation of the Glu side chains in Aβ(16-22) tubes, which should weaken the K-E ladders, results in one-residue shifted β-sheets, removing one H-bond per strand and placing the K and E residues on opposite faces of each sheet.

This shift in registry may well be driven by another pairwise constraint with V18, shifting the β-branched V18 from cross-strand pairing with F20 to being paired with the smaller A21. Only β-branching at residue 18 shifts the registry, such that residues of the same composition without β-branching only form in-register fibers. When the steric size of V18 is increased to terL, the one-residue shifted antiparallel β-sheet forms independent of the Lys and Glu side chain protonation states.

While these data make a compelling case for an energetic contribution from cross-strand pairing, several other elements require consideration. First, in the OspA sheet (Yan 2007, Lesser 1990), hydrophobic surface burial was critical, but does not appear to be a major contributor in self-assembly of the Aβ(16-22) V18 congeners. However, as a measure of surface area buired, the "lipophilic" surface area did appear more "complementary" in the one-residue shifted orientation. As shown in Figure 2.6., the sheet surfaces show little energetic preference for stacking top-top, top-bottom or bottom-bottom faces. In contrast, one surface of the in-register β-sheet is markedly more hydrophobic, such that assembly between two bottom surfaces, burying the most hydrophobic surfaces, might be anticipated. Such differences in lipophilic surface area could impact nucleation and growth of the in-register antiparallel β-sheets of the fiber. However, if the peptides are in the same registry, the inclusion of β-branching at position 18 in Aβ(16-22), or even the addition of a single methyl group to the peptide in the case

of terL, has little or no impact on the predicted lipophilicity of these surfaces and should not dictate registry.

A second important consideration of β-branching could be its impact on the peptide backbone. In the repeating antiparallel amyloid assembly, each side chain exists in H-bonding and non H-bonding positions with the same cross-strand neighbor (Scheme 1.1.), averaging these differences. Initial molecular modeling of Aβ(10-35) however suggested that the overall planarity of the β-sheet is limited by the length of the H-bonded peptide strand (Lakdawala 2002, Morgan 2002). Small segments of about 6 amino acids remained as planar H-bonded segments, but side-chain/backbone interactions destabilized longer stretches. Obviously, the one-residue shifted β-strands in the nanotubes of Aβ(16-22) possess one fewer residue involved in backbone H-bonding, however, MD identified no significant difference in the "flatness" of any of the Aβ(16-22) fiber and nanotube β-sheets, suggesting that such intra-strand interactions are not significant in determining the registry of these short sequences.

These results then highlight backbone registry as a delicate balance between pairwise K-E association and the steric demand at the β-carbon of residue 18. And terL-Ala cross-strand pairing appears to override the favorable K-E ladders even at their strongest electrostatic interaction when both side chains are ionized, underscoring the importance of pairwise associations, both electrostatic and β-branching, in amyloid strand assembly. While such pair correlations are typical of the constraints seen in globular protein folding (Chou 1974, Minor 1994, Kim 1993, Wouters 1995, Hutchinson 1998, Zaremba 1999), they appear to be of secondary importance for the thermodynamic stability of the exposed β-sheet of OspA. Rather, buried non-polar surface area has

emerged as most critical when both faces of the sheet are solvent exposed (Yan 2007), consistent with desolvation providing the critical energetic constraint for protein folding (Fernandez 2003, Avbelj 2002, Rodriguez-Larrea 2006, Fernandez 2002). Further, recent work on solvent effects on insulin self-assembly further stresses the critical impact of hydration on the amyloid nuclei (Dzwolak 2004, Dzwolak 2005, Smirnovas 2006). Therefore, current amyloid assembly models, which score for single solvent exposed sheets (Nguyen 2004, Urbanc 2004, Hwang 2004, Ikebe 2007, Jang 2008) where secondary structure and strand registry are set in the initial nucleus, by this analysis, should be controlled by non-polar surface area burial.

It may be that in the larger OspA protein cross-strand pair interactions in the single connecting sheet are dominated by the folding of the larger protein domains at either end of the sheet. Alternatively, the shorter Aβ(16-22) peptide may be desolvated early through some accumulating hydrophobic collapse, much like globular proteins, allowing the intrinsic β-sequence and pair correlations to regulate secondary assembly. The nature of such early desolvation events could be accounted for by early particle assemblies (Necula 2007, Kayed 2003), but the nature of these assemblies and their contribution to amyloid nucleation remains unclear. Accordingly, future efforts must focus on factors that contribute to sheet desolvation during the early stages of amyloid assembly. Resolving these differences could well open new strategies for controlling amyloid assembly and the regulation of misfolding diseases.

CHAPTER 3

PARALLEL AND ANTIPARALLEL β-SHEET IN AMYLOID

INTRODUCTION

To continue the investigation of the energetic factors which contribute to amyloid assemblies in Chapter 2, the self-assembly of Aβ(16-22) L17 congeners are reported in this chapter. Similar side chain modifications with Leu and Val isomers were introduced into the 17th residue of Aβ(16-22). The sequence differences among L17 congeners are not more than one methyl group, but besides the β-strand registry shift, the switch of β-strand orientation from antiparallel to parallel was also observed. Cross-strand pairwise interactions still play a role in determining the strand registry among L17 congeners. The β-strand orientation switch is indicated due to the preference of non-γ-branched χ2 rotamer packing in the parallel β-sheet. Surprisingly, the side chain interaction patterns in the lamination do not particularly endorse either β-strand orientation. This leads to the

conclusion that the inter-strand side chain interactions within a β-sheet are more critical to determine the assembled solvent-isolated β backbone conformation. This may be consistent with the requirement of backbone desolvation in β-sheet formation (Fernandez 2003). The self-assembly of L17 congeners supports the inter-strand side chain interactions may devote critical energetic contribution to amyloid early step assemblies and nucleation.

MATERIALS AND METHODS

Peptide Synthesis and Purification

L17 congeners were synthesized using standard FMOC peptide synthesis protocols on an Applied Biosystems ABI431 peptide synthesizer. The resulting peptides were cleaved from the resin using a solution of TFA/thioanisole/ehtanedithiol /anisole (90/5/3/2 v/v), precipitated from the cleavage solution using excess ice-cold diethyl ether, and washed repeatedly with ice-cold diethyl ether. Reverse phase HPLC (Water Delta 600) with a linear gradient of acetonitrile and water (0.1% TFA) was used for peptide purification. The molecular weight of each peptide was verified by MALDI mass spectroscopy. Peptides containing F19 [1-^{13}C] labels were synthesized as described using [1-^{13}C]-phenylalanine and also confirmed by MALDI mass spectroscopy.

Solid State NMR

All spectra were collected with a Bruker Avance 600 spectrometer and a Bruker 4 mm HCN magic-angle spinning (MAS) probe. ^{13}C (150.8MHz) magnetization was prepared by 1.5 ms ^{1}H-^{13}C cross-polarization (CP) (57) with a 50 kHz ^{13}C spin-lock pulse and a linear ramp on ^{1}H from 50 to 70 kHz with 125 kHz Spinal64 (58) ^{1}H decoupling. MAS frequency (ν_r) was kept under active control at 4850 kHz ± 2 Hz. Cooling and

spinning air exit temperature was maintained below -1° C to ensure MAS and RF heating did not denature the sample. The power level for ^{13}C Dipolar Recoupling with A Windowless Sequence (DRAWS) pulses were calibrated by fitting a ^{13}C nutation curve to an exponential damped sine function. An RF level was chosen such that the RF field = 8.5 * ν_r. All spectra were referenced externally to the down field peak of adamantane at 38.48ppm.

Circular Dichroism Spectroscopy (CD)

CD spectra were recorded at JESCO-810 CD spectropolarimeter at room temperature. Typically, spectra between 290 nm and 190 nm were collected with a 0.1mm path length cell, with a step size of 0.2 nm and a speed of 50nm/s.

MD Simulation

The system was constructed using the default options in DESMOND (Schrödinger, LLC) (Bowers 2006). The peptides were initially solved with a truncated octahedral box containing about 25,000 TIP4P water molecules. After initial energy minimization, molecular dynamics was run for 1.2ns, and a time step of 1.2ps was used. Velocities were maintained using a Nose-Hoover thermostat and pressure was maintained using a Martyna-Tobias-Klein barostat. Long-range interactions were modeled using a Particle-Mesh Ewald (PME) protocal. The resulting energy trajectory was analyzed using the Simulation Analysis Tool in Maestro.

RESULTS

Morphologies of Aβ(16-22) L17 Congener Self-assemblies

Chapter 2 introduced substitutions at the 18th position of Aβ(16-22) with a series of Val and Leu isomers, and the cross-strand pairing dictating the strand registry in the

antiparallel β-sheet was discussed. In this chapter, the substitutions were introduced to the 17th position of Aβ(16-22) with the same Val and Leu isomers. The amino acid replacements can be classified into four sets as shown in Scheme 2.1.: (i) β-branched side chains; (ii) extended side chains; (iii) structural isomers of the four-carbon side chains; (iv) non-γ-branched side chains. Among L17 congeners, only L17Abu forms nanotubes with large diameters under the acidic conditions (40% acetonitrile/water with 0.1% TFA) comparable to the Aβ(16-22) nanotubes, and all other congeners form fibers. Under neutral conditions (40% acetonitrile/water with the adjustment of 0.1M NaOH to neutral) the morphologies of L17 congeners do not change (Figure 3.1. and Figure 3.2.). The diameters of these fibers were also measured by small angle X-ray scattering (SAXS) (Figure 3.3. and Table 3.1.), and showed the amyloid characteristic cross-β pattern in wide angle X-ray scattering (WAXS) (Figure 3.4. and Table 3.1.), Even though their lamination scatterings were weaker in fibers.

Scheme 2.1.

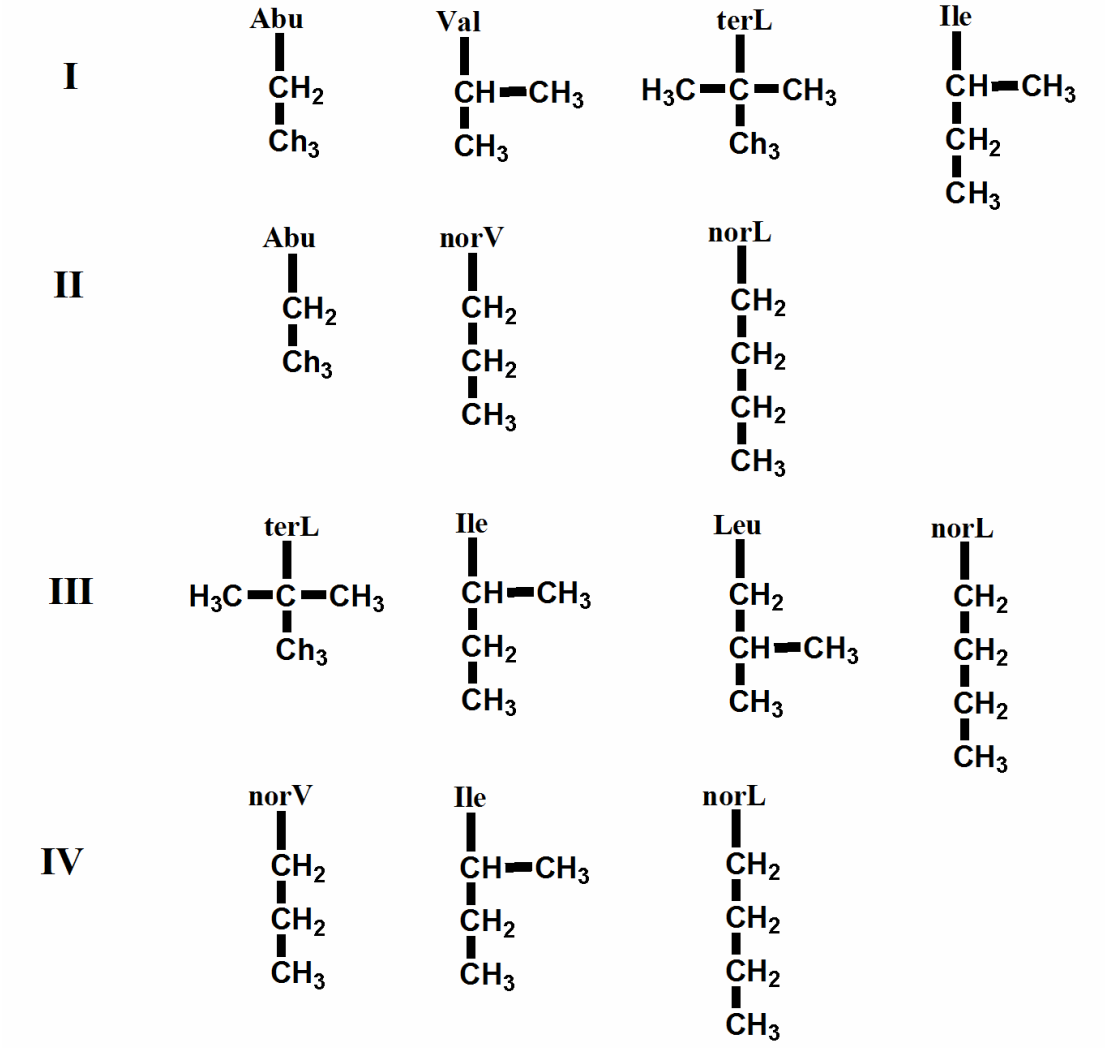
I
Abu
Val
terL
Ile
II
Abu
norV
norL
III
terL
Ile
Leu
norL
IV
norV
Ile
norL

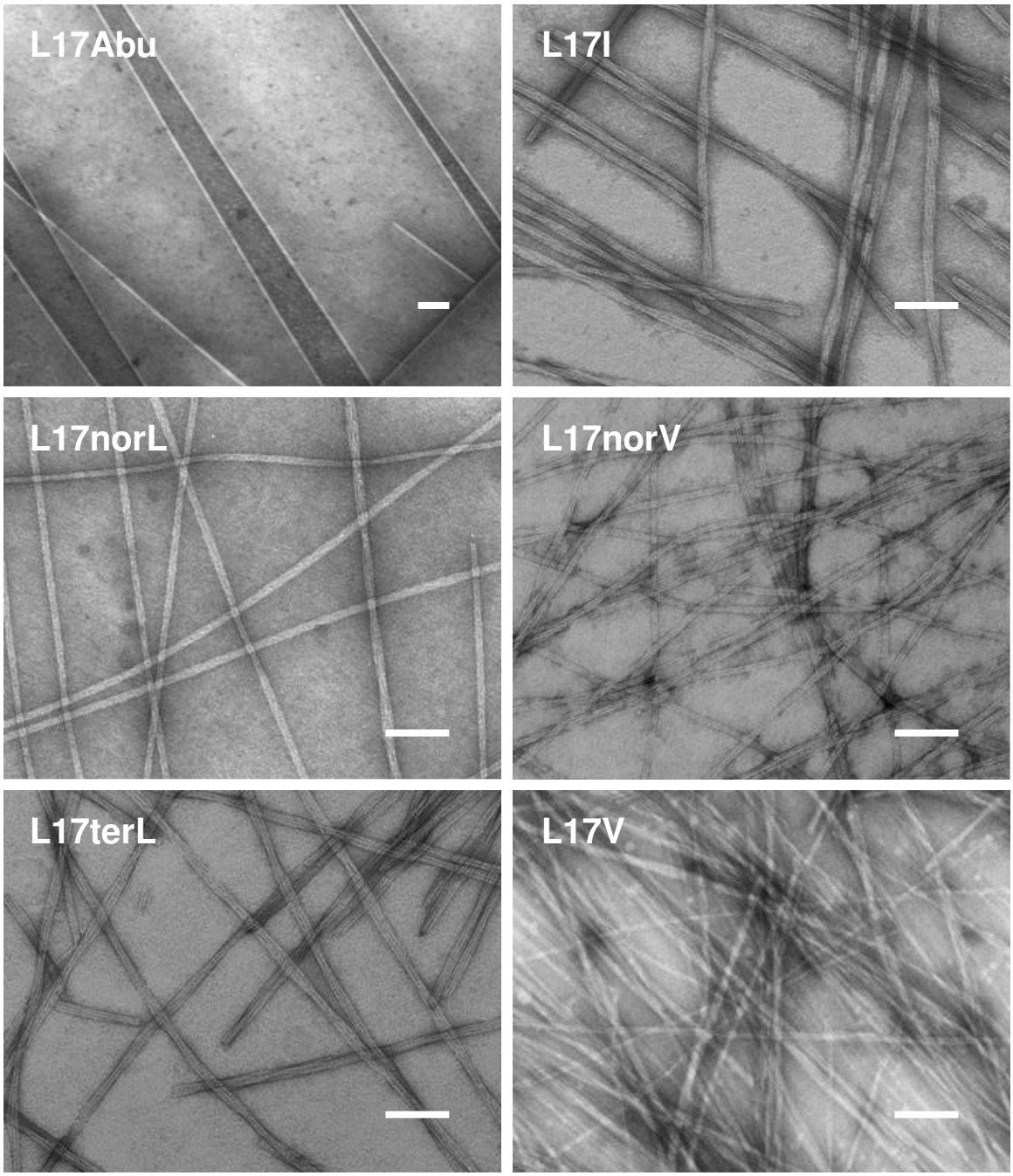

Figure 3.1. TEM of L17 congener assemblies under the acidic conditions

Scale=100nm

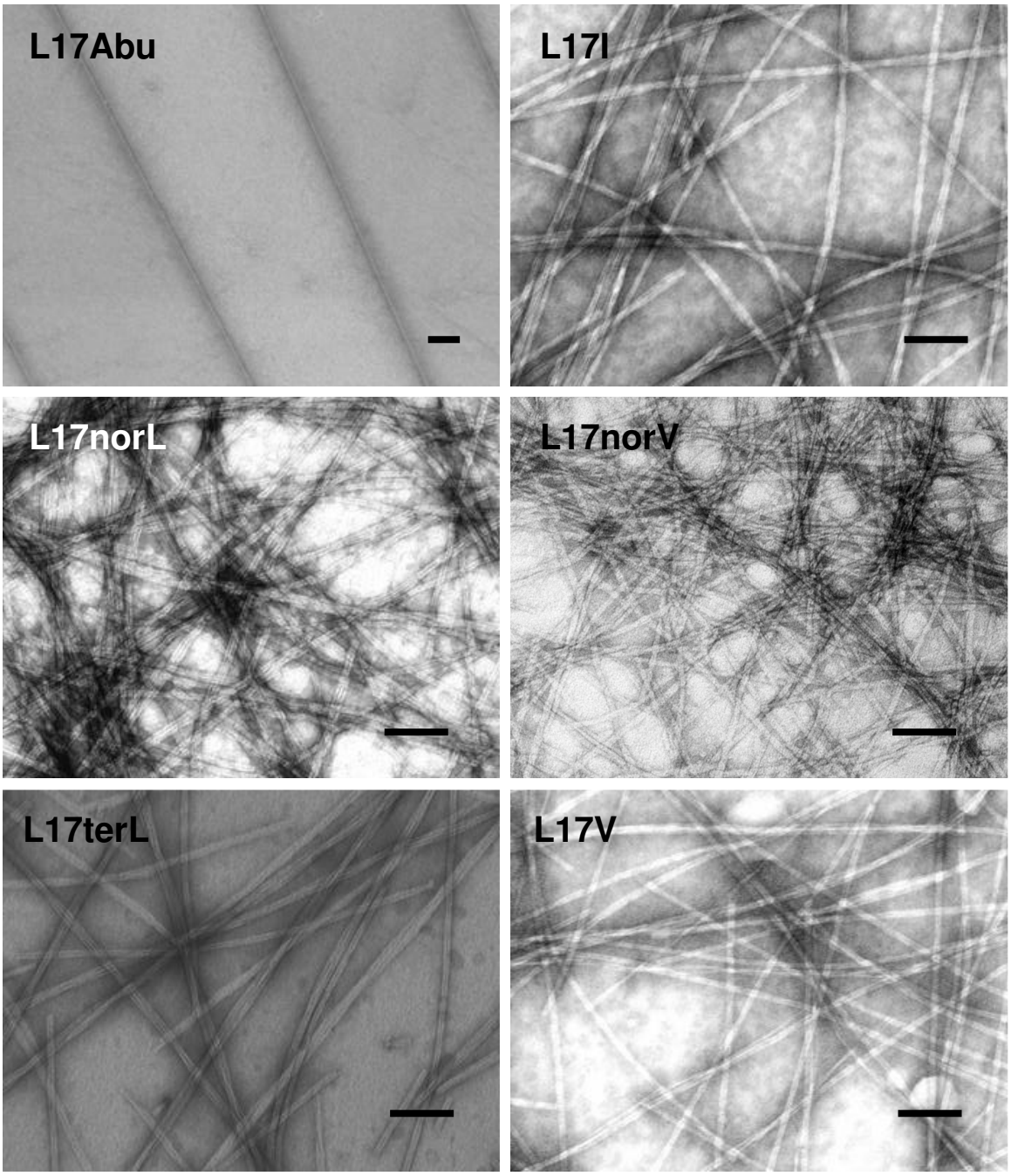

Figure 3.2. TEM of L17 congener assemblies under the neutral conditions

Scale=100nm

Figure 3.3. SAXS of L17 congener fibers

(a) SAXS at the acidic condition: L17I (△, blue), L17norL (▽, green), L17norV (○, cyan), L17terL (▷, orange), and L17V (□, yellow)

(b) Modified Guinier analysis of fibers with rod-like forms (fit in red) at the acidic condition: L17I (△, blue), L17norL (▽, green), L17norV (○, cyan), L17terL (▷, orange), and L17V (□, yellow)

(c) SAXS at the neutral condition: L17I (△, blue), L17norL (▽, green), L17norV (○, cyan), L17terL (▷, orange), and L17V (□, yellow)

(d) Modified Guinier analysis of fibers with rod-like forms (fit in red) at the neutral condition: L17I (△, blue), L17norL (▽, green), L17norV (○, cyan), L17terL (▷, orange), and L17V (□, yellow)

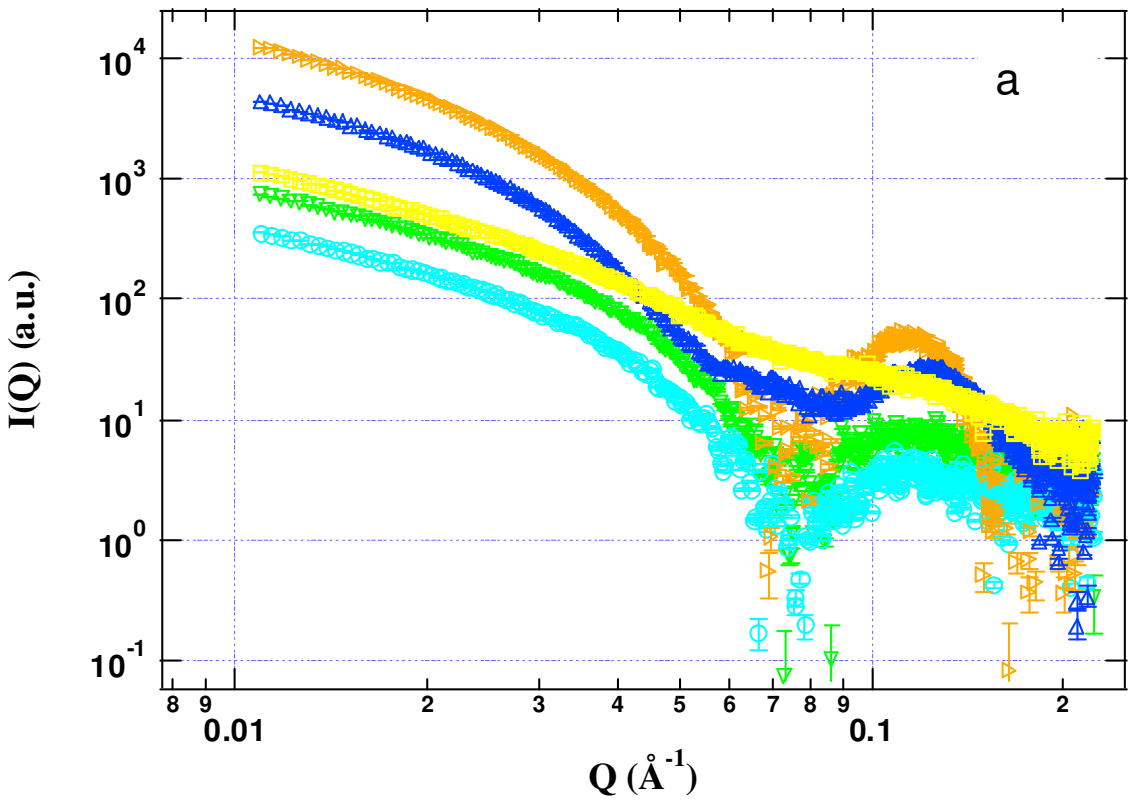
a
I(Q) (a.u.)
Q (Å^{-1})

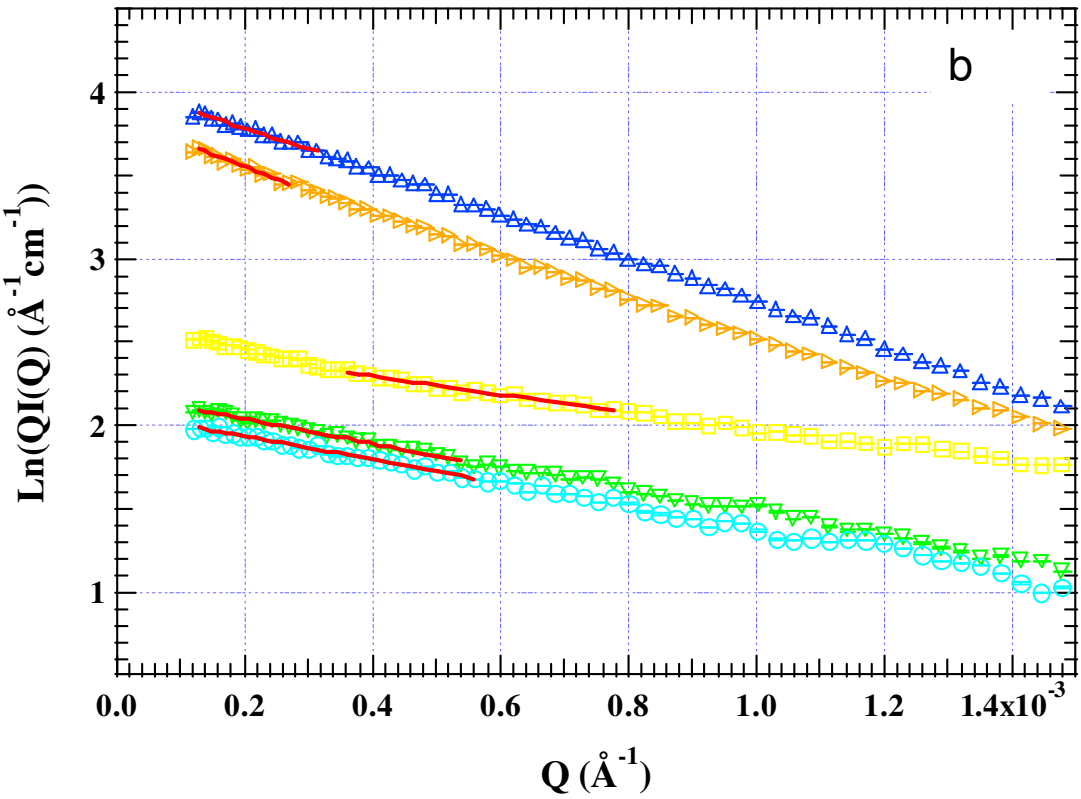
b
Ln(QI(Q) (Å^{-1}cm^{-1}))
Q (Å^{-1})

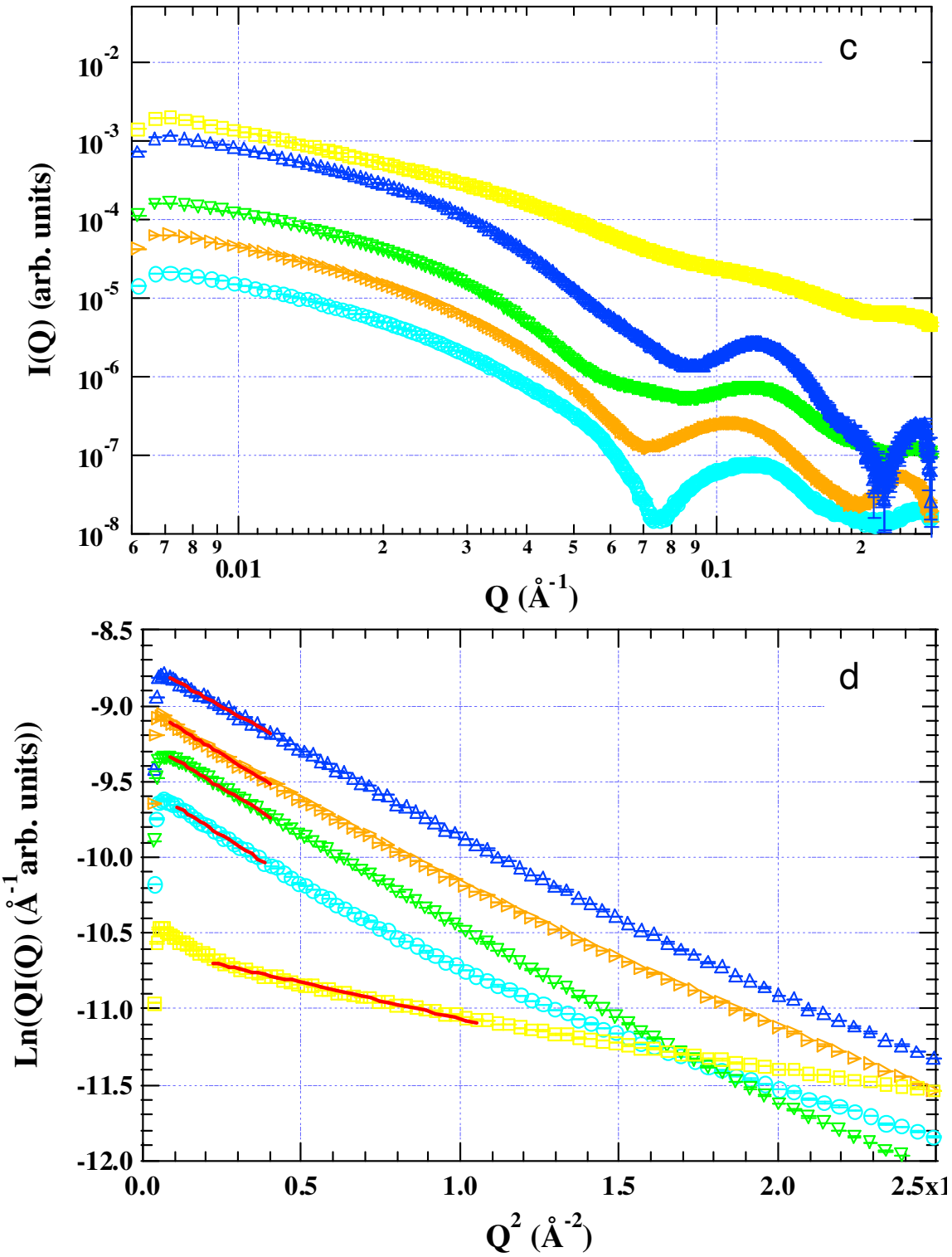
c
I(Q) (arb. units)
10^-2
10^-3
10^-4
10^-5
10^-6
10^-7
10^-8
6 7 8 9
0.01
2 3 4 5 6 7 8 9
0.1
2
Q (Å^-1)
d
Ln(QI(Q) (Å^-1arb. units))
-8.5
-9.0
-9.5
-10.0
-10.5
-11.0
-11.5
-12.0
0.0
0.5
1.0
1.5
2.0
2.5x1
Q^2 (Å^-2)

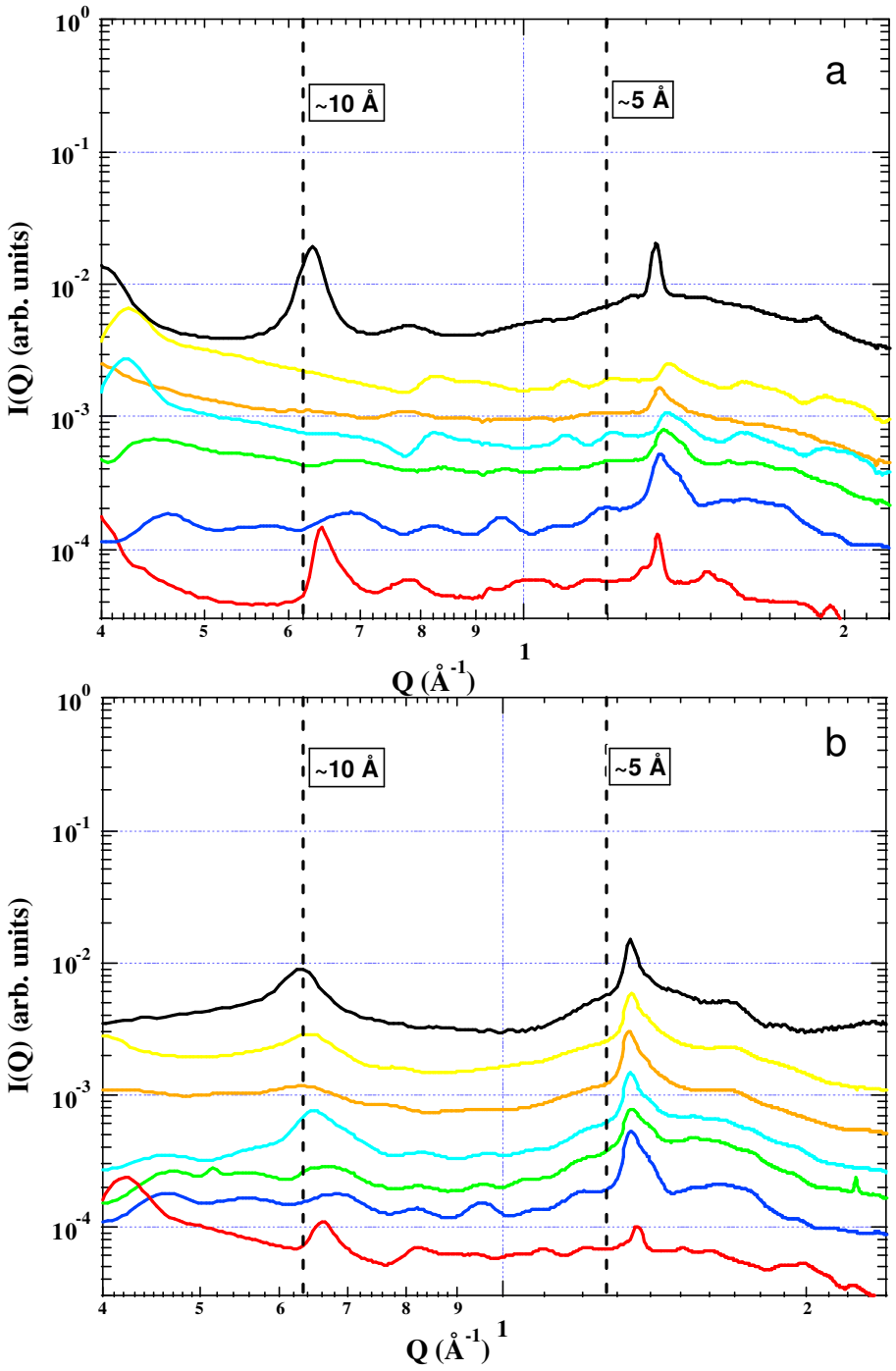

Figure 3.4. WAXS of assembly powders of Aβ(16-22) and L17 congeners

L17Abu (red), L17I (blue), L17norL (green), L17norV (cyan), L17terL (orange), L17V (yellow), and Aβ(16-22) (black) under the conditions of (a) acidic, (b) neutral.

Table 3.1. Dimension of L17 congener assemblies

Peptides	Solution SAXS			Powder Diffraction	
	Fibers (Å)	Tubes (Å)		Distance correlations (Å)	
	Outer Radius	Outer Radius	Shell Thickness	Inter-Strand	Inter-Sheet
Acidic Condition					
Aβ(16-22)	**/**	**263.7 ± 2.0**	**39.0 ± 1.0**	**4.7**	**9.9**
L17Abu	**-**	**-**	**-**	**4.7**	**9.7**
L17I	70.7 ± 0.1	/	/	4.7	n/a
L17norL	54.3 ± 0.1	/	/	4.6	n/a
L17norV	52.9 ± 0.1	/	/	4.6	n/a
L17terL	53.4 ± 0.2	/	/	4.7	9.7
L17V	55.3 ± 0.1	/	/	4.6	n/a
Neutral Condition					
Aβ(16-22)	**33.0± 0.1**	/	/	**4.7**	**9.9**
L17Abu	-	-	-	**4.7**	**9.7**
L17I	67.8± 0.1	/	/	4.7	n/a
L17norL	71.3± 0.1	/	/	4.7	n/a
L17norV	73.1± 0.1	/	/	4.7	9.7
L17terL	71.3± 0.1	/	/	4.7	10.0
L17V	43.5± 0.1	/	/	4.7	9.7

β-sheets of Aβ(16-22) L17 Congener Self-assemblies

The fibers or tubes formed by the L17 congeners all appear to contain the characteristic cross-β structure, but by CD can be divided into three groups. The characteristic CD signature of β-sheet was a negative ellipticity at 210-225nm (Fasman 1996), and both L17terL and L17V assemblies have a negative ellipticity at 215nm, similar with Aβ(16-22) (Figure 3.5.). The negative ellipticity of L17I, L17norL and L17norV is shifted to 220nm. The most distinct CD signature is seen with L17Abu with the negative ellipticity at 203nm and 215nm, resemble an a α-helix signal, but with a weak positive ellipticity at 223nm. Although it is not clear what causes the shift of β-sheet signals in L17 congener assemblies, the intrinsic β-sheet properties, such as, strand orientation, registry, and twist may be responsible for the changes.

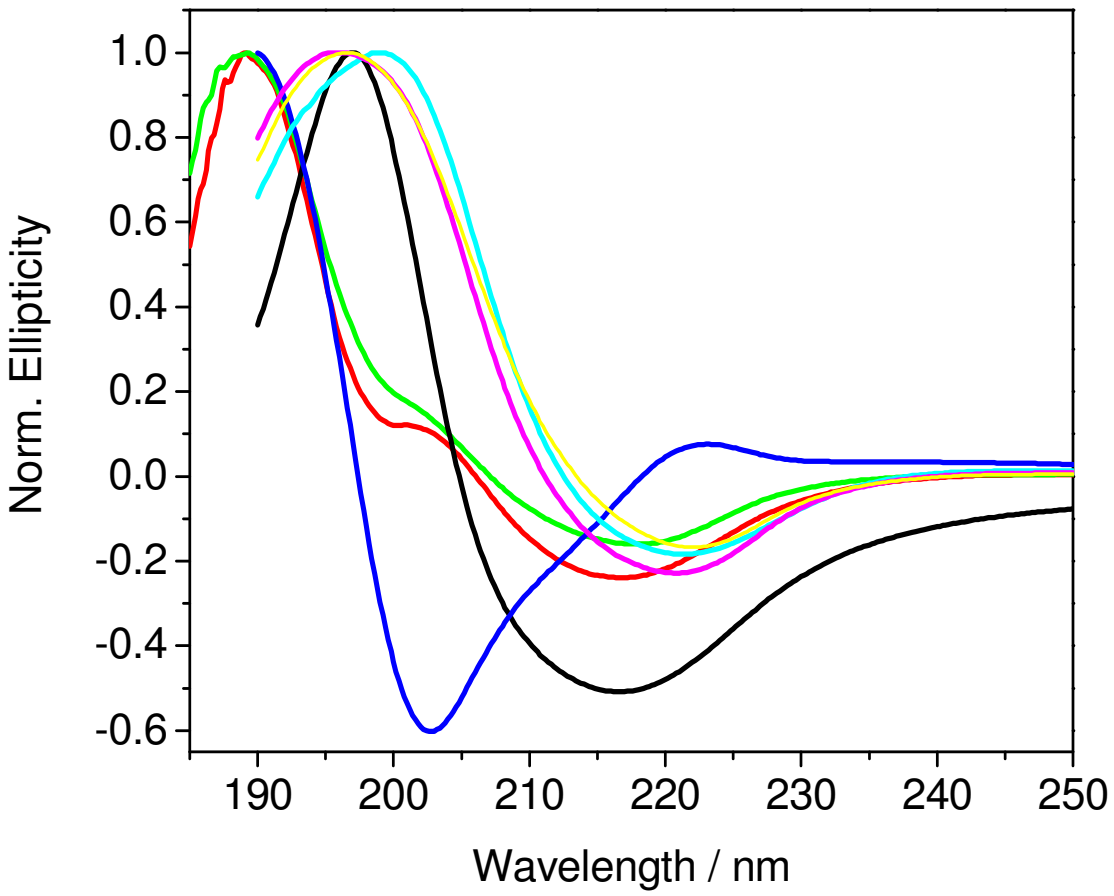

Figure 3.5. CD of L17 congener assemblies at the acidic condition

Aβ(16-22) (black), L17Abu (blue), L17I (cyan), L17norL (magenta), L17norV (yellow), L17terL (red), and L17V (green).

For L17Abu, L17terL and L17V, the characteristic β-sheet amide I infrared stretch centered at 1627cm^{-1} and the higher energy but weaker shoulder at 1694cm^{-1} (Figure 3.6.), are diagnostic of antiparallel sheets, independent of strand registry (Elliott 1950, Halverson 1991, Mehta 2008). Although L17Abu has a distinct CD signature, the FTIR absorbance confirmed an antiparallel arrangement of the β-sheet. However, the β-sheet amide I band of L17I, L17norL and L17norV occurred at 1630cm^{-1} with the higher energy shoulder at 1678cm^{-1}. All these assemblies have similar CD spectra. As described in Chapter 2, isotope-edited FTIR (IE-FTIR) reported on the β-sheet strand registry because the incorporation of a single ^{13}C carbonyl splits the amide I band into distinct transitions corresponding to the ^{12}C and ^{13}C components at higher and lower energy, respectively (Kubelka 2001, Hiramatsu 2005, Paul 2005, Petty 2005, Decatur 2006). With 1-[^{13}C] F19 modification, the L17Abu tubes have ^{12}C / ^{13}C band splitting of 40cm^{-1}, similar to the 42cm^{-1} splitting seen for Aβ(16-22) nanotubes (Figure 3.7. and Table 3.2.), suggesting the alignment of F19 carbonyls in the antiparallel one-residue-shifted registry. This is consistent with the antiparallel one-residue-shifted registry inducing the tube morphology. L17terL and L17V fibers have ^{12}C and ^{13}C band splits in a range of 30-32cm^{-1}, L17terL (30cm^{-1}) and L17V (32cm^{-1}), consistent with in-registry antiparallel β-sheets.

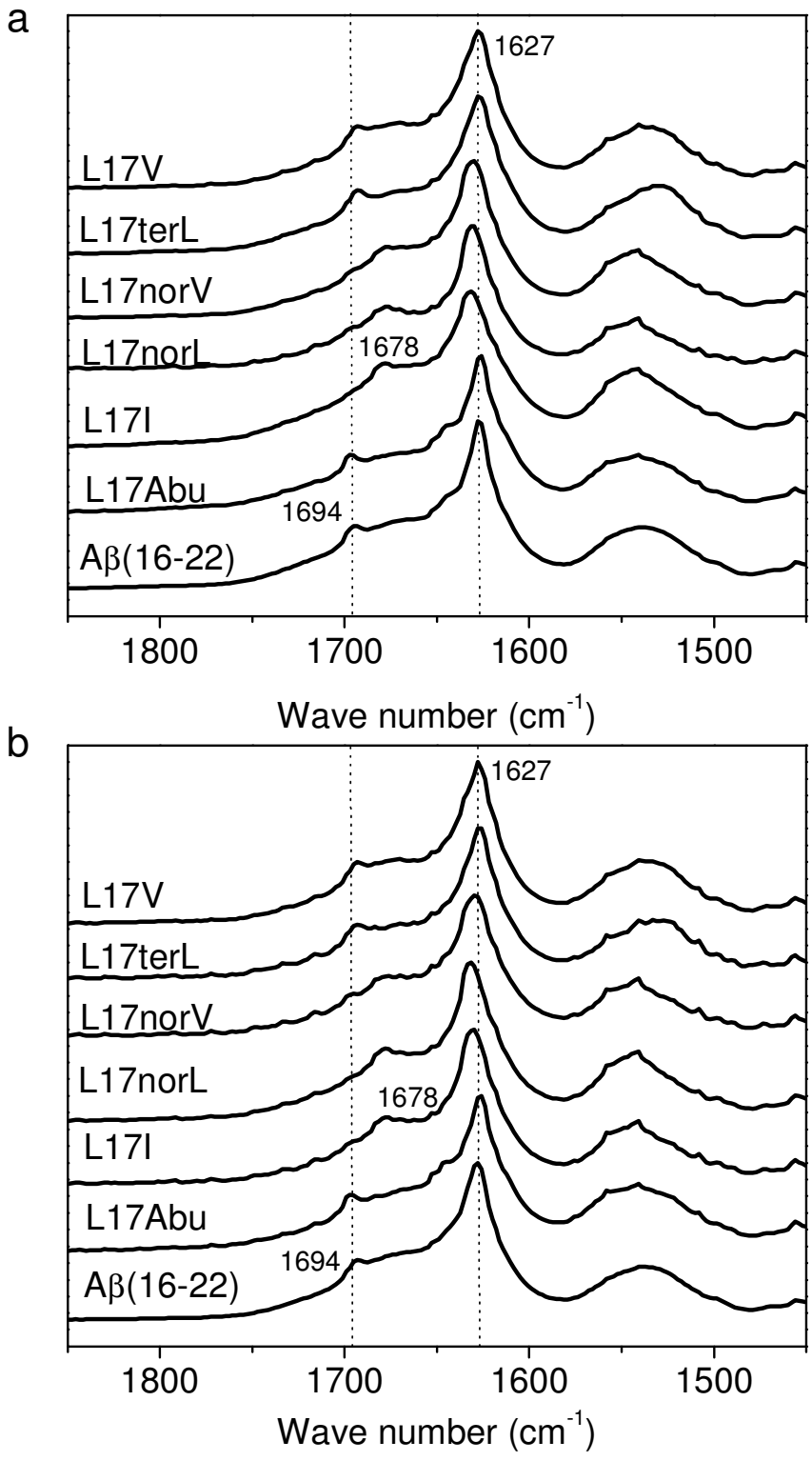

Figure 3.6. FTIR of L17 congener assemblies

(a) under acidic conditions, (b) under neutral conditions.

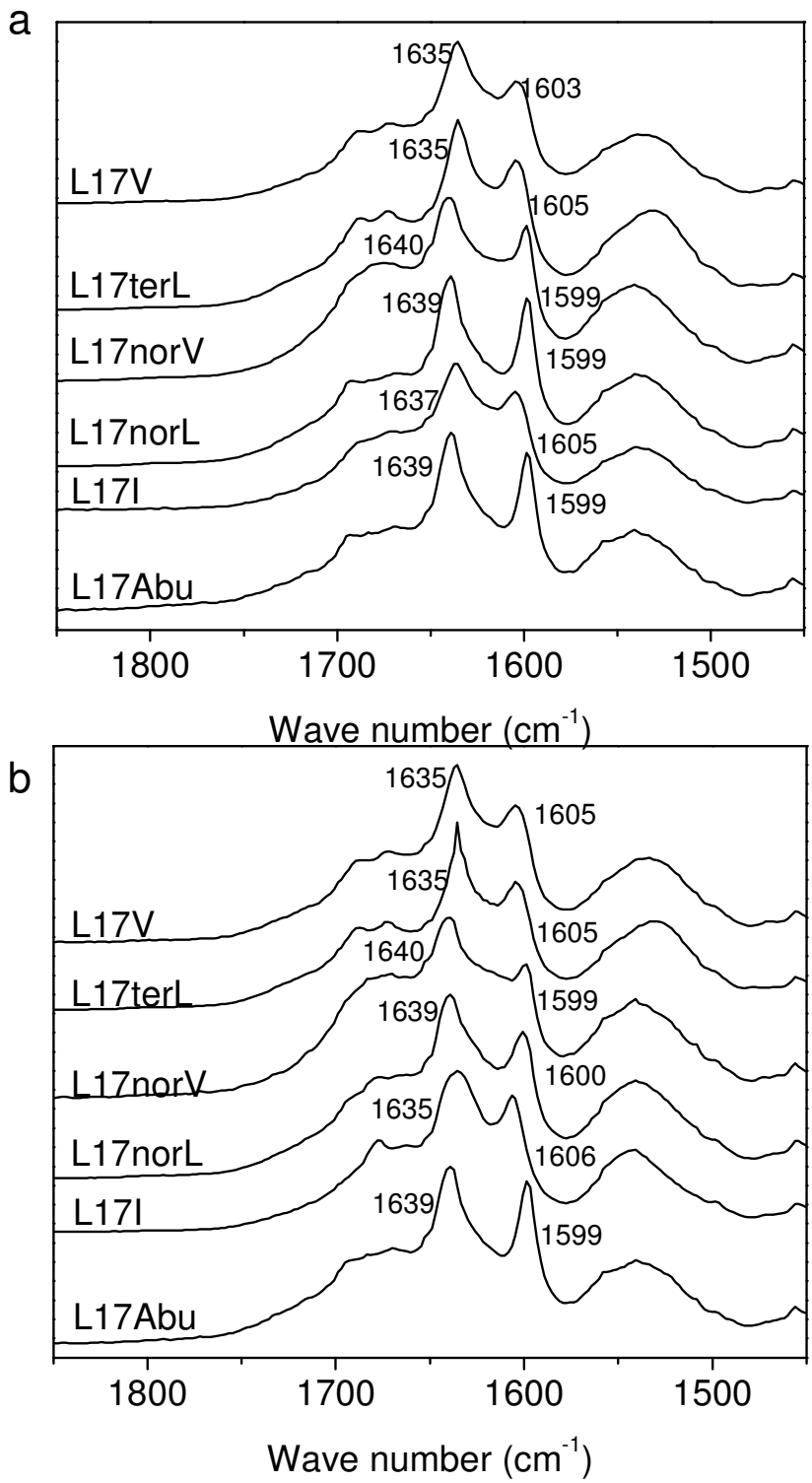

Figure 3.7. IE-FTIR of L17 congener assemblies

(a) under acidic conditions, (b) under neutral conditions.

Table 3.2. ^{12}C and ^{13}C amide I band shifts in IE-FTIR of fibers and nanotubes formed by Aβ(16-22) and its L17 congeners at acidic and neutral conditions.

	Amide I		Acidic			Neutral		
	Natural Abundance[1]		^{12}C shift	^{13}C shift	split	^{12}C shift	^{13}C shift	split
Aβ(16-22) fiber	1627	1694				8	21	29
Aβ(16-22) tube	**1627**	**1694**	**13**	**29**	**42**			
L17Abu	**1627**	**1694**	**12**	**28**	**40**	**12**	**28**	**40**
L17I	**1630**	**1678**	**7**	**25**	**32**	**5**	**24**	**29**
L17norL	**1630**	**1678**	**9**	**31**	**40**	**9**	**30**	**39**
L17norV	**1630**	**1678**	**10**	**31**	**41**	**10**	**31**	**41**
L17terL	1627	1694	8	22	30	8	22	30
L17V	1627	1694	8	24	32	8	22	30

[1]Note: the natural abundant amide I bands under acidic and neutral conditions are same for each L17 congener.

In L17I, L17norL and L17norV, the absorbance at 1678cm^{-1} was characteristic of parallel β-sheet array ([1]Hiramatsu 2005, [2]Hiramatsu 2005). To confirm the peptide orientation with this 1678cm^{-1} signature, solid-state NMR (SSNMR) was applied. The L17I peptides were enriched with [1-^{13}C]V18. An in-register parallel β-sheet gave an interstrand ^{13}C -^{13}C dipolar coupling among Val carbonyl carbons. The interstrand homonuclear dipolar coupling was measured using the double-quantum (DQ) filtered DRAWS sequence.

In DRAWS, ^{13}C magnetization is created with ^{1}H-^{13}C cross-polarization, followed by an initial DRAWS period. During the DRAWS sequence, DQ coherences are generated between coupled spins and the build-up rate of the DQ coherence is a function of the ^{13}C-^{13}C distance. The RF pulses applied during the DRAWS evolution period are matched to the spinning speed (ν_r) such that 8.5 ν_r = RF field strength. The magnetization is stored along the z-axis with a hard π/2 pulse for a single rotor cycle and then rotated back to the transverse plane with another hard π/2 pulse, followed by a second DRAWS evolution period. The second DRAWS period reconverts DQ magnetization to observable single quantum magnetization. Appropriate phase cycling of the DRAWS pulses ensures that at the end of the 2nd DRAWS evolution period, only signals between coupled ^{13}C

spins is observed, providing a double quantum filtered (DQF) signal (Figure 3.8.). The observed signal is normalized with respect to the ^{1}H-^{13}C cross-polarized signal with no DRAWS evolution.

In Figure 3.9., the solid squares are the DQF-DRAWS data for [1-^{13}C]V18 L17I fibers formed under the acidic conditions (40% acetonitrile/water with 0.1% TFA). The open squares are from DQF-DRAWS observed for un-enriched Aβ(16-22) fibers formed under the neutral conditions (40% acetonitrile/water with 0.1mM NaOH adjustment). Any double quantum coherence observed in the un-enriched fibers arises from coupling between natural abundance ^{13}C carbonyl carbons. The dashed line is the calculated DQ buildup for an infinite array of ^{13}C carbons separated by 4.7 Å, as would be expected for parallel in-register β-sheets. When the calculated curved is scaled by 0.45, arising from incomplete refocusing of the ^{13}C CSA interaction by the RF pulses applied during the DRAWS cycle, we can account for the difference between the calculated DRAWS curve and the observed DQ buildup that arises from relaxation of the DQ magnetization (T_2DQ) during the DRAWS evolution period. T_2DQ was measured by fixing the DRAWS evolution time at 7.42ms and inserting a composite π pulse, which refocuses the DQ magnetization, between the two DRAWS evolution periods. The magnetization as function of the refocusing time was fitted to a first order exponential decay of 9.1 ± 0.2 ms. The solid line represents the DQ buildup expected for an infinite array of carbons with a ^{13}C-^{13}C distance of 4.7 Å and a T_2DQ of 9.1 ms. The observed DQF-DRAWS signal of [1-^{13}C]V18 L17I fibers confirms the parallel β-strand orientation.

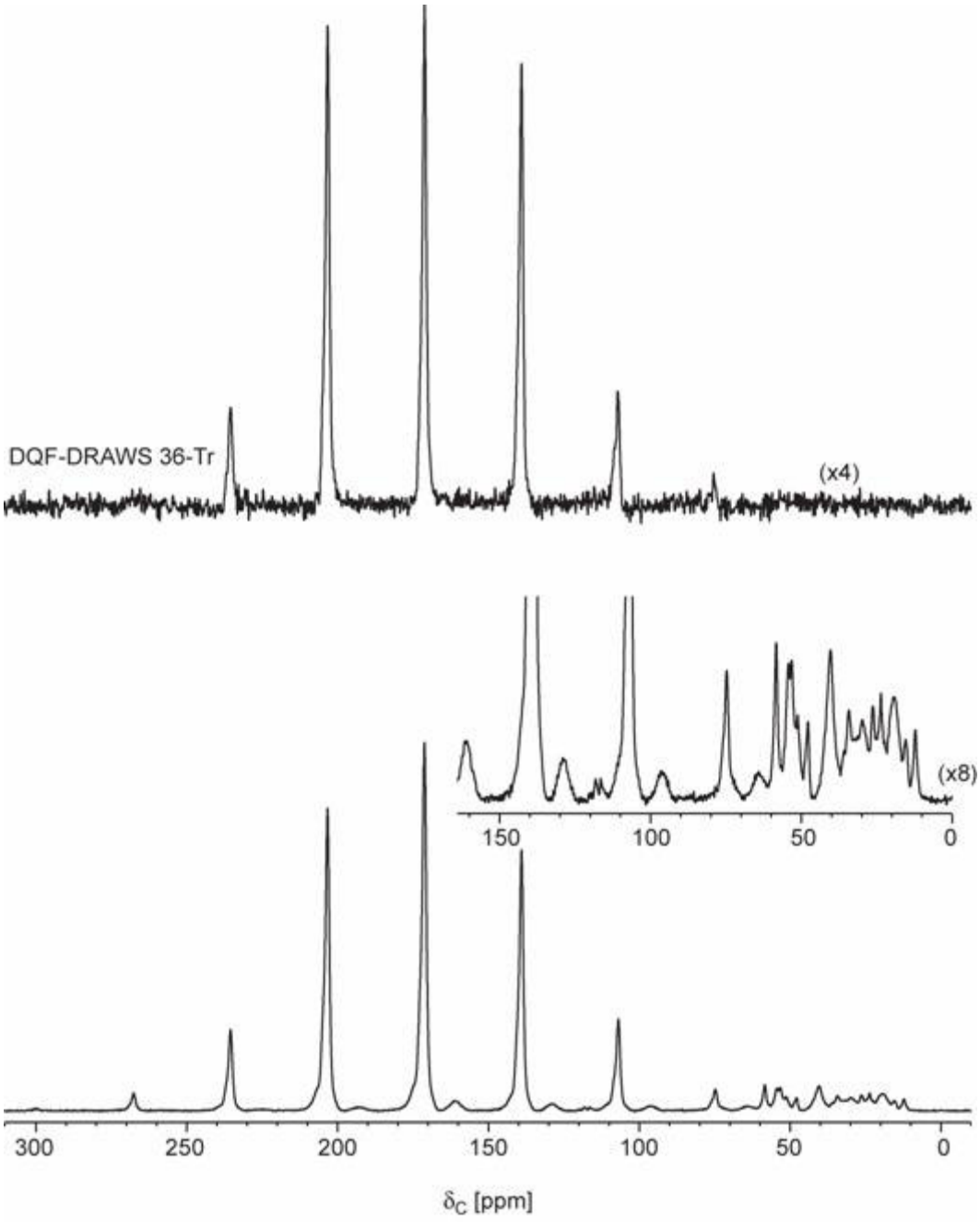

Figure 3.8. ^{13}C CP-ECHO (Bottom) and ^{13}C DQF-Filtered DRAWS (Top) spectra of [1-^{13}C]V18 L17I fibers.

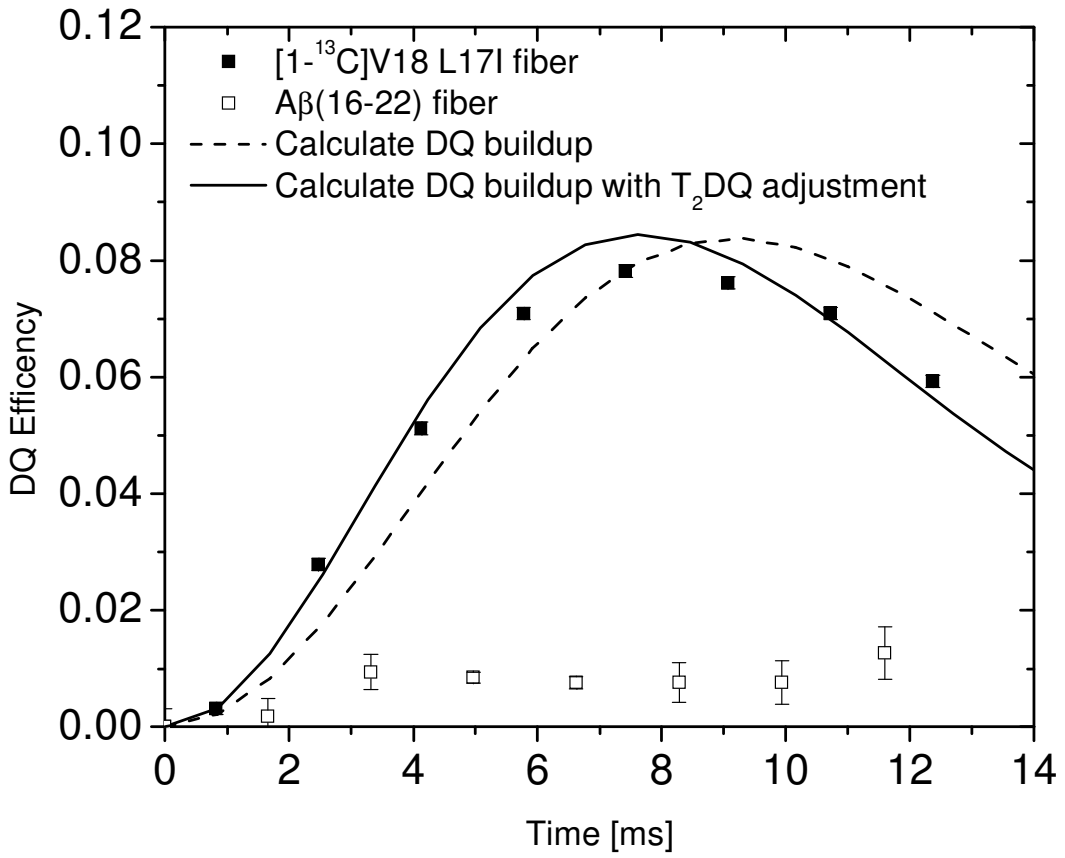

Figure 3.9. DQF-DRAWS of [1-^{13}C]V18 L17I fibers comparing with Aβ(16-22) fibers.

The calculated DQ buildup is for an infinite array of ^{13}C carbons separated by 4.7 Å, as in parallel in-register β-sheets. The relaxation of the DQ magnetization (T_2DQ) during the DRAWS evolution period was measured by fixing the DRAWS evolution time at 7.42ms and inserting a composite π pulse, which refocuses the DQ magnetization between the two DRAWS evolution periods. The magnetization as function of the refocusing time was fitting to a first order exponential decay of 9.1 ± 0.2 ms.

Molecular Modeling

L17 congeners established that β-strand orientation preference can result from a minor sequence modification within the amino acid side chains. The question raised here is whether a particular side chain conformation in L17 congeners can have predominant interactions to dictate the β-strand orientation. The side chains of these peptides in β-arrays are distributed with K, V, F, E on one side (4-aa side), and L, F, A on the other side (3-aa side) in Aβ(16-22). For parallel in-register β-sheet, all K,V, F, E residues are on the same side of the β-sheet surface, while all L, F, A residues are on the other side of the β-sheet surface (Figure 3.10.) The β-sheet interface interactions in the lamination can be classified as: 4aa-3aa, 4aa-4aa, and 3aa-3aa. Also the sheet-sheet interactions can be further defined as in parallel when the two sheets are oriented in the same direction (Figure 3.10.a(i)) and in antiparallel when the two sheets are orientated with opposite direction (Figure 3.10.a(ii)). Therefore, totally there are six parallel in-register β-sheet lamination patterns (Figure 3.10.a). For antiparallel in-register β-sheet, the side chain distribution is also with all K-V-F-E on one side of the β-sheet surface and all L-F-A on other side of the β-sheet surface. Therefore, the β-sheet interface interactions in lamination can be classified as: 4aa-3aa, 4aa-4aa, and 3aa-3aa (Figure 3.10.b). Because of the antiparallel interval of β-strands, the parallel and antiparallel sheet-sheet stackings for antiparallel in-register β-sheet are the same. However, by shifting one strand of the top sheet in Figure 3.10.b(i) in the direction as the side arrow indicating, the individual β-strand in the antiparallel in-register β-sheet can switch lamination side chain interaction from parallel to antiparallel (Figure 3.10.b(ii)). Considering individual β-strand side chain lamination packing, there are also six possibilities. For antiparallel one-residue-

shifted β-sheet, the side chain distribution on both sheet surfaces is with K-V-F-E and L-F-A intervals (Figure 3.10.c), i.e. both surfaces are the same. By shifting one strand as demonstrated above, the individual strand can pack the side chain in parallel or antiparallel patterns (Figure 3.10.c). However, the individual strand side chain lamination patterns, (4aa-3aa, antiparallel), (4aa-4aa, parallel), (3aa-3aa, parallel) are not possible for antiparallel one-residue-shifted β-sheet. If a side chain conformation predominately prefer the (4aa-3aa, antiparallel), (4aa-4aa, parallel), or (3aa-3aa, parallel) lamination side chain packing patterns, they cannot form the antiparallel one-residue-shifted β-sheet.

To estimate the side chain lamination interaction preference, the parallel in-register β-sheet is chosen as the model system. 6-strand parallel in-register β-sheets were packed in 3-sheet array to run MD at the acidic condition. To make the comparison, two of the three sheets always keep in 4aa-3aa, parallel pattern, and the arrangement of the third sheet was varied as the side chain interaction patterns in Figure 3.10.a, respectively. For every L17 congener, all its 3-sheet arrays were built from the same 6-strand parallel in-register β-sheet to limit the contribution from the backbone. The 3aa-3aa side chain interaction pattern only involves hydrophobic interaction, while the 4aa-4aa pattern can involve the terminal K-E side chain H-bonding and the middle hydrophobic interaction. The average energy of each side chain packing pattern over 1.2ns is listed in Table 3.3.. Among all L17 congeners, their 3aa-3aa interaction pattern has relatively the lowest average energy, as the most favorable side chain packing pattern. This may be reasonable as the 3aa-3aa pattern can bury more hydrophobic residues, and leave the more hydrophilic face side exposing to water. The next side chain interaction pattern with relatively lower energy is the 4aa-3aa one. The possible reason that in this side chain

interaction pattern the side chains are staggered to pack tighter between the residues from the K-V-F-E side and the L-F-A side as shown in Figure 3.11.. To do so, other side chain interaction patterns have to offset the peptide strand. This offset may cause certain residues be exposed without packing. Among L17 congeners, their sequence difference is not more than one methyl group. Independent on the backbone conformation, their favored side chain lamination interaction patterns do not differentiate dramatically from each other.

Figure 3.10 Side chain lamination interaction patterns

(a) For the parallel in-register β-sheet of Aβ(16-22), six lamination interaction patterns determined by β-sheet interface patterns: 4aa-3aa, 4aa-4aa, or 3aa-3aa; and β-strand orientation in lamination: parallel and antiparallel.

(b) For the antiparallel in-register β-sheet of Aβ(16-22), six lamination interaction patterns determined by β-sheet interface pattern: 4aa-3aa, 4aa-4aa, or 3aa-3aa; and β-strand orientation in lamination: parallel and antiparallel

(c) For the antiparallel one-residue shifted β-sheet of Aβ(16-22), two lamination interaction patterns determined by (i) β-sheet interface interaction with parallel 4aa-3aa side chain lamination interaction and (ii) β-sheet interface interaction with antiparallel 4aa-4aa side chain lamination interaction or antiparallel 3aa-3aa side chain lamination interaction.

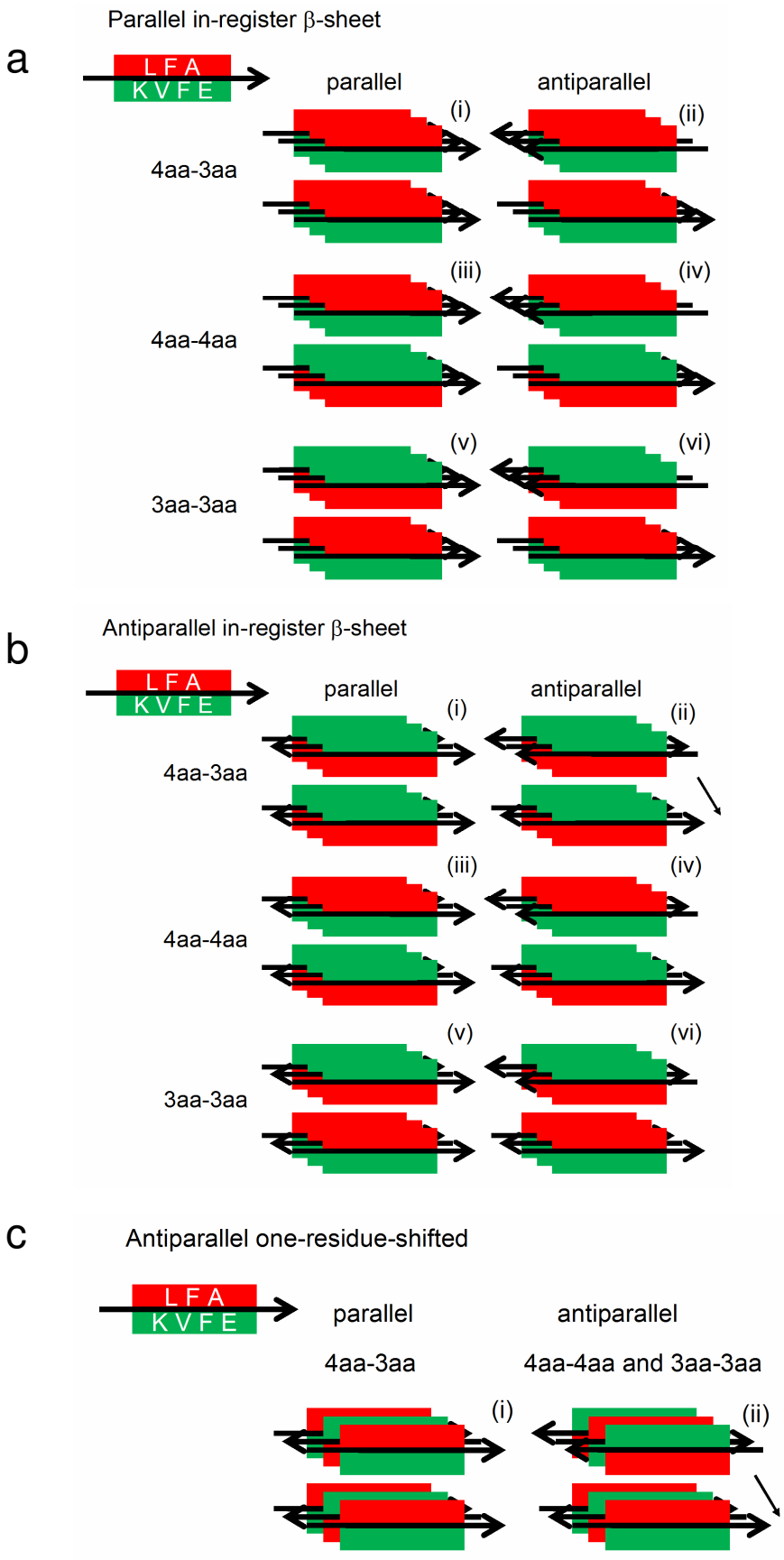
a
Parallel in-register β-sheet
L F A
K V F E
parallel
antiparallel
(i)
(ii)
4aa-3aa
(iii)
(iv)
4aa-4aa
(v)
(vi)
3aa-3aa
b
Antiparallel in-register β-sheet
L F A
K V F E
parallel
antiparallel
(i)
(ii)
4aa-3aa
(iii)
(iv)
4aa-4aa
(v)
(vi)
3aa-3aa
c
Antiparallel one-residue-shifted
L F A
K V F E
parallel
antiparallel
4aa-3aa
4aa-4aa and 3aa-3aa
(i)
(ii)

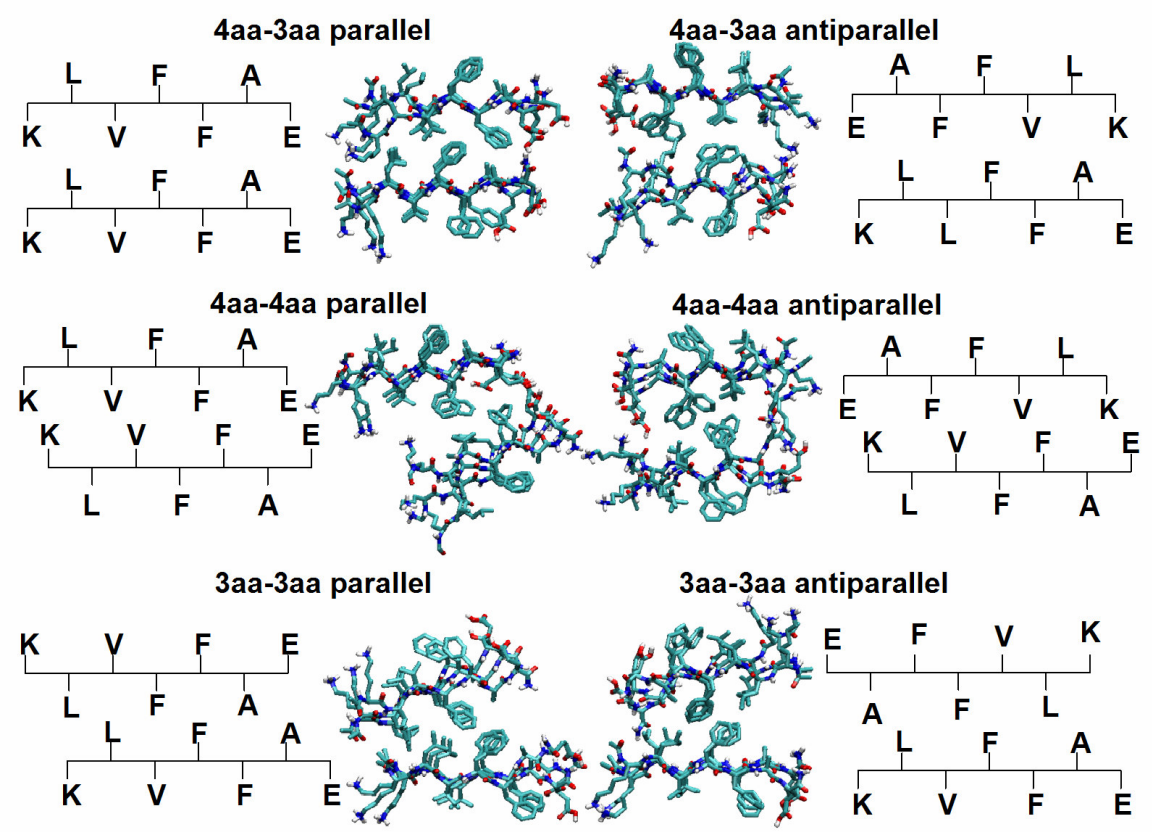

Figure 3.11. Six lamination interaction patterns in the parallel in-register β-sheet of Aβ(16-22) captured in MD

Table 3.3. Average energies of different side chain packing patterns of L17 congener parallel in-register β-sheets.

	4aa-3aa parallel	4aa-3aa antiparallel	4aa-4aa parallel	4aa-4aa antiparallel	3aa-3aa parallel	3aa-3aa antiparallel
Aβ(16-22)	-79032±44	-77745±108	-77978±173	-73715±97	-88336±162	-86801±147
L17Abu	-71197±81	-69263±97	-65103±108	-64626±76	-73342±122	-69173±111
L17I	-92510±70	-79411±97	-84669±182	-85618±217	-93201±79	-87578±59
L17norV	-67233±77	-69815±66	-69919±203	-69397±163	-78381±160	-79984±89
L17norL	-74124±49	-68124±44	-75272±182	-77918±107	-84476±174	-82241±137
L17terL	-68475±55	-70522±81	-76493±71	-63942±118	-78039±76	-67816±107
L17V	-76801±80	-75177±84	-77151±76	76645±90	-82605±116	-80729±108

Notes: the lowest energy for each packing pattern was highlighted in yellow, and the second lowest energy highlighted in green.

The buried solvent accessible surface area (SASA) has been shown to contribute to the overall stability of folded protein structures. Usually, to bury more hydrophobic surface area and less hydrophilic surface area is energetically favorable. To estimate the contribution of the side chain arrangements to the buried solvent accessible surface area among L17 congeners in each particular β-strand orientation, their antiparallel one-residue shifted and parallel in-register β-sheets built in the 6-strand and 3-sheet arrays were captured by averaging the middle 24ps of the trajectories of MD simulations. The 3-sheet arrays were packed in parallel pattern for both antiparallle and parallel β-sheets. For each peptide, the center sheet was used to calculate the buried surface area (Table 3.4.) by subtracting the SASA value in the β-sheet from its corresponding value in the random coil (Yan 2007, Lesser 1990). Although the side chains at the 17 position of L17 congeners differ by no more than a single methyl group, L17norV and L17norL bury less hydrophilic surface area, and more hydrophobic surface area in parallel β-sheets than in antiparallel array. Therefore, L17norV and L17norL are predicted to be more stable as parallel β-sheets, consistent with their experimental results. L17I also forms parallel β-sheet, and although L17I still buries more hydrophobic surface area, the difference is not large. The rest of the peptides, Aβ(16-22), L17Abu, L17terL and L17V all form antiparallel β-sheets, either one-residue-shifted or in-register registry, and show no significant surface area burial benefit to form parallel β-sheet.

Table 3.4. Buried surface area of Aβ(16-22) and its L17 congeners.

	Aβ(16-22)	L17Abu	L17I	L17norV	L17norL	L17terL	L17V
A^0_T	9035.4	8642.4	8962.8	8778.0	8946.0	9162.6	8863.8
A^0_{phi}	3639.0	3659.4	3612.6	3659.4	3659.4	3643.8	3643.8
A^0_{pho}	5396.4	4983.0	5350.2	5118.6	5286.6	5518.8	5220.0
Antiparallel one-residue-shifted							
A_T	3031.6	3069.4	3060.1	3050.5	3158.3	3001.0	3011.0
A_{phi}	2179.1	2203.8	2275.0	2166.8	2169.3	2260.7	2219.7
A_{pho}	852.5	865.6	785.0	883.7	989.0	740.2	791.2
ΔA_T	6003.8	5573.0	5902.7	5727.5	5787.7	6161.6	5852.8
ΔA_{phi}	1459.9	1455.6	1337.6	1492.6	1490.1	1383.1	1424.1
ΔA_{pho}	4543.9	4117.4	4565.2	4234.9	4297.6	4778.6	4428.8
Error (sd)	86.1	65.0	47.0	74.7	83.3	55.1	42.1
Parallel in-register							
A_T	3021.6	3140.7	2925.0	3120.6	3229.3	2993.4	3081.9
A_{phi}	2204.1	2266.1	2238.5	2383.1	2411.2	2279.8	2249.4
A_{pho}	817.5	874.5	686.5	737.5	818.0	713.6	832.6
ΔA_T	6013.8	5501.7	6037.8	5657.4	5716.7	6169.2	5781.9
ΔA_{phi}	1434.9	1393.3	1374.1	1276.3	1248.2	1364.0	1394.4
ΔA_{pho}	4578.9	4108.5	4663.7	4381.1	4468.6	4805.2	4387.4
Error (sd)	44.0	41.6	35.3	54.7	60.3	73.8	25.3
$\Delta\Delta A=\Delta\Delta A_{antiparallel}-\Delta\Delta A=\Delta\Delta_{Aparallel}$							
$\Delta\Delta A_{phi}$	25.0	62.3	-36.5	216.3	241.9	19.1	29.7
$\Delta\Delta A_{pho}$	-35.0	9.0	-98.5	-146.2	-170.9	-26.6	41.3

Notes: For each peptide, the simulation is done with the middle sheet of 6-strand 3-sheet system after MD simulation. The values are adopted by the average of 24ps trajectories. The unit is Å^2. $\mathbf{A^0_T}$ is the total surface area by adding the solvent accessible surface area (SASA) of all seven residues in each peptide, and multiplied by 3 since this is a 3-strand β-sheet. SASA value of each amino acid is from Lesser 1990. $\mathbf{A^0_{pho}}$ is the total SASA of the hydrophobic groups. $\mathbf{A^0_{phi}}$ is the total SASA of the hydrophilic groups. The side chain surface values of non-natural amino acids are adopted as, Abu: CH_2, 25.9, CH_3, 63.0; norV, CH_2 (β), 25.9, CH_2 (γ), 22.9, CH_3, 63.0; norL, CH_2 (β), 25.9, CH_2 (γ), 22.9, CH_2 (δ), 28, CH_3, 63.0, according to the similar group in Lys and Leu. Because our peptide are capped at the both termini, the surface values of CH_3, C=O are used as those in Ala, and the surface value of NH_2 is used as that in Lys. The "$\mathbf{A_{phi}}$" and "$\mathbf{A_{pho}}$" are hydrophilic and hydrophobic surface area of each 6-strand β-sheet calculated from *Maestro*. They are viewed as the hydrophilic or hydrophobic SASA in the folded state. $\mathbf{\Delta A_{phi}= A^0_{phi} - A_{phi}}$, $\mathbf{\Delta A_{pho}= A^0_{pho} - A_{pho}}$ (*Lesser 1990*).

DISCUSSION

Although the parallel and antiparallel β-sheets are equally distributed in protein structures, a preference exists for each folded protein. Although it is well accepted the β-sheet orientation is determined by the thermodynamic stability of the overall structure (Gellman 1998, Zhao 2006), the factors which determine β-sheet orientation remain largely unknown.

In the classical Pauling-Corey models the parallel β-sheet has somewhat more distorted and consequently weaker hydrogen bonds between the strands (Pauling 1951). Parallel β-sheets contain a 12-atom H-bonding ring, while antiparallel β-sheets contain one 14-atom and one 10-atom H-bonding ring. With the observation, the small parallel β-sheet structures occur rarely in globular proteins. This implies that antiparallel β–sheets may be more stable than parallel ones. However, recent studies indicate there is little energetic difference between parallel and antiparallel β-sheets (Gailer 1997, Scheiner 2006).

The factors which contribute to the parallel or antiparallel β-sheet formation remain unclear (Gellman 1998). Although some short peptides do not form stable parallel β-sheets (Freire 2008), short peptides, GNNQQNY (Sawaya 2007), HHQALVFFA ([2]Dong 2006) and NFGAIL (Melquiond 2007) were observed to be parallel β-sheets in amyloid assemblies. Therefore, the amyloid scaffold may have certain interactions which stabilize parallel β-sheets. The β-sheets in amyloid contain repetitive β-strands. The redundant inter-strand interactions within the β-sheet and the inter-sheet side chain interactions may play a role in maintaining the parallel orientation.

In Chapter 2, I discovered the side chain cross-strand paring of the adjacent strands within a β-sheet controls the β-sheet registry. In these V18 congeners, which all form antiparallel β-sheets, the bulkier β-branched residues, Ile, terL and Val, at the 18th position favor pairing with the smaller Ala21 than the larger Phe20. In these L17 congeners, cross-strand pairing still plays a role in determining the strand registry. For example, with Val at the 18th position, and another β-branched residue, Val or terL, at the 17th position, both L17V and L17terL pair the β-branched residue at the 17th position

with Ala21, to give the antiparallel in-register β-sheet array. Because the in-register β-sheet has one more H-bond in the backbone, as compared with the one-residue-shifted registry, the in-register registry array should be preferred for L17V and L17terL with one of the β-branched residues in their sequences being paired with Ala21. For the L17 congeners, the antiparallel in-register β-sheet is expected for β-branched replacements at the 17th position, and antiparallel one-residue-shifted β-sheets are expected for non-β-branched replacement.

However, when Ile, another β-branched residue, occurs at the 17th position, the L17I peptide forms parallel in-register β-sheets, instead of antiparalle in-register β-sheets. Ile is not only β-branched, but it also has χ_2 rotamers, while β-branched Val and terL only have χ_1 rotamers. Among the L17 congeners, L17I, L17norV and L17norL form parallel β-sheet, with Ile, norV and norL having same χ_2 rotamers. Leu also has χ_2 rotamers, but it is γ-branched, and Aβ(16-22) indeed form antiparallel one-residue-shifted β-sheet. L17Abu also forms antiparallel one-residue-shifted β-sheet. Both Leu and Abu are not β-branched; and as expected, the β-branched V18 still plays the role in pairwise interactions that determine the strand registry. Therefore, the structural similarity among L17 congeners which form parallel β-sheets may be the non-γ-branched χ_2 rotamers. These non-γ-branched χ_2 rotamers at the 17th position could induce a particular β-sheet orientation because the residues containing non-γ-branched χ_2 rotamers have longer "hydrophobic tails" in the side chain to pack in the hydrophobic core, relatively to those without γ-carbons; and the residues containing non-γ-branched χ_2 rotamers have less steric demand in the hydrophobic packing interactions.

These L17 congeners are all short peptides with the same seven-residue length. As described above, they can form two types and three kinds of β-sheets, parallel in-register, antiparallel in-registry, and antiparallel one-residue-shifted β-sheets. In searching the side chain packing preference, the 3aa-3aa packing pattern with mainly hydrophobic interaction among L-F-A residues has the lowest energy for each L17 congeners. This is consistent with burying more hydrophobic residues of the peptide, and exposing more hydrophilic residues of the peptide to water. However, every L17 congener favors the 3aa-3aa packing pattern among the six possible side chain lamination packing patterns, and shows no differentiation with their side chain modification, classified on their β- and γ-carbons as β-branched (Val and terL), non-β-branched (Abu), non-β-branched/γ-branched (Leu), non-β-branched/non-γ-branched (norV and norL), β-branched/non-γ-branched (Ile). Because the lamination side chain interactions did not differentiate the L17 congeners, the cross-strand side chain interactions by the non-β-branched/non-γ-branched (norV and norL) and β-branched/non-γ-branched (Ile) residues at the 17^{th} position may play a role in inducing the parallel β-strand orientation for L17norV, L17norL, and L17I. In the parallel in-register β-sheet, the residues at the 17^{th} position are on the same side of the β-sheet, and cross-strand paired with each other. The non-γ-branched extending side chain pairing can be favorable in burying more hydrophobic area (Yang 1995). However, similar side chain modifications were introduced at the 18^{th} position in Chapter 2, but all V18 congeners form antiparallel β-sheet, either in in-register or one-residue-shifted register. If the non-γ-branched extending side chain pairing with themselves is favored, and drives the peptide to be in the parallel orientation, V18norL, V18norV and V18I would also prefer to be parallel. The non-γ-

branched extending side chain pairing seems also to depend on the residue position. When Aβ(16–22) forms β-sheets, the side chain of its 17th residue is at the N-terminal edge (Figure 3.10). Being close to the β-sheet edge causes the 17th residue side chain to be exposed to solvent. This may drive the hydrophobic long chains to pack when residues with non-γ-branched extending side chain reside at the 17th position. However, the side chain at the 18th position is not at the edge, but under the shielding of Lys16 side chain. Therefore, the solvent may not have the significant effect to drive the hydrophobic long chain to pack together. Instead, the steric β-branching demand is more critical to determining the cross-strand pairwise interaction of the more buried 18th residue side chains.

In addition, comparing the buried area in forming parallel in-register and antiparallel one-residue-shifted β-sheet for each L17 congener (Table 3.4.), L17norL and L17norV prefer parallel β-sheet by burying more hydrophobic area and less hydrophilic area, explaining the contribution of these non-γ-branched extending side chain pairing to the parallel β array. Neither antiparallel in-register array nor antiparallel one-residue-shifted array can make the 17th residue cross-strand pair with each other. In forming the β-sheet, non-γ-branched extending side chains may became predominant, and drive the peptide sequence to be in parallel orientation. Recent studies reported that changing the amphiphilicity of Aβ(16–22) by adding alkyl chain on the peptide backbone can switch the β-strand orientation from antiparallel to parallel (Gordon 2004). The side chain modifications in L17 congeners do not change the peptide amphiphilicity dramatically. Here, I argue the switch of the β-strand orientation in L17 congeners is the result of preferred cross-strand side chain interactions.

Therefore, in the L17 congeners, the side chain packing patterns do control backbone β-sheet orientation in amyloid assembly. The nucleation dependence is a featuer in amyloid assembly. The β-sheet and lamination in the characteristic amyloid cross-β structure are peptide specific, should be resulted from the first favorable amyloid repetitive unit by selecting the most stable patterns in terms of both the peptide backbone and side chain interactions. It appears that the backbone interaction and the side chain packing are correlated with each other. L17 congeners provide clear examples of predominant side chain packing to direct the backbone β-sheet orientation.

CHAPTER 4

HYDROPHOBIC CORE PACKING IN AMYLOID NANOTUBES

INTRODUCTION

Amyloid assemblies are characterized with extensive backbone β structural networks with sheet-sheet side chain packing, i.e. the cross-β spine (Blake 1996, Sunde 1997, Sikorski 2003). Current models of amyloid assembly widely accept a nucleation event occurs early, and this early structure plays as a template to create the final assembly (Harper 1997, Westermark 2005, Wetzel 2006). To define the nuclei, the debate is over whether the backbone or the side chains have the major role in controlling the amyloid assembly. Because the backbone β networks are ubiquitous in amyloid assemblies, and can be independent of protein sequences, the backbone conformation was accepted as the main factor in determining the amyloid assembly (Dobson 2003). However, the amino acid side chains carry the functionality of the main chain, and backbone H-bonding requires desolvation (Fernandez 2003), arguing that the side chain interactions can

modify the amyloid propensity of a sequence. In addition, being an important component in amyloid cross-β spine, the sheet-sheet stacking requires the energetic contribution of side chain interactions. New forces introduced in the side chain interactions, such as metal coordination (Dong 2006) or extra H-bonding (Liu 2008), have been reported to strengthen the side chain interactions, and induce the amyloid sheet-sheet stacking.

Our recent studies established that the cross-strand pairing between residues in adjacent β-strands determines the registry of amyloid β-sheets (Liang 2008), suggesting the side chain interactions as essentials for amyloid β-sheet assembly. The side chain distribution on the β-sheet surface varies with the β-strand registry. A symmetric side chain distribution produced by an antiparallel one-residue-shifted β-sheet registry induced large number of sheets to stack (Mehta 2008). Therefore, the induced sheet-sheet stacking can also be achieved by shifting the β-strand registry. Indeed, the backbone β conformation was changed when the metal ions were introduced into the side chain interactions (Dong 2006). This raises a critical issue for in amyloid assembly, the side chain interactions not only display in the amyloid sheet-sheet stacking, but maybe more important, also determine the backbone β conformations. To clarify, the side chain interactions can be classified as the inter-strand interaction within a β-sheet (cross-strand pairing) and the inter-sheet interactions within lamination (sheet-sheet stacking). Due to the effect of the side chain interactions on the backbone conformations, the intrinsic side chain packing contribution to the sheet-sheet stacking may be misinterpreted. Our question is independent on the backbone conformation, how the amyloid sheet-sheet stacking is affected by the side chain interactions, and whether the side chain interactions in sheet-sheet stacking are important to determine the amyloid nuclei.

The side chain complimentary interactions on amyloid β-sheet surface were suggested to determine the sheet-sheet stacking (Mehta 2008). Large number sheet-sheet stacking of amyloid β peptides can produce amyloid nanotubes with a helical pitch ([2]Dong 2006, Mehta 2008). The steric effect of the end groups on the twisted β-sheets of a tripeptide amphiphile system was reported to be able to tune supramolecular β-sheet helical pitches (Li 2007). The steric demand of the end groups on the helical pitch somewhat indicates the complimentary packing of this tripeptide amphiphile. In whole peptide assembled amyloid systems, the steric demand of the side chains may also play a role in amyloid β-sheet helical assemblies.

During our recently work on the self-assembly of Aβ(16-22) nanotubes (Liang 2008), we observed the modification at the hydrophobic core of Aβ(16-22) can generate different nanotube diameters. Because all these tubes contain same antiparallel one-residue-shifted β-sheet as the wild type Aβ(16-22) (Mehta 2008), the packing of the modified side chains in the hydrophobic core should be responsible in determining the tube diameters. The structural difference of these Aβ(16-22) nanotube-formation congeners is not more than one CH_2 in their side chains, but the correlation of individual β-strand offsets with the side chain conformations was observed. In addition, the conformational entropy of the side chains in the hydrophobic core, corresponding to the side chain degree of freedom in the term of the number of rotamers and the size of the side chain, is correlated with the stability of the sheet-sheet stacking. The work presented here explains the helical twist of extended-peptide nanotubes, and the contribution of side chain hydrophobic packing to amyloid sheet-sheet stacking. The loss of side chain conformational entropy is well-known as one of the major forces against protein folding

(Doig 1995, Penel 2001). The observed correlation of the conformational entropy and the stability of the amyloid sheet-sheet stacking supports amyloid assembly events may follow similar pathways as protein folding.

MATERIALS AND METHODS

Electron Diffraction

Diffraction patterns were recorded using a Philips 410 EM transmission electron microscope in diffraction mode. *d*-spacing was calculated with $d = \lambda L/R$, where R is the distance (mm) from the central bright spot to the arc of interest, L is the camera length (distance in mm between specimen and photographic film), and λ is the electron wavelength (80 kV = 4.2 pm). Camera length was calibrated using an aluminum polycrystalline standard (Electron Microscopy Sciences, Hartfield, PA).

RESULTS

β-sheet Strand Registry of Aβ(16-22) Congener Nanotubes

The hydrophobic core of Aβ(16-22) comprises five residues: Leu17, Val18, Phe19, Phe20, and Ala21. The N- and C-termini are buffered with hydrophilic residues Lys and Glu, respectively. Nanotubes can be formed by Aβ(16-22) in 2:3 (v:v) CH_3CN:H_2O with 0.1% TFA. The structural perturbations at the hydrophobic core were applied to the 17 or 18 position by replacing with a series amino acids that varied in side chain steric demand as described in Chapter 2 and 3 ([1]Liang 2008). The structural difference is not more than a single CH_2 from Val or Leu. The resulted Aβ(16-22) congeners were allowed to self-assembly in the same 2:3 (v:v) CH_3CN:H_2O with 0.1%

TFA as Aβ(16-22) tubes. Their self-assembly morphologies were investigated by TEM, in which only three peptides have the tube morphology, i.e., V18I, V18terL and L17Abu (Figure 4.1.). The cross-strand pairing of β-branched residues at 18 position, and the electrostatic interactions of the terminal residues have been reported as factors which dictate the strand registry ([1]Liang 2008). The removal of the electrostatic interactions by replacing Glu with Ile, Leu or Val also results in the tube morphology (Figure 4.1.). Sequences of these tube-formation congeners are listed in Table 4.1.. The antiparallel one-residue-shifted β-sheet generates same side chain distribution on the top and bottom β-sheet surfaces, which induces large lamination, and promises the tube morphology (Mehta 2008, [1]Liang 2008). No exception, all Aβ(16-22) congener tubes contain the antiparallel one-residue-shifted β-sheet as investigated by IE-FTIR (Figure 4.2. and Table 4.2.) (Mehta 2008, [1]Liang 2008).

Table 4.1. Selected core-sequence congeners which form the tube morphology.

	16	17	18	19	20	21	22
WT	**Lys**	**Leu**	**Val**	**Phe**	**Phe**	**Ala**	**Glu**
V18I	Lys	Leu	**Ile**	Phe	Phe	Ala	Glu
V18terL	Lys	Leu	**terL**	Phe	Phe	Ala	Glu
L17Abu	Lys	**Abu**	Val	Phe	Phe	Ala	Glu
E22I	Lys	Leu	Val	Phe	Phe	Ala	**Ile**
E22L	Lys	Leu	Val	Phe	Phe	Ala	**Leu**
E22V	Lys	Leu	Val	Phe	Phe	Ala	**Val**

Table 4.2. ^{12}C and ^{13}C amide I band shifts in IE-FTIR of Aβ(16-22) congener tubes.

Peptides	^{12}C shift (cm^{-1})	^{13}C shift (cm^{-1})	The split between ^{12}C and ^{13}C (cm^{-1})
Aβ(16-22)	13	29	42
V18I	12	28	40
V18terL	14	29	43
L17Abu	12	29	41
L17A	13	28	41
E22I	12	30	42
E22L	12	29	41
E22V	12	29	41

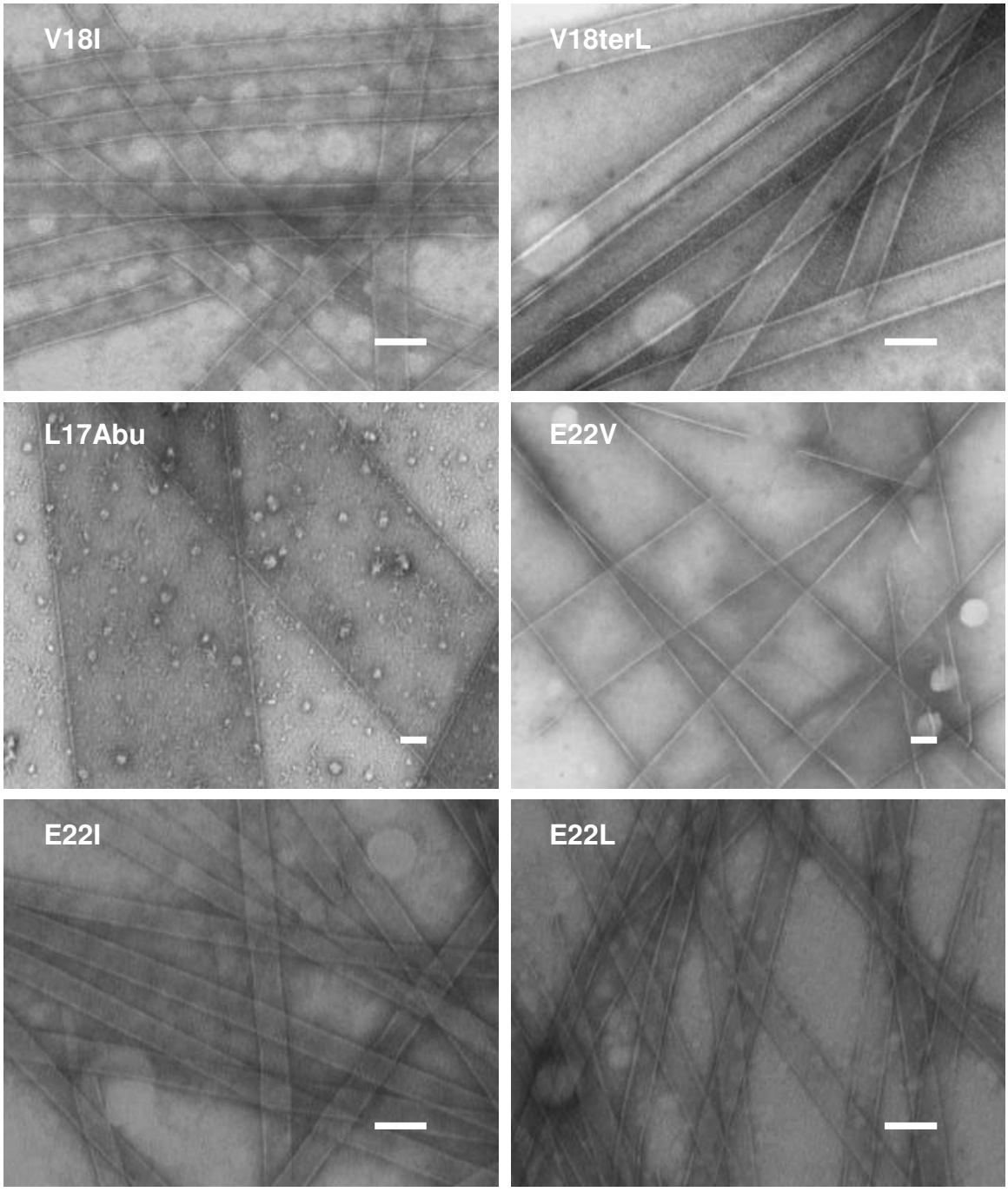

Figure 4.1. TEM of self-assembled nanotubes by Aβ(16-22) congeners

Under acidic conditions. Scale=100nm.

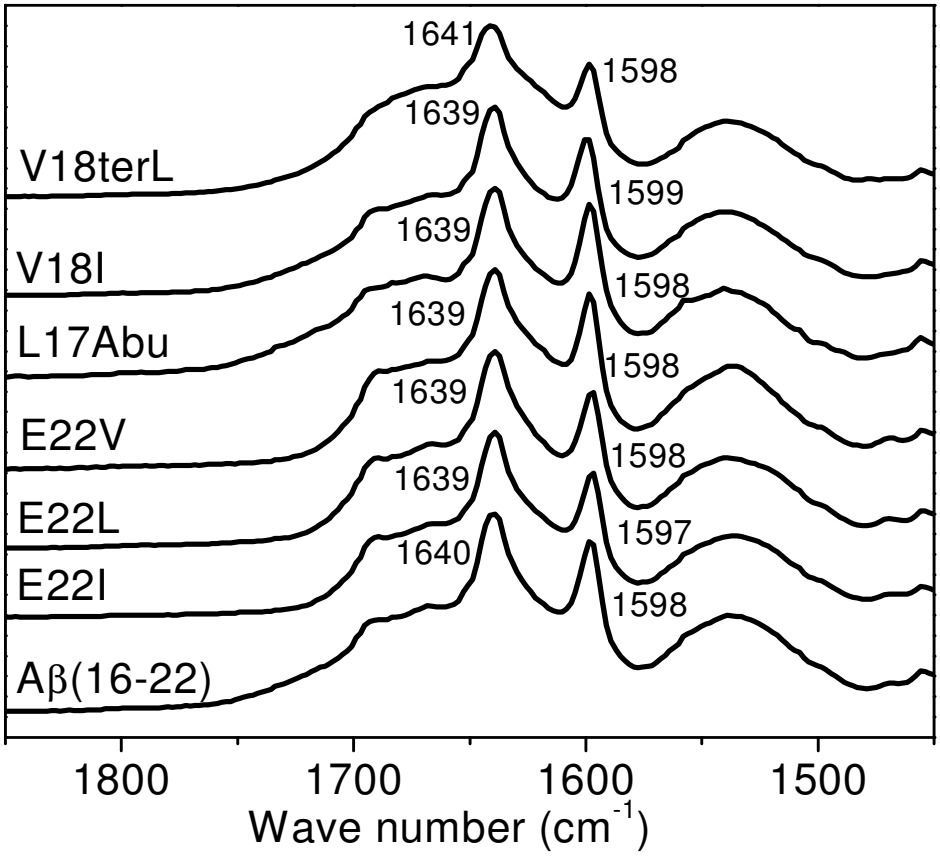

Figure 4.2. IE-FTIR of Aβ(16-22) congener tubes under acidic conditions.

Each congener was [1-^{13}C] F19 labeled. The centers of ^{12}C and ^{13}C amide I absorbance are labeled.

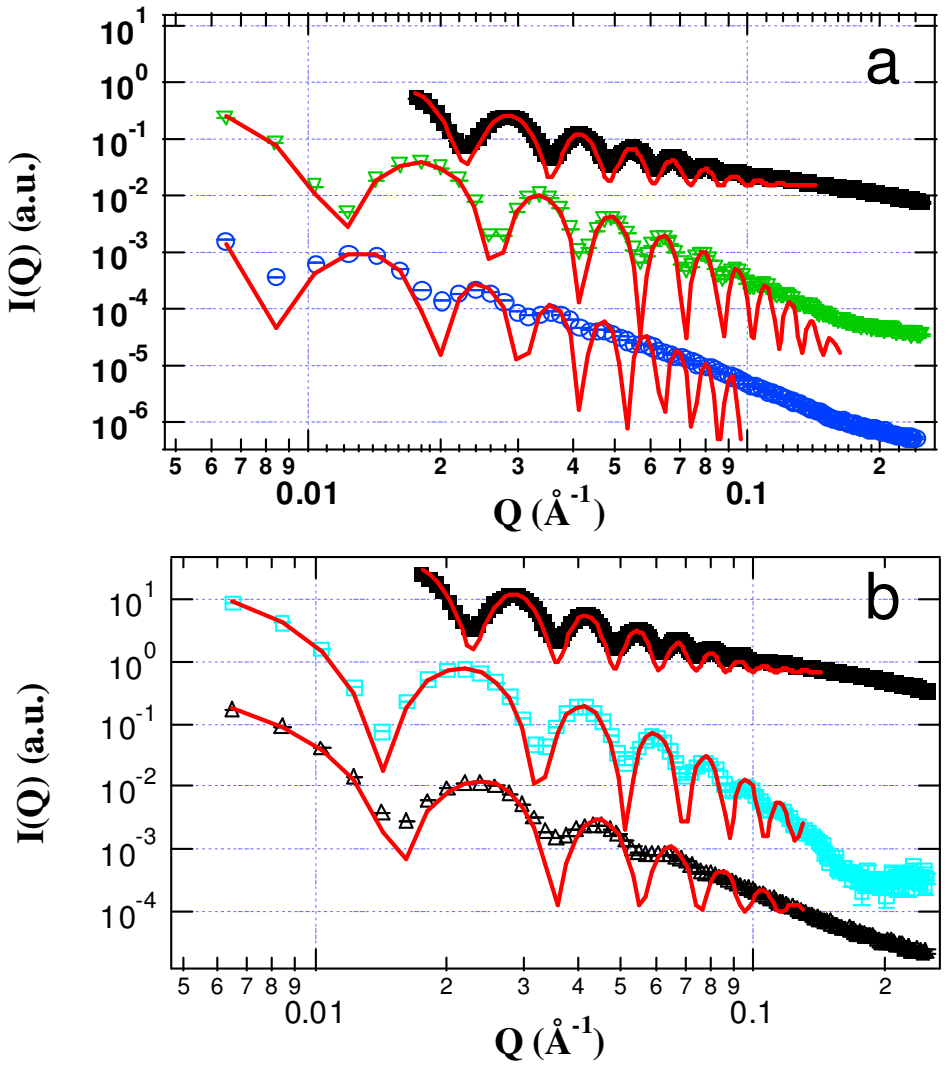

Figure 4.3. SAXS of self-assembled nanotubes by Aβ(16-22) congeners

Under 2:3 (v:v) CH_3CN:H_2O with 0.1% TFA:

(a) Aβ(16-22) (■, black), V18I ((▽, green), and V18terL (○, blue), their shell core circular cylinders were fitted in red;

(b) Aβ(16-22) (■, black), E22I (△, black), and E22L (□, cyan), their shell core circular cylinders were fitted in red.

Dimensions of Aβ(16-22) Congener Nanotubes

Because TEM images were obtained after the tubes were dried on the sample grids, the tubes are usually collapsed and flat on the TEM grid. Therefore, the diameters measured in TEM are not precise. To precisely comparing the tube diameters of Aβ(16-22) congeners, small angle X-ray scattering (SAXS) was applied to measure the tube diameters in solution (Figure 4.3. and Table 4.3.). For congeners with alkyl side chain modifications at 18 position, Aβ(16-22), V18I, and V18terL tube diameters are slightly different with ±8nm comparing with Aβ(16-22) tubes: Aβ(16-22) (52±0.4nm), V18I (44±2nm), and V18terL (60±1nm). For the congeners with electrostatic modification at 22, E22I and E22L, their tube diameters are much smaller than Aβ(16-22) tubes, with diameters as 35±0.8nm and 38±0.6nm, respectively. L17Abu and E22V both form larger size tubes (Figure 4.1.). In SAXS, E22V diameter is up to 276nm (Lu 2006). Because L17Abu tube diameter is too big, and with the hollow inside, they were deformed during the SAXS measurement. In the cryo-SEM analysis, which avoids the tube drying collapse, the tube diameter of L17Abu is up to 500nm (Figure 4.4.a).

Tubes formed by Aβ(16-22) congeners have the cylindrical shape. The shell thickness is another parameter of these tubes. In AFM, the tubes are dried and collapsed flat on the AFM grids. The height in the z-dimension as shown in Figure 4.4.b represents twice the shell thickness. Table 4.3. summarizes all the tube shell thicknesses (AFM images of all the congener tubes are in Figure 4.4.c). Most of them have the shell thickness around 4nm. Given the peptide lengths are about 2.6nm, the tube shell is about twice the peptide length, which was the experimental support to propose Aβ(16-22) nanotubes have a peptide bilayer in the nanotube wall (Lu 2003, Mehta 2008). Twice of

the peptide length is 5.2nm, which is longer than the measured shell thickness. Therefore, the peptides should tilt in the shell, which will discuss in detail below.

Table 4.3. Tube dimensions of Aβ(16-22) congeners.

	Diameter(nm)		Pitch angle (°)	Shell thickness (nm)
	Cyro-SEM(nm)	SAXS (nm)		
Aβ(16-22)		52±0.4	23-25	3.9±0.1
V18I		44±2	23-25	3.4±0.1
V18terL		60±1	23-25	3.8±0.1
L17Abu	500	/	32-34	3.9±0.1
E22I		35±0.8	10-15	3.8±0.1
E22L		38±0.6	10-15	3.6±0.1
E22V		278	32-34	3.1±0.1

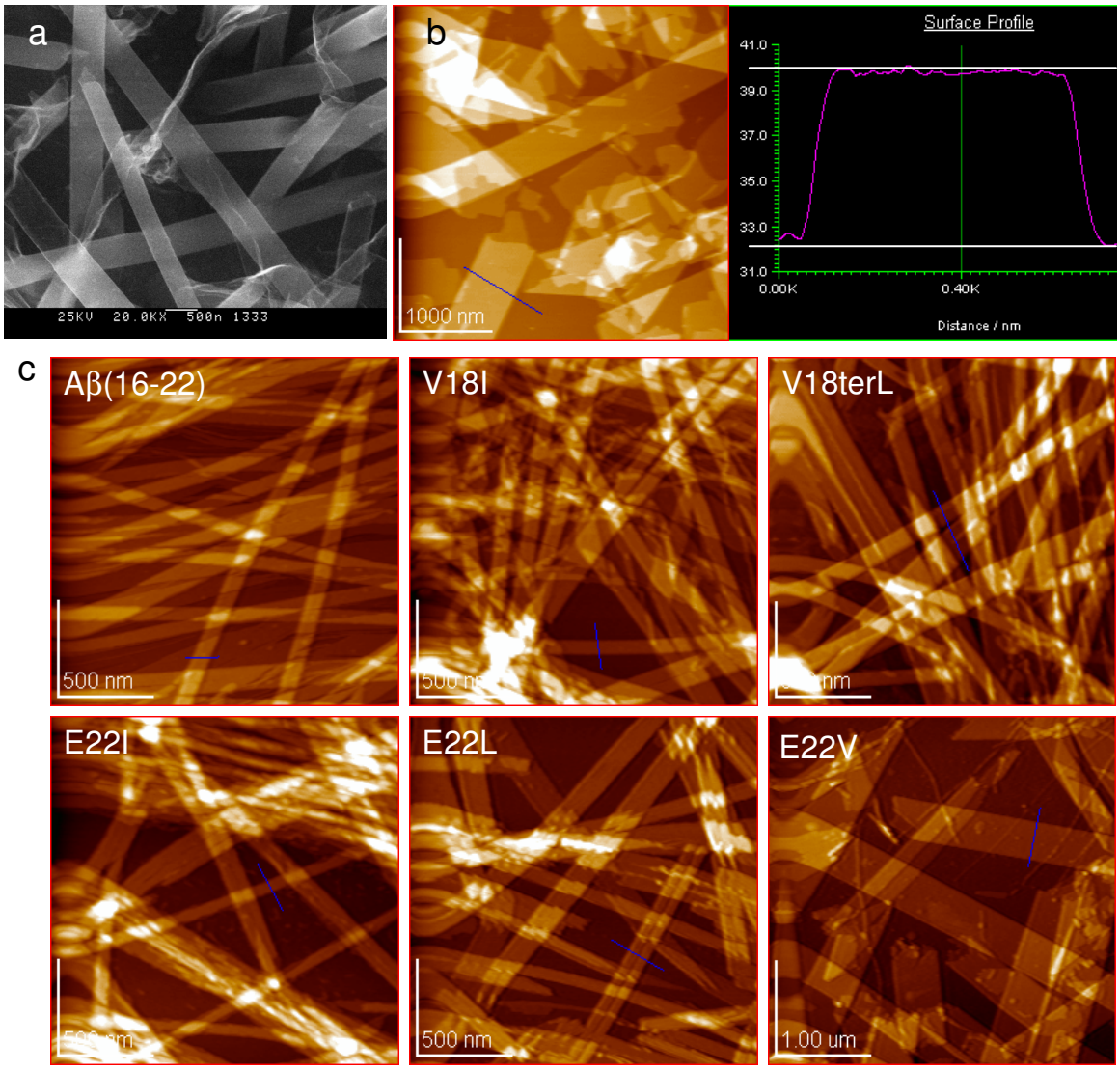

Figure 4.4. Shell thickness measurement of Nanotubes

(a) Cyro-SEM to determine the L17Abu tube diameters in water with 0.1% TFA

(b) AFM to determine the shell thickness of L17Abu tubes

(c) AFM of self-assembled nanotubes by Aβ(16-22) congeners at CH_3CN: H_2O (v:v, 2:3) with 0.1% TFA

Cross-β Structure of Nanotubes

All the tubes contain the amyloid characteristic cross-β structure, which appears as the H-bonding scattering at ~5Å and the lamination scattering at ~10Å (Figure 4.5. and Table 4.4). Obviously, the lamination scattering of E22 congeners has longer distance centered at 10.4Å and relatively broader than the V18 and L17 tube congeners. Most strikingly, E22V tubes have the broadest lamination scattering and largest lamination distance centered at 11Å. Because WAXS signals represent the structural repetition in the detection volume, the structural disorder will generate the broader scattering distribution. This suggests peptides in E22 tubes are structurally more disordered comparing with V18 and L17 tubes. Interestingly, L17Abu tubes have the shortest lamination distance, centered at 9.7nm. This may not be a surprise because Abu has much smaller side chain comparing with Leu. This is also true among Aβ(16-22), V18I and V18terL. Val has one less CH_3, then the lamination distance of Aβ(16-22) tubes is slightly shorter than V18I and V18terL. However, this rule does not apply to E22V. Although it has one less CH_3, the lamination distance of E22V tubes is surprisingly larger than E22I and E22L. The possible reason is the residue at 22 is the C-terminal residue close to the hydrophobic core. The modifications in E22 congeners not only change the hydrophobic core, but also may affect the peptide terminal interactions in the tubes. The terminal residues may play a role in the bilayer association, and may require the specific structural recognition. The deletion of one CH_3 may cause the structural crush, and generate disorder.

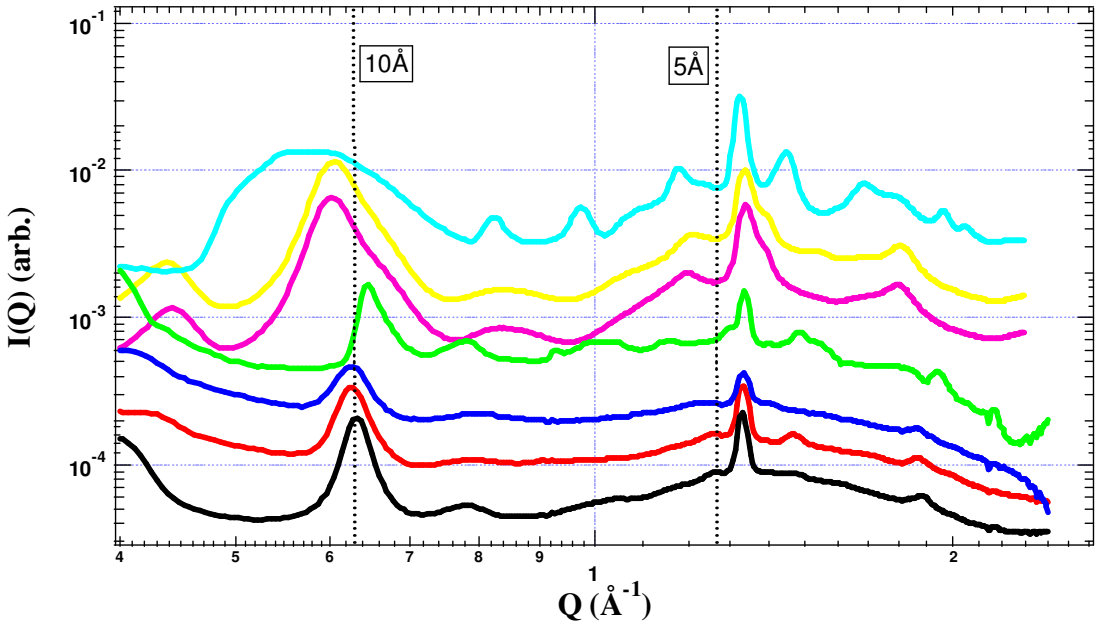

Figure 4.5. WAXS of nanotube powders formed by Aβ(16-22) congeners

Aβ(16-22) (black), V18I (red), V18terL (blue), L17Abu (green), E22I (pink), E22L (yellow), and E22V (cyan).

Table 4.4. The H-bonding and lamination scatterings in WAXS of Aβ(16-22) congener tubes.

	H-bonding (Å)	Lamination (Å)
Aβ(16-22)	4.7	9.9
V18I	4.7	10.1
V18terL	4.7	10.1
L17Abu	4.7	9.7
E22I	4.7	10.4
E22L	4.7	10.4
E22V	4.7	11.0

Pitch Angles and the Number of Lamination in Tubes

The Aβ(16-22) amyloid tubes were proposed to arrange by the bilayer β-sheet lamination tape helically coiling up as shown in Figure 4.6.a (Lu 2003, [1]Dong 2006). In this helical twist model, the tube radius (ρ) is correlated with the tape width (δ) and the pitch angle (ψ). The tape width is in the lamination dimension (the yellow arrow in Figure 4.6.a), and the H-bonding dimension is perpendicular to the lamination dimension (the green line in Figure 4.6.a). In electronic diffraction of Aβ(16-22) congener tubes, the H-bonding and lamination diffraction both have two arcs, which is consistent with helical twist model of these tubes (Mehta 2008). On TEM grids, the tube cylinder is collapsed to two tube-wall sheets when they are dried. Because of the pitch, the directions of H-bonding or lamination in the top and bottom wall sheets are changed corresponding to pitch angle. For example, the H-bonding diffraction appeared as two separated arcs at ~4.7Å (the green line connected in Figure 4.6.b) and the lamination diffraction appeared as two separated arcs at ~10Å (the yellow line connected in Figure 4.6.b). The H-bonding and lamination diffractions of the same sheet are perpendicular. The angle θ between the two H-bonding arcs or lamination arcs is determined by the pitch angle.

The relationship between the pitch angle ψ and the angle θ can be determined by a mathematical model. As shown in Figure 4.6.a, a tube can be viewed as a cylinder with 2ρ diameter. When the cylinder is flattened, two rectangles (the tube wall sheets) with πρ as one width are produced. Solid-line rectangle represents the top sheet, and the dot-line rectangle represents the bottom sheet. The β-sheet lamination tape can be drawn by jointing the diagonal (the green line). In the tape (BCDH), the length of the tape is in the H-bonding dimension (the green lines), and the width is in the lamination dimension (the

yellow line). ψ is defined in Figure 4.6.a as the angle between H-bonding dimension and the cross-section dimension (∠BDC), or the angle between the lamination dimension and the tube axis (∠CBF). Based on these definitions, the tape width, ω, (BF in Figure 4.6.a) can be described as

$$w = 2\pi\rho \sin\psi$$

The pitch, δ, (BC in Figure 4.6.a) can be calculated by

$$\delta = \frac{w}{\cos\psi} = \frac{2\pi\rho \sin\psi}{\cos\psi} = 2\pi\rho \tan\psi$$

Line AC is co-linear with the hydrogen bonding dimension of the top sheet, and BF is in the lamination width. The dashed line AB and CE are the H-bonding and lamination dimension in the bottom sheet when the tube is folded. θ is the angle between the H-bonding orientations of the top and bottom sheets (AC and AB), or between the lamination orientations BF and CE. θ can be obtained from the measurement of the angle between the two separated arcs of H-bonding or lamination in the electron diffraction. Because of AB=AD=AC in triangle BCD, ψ=0.5θ. According to this calculation, the pitch angles of all the tubes were obtained and listed in Table 4.4. (the 2D electron diffractions of all the tubes are in Figure 4.7.). There are three pitch angle ranges. E22I and E22L have similar pitch angles, the smallest, 10-15^{o}. Aβ(16-22), V18I and V18terL have similar pitch angle (23-25^{o}). L17Abu and E22V, which form large diameter tubes, have the largest pitch angle (32-34^{o}). As described above, the widths of the tape were calculated (Table 4.5.). Because β-sheets are ~10Å apart in lamination, dividing the tape width by the distance between the laminants (Table 4.4.), the number of laminants within

the tape can be estimated. Indeed, the bigger tube diameter is correlated with the larger number of laminants in the tape.

Table 4.5. β-strand offsets in Aβ(16-22) congener tubes.

	Tape Width (nm)	Number of laminants	β-strand intersheet Offset(°)	β-sheet length (nm)[1]	Number of β-strands[2]	β-strand intrasheet Offset(°)
Aβ(16-22)	69	70	1.44	180.1	383	0.26
V18I	58	57	1.73	152.4	324	0.31
V18terL	80	79	1.27	207.9	442	0.23
L17Abu	878	905	0.15	1893.4	4028	0.03
E22I	28	27	2.19	113.8	242	0.25
E22L	31	30	2.02	123.5	263	0.23
E22V	488	444	0.31	1052.7	2240	0.06

Notes: 1. The β-sheet length is the length of β-sheet across one pitch in the tube cylinder. 2 the number of β-strands is the number of β-strand within the β-sheet across one pitch in the tube cylinder.

Figure 4.6. The nanotube model

(a) The nanotube cylinder is formed from helically coiled tape. Given 2ρ as the tube diameter, the tube cylinder can spread into a rectangle with width 2πρ; The definition of pitch angle ψ and pitch δ, H-bonding (green lines) and lamination (yellow lines) dimensions are labeled in the model.

(b) 2D electronic diffraction of L17Abu tubes with the angle θ between the orientations of H-bonding (green lines) or lamination (yellow lines) in the top and bottom sheets; The H-bonding dimension is perpendicular to the lamination dimension.

(c) The pitch angle and the tilt of β-sheet corresponding to the cross-section plane of tubes.

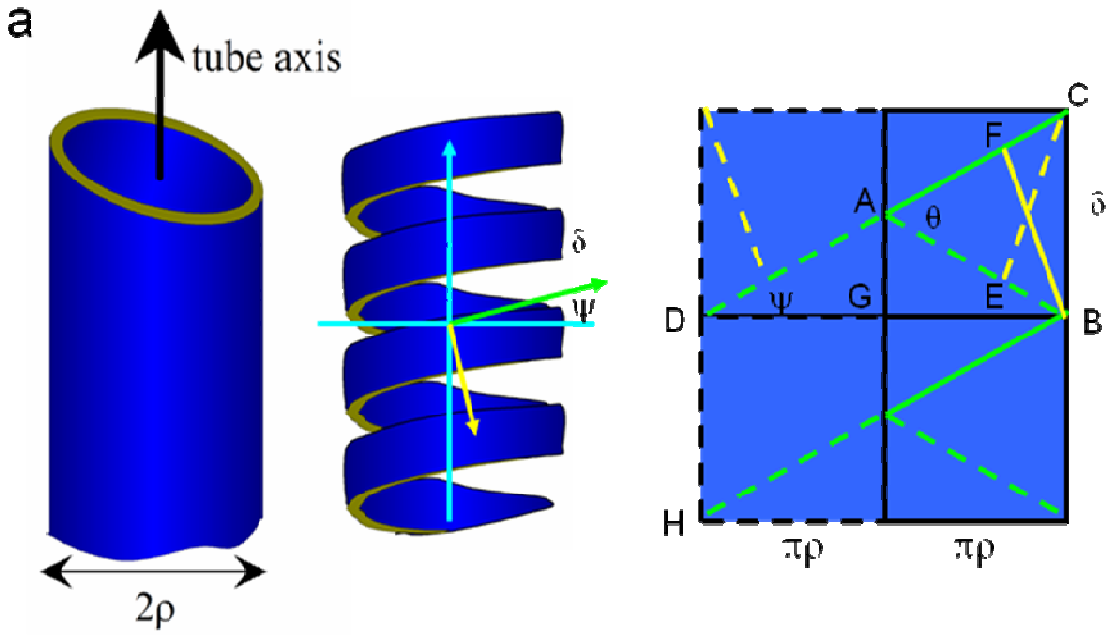
a
tube axis
δ
ψ
2ρ
C
F
A
θ
δ
ψ
G
E
D
B
H
πρ
πρ

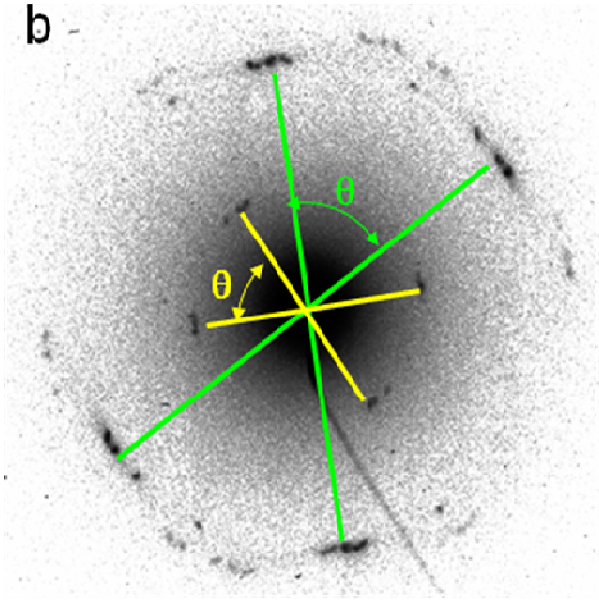
b
θ
θ

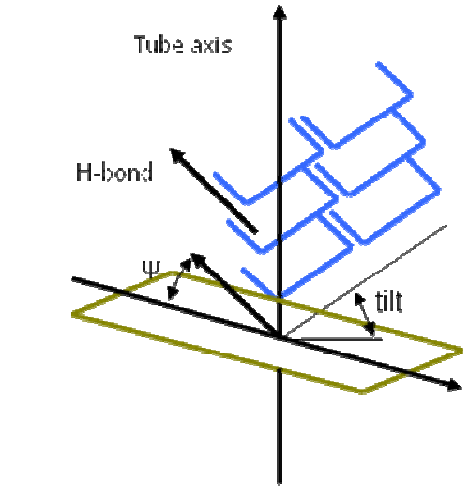
c
Tube axis
H-bond
ψ
tilt

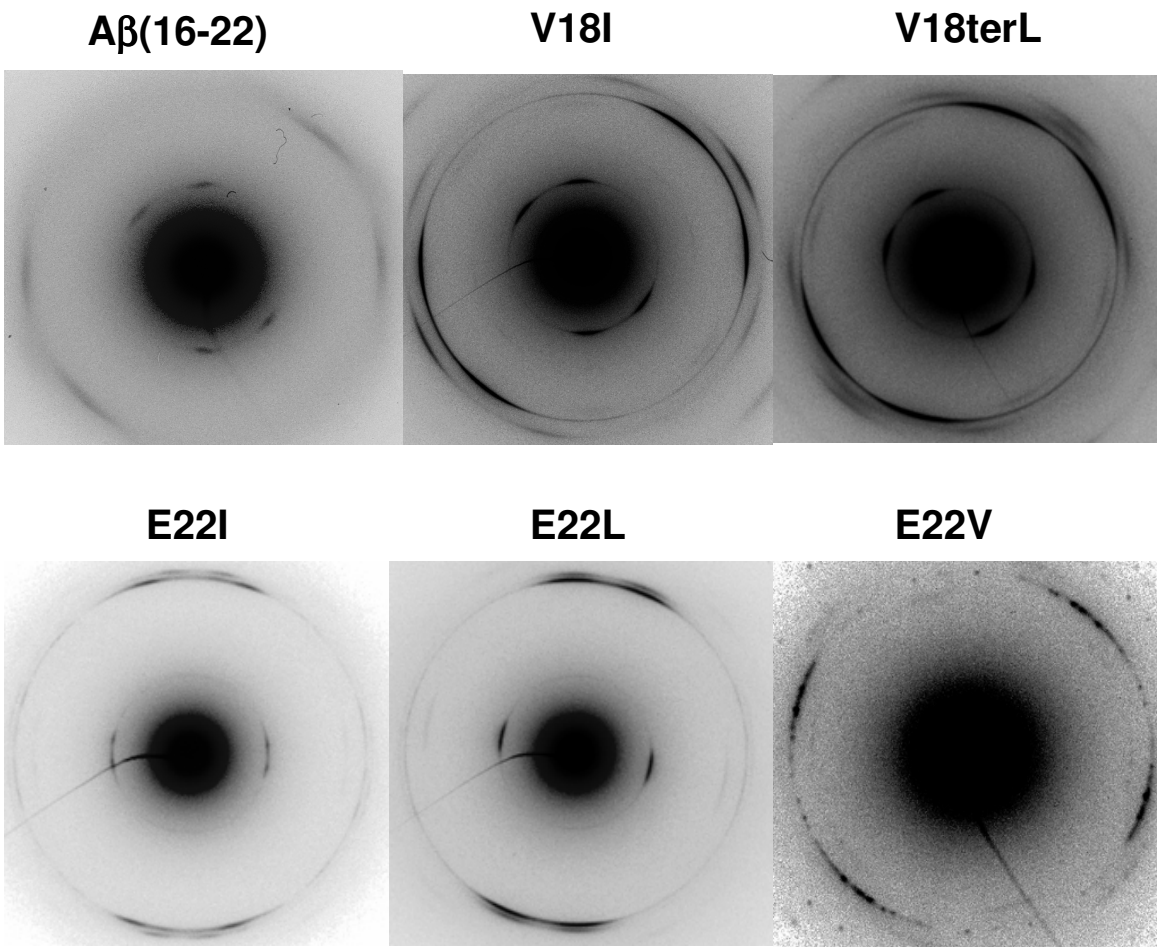

Figure 4.7. 2D electronic diffraction of nanotubes formed by Aβ(16-22) congeners Under acidic conditions.

Melting Temperature of Nanotubes

Amyloid tubes are assembles with cross-β structure. At high temperature, the tubes can be melted by breaking the backbone H-bonding and lamination interaction of the side chains. The melting experiment was done in CD by monitoring the β-sheet signals when increasing the temperature. The melting of each tube represents the strength of intrinsic interactions within the tube frame. Among the V18 and L17 congeners, V18I has the lowest melting temperature at around 25^{o}C. Aβ(16-22) comes as the second with

37^{o}C melting temperature. V18terL and L17Abu did not appear the sigmoid-shape melting curve, and there were still β-sheet signals in the system when the temperature reached 60^{o}C (Figure 4.8.). The temperature did not go above 60^{o}C to avoid the dramatic solvent evaporation. Relatively, V18terL and L17Abu tubes are harder to be melted comparing with Aβ(16-22). This means both L17Abu and V18terL have stronger interactions than Aβ(16-22) in the tube frame, while the interaction within V18I tubes is weakest. When the temperature reached 60^{o}C, all E22 congeners cannot be melted either because of the left β-sheet signals. E22 congeners have one more hydrophobic residue in the sequence, which can strengthen the hydrophobic interaction in the lamination. Therefore, it may not be a surprise all E22 congeners can not be melted. However, the strange part is if they have stronger hydrophobic interaction, they should have produced more lamination, and larger size tubes. Well, only E22V generates larger size tubes than Aβ(16-22). Possibly, the one more hydrophobic residue in the seven-residue sequence causes the E22 congeners to have more structural recognition in the hydrophobic core, which can crush the lamination.

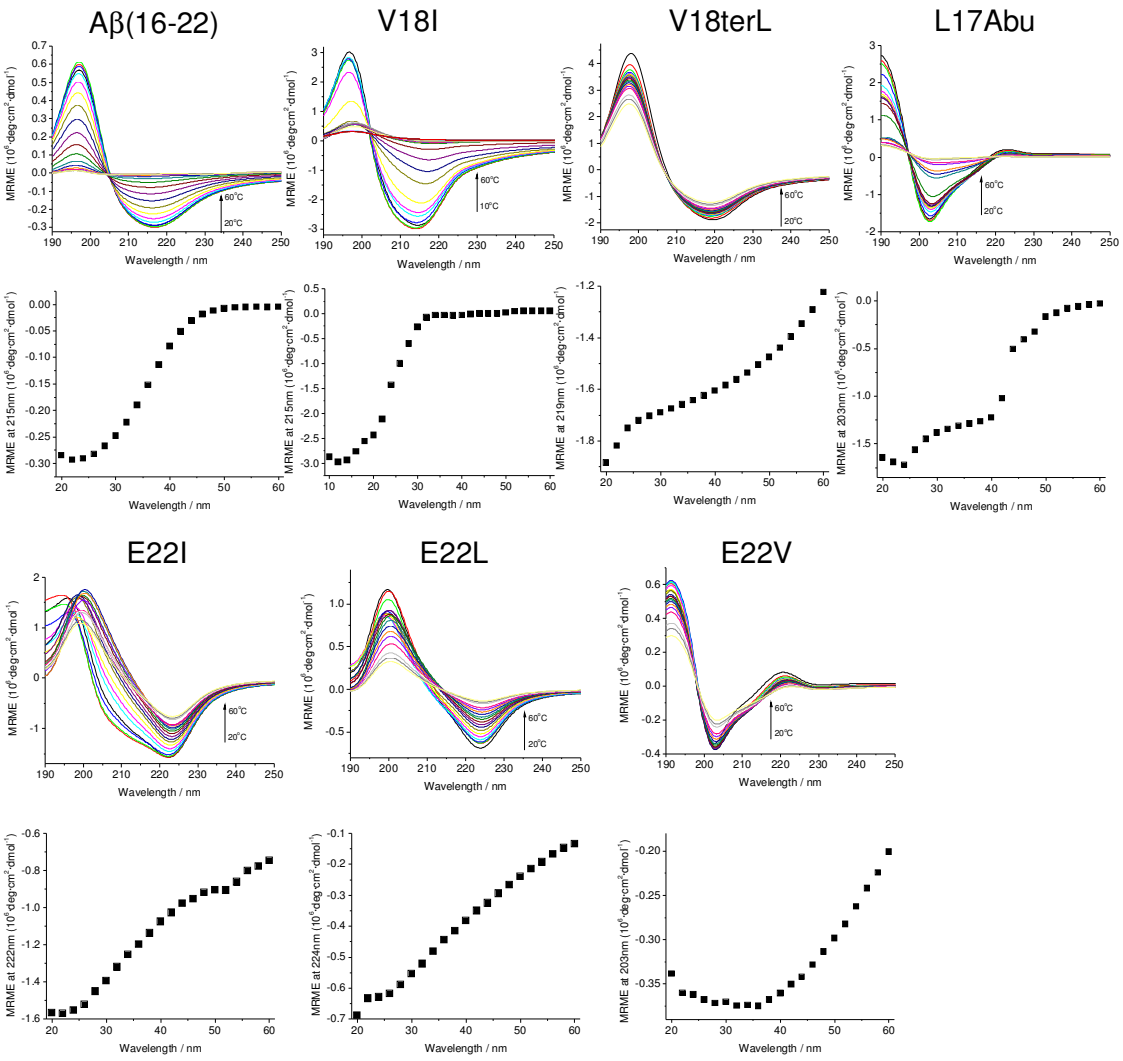

Figure 4.8. CD melting curves of nanotubes formed by Aβ(16-22) congeners

Top: the melting CD curves followed from 20°C to 60°C except V18I tubes, which is followed from 10°C to 60°C.

Bottom: the mean residue molar ellipticity of the negative absorbance plotted as the function of temperature.

Molecular Modeling

The Aβ(16-22) tube-formation congeners can be divided into two groups by their hydrophobic and hydrophilic sequence, Group I includes Aβ(16-22), V18I, V18terL and L17Abu, which have hydrophilic residues at the both termini; Group II includes E22L, E22I and E22V, which have one more hydrophobic residue in their sequences, and only have hydrophilic residue at the N-terminus. They all form the same antiparallel one-residue-shifted β-sheet. To approximate side-chain arrangements, the structural features of 6-strand, 5-sheet E22L, E22V, Aβ(16-22) or V18I arrays were captured by averaging over the middle 20 ps of the trajectories of molecular dynamics (MD) simulations. The surface area buried in β-sheet formation is calculated by subtracting the average hydrophobic or hydrophilic surface areas of the three individual β-sheets in the middle from the corresponding solvent accessible surface area (SASA) in their random coil state (Lesser 1990, Yan 2007, [1]Liang 2008). The surface area buried in lamination is calculated by comparing the two-sheet area of the middle three β-sheets with the twice of the single sheet area. The calculations are listed in Table 4.6. and 4.7.. Among these four peptides, due to their similar sequence hydrophobicity, Aβ(16-22) and V18I have similar SASA; and E22L and E22V have similar SASA. Although E22L and E22V are more hydrophobic than Aβ(16-22) and V18I, their buried hydrophobic area in the single β-sheet formation is not significant, only around 1% more. However, E22 congeners buried more hydrophilic area during the β-sheet formation, which is up to 70% more than Aβ(16-22). The buried hydrophobic area contributes to the free energy, but the buried hydrophilic area has negative correlation with the free energy, which is because of the unfavorable desolvation of the polar groups (Yan 2007). Therefore, the β-sheets of E22

congeners should be less stable than those of Aβ(16-22). The buried hydrophobic area of E22 congeners in lamination are much more than Aβ(16-22) and V18I. For example, the buried hydrophobic area of E22L is around 20% more than Aβ(16-22) and V18I. Moreover, E22 congeners buried less hydrophilic area in lamination than Aβ(16-22) and V18I, around 90%. This suggests E22 congeners would have stronger laminations. Although the E22 congeners have stronger lamination, their β-sheets are less stable due to burying more hydrophilic surface area. These results may explain the broader scattering in WAXS and higher melting temperature of E22 congener tubes. The stronger lamination can be the main contribution to cause the E22 congener tubes hard to melt because the β-sheet networks are ubiquitous although they may be weaker, while the more dynamic β-strands within the β-sheet networks can result in broader scatterings in WAXS.

Table 4.6. Buried surface area of Aβ(16-22) congeners during single β-sheet formation.

	Aβ(16-22)	V18I	E22L	E22V
A^0_T	9035.4	9134.4	9076.8	8905.2
A^0_{S-C}	5396.4	5526.6	5983.2	5806.8
A^0_{B-B}	3639	3607.8	3093.6	3098.4
A_T	3824.8	3923.6	3059.8	2815.3
A_{pho}	918.5	1009.8	1234.0	1147.0
A_{phi}	2906.2	2913.9	1825.9	1668.3
ΔA_T	5210.6	5210.8	6017	6089.9
ΔA_{pho}	4477.9	4516.8	4749.2	4659.8
ΔAphi	732.8	693.9	1267.7	1430.1

Table 4.7. Buried surface area of Aβ(16-22) congeners during lamination formation.

	Aβ(16-22)	V18I	E22L	E22V
$2A_T$	7649.6	7847.2	6119.6	5630.6
$2A_{pho}$	1837.1	2019.6	2467.9	2294.0
$2A_{phi}$	5812.5	5827.7	3651.7	3336.6
A_{T2}	6384.4	6433.3	5041.1	5072.7
A_{pho2}	1045.9	1166.7	1437.7	1473.9
A_{phi2}	5338.5	5266.5	3603.5	3598.7
ΔA_{T2}	1265.2	1413.9	1078.5	557.9
ΔA_{pho2}	791.1	852.8	1030.3	820.1
ΔAphi2	474.0	561.2	48.3	-262.1

Because of the backbone chiral centers, β-sheets are well-known to naturally twist with each β-strand relative offset to its adjacent neighbor (intrasheet twist, Figure 4.9.a). The origin of the amyloid tube helical twist should be the result of these β-strand relative offsets in the tube assemblies. In amyloid structures, the β-sheets are further laminated through the side chain interactions. Interestingly, in the MD simulation, the β-strands are observed also twisting in the lamination dimension (intersheet twist, Figure 4.9.b). Because the simulation was carried on in the 6-strand and 5-sheet system, which is not like the whole tube holding all the structural forces, the twist angles are not exactly match. In Figure 4.6.a, CD is the length of β-sheet across one pitch, which can be calculated as $CD=2\pi\rho/\cos\psi$. Because the β-sheet H-bonding distance is around 4.7Å, given the length of β-sheet across one pitch, the number of β-strands across one pitch can be obtained (Table 4.5.). Angle θ is the angle between the beginning and the end β-strands across one pitch. Then the intrasheet twist of the β-strand can be obtained by dividing θ with the number of β-strands across one pitch. Similarly, the lamination direction is off θ degree over one helical pitch. Given the number of laminants, the intersheet twist in lamination can be obtained too (Table 4.5.). As described above, peptides need to tilt in the shell wall to match the shell thickness. When the β-sheet lamination tapes helically coil up, the H-bonding distances in the inner leaflet have to be smaller than the outer leaflets. This structural tension should be the reason which causes the tilt of β-strands in the shell.

The modeling also indicates β-sheets of Aβ(16-22) congeners have offsets in lamination as shown in Figure 4.9.c. This is reasonable to achieve the maximum hydrophobic overlapping in the lamination. Because of the E22 congeners with

hydrophobic replacement at 22 position with Ile, Leu and Val, they are more hydrophobic toward the C-terminus. More β-sheet offsets are observed in their lamination comparing with Aβ(16-22). Because the peptide termini are on the tube surface, and roughly they should perpendicular to each other, these β-sheet lamination offsets can also contribute to the β-strand tilt in the shell wall (Figure 4.9.c).

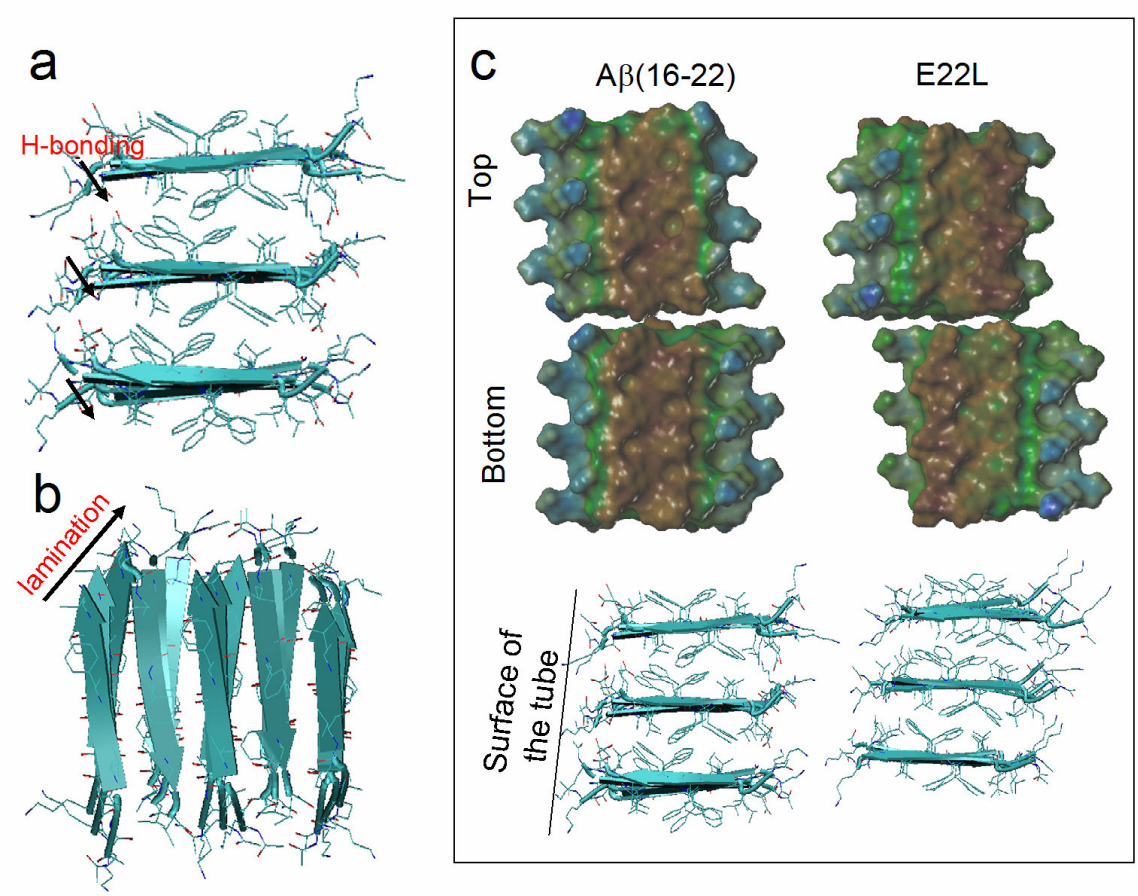

Figure 4.9. Offset of β-strand in nanotubes formed by Aβ(16-22) congeners

(b) β-strand offset within the β-sheet

(c) β-strand offset in lamination.

(a) The lypophilicity of the top and bottom β-sheet surface of E22L and Aβ(16-22) to demonstrate E22 congeners need to have more offset in β-sheet lamination to bury maximum hydrophobic surface area;

DISCUSSION

The sheet-sheet stacking is important in amyloid assembly for its contribution to the characteristic amyloid cross-β structure. Given a formed β-sheet, the sheet-sheet stacking mainly involves protein/peptide side chain interactions. In protein folding, to direct proteins into the lowest energetic states, from highly exposed and disordered unfolded states to tightly packed folded states, proteins have to sort out the ideal position for every residue. Upon this process, the loss of conformational entropy of the polypeptide chain is one of the major forces opposing protein folding (Doig 1995, Penel 2001). The side chain burial and packing are critical to determine these conformational entropy lost (Ryu 1996, Lazar 1997, Ventura 2002, Farber 2008). However, a measurement of thermodynamic parameters of amyloid formation suggests the side chain packing is not as optimal as in the globular protein folding because the amyloid structures were accepted mainly through the backbone β structure (Kardos, 2004). The backbone β structure does play an important role in amyloid assembly, while the contribution of the side chain contribution to amyloid assembly may be underestimated or misinterpreted due to the lack of good model system to separate the role of the backbone and side chains. Aβ(16-22) congener tubes all contain antiparallel one-residue-shifted β-sheet, but with varied tube diameters, which makes them a good model system by focusing on only side chain packing contribution to the sheet-sheet stacking. The one methyl group difference does not cause dramatic buried area changes, such as between Aβ(16-22) and V18I or between E22L and E22V as shown in ΔSASA calculation. However, the assembly difference of Aβ(16-22) tube-formation congeners is correlated with the conformational entropy of their hydrophobic core side chains. First, reducing the number

of rotamers a side chain can adopt can induce sheet-sheet stacking by increasing the number of laminants. For example, the number of rotamers at the modified residue in V18terL, Aβ(16-22) and V18I side chains has the order, V18terL<Aβ(16-22)<V18I (Table 4.8.). The reversed order of their number of laminants, V18terL>Aβ(16-22)>V18I implies V18terL tubes have the strongest hydrophobic core side chain packing in the sheet-sheet stacking, Aβ(16-22) tubes as the second, and V18I tubes have the weakest sheet-sheet stacking. The melting experiment is also consistent with V18terL tubes are thermodynamically more stable than Aβ(16-22), and V18I tubes are least stable among the three. Similarly, smaller side chains with fewer atoms in the side chain also can reduce the side chain conformational entropy. Abu has fewest atoms in the side chain and it forms tubes with the largest diameter. Besides the higher melting temperature comparing with Aβ(16-22) tubes, L17Abu tubes also have the shortest lamination distance (9.7Å, Table 4.4), implying stronger sheet-sheet stacking.

Table 4.8. The degree of freedom in the amino acid side chain

	# of rotamers	# of carbon atoms	Length of the side chain (nm)
Abu	3	2	2.6
Val	3	3	2.6
terL	1	4	2.6
Ile	9	4	4.0
Leu	9	4	4.0

E22 congeners contain one more hydrophobic residue in the sequence. In the lamination hydrophobic surface burial, E22 congeners bury more hydrophobic surface in sheet-sheet stacking than Aβ(16-22), which should make their sheet-sheet stacking more thermodynamically favorable. However, one more hydrophobic residue also increases the

number of atoms and rotamers in the hydrophobic core, which increases the freedom degree of side chains, and increases the side chain conformational entropy in sheet-sheet stacking. Most likely, this is the reason why E22I and E22L did not form large lamination although they can bury more hydrophobic surface. By the deletion of one methyl group, Ile → Val, E22V forms largest diameter tubes among the E22 congeners. This follows the same rule that the decrease of the side chain freedom strengthens the hydrophobic core interactions in sheet-sheet stacking.

β-strands are naturally twisted. β-strand intrasheet twist within β-sheets and intersheet twist in lamination are the original source for the helical pitch in the Aβ(16-22) congener tubes. These two twists are directly related to the peptide packing in these tubes. Comparing their intersheet twist in lamination, E22I and E22L have larger twist than Aβ(16-22). This can be due to E22 congeners have more side chain freedom in the hydrophobic core packing, and they require more complimentary adjustments to the relatively ideal position. Similarly for V18I and V18terL, V18I has more side chain conformations, while V18terL has less side chain conformation comparing with Aβ(16-22). Then V18I has more intersheet twist, while V18terL has less intersheet twist comparing with Aβ(16-22). Surprisingly, the larger tubes formed by L17Abu and E22V both have relatively small intersheet twists. Even more surprisingly, their intrasheet offsets are also much smaller than the rest congeners. Because all tubes contain antiparallel one-residue-shifted β-sheet, similar intrasheet twists are expected among these congeners. Indeed, E22I, E22L, V18I, V18terL and Aβ(16-22) all have similar intrasheet twist. One critical feature of L17Abu and E22V needs to be recognized that in the antiparallel one-residue-shifted β-sheet, the 17 and 22 residues are cross-strand paired

([1]Liang 2008), and close to the tube surface. The 17 and 22 residue can be partially exposed to the solvent on the tube surface. When there are holes in the exposed hydrophobic packing, such as smaller size side chains, sheets may stack tighter, which may cause the β-sheet to be more flat. The flatter β-sheet can further induce lamination (Lakdawala 2002), which is consistent with both L17Abu and E22V have largest number of laminants among each group.

The introduced six Aβ(16-22) tube-formation congeners provide an ideal model system to investigate the factors in amyloid sheet-sheet stacking in the content of same backbone conformation. This does not lessen the contribution of backbone conformation in the sheet-sheet stacking. Previously, we demonstrated the pairwise K-E association and the steric demand of the β-branched residue at 18 position of Aβ(16-22) can dictate the backbone registry ([1]Liang 2008). Specifically, the antiparallel one-residue-shifted backbone conformation with symmetric side chain distribution on the top and bottom β-sheet surface is required in Aβ(16-22) tube formation. No exception, all these six Aβ(16-22) tube-formation congeners form the antiparallel one-residue-shifted β-sheet, which further confirms the advantage of this backbone conformation to induce sheet-sheet stacking in tube formation because of little energetic preference of packing top-top, bottom-bottom, top-bottom surfaces.

In Aβ(16-22) assembly model system, the early desolvation events through hydrophobic collapse are accountable for the nucleic formation ([1]Liang 2008). The side chain cross-strand correlations have been demonstrated in Chapter 2 and 3 as the factors to determine the β-sheet registry and orientation, i.e. the properties of the amyloid nuclei. Here, these tube-formation congeners demonstrate the contribution of the hydrophobic

core side chain interactions to amyloid sheet-sheet stacking, another critical property in amyloid assembly. Our ultimate goal is to determine and control molecular factors in amyloid molecular self-assembly. The message delivered in the amyloid assembly of Aβ(16-22) model system is the optimum packing of peptide sequences to determine the final stable amyloid scaffold, which possibly follows the similar rule as protein folding. The amyloid assembly, well-known as the protein misfolding process, is most likely initiated from the accumulation of polypeptide chains, not like protein folding mostly involving only one polypeptide single chain, evolving through conformational transitions to form cross-β.

CHAPTER 5

AMYLOID CO-ASSEMBLY

INTRODUCTION

Amyloid assembly is a nucleation-dependent process, in which the characteristic nuclei determine the amyloid fibril forms. Although the mechanism of nucleation is not clear, the amyloid nucleation-dependence provides great opportunities to co-assemble amyloid structures containing more than one protein or peptide. The co-assembled amyloid systems are beneficial. For example, because of the amyloid aggregation, traditional structural analysis, such as X-ray crystallography and solution NMR, are not useful in determining amyloid structures. Optical techniques have been applied in studying the amyloid self-assembly process (Crick 2006, Mukhopadhyay 2007, Scheibel 2003). Congo Red is a well-known dye bound to amyloid by showing a birefringence to indicate amyloid fibril formation (Elghetany 1989). However, the poor identification of dye binding sites causes this method to be insufficient. The fluorescent co-assembled

systems can be beneficial because the associations between the fluorescence labeled peptides and non-labeled peptides are only within peptide sequences. In co-assembling, the fluorescent dye could not only report the earliest events in amyloid formation, but also could be used to follow the entire amyloid assembly process. This will open tremendous opportunities for using optical methods to study amyloid assembly.

Amyloid seeding has been reported in many amyloid systems (Hess 2007, Lu 2006), such as peptide cross-seeding, seeding non-assembled peptide to form amyloid. The seeding event has been proposed as a critical pathological pathway in prion disease (Lundmark 2005). However, the seeding mechanism remains elusive due to the lack of structurally well-determined model systems. The co-assembly is a seeding process. Therefore, generating co-assembly systems with structurally determined β-sheets and lamination arrays will be useful to address the feature of amyloid seeding effect.

In this chapter, amyloid co-assembly studies were applied to Aβ(16-22) and its congeners. As introduced in previous chapters, the seven-residue truncated amyloid β peptide, Ac-KLVFFAE-NH_2, self-assembles into nanotubes under the condition of 2:3 acetonitrile:water (v:v) with 0.1% TFA. The Aβ(16-22) nanotubes have been structurally determined with antiparallel one-residue shifted β-sheet (Lu 2003, Mehta 2008) as shown in Figure 5.1.. Here, I will explore the use of Aβ(16-22) congeners, including fluorescence peptide probes and peptides with regulated morphologies, in the studies of amyloid co-assembly.

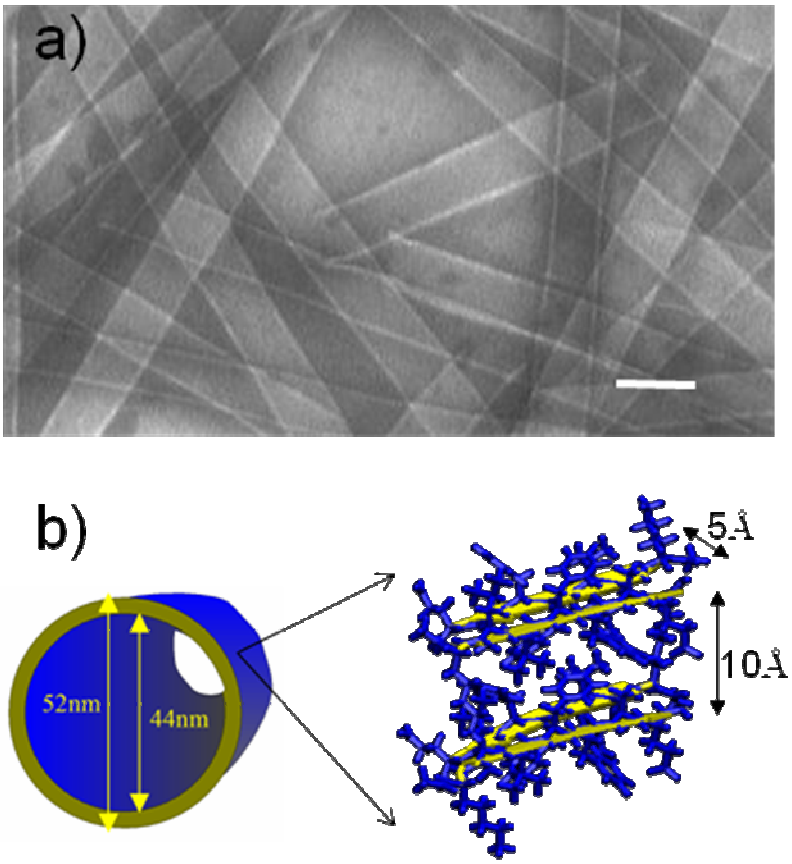

Figure 5.1. Nanotube formed by Aβ(16-22)

Under 2:3 acetonitrile:water (v:v) with 0.1% TFA.

(a) TEM image, scale=100nm;

(b) The proposed model and diameters of the nanotubes. The inset shows the Aβ(16-22) cross-β pattern within nanotubes.

MATERIALS AND METHODS

Fluorescent Modifications

Fluorescence peptides were synthesized using standard FMOC peptide synthesis protocols with an Applied Biosystems ABI431 peptide synthesizer. Rh110 was attached to the peptide backbone at the N-terminus through standard FMOC peptide synthesis protocols. The peptide was cleaved from the resin using the solution of TFA/thioanisole/ethanedithiol/anisole (90/5/3/2). The peptide was then precipitated from the cleavage solution and washed repeatedly using excess ice-cold diethyl ether. Reverse phase HPLC was used for the peptide purification. The solvents used for purification were acetonitrile and water, both of which contained 0.1% TFA. The molecular weights of the peptides were verified by MALDI mass spectroscopy. Peptides containing F19 [1-^{13}C] labels were synthesized as described using [1-^{13}C]-phenylalanine and also confirmed by MALDI mass spectroscopy.

Co-assembly of Aβ(16-22) and its Congeners

The co-assembly systems were prepared by dissolving purified Aβ (16-22) and its congeners with corresponding ratios in 2:3 acetonitrile:water (v:v) with 0.1% TFA to a final concentration of 1.0mM. The peptide solution was allowed to self-assemble and mature at room temperature for 2 weeks.

Two Photon Fluorescence Imaging

Two-photon fluorescence images were acquired on a home built laser scanning microscope (Nagy 2005). Samples were excited at 780 nm using a mode-locked Tsunami Ti:Sapphire laser pumped with a 532-nm 5W Millenia solid-state Nd:YVO_4 laser (Spectra-Physics, Mountain View, CA). The 5x-expanded laser beam was directed into

an IX-71 Olympus microscope (Olympus America, Center Valley, PA) and focused into the sample with a 60× UPlanSApo 1.2 NA water-immersion objective lens (Olympus America, Center Valley, PA). Fluorescence collected through the objective lens passed through a dichroic mirror (675 DCSX) and a short pass filter (E680SP, Chroma Technology, Rockingham, VT), and was focused onto a photon-counting photomultiplier tube (Hamamatsu, H7421). Images were acquired with custom software.

RESULTS

Co-assembly of Aβ(16-22) with Rh16-22 and Rh17-22

Aβ(16-22) contains a hydrophobic core, LVFFA, and is capped with the hydrophilic termini, Lys and Glu. The fluorescence labeled peptide is designed to keep the hydrophobic core, and under acidic conditions with 0.1% TFA, both Lys and Glu side chains are expected to be protonated and the peptide maintain a single positive charge at the N-terminus. A dye containing positive charges, Rh110, was selected, and placed at the N-terminus, forming Rh16-22. By introducing Rh110 at the N-terminus, more positive charges appear at the N-terminus of Rh16-22. To reduce the number of positive charges to that seen in Rh16-22, Rh17-22 is synthesized by deleting Lys from the peptide sequence.

Figure 5.2. Self-assembly of fluorescence labeled peptides Rh17-22 and Rh16-22.

(a) TEM of Rh17-22 fibers, scale=100nm.

(b) TEM of Rh16-22 fibers, scale=100nm.

(c) FTIR of

1mM Aβ(16-22) nanotubes (black),

Non-assembled 1mM Rh16-22 at 2:3 acetonitrile: water (v:v) with 0.1% TFA (red),

1mM Rh16-22 fibers at 5:2 acetonitrile:water (v:v) with 0.1% TFA (green),

1mM Rh17-22 fibers at 2:3 acetonitrile:water (v:v) with 0.1% TFA (blue).

(d) Molecular structure of Rh110

(e) WAXS of

Aβ(16-22) nanotubes (black),

Rh16-22 fibers at 5:2 acetonitrile:water (v:v) with 0.1% TFA (red),

Rh17-22 fibers at 2:3 acetonitrile:water (v:v) with 0.1% TFA (blue).

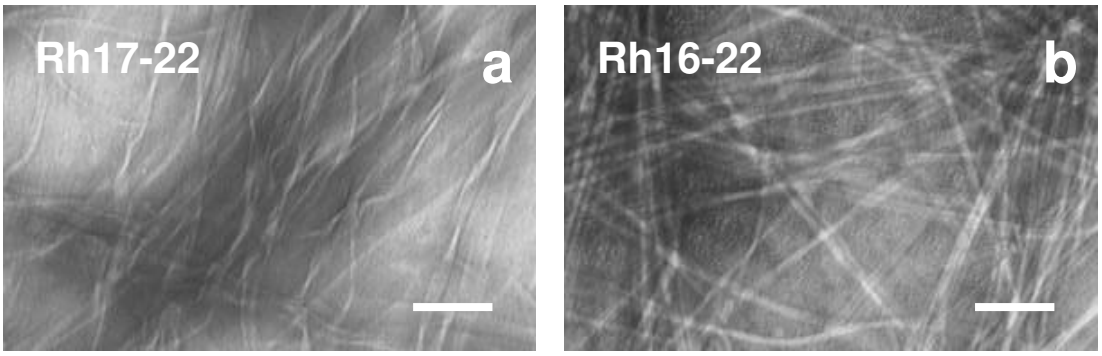
Rh17-22
a
Rh16-22
b

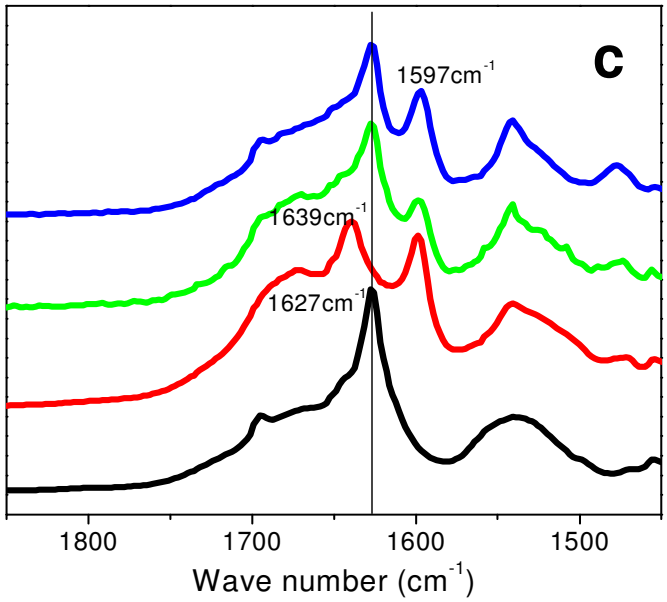
c
1597cm-1
1639cm-1
1627cm-1
1800
1700
1600
1500
Wave number (cm-1)

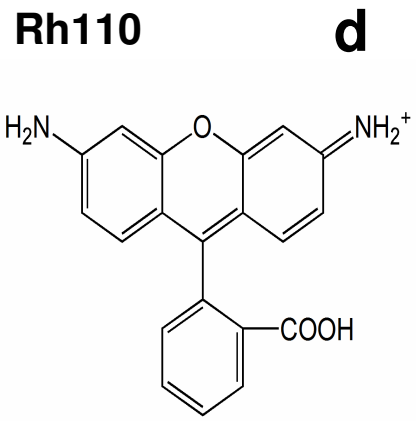
Rh110
d
H2N
O
NH2+
COOH

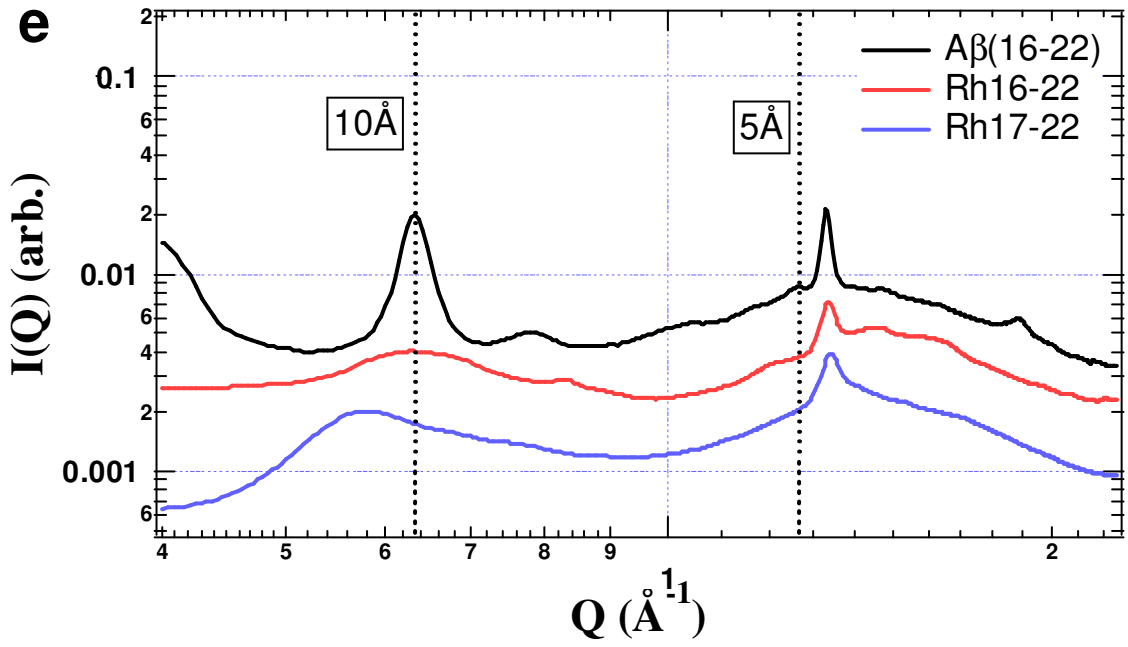
e
Aβ(16-22)
Rh16-22
Rh17-22
10Å
5Å
I(Q) (arb.)
Q (Å-1)

Amyloid assemblies are organized through peptide backbone hydrogen bonding and side chain interaction. Under the same condition that Aβ(16-22) nanotubes assemble (2:3 acetonitrile:water with 0.1% TFA), Rh17-22 does self-assemble into fibers (Figure 5.2.a), but Rh16-22 do not. The additional charges in Rh16-22 may cause the peptide to be too soluble, and by reducing the acetonitrile:water ratio to 2:5 (v:v), Rh16-22 assemble into fibers (Figure 5.2.b). Fourier transform infrared (FTIR) analysis showed that both Rh16-22 and Rh17-22 fibers contain the amide I band at 1627cm^{-1}, characteristics of β-sheet, which is same as Aβ(16-22) nanotubes (Lu 2003, Mehta 2008) (Figure 5.2.c). Because Rh16-22 did not self-assemble at 2:3 acetonitrile:water with 0.1% TFA, the amide I band was shown at 1639cm^{-1}, but Rh16-22 fibers formed under 2:5 acetonitrile:water with 0.1% TFA have the same 1627cm^{-1} amide I band (Figure 5.2.c). The FTIR analysis confirmed both Rh16-22 and Rh17-22 fibers have β-sheet secondary structure. Moreover, these fibers both have the amyloid cross-β signature with 5Å scattering (H-bonding) and 10Å scattering (lamination) (Figure 5.2.e) in wide angle X-ray scattering (WAXS) (Liang 2008). Therefore, both Rh16-22 and Rh17-22 can self-assemble into amyloid fibers. The attachment of a large fluorophore at the N-terminal may interrupt the structural interactions required in the nanotube formation.

The fiber self-assembly of Rh16-22 and Rh17-22 exhibits their ability to assemble into amyloid in the similar condition as Aβ(16-22). Co-assembling of the fluorescence labeled peptides with Aβ(16-22) was prepared by mixing Aβ(16-22) with either Rh16-22 or Rh17-22 under 2:3 acetonitrile:water (v:v) with 0.1% TFA at a total peptide concentration was 1mM. The solvent condition was the same as Aβ(16-22) nanotubes, and Aβ(16-22) was kept as the dominant peptide. Therefore, nanotubes were expected to

be the morphology in the co-assembling systems. The right panels of Figure 5.3.a and 5.3.b are TEM images of nanotubes formed by the co-assembling systems of Aβ(16-22) with Rh17-22 and Rh16-22, respectively, which do not show significant differences from the nanotubes formed by Aβ(16-22) alone (Figure 5.1.a). Fluorescence appears equally distributed on the nanotubes (Figure 5.3.a and 5.3.b left panel). In fluorescence imaging, the fluorescence-labeled peptide concentration was reduced to 4μM, and the total peptide concentration remains 1mM. With Rh110 dye alone, as shown in Figure 5.3.c, no association of fluorescence dye with Aβ(16-22) nanotubes was observed. This suggests the interaction between the labeled peptides and Aβ(16-22) is specifically within the peptide sequences.

Although the fluorescence imaging indicates the interaction between the fluorescence-labeled peptides and Aβ(16-22) are within the peptide sequences, the imaging alone cannot tell whether the fluorescence-labeled peptides incorporate into the β-sheets of Aβ(16-22) nanotubes through co-assembling. To test the co-assembly, isotope-edited FTIR (IE-FTIR) is used to determine the incorporation of fluorescence peptides. As introduced in previous chapters, when the peptide with [1-^{13}C] replacement forms β-sheet, the main amide I band will split into the ^{13}C component showing at the lower wave number and the ^{12}C component at a higher wave number (Hiramatsu 2005, Petty 2005, Paul 2005). The split is caused by the coupling limit between the ^{12}C and the ^{13}C dipoles because of the vibration frequency decrease of the heavier oscillator (Hiramatsu 2005, Petty 2005, Paul 2005). For example, when F19 carbonyl of Aβ(16-22) is ^{13}C labeled, the main amide I band splits into two components as shown in Figure 3b (Lu 2003, Mehta 2008).

In the IE-FTIR analysis of the co-assembly systems, the carbonyl of the middle residue, F19 of Rh16-22 or Rh17-22, is ^{13}C labeled. The reason to choose F19 is to put the label in the middle of the peptide, and avoid the disturbance at the termini. The concentration of [1-^{13}C]F19 labeled Rh17-22 or Rh16-22 was 0.15mM, which is higher than in the fluorescence imaging analysis, and the Aβ(16-22) concentration was 1.5mM. When the fluorescence labeled peptide concentration went higher, the co-assembly systems still can form homogenous nanotubes. In addition, the labeled peptide self-assembly can be ruled out in the IE-FTIR analysis because the 0.15mM concentration is too low for them to self-assemble.

Figure 5.3. Co-assembly of fluorescence labeled peptides with Aβ(16-22) into nanotubes.

The concentration of Aβ(16-22) is 1mM, and the concentration of fluorescence labeled peptide is 4μM.

Right panel: TEM, scale=100nm.

Left panel: Two photon fluorescence imaging, scale=5μm.

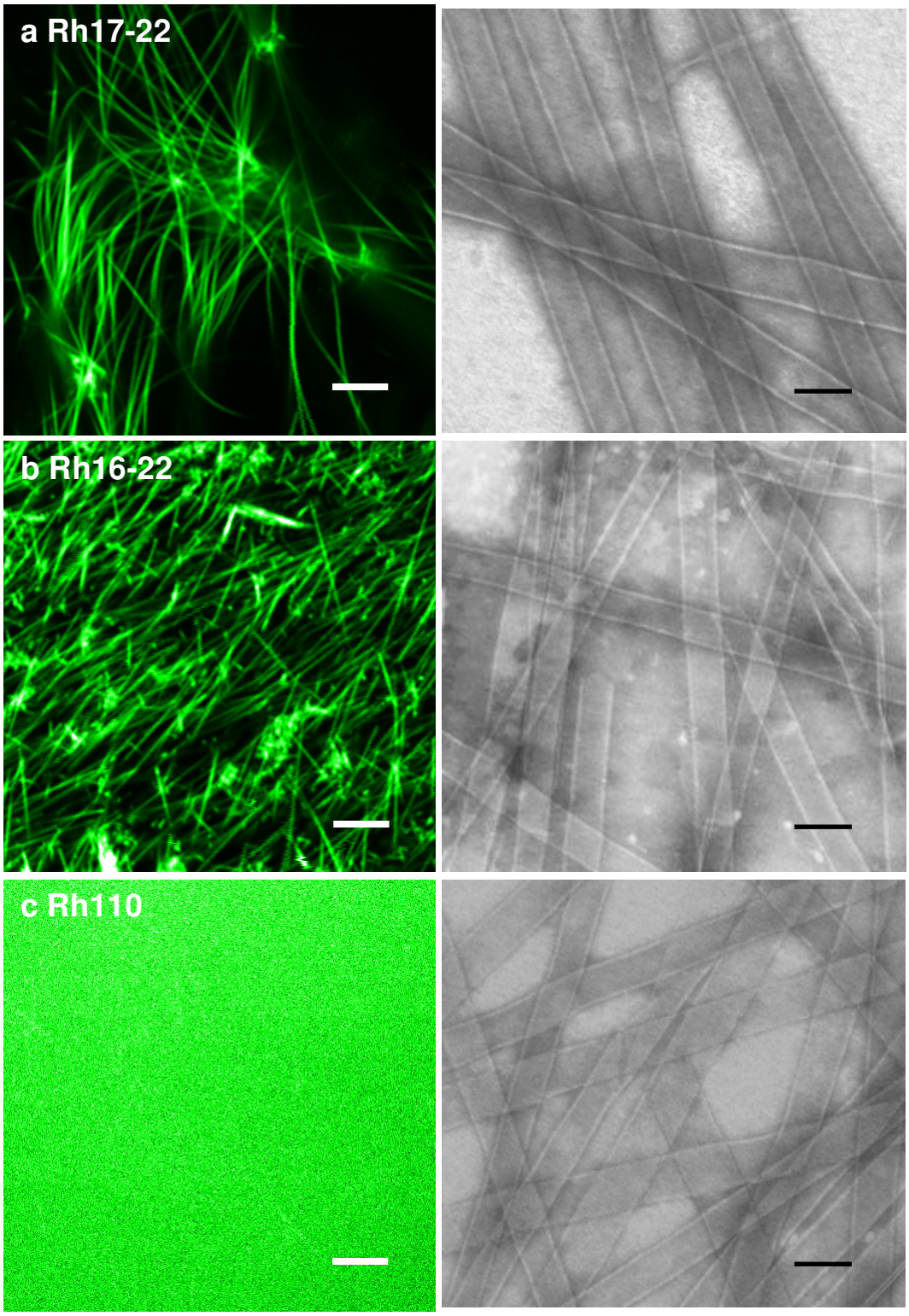
a Rh17-22
b Rh16-22
c Rh110

IE-FTIR analysis of the co-assembling systems identified a shoulder, at around 1610 cm^{-1} adjacent to the main β-sheet amide I band, which was slightly shifted to higher wave numbers (Figure 5.4.). Because the co-assembling system only had 10% of ^{13}C labeled peptides, the ^{13}C band appeared only as a shoulder near the ^{12}C band. An additional band at 1597cm^{-1} in fluorescence labeled peptide fiber samples was assigned from rhodamine, which may contribute to this 1610cm^{-1} shoulder. To confirm the ^{13}C band appearance, the co-assembling sample with the same concentration ratio of unlabeled Rh16-22 and Aβ(16-22), was examined. A weak stretch appeared at 1597cm^{-1}, but not around 1610cm^{-1}. This result confirmed the shoulder adjacent to the main amide I band at 1610cm^{-1} is the ^{13}C band within the β-sheet, i.e. fluorescence labeled peptides indeed co-assembled into Aβ(16-22) nanotubes. Aβ(16-22) and Rh17-22 co-assembled nanotubes have similar IE-FTIR signal as Rh16-22 (Figure 5.4.).

Neither Rh16-22 norRh17-22 self-assembles in the concentration under the co-assembly condition. The resulted co-assembled fluorescence tubes suggest Aβ(16-22) tube nuclei have seeding effects on Rh17-22 and Rh16-22, and the fluorescence peptides incorporate into Aβ(16-22) nanotubes. One question raised here is if both the co-assembled peptides can self-assemble under the co-assembly condition with different morphologies, do they co-assemble, and which morphology will they select to be the co-assembly morphology?

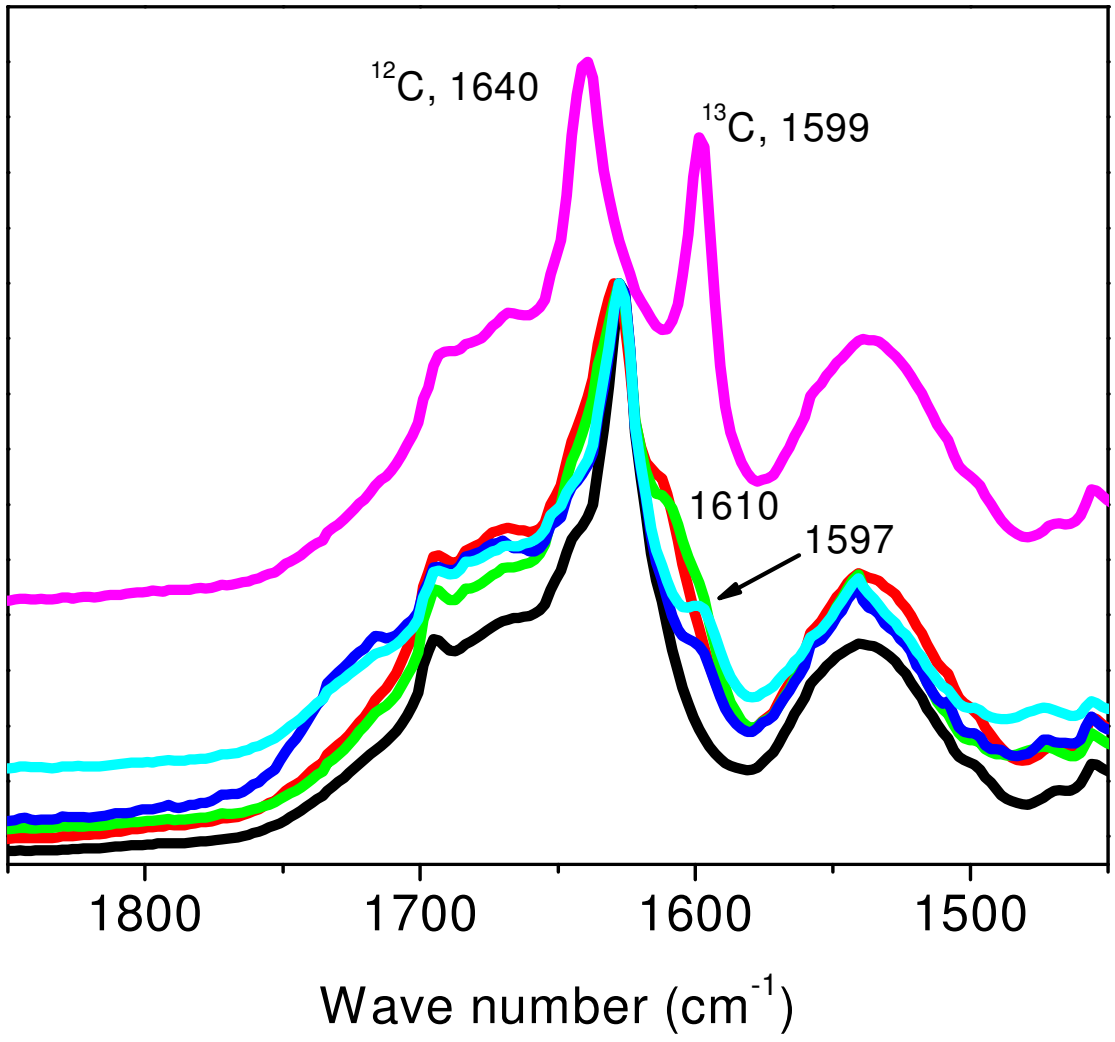

Figure 5.4. IE-FTIR of the co-assembled Aβ(16-22) nanotubes with fluorescence labeled peptides, Rh16-22 and Rh17-22

In co-assembly, Aβ(16-22) concentration is 1.5mM.

Purple, 1mM [1-^{13}C] F19 Aβ(16-22) nanotubes,

Red, Aβ(16-22) nanotubes co-assembled with 10% (molar ratio) [1-^{13}C] F19 Rh16-22,

Green, Aβ(16-22) nanotubes co-assembled with 10% (molar ratio) [1-^{13}C] F19 Rh17-22,

Blue, Aβ(16-22) nanotubes co-assembled with 10% (molar ratio) Rh16-22,

Cyan, Aβ(16-22) nanotubes co-assembled with 10% (molar ratio) Rh17-22.

Co-assembly of Aβ(16-22) with Fmoc-labeled Peptide (Fmoc16-22): Co-assembly of Peptides Which Form Same β-sheet but Different Morphology

The FTIR of Rh16-22 and Rh17-22 fibers exhibit an absorbance at 1597cm^{-1}, which unfortunately interrupts strand registry assignment because the expected ^{13}C amide I band appears at 1599cm^{-1} in antiparallel one-residue-shifted β-sheet as described. Therefore, Fmoc (9-fluorenylmethyl chloroformate, Figure 5.5.d) was introduced to cap the N-terminus of Aβ(16-22), forming Fmoc16-22. Fmoc16-22 self-assembles into fibers in the solution of 2:3 (v:v) acetonitril:water with 0.1% TFA (Figure 5.5.a). FTIR of Fmoc fibers show the β-sheet amide I signature at 1627 cm^{-1}with a weak band at 1694 cm^{-1} (Figure 5.5.c, red), the indication of the antiparallel β-sheet (Liang 2008). In IE-FTIR analysis of[1-^{13}C]F19 labeled Fmoc16-22 fibers, the ^{12}C amide band appears at 1637 cm^{-1}, and the ^{13}C amide band shows at 1599cm^{-1} (Figure 5.5.c, black), a split of ^{12}C and ^{13}C amide bands that indicates Fmoc16-22 fibers have one-residue shifted registry in the antiparallel β-sheet (Mehta 2008, Liang 2008). In Chapter 2 and 3, Aβ(16-22) congeners which can form antiparallel one-residue shifted β-sheet all have the tube morphology. This makes Fmoc16-22 an exception for forming fibers with antiparallel one-residue-shifted β-sheet. One significant structural difference between fibers and tubes is tubes have larger lamination, up to 100 laminants, while fibers have smaller lamination with 4-6 laminants (Mehta 2008). The symmetry of the antiparallel one-residue shifted β-sheet has been discussed as the critical factor contributing to the large lamination of Aβ(16-22) (Mehta 2008, Liang 2008). Here, Fmoc16-22 contains the symmetric antiparallel one-residue shifted β-sheet, but does not induce the tube morphology. The bulky N-terminus

of Fmoc16-22 may prevent the large lamination and limit the tube morphology, or may alter the nuclei and induce the twist in fiber morphology.

When Aβ(16-22) co-assembles with Fmoc16-22, the system does not have dominant tube morphology, but appears as ribbons and sheet-like assemblies (Figure 5.5.b). In the IE-FTIR spectrum of Aβ(16-22) with ^{13}C F19 carbonyl modified Fmoc16-22 (molar ratio 10:1, total peptide concentration is 1.5mM), there is a shoulder adjacent to the main amide I band (Figure 5.5.c, green), which confirms Fmoc16-22 peptides incorporate into Aβ(16-22) β-sheets. Ribbons are usually observed as the intermediate species of tubes, and may be produced when less β-sheets stacking. The co-assembled ribbon and sheet-like species suggest although Fmoc16-22 co-assembles with Aβ(16-22), the β-sheet lamination was interrupted. Given Fmoc16-22 can form antiparallel one-residue shifted β-sheet with fiber morphology, the antiparallel one-residue-shifted β-sheet is only one pre-condition, but does not promises for the tube morphology. Therefore, amyloid morphologies also rely on interactions beyond the secondary structures.

Figure 5.5. Self-assembly of Fmoc16-22 and co-assembly of Fmoc16-22 with Aβ(16-22).

(a) TEM of Fmoc16-22 fibers at 2:3 acetonitrile:water (v:v) with 0.1% TFA (1mM).

(b) TEM of sheet-like species of the co-assembly of Fmoc16-22 and Aβ(16-22) at 2:3 acetonitrile: water (v:v) with 0.1% TFA. The molar ratio of Fmoc16-22 and Aβ(16-22) is 1:9, with 1mM total concentration.

(c) IE-FTIR of Aβ(16-22) co-assemble with [1-^{13}C] F19 Fmoc16-22 at 2:3 acetonitrile: water (v:v) with 0.1% TFA. The molar ratio of Aβ(16-22) and Fmoc16-22 is 10:1, and the Aβ(16-22) concentration is 1.5mM (green). The comparison is made to,

Aβ(16-22) tubes (blue), peptide concentration is 1mM,

Fmoc16-22 fibers (red), peptide concentration is 1mM,

[1-^{13}C] F19 Fmoc16-22 fibers (black), peptide concentration is 1mM.

(d) Molecular structure of Fmoc

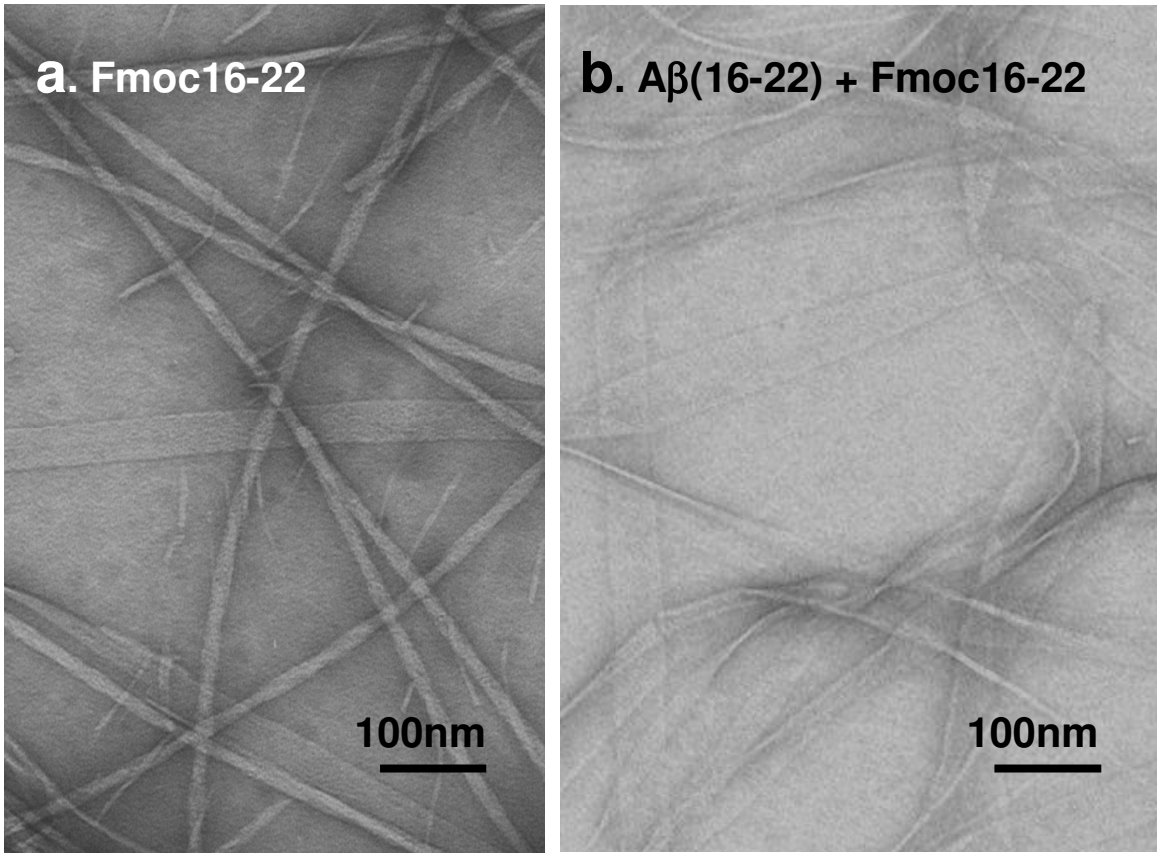
a. Fmoc16-22
100nm
b. Aβ(16-22) + Fmoc16-22
100nm

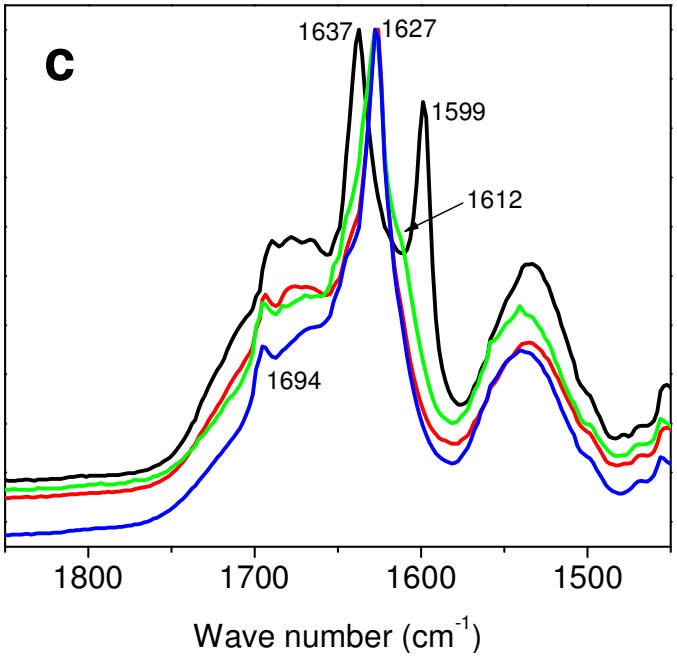
c
1637
1627
1599
1612
1694
1800
1700
1600
1500
Wave number (cm-1)

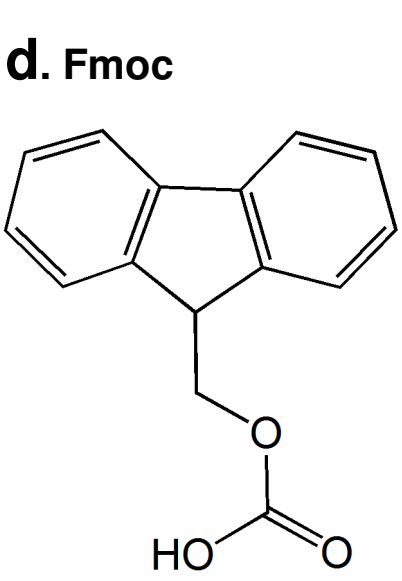
d. Fmoc
O
HO
O

Sequence Dependence of Amyloid Co-assembly

The co-assembly is further investigated by using fluorescence labeled peptides with extending at N-terminal residues, Rh15-22, R14-22 and Rh10-21(Table 5.1.). None of these fluorescence labeled peptides self-assemble in the acidic acetonitrile/water solution conditions. Rh15-22 peptides do co-assemble with Aβ(16-22), but the assemblies are not homogeneous. Under fluorescence imaging and TEM (Figure 5.6.a), besides tubes, many sheets and ribbons are present. In IE-FTIR, [1-^{13}C] amide I band is observed at 1604cm^{-1}, confirming Rh15-22 is incorporated into the β-sheet of Aβ(16-22) nanotubes (Figure 5.6.d). Neither Rh14-22 nor Rh10-22 co-assembles with Aβ(16-22), and no fluorescence tubes were detected under fluorescence imaging (Figure 5.6.b and c). Because Rh15-22 cannot self-assemble under the acidic acetonitrile/water conditions, but it can co-assemble with Aβ(16-22) into nanotubes, the ability of peptide self-assembly is not required for the peptides to co-assemble. This is exactly consistent with the nucleation-dependence or seeding effect of Aβ(16-22) tube nuclei. The co-assembly is observed to be sequence-dependent. In acidic conditions, Aβ(16-22) contain a positive charge on Lys side chain. When extending the peptide sequence at N-terminus, not only does the peptide length increase, but also the number of positive charges is increased at acidic conditions (Table 5.1.). Rh15-22 contains one additional amino acid residue at the N-terminus comparing with Aβ(16-22), but has the same number of positive changes as Rh16-22 in 0.1% TFA. The co-assembly of Rh15-22 with Aβ(16-22) suggests Aβ(16-22) tube nucleus still seeds Rh15-22 peptides, but the additional residues in the Rh15-22 peptide sequence do interrupt the Aβ(16-22) tube assembly. Rh14-22 has one more additional charge under 0.1% TFA, and two additional amino acid residues at N-

terminus. The charge repulsion most likely drives Rh14-22 from Aβ (16-22) nuclei and two more amino acid residues at N-terminus also can reduce the chance of co-assembly. Neither does Rh10-21, which has two more additional positive charges and six more residues in its sequence comparing with Rh16-22. These sequence-dependence co-assemblies indicate the structural requirement in amyloid nucleic seeding.

Table 5.1. Sequence comparison of fluorescence labeled peptides

name	sequence	Length (peptide +dye)	Charges in 0.1%TFA	Incorporation into Aβ(16-22) tubes
Aβ(16-22)	**KLVFFAE**	**7**	+	
Rh17-22	**Rh-LVFFAE**	**6+1**	++	√
Rh16-22	**Rh-KLVFFAE**	**7+1**	+++	√
Rh15-22	**Rh-QKLVFFAE**	**8+1**	+++	√
Rh14-22	**Rh-HQKLVFFAE**	**9+1**	++++	×
Rh10-21	**Rh-YEVHHQKLVFFA**	**12+1**	++++	×

Figure 5.6. Co-assembly of Aβ(16-22) nanotubes with fluorescence labeled peptides: Rh15-22, Rh14-22, and Rh10-21

Aβ(16-22) co-assemble with fluorescence labeled peptide in 2:3 acetonitrile:water (v:v) with 0.1% TFA**.** Aβ(16-22) concentration is 1mM, and the concentration of fluorescence labeled peptides is 4μM.

(a) Rh15-22

(b) Rh14-22

(c) Rh10-21

Top panels: two-photon fluorescence imagining, scale=5μm,

Bottom panels: the corresponding TEM images, scale=100nm.

(d) IE-FTIR of Aβ(16-22) co-assemble with 10% (molar ratio) of [1-^{13}C] F19 Rh15-22 under acidic conditions, the Aβ(16-22) concentration is 1.5mM (red), comparing with Aβ(16-22) tubes (red), the peptide concentration is 1mM.

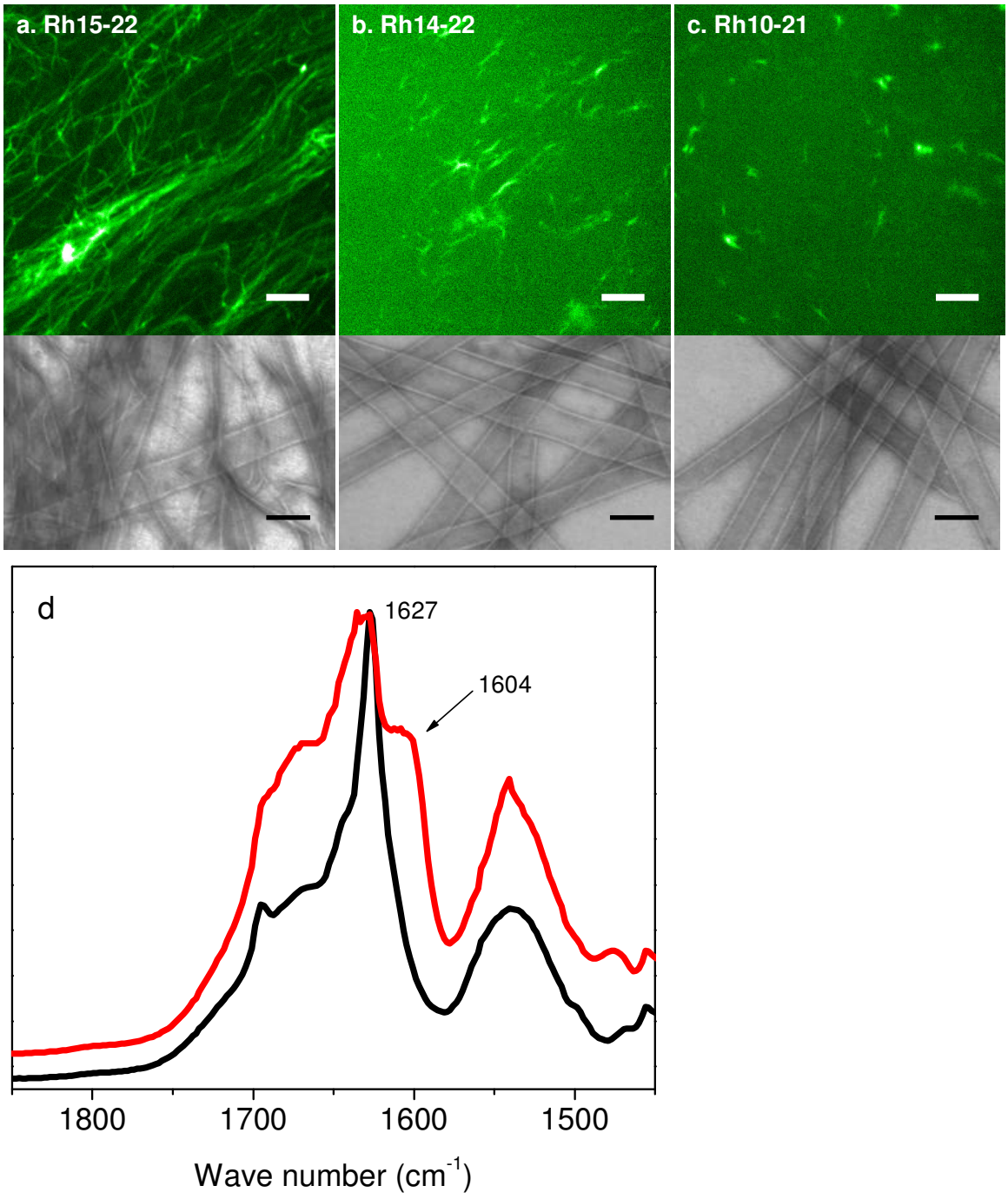
a. Rh15-22
b. Rh14-22
c. Rh10-21
d
1627
1604
1800
1700
1600
1500
Wave number (cm-1)

Co-assembly of Aβ(16-22) with Congeners, V18I, E22L and E22V: Co-assembly of Peptides Which Form Tubes with Different Tube Diameters.

Aβ(16-22) congeners, V18I, E22L and E22V, form tubes, but with different diameters as described in previous chapters. All these tubes have the antiparallel one-residue shifted β-sheet. In chapter 4, the number of laminants was argued to determine the tube diameters. To form large tubes, favorable side chain interactions and packing are required in the β-sheet-sheet stacking. If the introduced side chain modifications in V18I, E22L, and E22V peptides alter the sheet-sheet stacking in their amyloid tubes, will they still co-assemble with Aβ(16-22)?

Although Aβ(16-22), V18I, E22L, and E22V all have antiparallel one-residue shifted β-sheets, E22L and E22V have distinct CD signatures. β-sheet signature usually appears as a negative absorbance at around 210-225nm (Fasman 1996). As shown in Figure 5.7.a, E22L's negative ellipticity appears at 225nm, E22V's is at 202nm, and both Aβ(16-22)'s and V18I's are around 215nm. When mixing V18I, E22L and E22V with Aβ(16-22) in 1:10 molar ratio with 1mM total peptide concentration, the dominant peptide in the system is Aβ(16-22), and the mixed system is expected to behave more like Aβ(16-22). However, the negative CD ellipticity of mixed system of Aβ(16-22) with E22L is at 225nm (Figure 5.7.b), and mixed with E22V, the negative ellipticity is at 220nm (Figure 5.7.b). The CD signature shift in the mixed systems indicates the possible peptide co-assembly. Indeed, the IE-FTIR of Aβ(16-22) mixed with [1-^{13}C] F19 E22L, E22V or V18I in 10:1 molar ratio showed a shoulder adjacent to the main amide I bands at ~1610cm^{-1}, similar to the IE-FTIR analysis of the co-assembled systems described previously (Figure 5.8.). This shoulder is absent when mixed mature Aβ(16-22) tubes

with the same amount of [1-^{13}C] F19 E22L, E22V or V18I stock solution without co-assembly, but showed a shoulder at ~1599cm^{-1}. In the co-assembled systems, the concentrations of E22L and E22V is sufficient to allow them to self-assemble as shown in CD (Figure 5.7.c), giving E22L and E22V tubes with 100% [1-^{13}C] F19 peptides. As described in the previous chapters, ^{13}C carbonyls are aligned in the antiparallel one-residue-shifted β-sheet, and the ^{13}C amide I band move to lower wave numbers (~1599cm^{-1}). The ~1599cm^{-1} signal observed in the IE-FTIR analysis of non-co-assembled samples is consistent with ^{13}C carbonyls being aligned, meaning [1-^{13}C] F19 E22L, E22Vor V18I did not co-assemble with Aβ(16-22). However, if the ^{13}C labeled peptides are co-assembled with unlabeled Aβ(16-22) peptides, the peptides with the ^{13}C labeled are distributed within tubes of unlabeled peptides. Therefore, ^{13}C carbonyls have less chance to be aligned, and ^{13}C amide I band would appear at the higher wave numbers (~1610cm^{-1}) than the aligned ^{13}C carbonyl amide I band. The CD and IE-FTIR results both suggest E22L, E22V and V18I can co-assemble with Aβ(16-22).

Figure 5.7. Co-assembly of Aβ(16-22) with E22L, E22V and V18I

(a) CD of Aβ(16-22) tubes (blue), E22L tubes (black), E22V tubes (red), and V18I tubes (green) under 2:3 acetonitrile: water (v:v) with 0.1% TFA, the peptide concentrations are 1mM.

(b) CD of the co-assembled systems; Aβ(16-22) with E22L (black), Aβ(16-22) with E22V (red), and Aβ(16-22) with V18I (green) in 10: 1 molar ratio under 2:3 acetonitrile: water (v:v) with 0.1% TFA , and Aβ(16-22) concentration is 1.5mM.

(c) CD of the stock solution (0.15mM) of E22L (black), E22V (red) and V18I.

(d) TEM of corresponding Aβ(16-22) and E22L co-assembled system in (b).

(e) TEM of corresponding Aβ(16-22) and E22V co-assembled system in (b).

(f) TEM of corresponding Aβ(16-22) and V18I co-assembled system in (b).

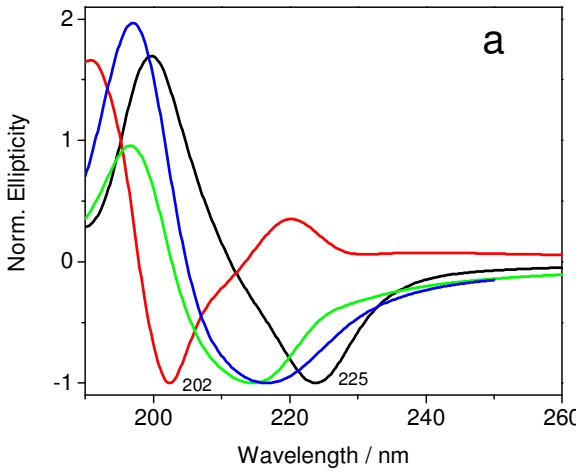
a
Norm. Ellipticity
Wavelength / nm
202
225

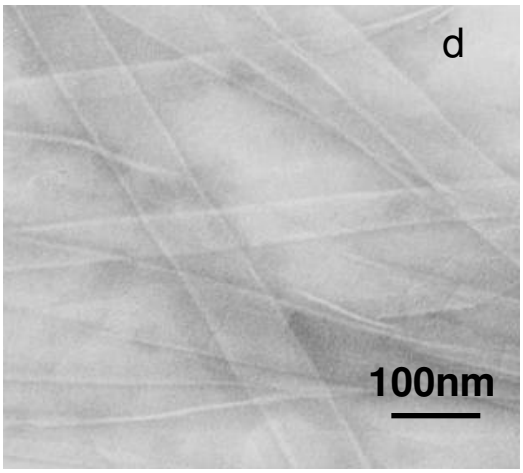
d
100nm

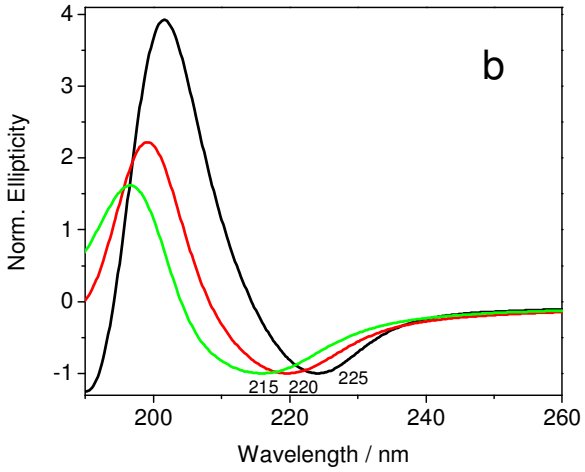
b
Norm. Ellipticity
Wavelength / nm
215
220
225

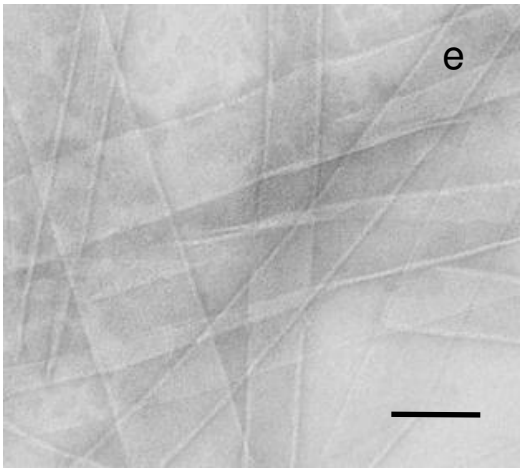
e

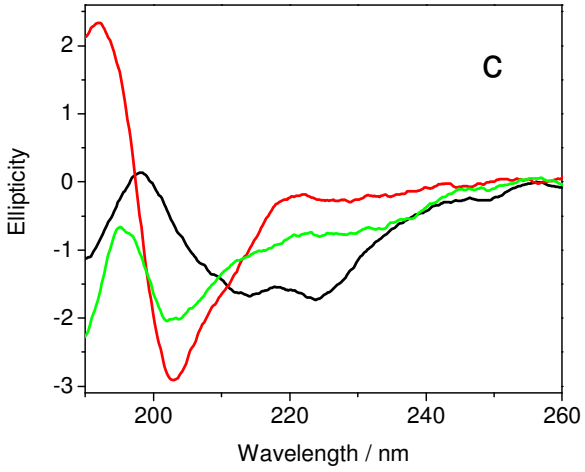
c
Ellipticity
Wavelength / nm

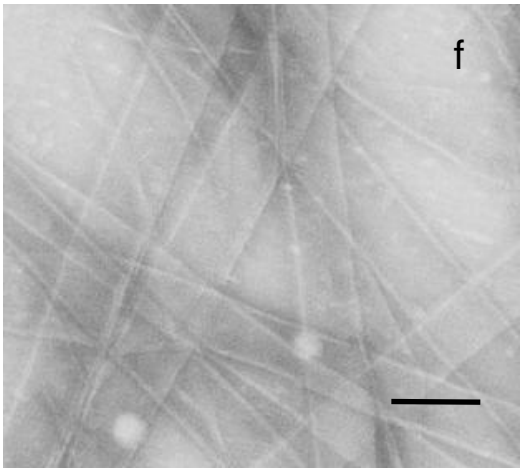
f

Figure 5.8. IE-FTIR of co-assembly of Aβ(16-22) with E22L, E22V and V18I

At 2:3 acetonitrile: water (v:v) with 0.1% TFA.

Black, Aβ(16-22) tubes co-assembled with [1-^{13}C F19] E22L with 10: 1 molar ratio, and Aβ(16-22) concentration is 1.5mM;

Red, Aβ(16-22) tubes co-assembled with [1-^{13}C F19] E22V with 10: 1 molar ratio, and Aβ(16-22) concentration is 1.5mM;

Green, Aβ(16-22) tubes co-assembled with [1-^{13}C F19] V18I with 10: 1 molar ratio, and Aβ(16-22) concentration is 1.5mM;

Yellow, Aβ(16-22 tubes (1.5mM);

Dark yellow, [1-^{13}C F19] Aβ(16-22 tubes (1.5mM);

Blue, [1-^{13}C F19] E22L stock solution (0.15mM);

Cyan, [1-^{13}C F19] E22V stock solution (0.15mM);

Magenta, [1-^{13}C F19] V18I stock solution (0.15mM);

Navy, Aβ(16-22) mature tubes (1.5mM) mixed with [1-^{13}C F19] E22L stock solution (0.15mM) without co-assembly;

Purple, Aβ(16-22) mature tubes (1.5mM) mixed with [1-^{13}C F19] V18I stock solution (0.15mM) without co-assembly.

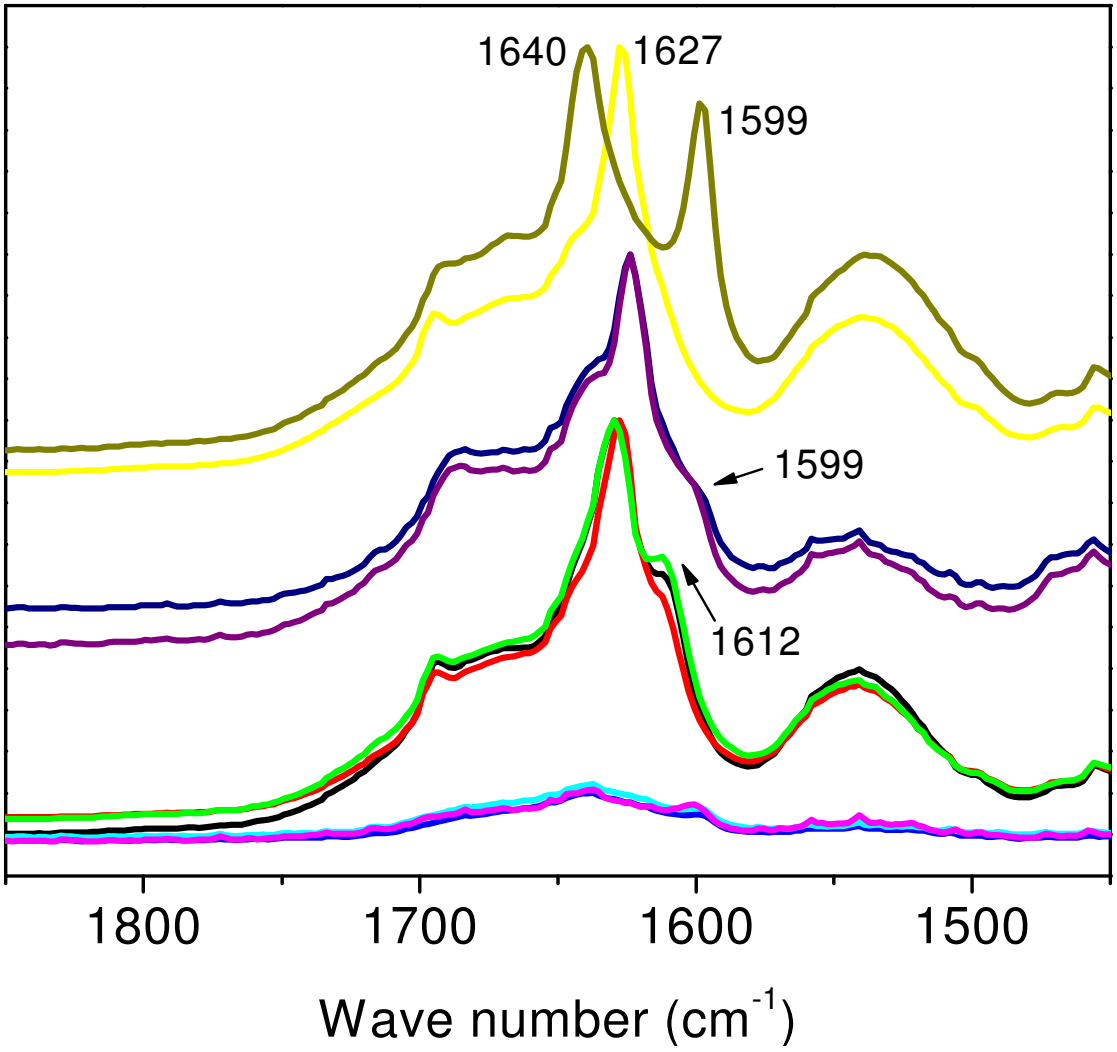
1640
1627
1599
1599
1612
1800
1700
1600
1500
Wave number (cm-1)

Co-assembly of Aβ(16-22) Congeners, L17I and L17V: Co-assembly of Peptides Which Form Amyloid Fibers with Different β-sheets

In the above section, I introduced the co-assembled systems with peptides forming the same β-sheet but with different morphologies, fibers or tubes, or with different tube diameters. As described in Chapter 3, L17I and L17V both form amyloid fibers. L17I fibers contain parallel in-registry β-sheets, while L17V fibers have antiparallel in-registry β-sheets. Here, L17I and L17V are introduced as a model system to study the co-assembly of peptides forming different β-sheets. Similarly, the co-assembly test was done by mixing L17I and [1-^{13}C] F19 L17V with 10:1 molar ratio in 2:3 acetonitrile: water (v:v) with 0.1% TFA. The L17I peptide concentration is 1.5mM. As shown in IE-FTIR (Figure 5.9.), the ^{13}C amide I band shoulder appears at 1610cm^{-1}, indicating L17V is incorporated into the β-sheet of L17I. This shoulder is absent when mixing the same amount of [1-^{13}C] F19 L17V with mature L17I fibers without co-assembly, but appears at a slightly lower wave number. This result indicates L17V can co-assemble with L17I.

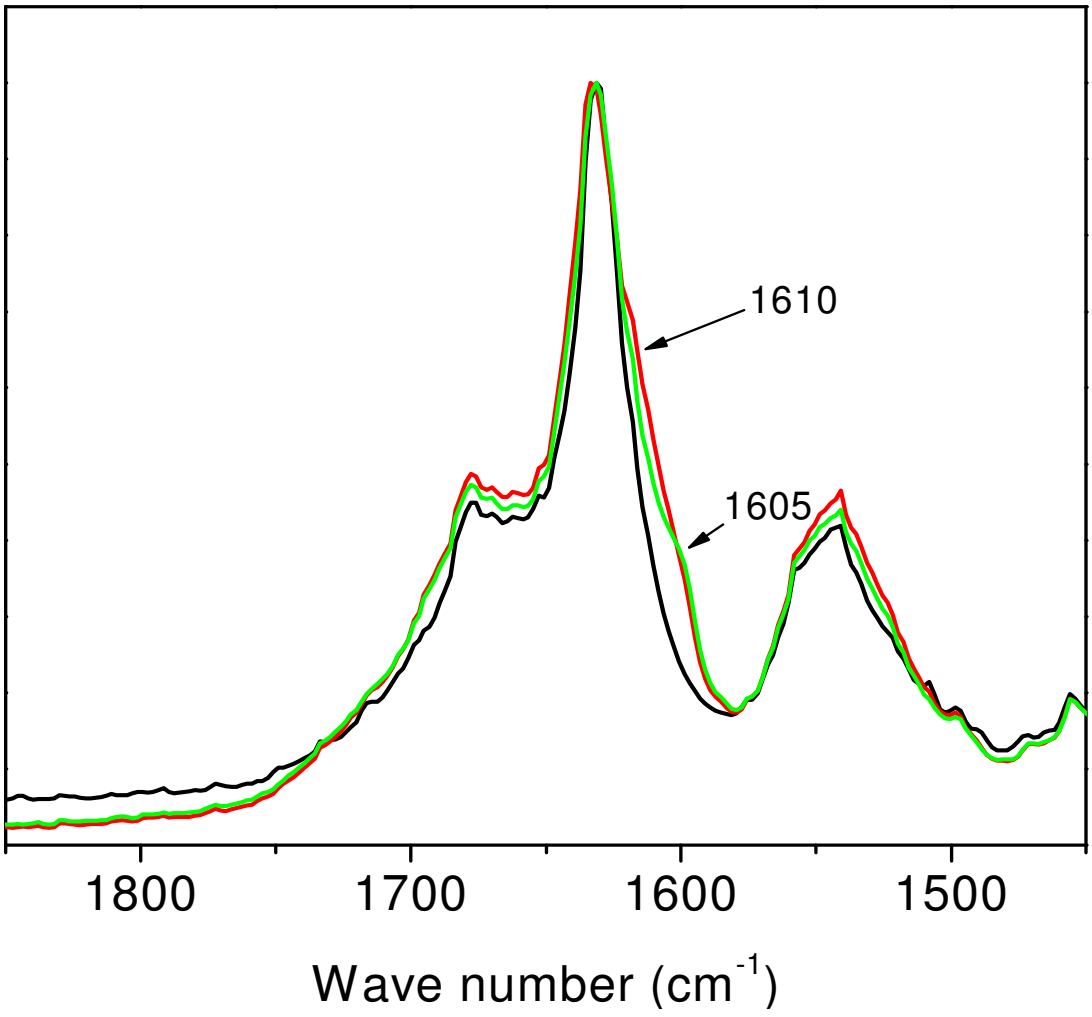

Figure 5.9. IE-FTIR of co-assembly of L17I with L17V

In 10: 1 molar ratio under 2:3 acetonitrile: water (v:v) with 0.1% TFA, and L17I concentration is 1.5mM (red), comparing with

L17I fibers (black), L17I concentration is 1.5mM;

L17I fibers (1.5mM) mixed with [1-^{13}C] F19 L17V stock solution (0.15mM) without co-assembly (green).

DISCUSSION

The co-assembly reported here involves two different peptide sequences. To achieve the co-assembly, one peptide's nuclei have to attract the other peptide to assemble. This, on the other hand, is similar as the amyloid seeding event. What I focus on is the β-sheet incorporation of co-assembled peptides, and the co-assembled amyloid morphology.

Amyloid formation is proposed to be directed by nuclei, so called nucleation-dependent growth. The seeding of one nucleus is directly related to the nucleation-dependence of amyloid formation, and was proposed to follow the conformational memory theory (Jones 2003), in which amyloids copy every structural property from the seeds, and maintain exactly the same structure as the seeds. In addition, amyloid seeding was also observed undergoing "adaptation theory", in which the seeded amyloid can have structural transformation from the seeds depending on the structural feature of the dominant peptides in the amyloid frame (Ban 2006). The co-assembled morphologies of all the co-assembled systems presented in this chapter do not maintain the corresponding pure peptide self-assembled morphology, which suggests the co-assemblies most likely follow the "adaptation theory".

The co-assembled systems of Aβ(16-22) with V18I, E22L, or E22V did not produce the same diameter as Aβ(16-22) amyloid tubes. As discussed in Chapter 4, the number of laminants a system produces is responsible for the tube diameters. The varied tube diameters in the co-assembled system suggest that the generated co-assembled tubes have a different number of laminants. As discussed previously V18I, E22L, and E22V have different side chain packing preferences in their sheet-sheet stacking. The varied

tube diameters in the co-assembled systems indicate the lamination can adopt the features of each co-assembled peptide. Also, when Aβ(16-22) co-assembles with Fmoc16-22, amyloid sheets are the dominant morphology, which is consistent with Fmoc16-22 reducing the lamination in its self-assembled amyloid.

If the nuclei do not direct the target peptide to form one amyloid, the question here is what the nuclei provide in directing peptides to assemble. The nuclei are proposed to have the minimum amyloid repeating structural unit. Because amyloid assembly has multiple dimensions, such as backbone H-bonding, side chain lamination, and peptide terminal association, the nuclei should be able to direct the assembly in all these directions. Elongation occurs after nucleation, and uses the formed nuclei as the templates. Possibly, elongation is an accumulation process directed by amyloid nuclei to form β-sheets and lamination, and amyloid morphology is the result of this nuclei-directed peptide accumulation. To assemble into amyloid, the free peptides in solution need to be desolvated (Fernandez 2002, Fernandez 2003, Kim 2006, Meijer 2007, [1]Liang 2008). This may be the critical role of nuclei as the templates to direct the target peptides to assemble. The resulted β-sheet or lamination that a protein adopts is related to the packing preference of this protein sequence. Therefore, it may not be necessary for the desolvated peptide to form the same β-sheet and lamination as the nuclei. Fmoc16-22, V18I, E22L, and E22V all maintain their lamination preference in their co-assembled systems with Aβ(16-22). Although L17I and L17V can co-assemble, the L17V β-sheet in the co-assembled amyloid is not determined. There is a possibility that L17V still maintains the antiparallel orientation in the parallel L17I β-sheets as its preference in its self-assembled amyloid. The co-assembly of fluorescence-labeled peptides with Aβ(16-

22) also supports the sequence-dependence in amyloid nucleus-template elongation. With more positive charges and additional residues in the Rh14-22 and Rh10-21 sequences, their co-assembly with Aβ(16-22) did not occur, which is consistent with the reduced association possibility of Rh14-22 and Rh10-21 with Aβ(16-22) nuclei due to the charge repulsion and sequence complexity. Rh15-22 with one additional residue at the N-terminus co-assembles with Aβ(16-22), but with heterogeneous morphologies, indicating the resulted co-assembly amyloid morphology is determined by the packing preference of involved individual peptides.

The co-assembly reported here in the Aβ(16-22) model system exhibits sequence-dependence in the nucleus-template elongation. This supports the hypothesis that the polypeptide sequence association is the determination of amyloid assembly.

CHAPTER 6

AMYLOID ASSEMBLY THROUGH AN INTERMOLECULAR MOLTEN GLOBULE

INTRODUCTION

Amyloid assembly is a complicated process, undergoes nucleation and elongation phases (Haper 1997), and the mechanisms of amyloid nucleation and growth remain poorly understood. A variety of studies have pointed towards the possibility that protein monomers may first form soluble oligomeric particles, or perhaps multiple intermediate species, prior to self assembly into fibers with the characteristic cross-β amyloid structure (Blake 1996, Sunde 1997, Sikorski 2003). In addition, these soluble oligomers exist in the disease pathological pathway, and are indicated to be more cytotoxic than mature fibers (Haass2007, Walsh 2007), but the direct evidence which supports these soluble oligomers are related to the amyloid early nucleation is short. Therefore, it remains

unclear whether the soluble oligomers are intermediates within the pathway of amyloid fiber formation (Bashakov 2002, Modler 2003, Gosal 2005, Kaylor 2005, Necula 2007).

Global polypeptide ordering through hydrophobic collapse provides the principle driving force in current theories for globular protein folding (Dinner 2000, Dobson 2003, Pace 1996). The resulting intermediate aggregated state remains disordered, but creates the desolvated interior necessary for structural element nucleation (Rose 2006). Amyloids share the characteristic cross-β structure. In previous chapters, I have introduces factors, such as cross-strand pairing and side chain conformational entropy, which play a role in determining the backbone and side chain associations. The correlation between backbone H-bonding and side chain interaction suggests an important desolvation event in amyloid nucleation. In the lack of determined common intermediates and pathways, we now ask in amyloid assembly, do polypeptides follow a similar pathway like protein folding to reach the final cross-β scaffold? In this chapter, fluorescence microscopy is applied to follow the assembly process of Aβ(16-22). The real time nucleation and elongation were observed. Consistent with the early chapter results, large aggregates with molten globular structure were observed, exhibiting the occurrence of hydrophobic collapse during the early Aβ(16-22) assembly, and therefore, indicating the occurrence of the desolvation event.

MATERIALS AND METHODS

Aβ(16-22) Assembly System Preparation

Aβ(16-22) powder was dissolved in HFIP by 10mg/mL, and incubated overnight at room temperature. The volatile HFIP solvent was removed by vacuum. The resulted

pretreated Aβ(16-22) was dissolve in 40% acetonitrile/water with 0.1% TFA to the desired concentration.

Fluorescence Correlation Spectroscopy (FCS)

In FCS experiment, fluorescence fluctuation is measured. To analyze these fluctuations, the intensity autocorrelation function **G(τ)** of the time-dependent fluorescence intensity **(F(t)**) defined as (lag time **τ** is a variable interval, and it is averaged over all data points in the time series) (Tjernberg 1999, Medina 2002, Haustein 2003, Sengupta 2003):

$$G(\tau) = \frac{< \delta F(r,t) \bullet \delta F(r't+\tau) >}{< F >^2}$$

$$\delta F(t) = F(t) - F$$

<F> is the time-average fluorescence intensity. For a defined number of molecular species **G(τ)** is given by:

$$G(\tau) = \frac{\gamma_{3DG}}{< C > V_{3DG}} \frac{1}{(1+8D\tau/\omega_0^{\,2})(1+8D\tau/z_0^{\,2})^{1/2}}$$

Where **<C>** is the average concentration of fluorescent molecules in the detection volume $\mathbf{V_{3DG}}$; $\boldsymbol{\tau_D}$ is the lateral diffusion time, and **D** is the diffusion constant; the beam waists, $\boldsymbol{\omega_0}$ is along the radial direction, and $\mathbf{z_0}$ is along the axial direction. The detection volume $\mathbf{V_{3DG}}$ is,

$$V_{3GD} = \frac{\pi^{\frac{3}{2}}}{8} \omega_0^{\,2} z_0$$

The factor, $\gamma_{3DG} = \frac{1}{2\sqrt{2}}$

Moreover, the lateral diffusion time $\boldsymbol{\tau_D}$ and the diffusion coefficient, **D**, which is independent of the particular setup used, have the relationship as:

$$\tau_D = \frac{\omega_0^2}{8D}$$

The half of the decay time depends on the mean diffusion time which is controlled by the molecular mobility. The diffusion coefficient **D** can be obtained from the lateral diffusion time, which is characterized as the decay time τ_D of the autocorrelation curve.

When plotting the autocorrelation curve based on autocorrelation function, the average concentration within the illumination region is proportional to the inverse amplitude of the correlation function,

$$G(0) = \frac{\gamma_{3DG}}{< C > V_{3DG}}, \tau = 0$$

The two-photon excitation experimental setup is similar to what has been described in Chapter 5. For FCS measurement, fluorescence is collected by an avalanche photodiode (APD) (EG&G, Vaudreuil, Canada). A home-built beam scanning and imaging system was used for imaging, and a software controlled motor stage ASI MS200 (Applied Scientific Instrumentation, Eugene, Oregon) was used to move the spots of interest to the laser focus. The wavelength used was 780nm. The eight-well chambers (Naglenunc International, Rochester, New York) and 22×30mm cover glasses (Corning Life Science) were both used in the sample preparation.

Fluorescence Recovery After Photobleaching (FRAP)

Fluorescence Recovery after Photobleaching experiment started with searching for the region of interst by motor stage software under a suitable laser power (~2.8mW at the sample). Photobleaching was performed in the region of interest with 5× laser power and 30 scans with 100μs scanning mode. The fluorescence recovery was recorded by

switching back to the original laser power and imaging at predetermined time interval (in minutes). The time-course fluorescence recovery curve was plotted by measuring the fluorescence intensity at the bleached region of interest with image analysis package in Igor Pro 6 software (WaveMetrics, Inc).

Dual Color Fluorescence Imaging of Alexa 633 and Rh17-22

The two-photon excitation experimental setup is similar to what has been described in the Chapter 5. The experiment was under 780nm excitation. By applying synchronized two channel imaging with 570nm dichroic, and filters 530/50 for Rh17-22 and 645/75 for Alex633, Alexa 633 allows visualizing the mature tubes, and Rh17-22 captures the dynamic events of Aβ(16-22) assemblies.

RESULTS

Large Aggregate Formation during Aβ(16-22) Assembly

Previous studies show that amyloid fibril formation is a nucleation-dependent process, in which ordered nuclei have to be formed before the fully developed fibers. Soluble oligomeric particles were implicated in amyloid fibrillation pathways, and suggested to be relevant to amyloid nucleation (Harper 1997, Stine 2003). Given the size of these oligomers, fluorescence correlation spectroscopy (FCS) should be sensitive to their existence during the amyloid assembly process. Because Rh17-22 can co-assemble with Aβ(16-22) as described in Chapter 5, FCS should be able to distinguish the Rh17-22 monomers in solution and when Rh17-22 peptides are in the Aβ(16-22) oligomeric species. Figure 6.1.a is the FCS correlation curves when Rh17-22 mixed with different Aβ(16-22) concentrations. Surprisingly, there was no difference among the correlation

curves when Aβ(16-22) concentration was 0.1, 0.2, and 0.3mM. They all exhibited as Rh17-22 monomers. This indicates Rh17-22 was still in monomer state when it mixed with Aβ(16-22) in the above concentrations. Either there was no other species except the monomers, or Rh17-22 was not involved in Aβ(16-22) oligomerization. However, when Aβ(16-22) concentration was above 0.5mM, large bright aggregates appeared. Because the aggregates are large, and they move slowly, the FCS correlation curves became deformed. When the large size aggregates appear, FCS is not suitable to determine their defined size. From fluorescence imaging (Figure 6.2.), these large size aggregates are not Aβ(16-22) nanotubes, but cluster-shaped aggregates. Their size can be in the range 2-8μm. In addition, the tubes can protrude out from these large aggregates as shown in Figure 6.2..

Figure 6.1. FCS to follow the early assemblies of Aβ(16-22)

(a) FCS of Rh17-22 mixed with Aβ(16-22) in different concentrations, 0.05mM, 0.1mM, 0.2mM, 0.3mM, and 0.5mM. The concentration of Rh17-22 is 400nM.

(b) CD of Aβ(16-22) self-assembly after one month incubation at different concentration, 0.8mM (black), 0.7mM (red), 0.6mM (green), 0.5mM (blue), 0.4mM (cyan), 0.3mM (magenta) and 0.2mM (yellow); Inset: the zoom-in of the CD of Aβ(16-22) self-assembly at the lower concentration, 0.5mM (blue), 0.4mM (cyan), 0.3mM (magenta), and 0.2mM (yellow).

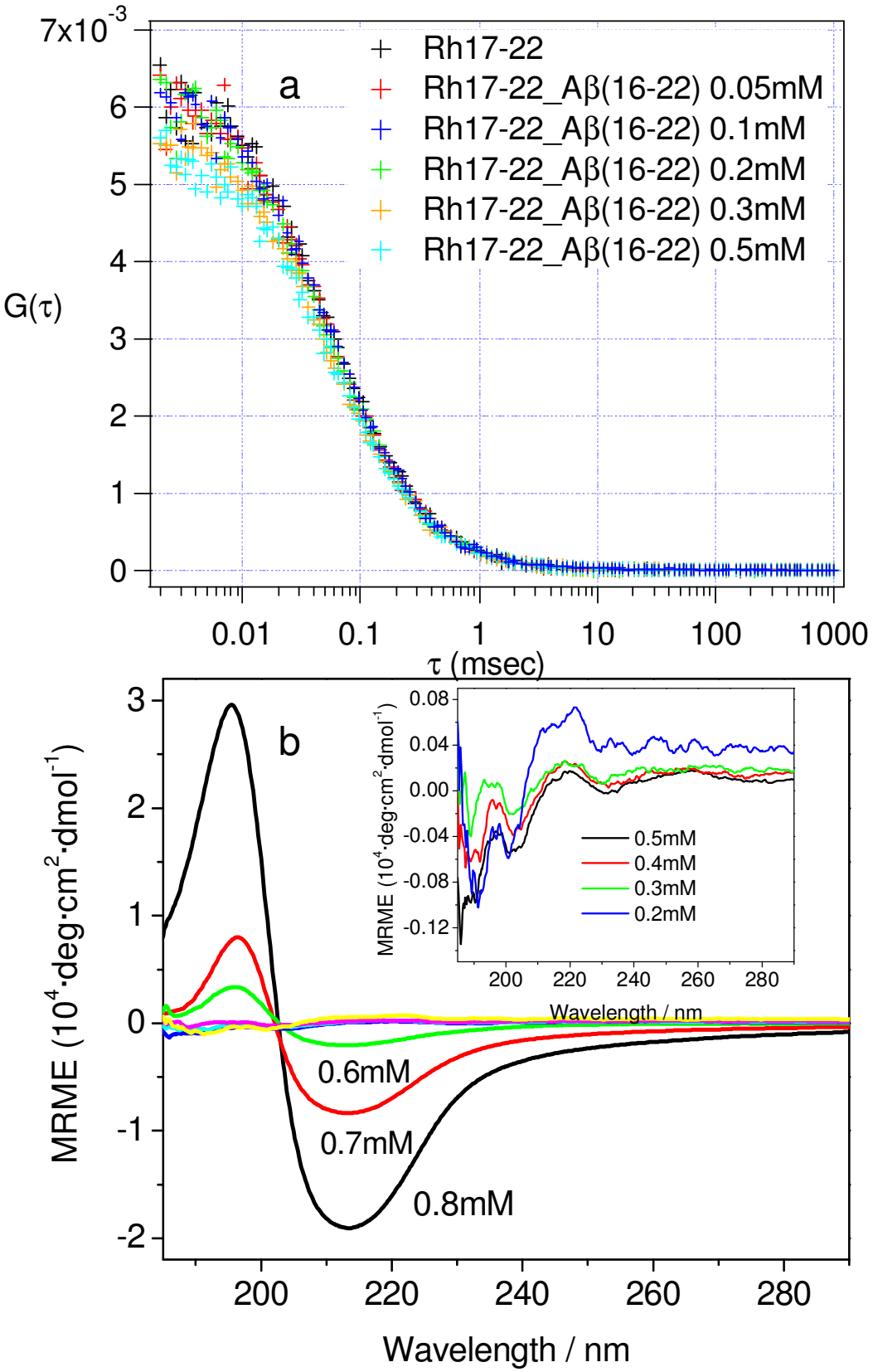
7x10-3
6
5
4
3
2
1
0
G(τ)
a
Rh17-22
Rh17-22_Aβ(16-22) 0.05mM
Rh17-22_Aβ(16-22) 0.1mM
Rh17-22_Aβ(16-22) 0.2mM
Rh17-22_Aβ(16-22) 0.3mM
Rh17-22_Aβ(16-22) 0.5mM
0.01
0.1
1
10
100
1000
τ (msec)
b
MRME (10⁴·deg·cm²·dmol⁻¹)
3
2
1
0
-1
-2
0.6mM
0.7mM
0.8mM
200
220
240
260
280
Wavelength / nm
MRME (10⁴·deg·cm²·dmol⁻¹)
0.08
0.04
0.00
-0.04
-0.08
-0.12
0.5mM
0.4mM
0.3mM
0.2mM
200
220
240
260
280
Wavelength / nm

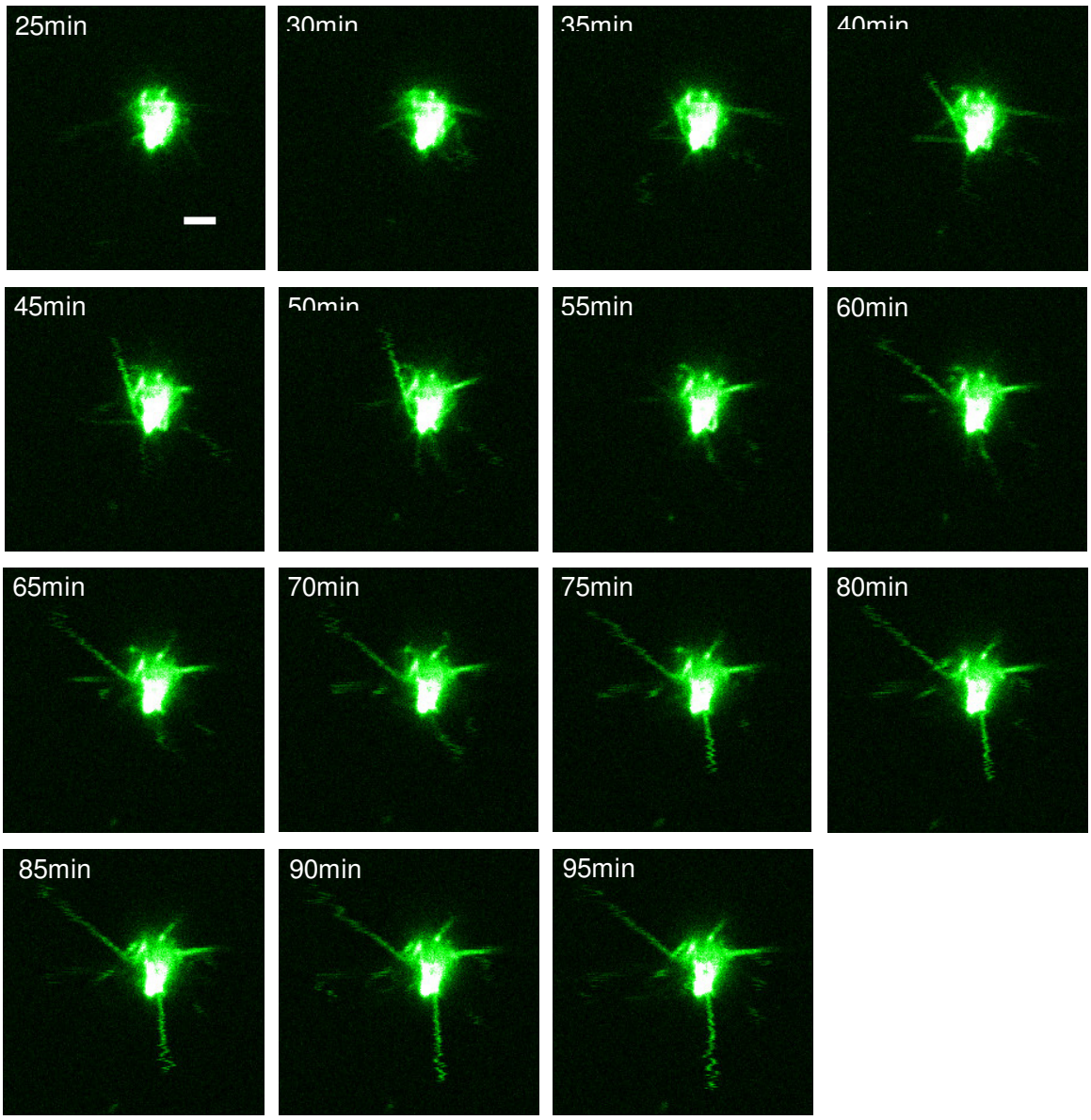

Figure 6.2. Fluorescence imaging of Aβ(16-22) tubes protruding out from the aggregates

The images were acquired over 2 hours with 5min intervals. Scale=2μm.

The first consideration of these large aggregates is whether they are the preformed species when the peptide powder is dissolved into solution. To confirm, Hexafluoro-2-propanol (HFIP) is used to pre-dissolve the peptide. As a fluorinated alcohol, HFIP exhibits strong hydrogen bonding properties, can dissolve substances that serve as hydrogen-bond acceptors, such as amides and ethers (Shuklov 2007). HFIP is widely used in amyloid kinetic study to dissolve the preformed structure during amyloid self-assembly (Wood 1996, Quijano 2006, Kayed 1999). For Aβ(16-22) assembly system, HFIP does dissolve Aβ(16-22) tubes as shown in Figure 6.4., which is promising for using HFIP to dissolve any Aβ(16-22) preformed structures. However, after HFIP pre-treatment, large clusters appear, suggesting the larger aggregates are formed during Aβ(16-22) assembly, and possibly on pathway to Aβ(16-22) amyloid.

In addition, the large aggregate formation has a critical concentration, below which there is no large aggregates observed (Figure 6.1.a). The critical concentration for the large aggregate appearance is comparable to the critical concentration of Aβ(16-22) assemblies. As shown in Figure 6.1.b, after a month incubation, Aβ(16-22) does not assembly in the concentration below 0.5mM, which is similar to the concentration when the large aggregates start appearing. Because the large aggregates only can form above a critical concentration, which, on the other hand, indicates the aggregates are formed during Aβ(16-22) assembly, but not from certain preformed structures during peptide powder desolvation.

Although oligomers or small size assemblies are not observed at lower concentrations, their co-existence with those large aggregates is possible at higher concentration. To test whether oligomers co-exist with large aggregates, FCS is applied

to the background solution of the large aggregates. To reduce the movement of large aggregates on the sample holder, the sample was prepared on cover slips. As the image shown in Figure 6.3., the large aggregates stay still, and FCS was applied in the regions between aggregates. In this FCS analysis, the number of Rh17-22 decreased, which was correlated with the photon count rate (F in Table 6.1.) decrease, comparing with the count rate of Rh17-22 at the same concentration in the absence of Aβ(16-22), consistent with the involvement of Rh17-22 into the large clusters. However, the diffusion constant (D) of the Rh17-22 in the Rh17-22/Aβ(16-22) mixed sample stays same as Rh17-22 monomers, indicating no oligomers or smaller assembled species co-exist with the large aggregates.

In the FCS analysis, G_0 has reverse correlation with the chromophore concentration in the detection volume. In the background solution of large aggregates, G_0 increased around 3 times comparing with the G_0 of Rh17-22 when Aβ(16-22) is absent (Figure 6.3. and Table 6.1.), which suggests the amount of Rh17-22 in the background solution is 3 times less than when Aβ(16-22) is absent. Therefore, 40% of Rh17-22 peptides are in the background solution, and about 60% of Rh17-22 peptides are in the aggregates. Now the question is whether the ratio of Aβ(16-22) in the aggregates and in solution is comparable with the Rh17-22 ratio.

Assuming the peptide density in the aggregates maintains the density of proteins, around 1.35g/cm^3, assuming the aggregates are spherical, and the aggregate diameter is 2μm, the total amount of peptide in the aggregates is (the molecular weight of Aβ(16-22) is 894g/mol),

$$V_{aggregate} = \frac{4}{3}\pi R^3 = \frac{4}{3}\pi(\frac{2}{2})^3 \approx 4\mu m^3$$

$$\rho_{protein} = \frac{1.35g}{cm^3} \times \frac{1mol}{894g} \times \frac{10^3 mmol}{1mol} \times \frac{10^{-12} cm^3}{1\mu m^3} \approx 1.35 \times 10^{-12} mmol/\mu m^3$$

$$N_{total} = \rho_{protein} V_{aggregate} = \frac{1.35 \times 10^{-12} mmol}{\mu m^3} \times 4\mu m^3 \approx 5 \times 10^{-12} mmol$$

Here, $V_{aggregate}$ is the aggregate volume, R is the aggregate radius estimated from imaging, $\rho_{protein}$ is the protein density, N_{total} is the total amount of peptide in the aggregate.

Total number of peptide in the aggregate is,

$$5 \times 10^{-12} mmol \times \frac{10^{-3} mol}{mmol} \times \frac{6.02 \times 10^{23}}{mol} = 3 \times 10^9$$

Also, given the peptide length is 2.6nm (extended), the side chain length is 1nm, the width is 0.5nm, a typical Aβ(16-22) peptide volume ($V_{monomer}$) is $1.3nm^3$. Knowing the aggregate volume, then the total number of peptide in the aggregates is

$$\frac{V_{aggrgate}}{V_{monomer}} = \frac{4\mu m^3}{1.3nm^3} \times \frac{10^9 nm^3}{\mu m^3} = 3 \times 10^9$$

These two estimations are comparable. Well comparing with oligomer, these aggregates contain billion monomers. Given the peptide concentration is 0.5mmol/L in assembly, the volume of the solution is 300μL, and then total number of A□ (16-22) originally put into the solution is,

$$\frac{0.5mmol}{L} \times 300\mu L \times \frac{10^{-6} L}{\mu L} \times \frac{10^{-3} mol}{mmol} \times 6.02 \times 10^{23} = 9 \times 10^{16}$$

These peptides will distribute to the aggregates and the background solution. We do not know how many aggregates are formed in solution. If all the Aβ(16-22) peptides in the solution form aggregates, there will be ~3×10^7 aggregates. Usually, 10μL of the sample was prepared in a 22×30mm cover glass, and the imaging window is 40×40μm. If

averagely there are 2 observed in the imaging window, then the number of aggregates in this 300μL solution is,

$$\frac{300\mu L}{10\mu L}\times\frac{22mm\times 30mm}{0.04mm\times 0.04mm}\times 2\approx 2\times 10^{7}$$

The magnitude of the number of Aβ(16-22) aggregates formed in the solution based on the Rh17-22 imaging experiment is comparable with the magnitude of the aggregate number when all Aβ(16-22) peptides in the solution form aggregates. This indicates Aβ(16-22) possibly have similar ratio as Rh17-22 to be in the aggregates and in the solution.

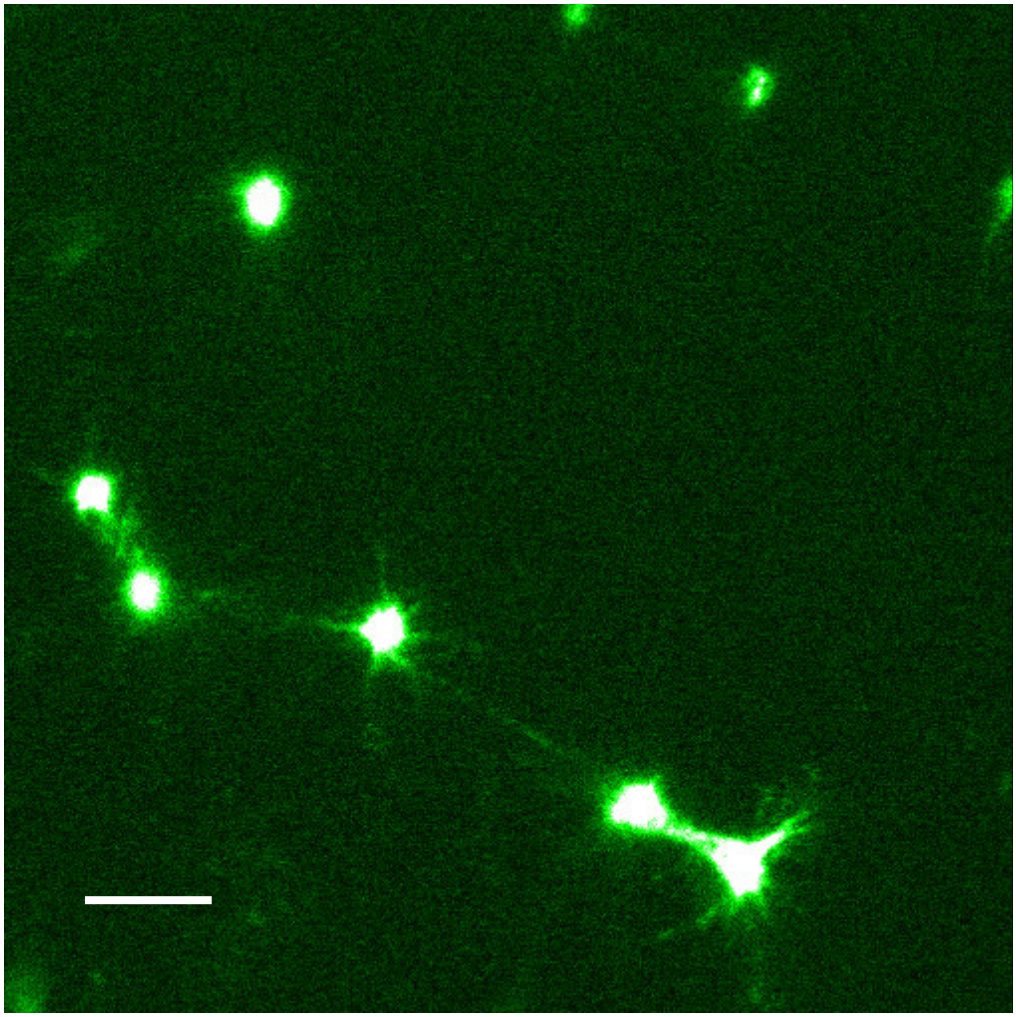

Figure 6.3. The fluorescence image of FCS in the aggregate background

Comparing with the bright aggregates, the background solution is relative dark. The image is to demonstrate the background of the aggregates is applicable to FCS. With a software controlled motor stage ASI MS200 (Applied Scientific Instrumentation, Eugene, Oregon), the laser focus can be moved to the spots of interest. Scale=5μm**.**

Table 6.1. FCS acquired in the background of large aggregates (Figure 6.3.).

	F(kHz)	G_0	$F \times G_0$	D
Rh17-22_1	154.09	0.0418	6.44	0.173
Rh17-22_2	161.41	0.0392	6.33	0.171
Rh17-22_Aβ(16-22)_1	66.45	0.0961	6.38	0.178
Rh17-22_Aβ(16-22)_2	63.13	0.1012	6.38	0.178
Rh17-22_Aβ(16-22)_3	58.9	0.112	6.60	0.177
Rh17-22_Aβ(16-22)_4	57.21	0.116	6.64	0.175

Notes: the serial numbers in the sample name column are noted as the repeated experiments. F is the photon count rate and D is the diffusion constant of the chromophore in the detection volume.

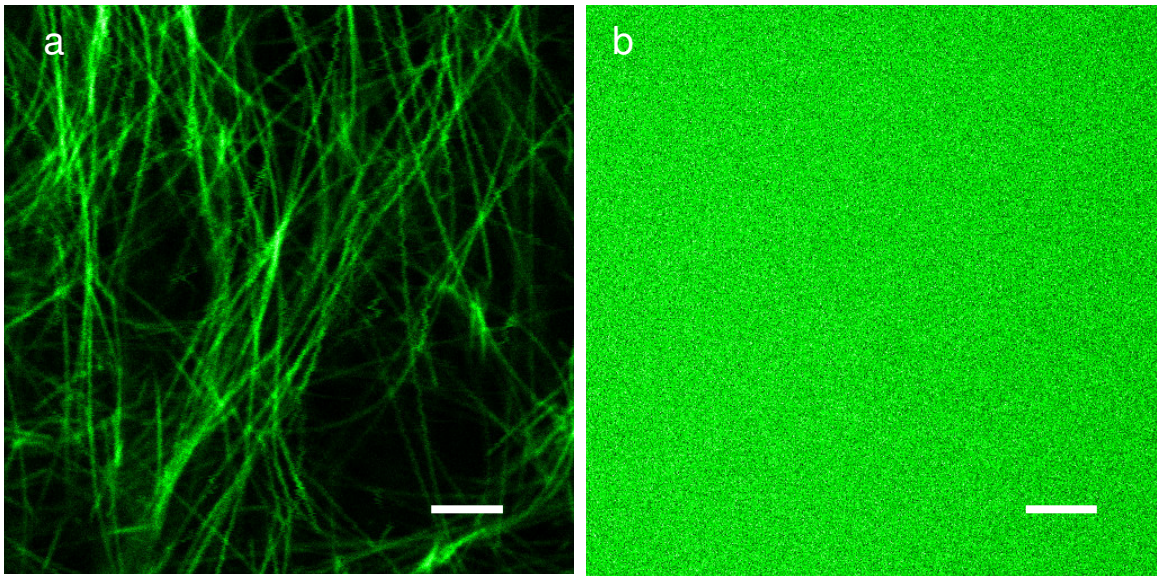

Figure 6.4. HFIP can dissolve mature Aβ(16-22) tubes

Rh17-22 co-assembled mature Aβ(16-22) tubes (Aβ(16-22) concentration is 1mM, and Rh17-22 concentration is 4μM) mixed with HFIP in 1:1 (v:v) ratio in an hour before acquiring the images. Comparing with the Rh17-22 co-assembled mature Aβ(16-22) tubes without mixing with HFIP (a), the mature tubes are dissolved (b). Scale=5μm.

Peptide Dynamics within the Aggregates

Using CD to follow amyloid assembly process, the transition from random coil to β-sheet (Figure 6.5.d) was co-incident with the appearance of the detected amyloid assembly (Lu 2003). Amyloid nucleation within the peptide aggregates requires the peptides actively rearrange as in a molten globule to reach the proper peptide chain associations. Indeed, simple photobleaching experiments demonstrated the peptides to be dynamically reorganized within the aggregates. Figure 6.5.a shows a series of fluorescence recovery images following spot photobleaching within an Aβ(16-22) aggregate. The time course of the fluorescence recovery is plotted in Figure 6.5.c, which confirms the interior of the aggregate is truly accessible to rearrangement. In contrast, the fluorescence recovery after the photobleaching of mature Aβ(16-22) nanotubes, only showed minimal fluorescence recovery in similar timescales (Figure 6.5.b and 6.5.c), which is expected as the fluorescent peptides within mature tubes are H-bonded into the β-sheet structure and the exchange rate should be very slow. Therefore, the peptides within the aggregates do not have strong fixed interactions, and they should be randomly collapsed, similar to the molten globular state, and likely do not have well defined structure prior to nucleation. The tubes protrude out from the aggregates, which implies nuclei are generated within the aggregates. The polypeptide accumulated molten globular state has become important for the formation of Aβ(16-22) nuclei.

Figure 6.5. Peptides are dynamic within the aggregates

(a) Fluorescence recovery after the photobleaching on an Aβ(16-22) aggregate. The photobleached region is shown by the red circle. The recovery images were acquired over an hour with 3-4min intervals. Scale=5μm.

(b) Fluorescence recovery after the photobleaching of mature Aβ(16-22) tubes. The recovery images were acquired over 30min with 5min intervals. Scale=5μm.

(c) Normalized time-dependent fluorescence recovery, (■) in aggregate, the recovery is calculated by the fluorescence intensity measurement in the pixel range x: 250-270, y: 240-260; (●) in mature tubes, the recovery is calculated by the fluorescence intensity measurement in the pixel range x: 140-220, y: 140-220.

(d) Time-dependent CD spectra of Aβ(16-22)/Rh17-22 co-assembly system. (Inset) Mean residue ellipticity at 215 nm as a function of time for 0.5mM Aβ(16-22) and 4μM Rh17-22 in 40% acetonitrile/water with 0.1% TFA.

a

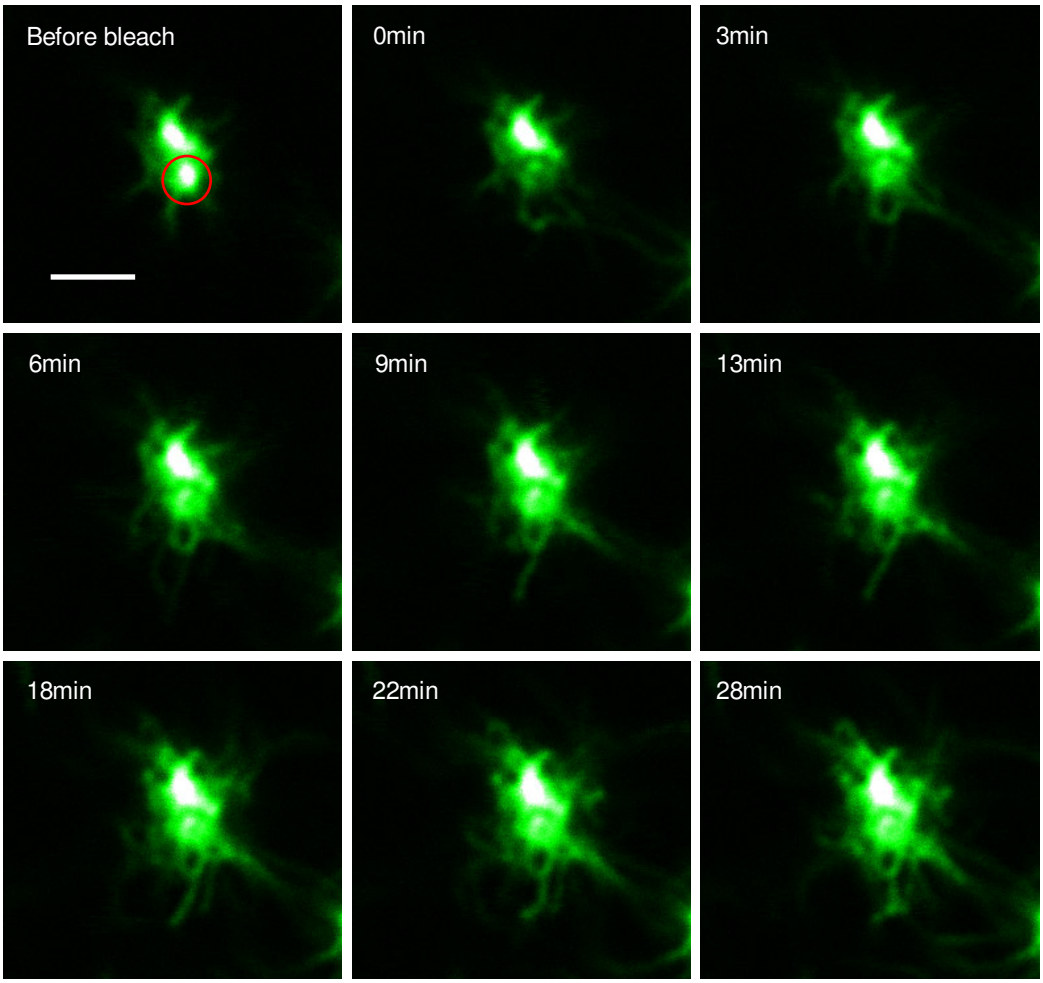
Before bleach
0min
3min
6min
9min
13min
18min
22min
28min

b

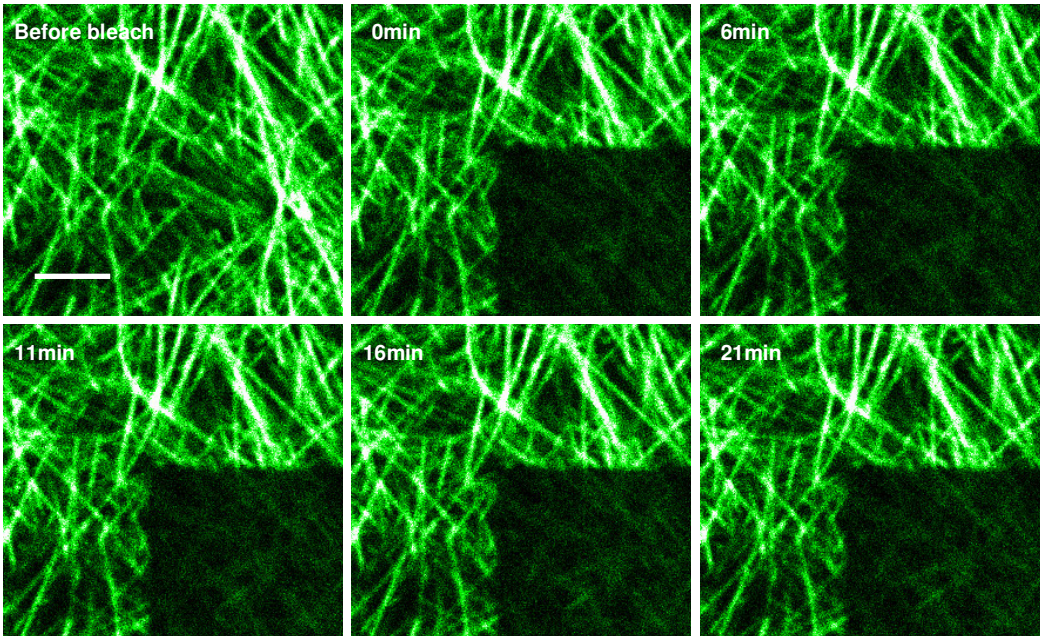
Before bleach
0min
6min
11min
16min
21min

c

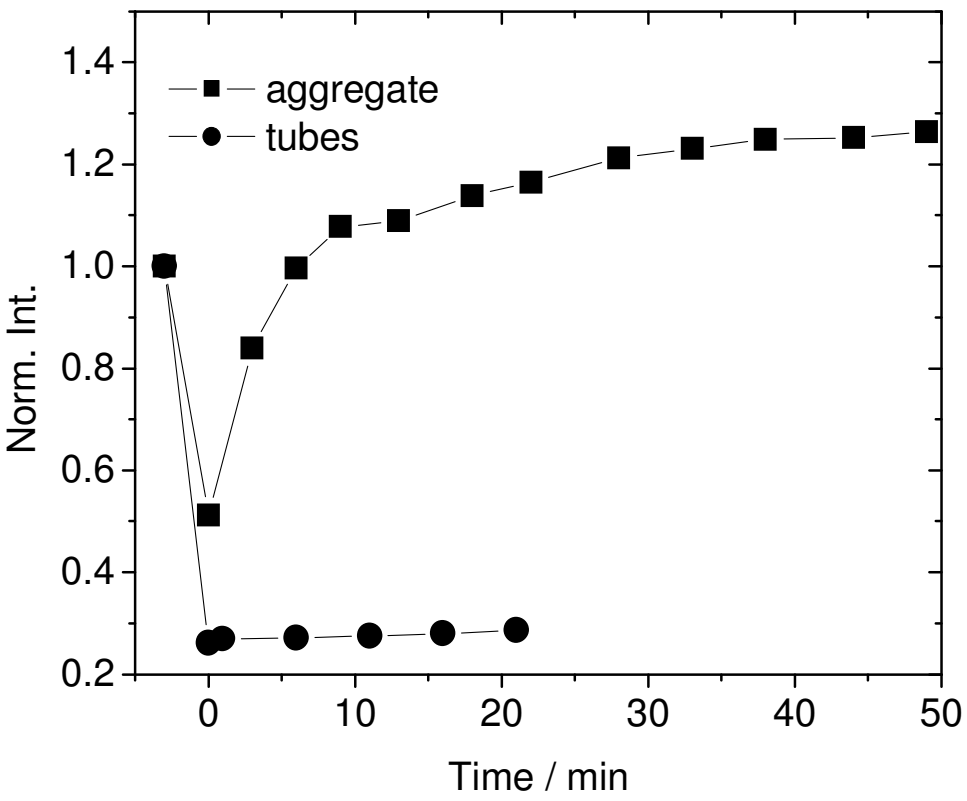
aggregate
tubes
Norm. Int.
Time / min
1.4
1.2
1.0
0.8
0.6
0.4
0.2
0
10
20
30
40
50

d

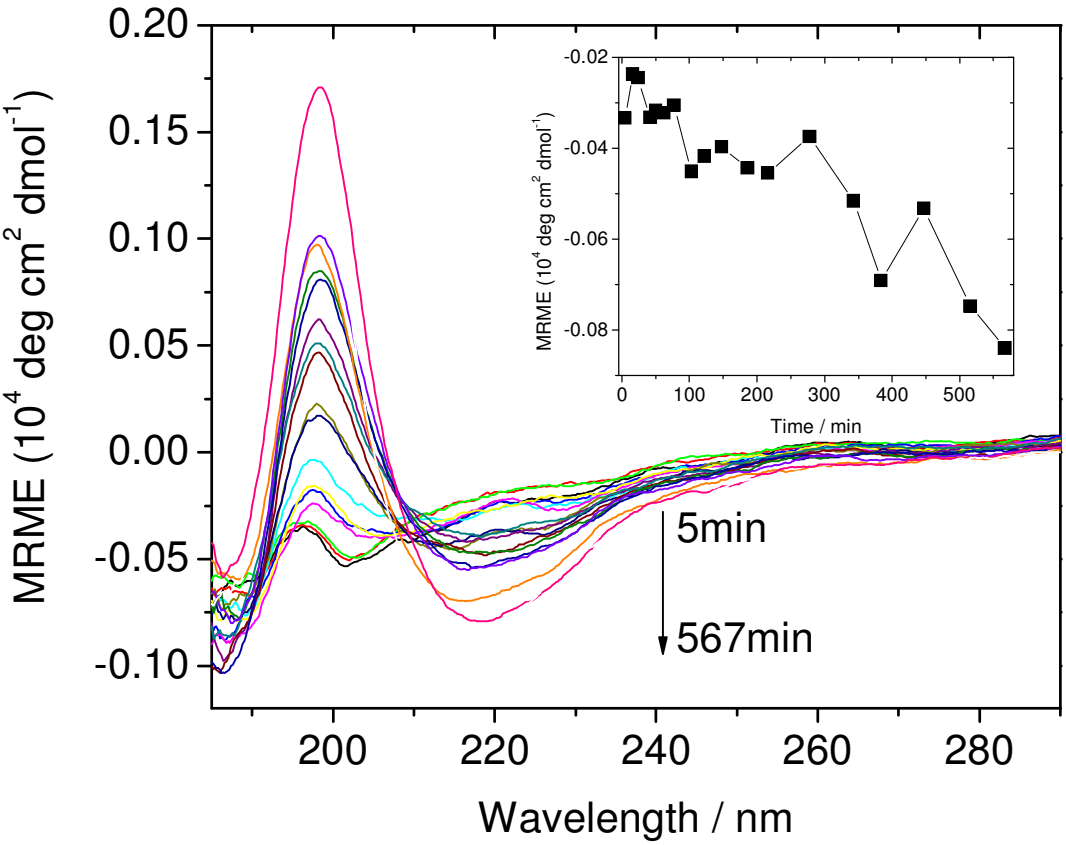
MRME (10^4 deg cm^2 dmol^-1)
Wavelength / nm
5min
567min
MRME (10^4 deg cm^2 dmol^-1)
Time / min
0.20
0.15
0.10
0.05
0.00
-0.05
-0.10
200
220
240
260
280
-0.02
-0.04
-0.06
-0.08
0
100
200
300
400
500

Nanotubes Growth

Figure 6.2. are the snapshots of Aβ(16-22) nanotube growth by protruding out from the aggregates. Because the aggregates gather up to 50% peptides, and the tube growth is a rapid process to assemble peptides into amyloid. The question is whether the tube growth also occur inside the aggregates, and are pushed out of the aggregates after they are formed, visualized as protruding from the aggregate.

To test this hypothesis, the tube growth was monitored by fluorescence photobleaching experiment. In Figure 6.6.a, one tube was photobleached, and left a dark region. By following the growth after photobleaching, if the dark region moves along with the tube growth, it would confirm the tubes are grown inside the aggregates. However, the dark region stayed still, but the tubes were grown by the elongation from the tube ends (Figure 6.6.b), which is consistent tubes elongated from their ends. In addition, FCS in the background of the aggregates indicates the background solution contains mainly peptide monomers, which supports tubes grow by adding monomers to the ends. These observations further indicate nucleation and elongation are distinct processes within the amyloid self-assembly pathway, and elongation, which is spatially separated from the nucleation sites within the aggregates, can proceed independently once the growth is nucleated. This finding is consistent with the ability to "seed" amyloid growth by adding pre-nucleated structures to solutions of amyloid forming peptides (Schilling 2006, Colby 2007).

When Aβ(16-22) assembly reaches the steady-state, i.e. when Aβ(16-22).tubes are mature, the large aggregates disappear. Further, FCS was applied to the background solution of Aβ(16-22) tubes. Still, only monomer Rh17-22 was observed in the

background (Figure 6.7. and Table 6.2.), which implies the equilibrium among peptide monomers, aggregates and mature Aβ(16-22) tubes. Most likely, the aggregates first form, dynamic rearrangement promotes nucleation within the aggregates, and finally elongation grows amyloid tubes. Along these processes, peptides release from the aggregates into the solution, and peptide monomers add to the tube ends to elongate the tubes, and finally the system reaches the steady state with the equilibrium between the peptide monomers and mature tubes (Figure 6.6.c).

Figure 6.6. The growth of Aβ(16-22) nanotubes

(a) Photobleaching of one tube as the yellow circle indicated, the fluorescence recovery after the photobleaching was recorded over an hour with 5min intervals.

(b) Zoom in to the photobleached tube, the photobleached dark region stayed still, and the tube grew by the elongation from the ends.

(c) The model of equilibrium among peptide monomers, large aggregates, and mature tubes during Aβ(16-22) assembly. Large aggregates disappear by releasing monomers to the solution, tube growth is by adding peptide monomers to the tube ends, and finally the steady state is the equilibrium between the peptide monomers and mature tubes.

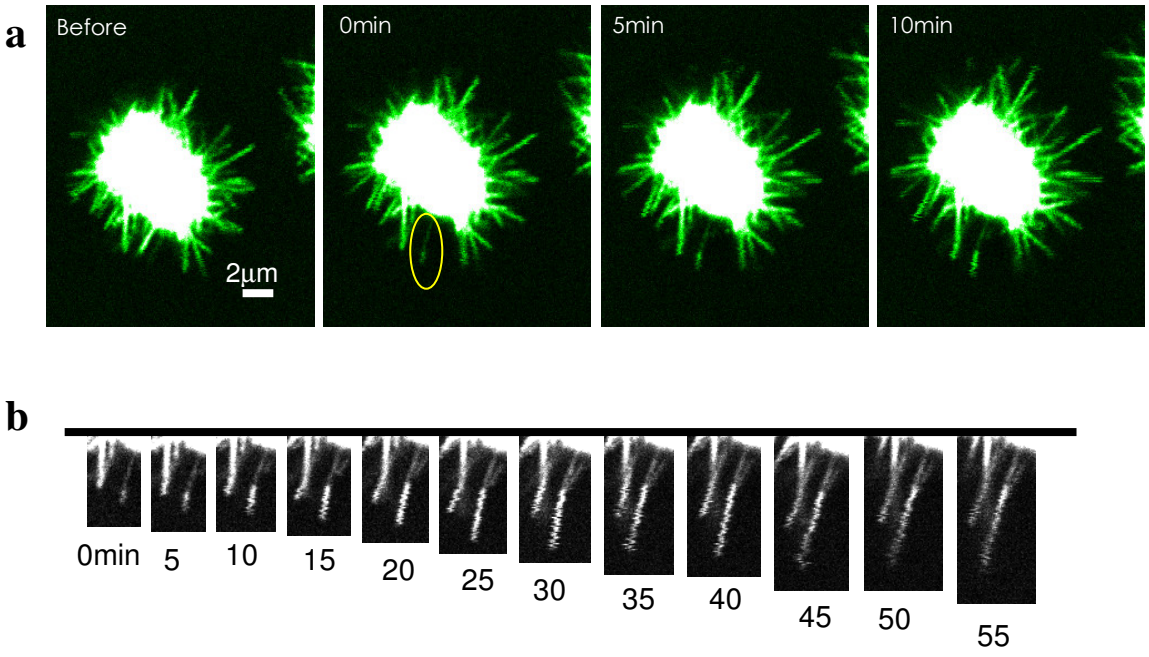
a
Before
0min
5min
10min
2μm
b
0min
5
10
15
20
25
30
35
40
45
50
55
c
Monomers release from the aggregates
Monomers add to the tube end
Steady-state

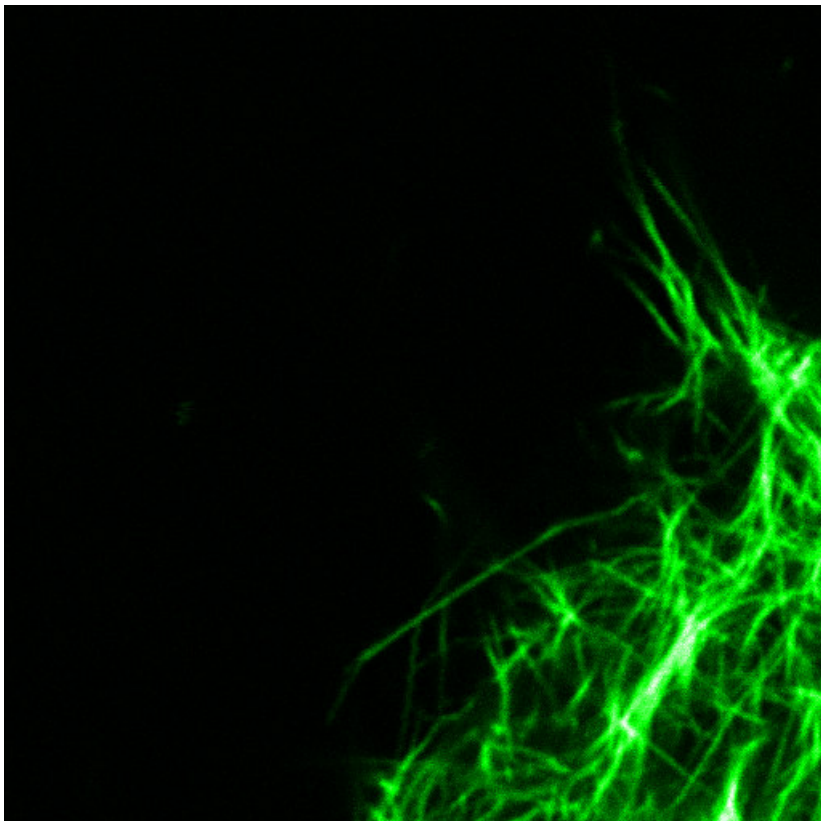

Figure 6.7. The fluorescence image of FCS in the solution of mature tubes

The background solution is relative dark comparing with the bright tubes. The image is to demonstrate the background of mature tubes is applicable to FCS. With a software controlled motor stage ASI MS200 (Applied Scientific Instrumentation, Eugene, Oregon), the laser focus can be moved to the spots of interest. Scale =5μm.

Table 6.2. FCS acquired in the background of mature tubes (Figure 6.7.).

	F(kHz)	G_0	$F \times G_0$	D
Rh17-22_1	298	0.005	1.49	0.168
Rh17-22_2	303	0.005	1.52	0.180
Rh17-22_Aβ(16-22)_1	144	0.013	1.87	0.172
Rh17-22_Aβ(16-22)_2	144	0.013	1.87	0.172
Rh17-22_Aβ(16-22)_3	150	0.014	2.10	0.182
Rh17-22_Aβ(16-22)_4	153	0.013	1.99	0.181

Notes: the serial numbers in the sample name column are noted as the repeated experiments. F is the photon count rate and D is the diffusion constant of the chromophore in the detection volume.

Dynamics in the Aβ(16-22) Assembly Steady State

As described above, equilibrium is indicated between the peptide monomers and mature tubes when the system reaches the steady state. Possibly, there will be monomer exchange at the tube ends. To test this hypothesis, a dual color experiment was designed to visualize the dynamics at the tube ends (Figure 6.8.), in which one dye is used to see all Aβ(16-22) tubes, and the other dye specifically detect the new growth at the tube ends. The two dyes are required not to have spectra overlap. Aβ(16-22) tubes contain positive charges on the surface (Mehta 2008), and it can be coded with dyes containing negative charges, such as Alexa 633 ([2]Liang 2008,), which can be used to see all the existing Aβ(16-22) tubes. Rh17-22 can incorporate into Aβ(16-22) β-sheets, which was used to detect the new growth at the tube ends. Alex 633 and Rh1722 do not have any spectral overlap (Figure 6.8.d). By applying synchronized two channel imaging with a 570nm dichroic, and filters 530/50 for Rh17-22 and 645/75 for Alex633, Alexa 633 allows visualizing the mature tubes, and Rh17-22 indeed captured a new growth event at Aβ(16-22) tube ends (Figure 6.8.e), consistent with Aβ(16-22) tube ends being dynamic. This is comparable with the seeding experiments, where the tube ends play the role as nucleated sites to attract monomer addition. The monomer exchange may be a better description for this dynamics, in term of monomer addition and releasing at the tube ends. However, the tube growth (monomer addition) was the major event observed, which may be due to the monomer releasing is not sensitive in visualization. It is also true that the preparation of the Alexa 633/ Rh17-22/ Aβ(16-22) tube mixing system is by adding Alexa 633 and Rh17-22 to Aβ(16-22) tubes. The “new growth” observed is maybe the result of the system disturbing by adding new peptide solution.

Occasionally in the fluorescence recovery after photobleaching experiment of mature Aβ(16-22) tubes, the “new growth” can appear within the photobleached region (Figure 6.9.). This event only happened when there are tube ends in the photobleached region. Under photobleaching and recovery, there is no significant disturbing to the tube system by adding any new component. This further confirms the dynamics at the tube ends. Still, the monomer releasing is not captured by these experiments.

Figure 6.8. The dynamics in Aβ(16-22) assembly steady state

Synchronized dual-color imaging of Rh17-22 mixed with Alexa633 coded Aβ(16-22) tubes under 780nm two-photon excitation and with a 570nm dichroic and filters 530/50 for Rh17-22 and 645/75 for Alex633.

(a) The image of Alexa 633 coded on Aβ(16-22) tubes at the 5min time point after Rh17-22 mixed with Alexa633 coded Aβ(16-22) tubes.

(b) The corresponding image of Rh17-22 indicating the new growth at the tube ends at the same time point.

(c) The overlay of a and b. The Alexa633 signal is in red, and the Rh17-22 signal is in yellow.

(d) Absorbance and fluorescence of Alexa 633 and Rh110, indicating they do not have spectra overlap.

(e) Snapshots over 3 hours of a zoomed-in spot indicated with the cyan rectangle. The tube new growths appeared at the tube ends. The black-and-white images exhibit the new growth with the Rh17-22 fluorescence. The colored images include the background tubes exhibited in red by Alexa633, and the new growth is exhibited in yellow by Rh17-22.

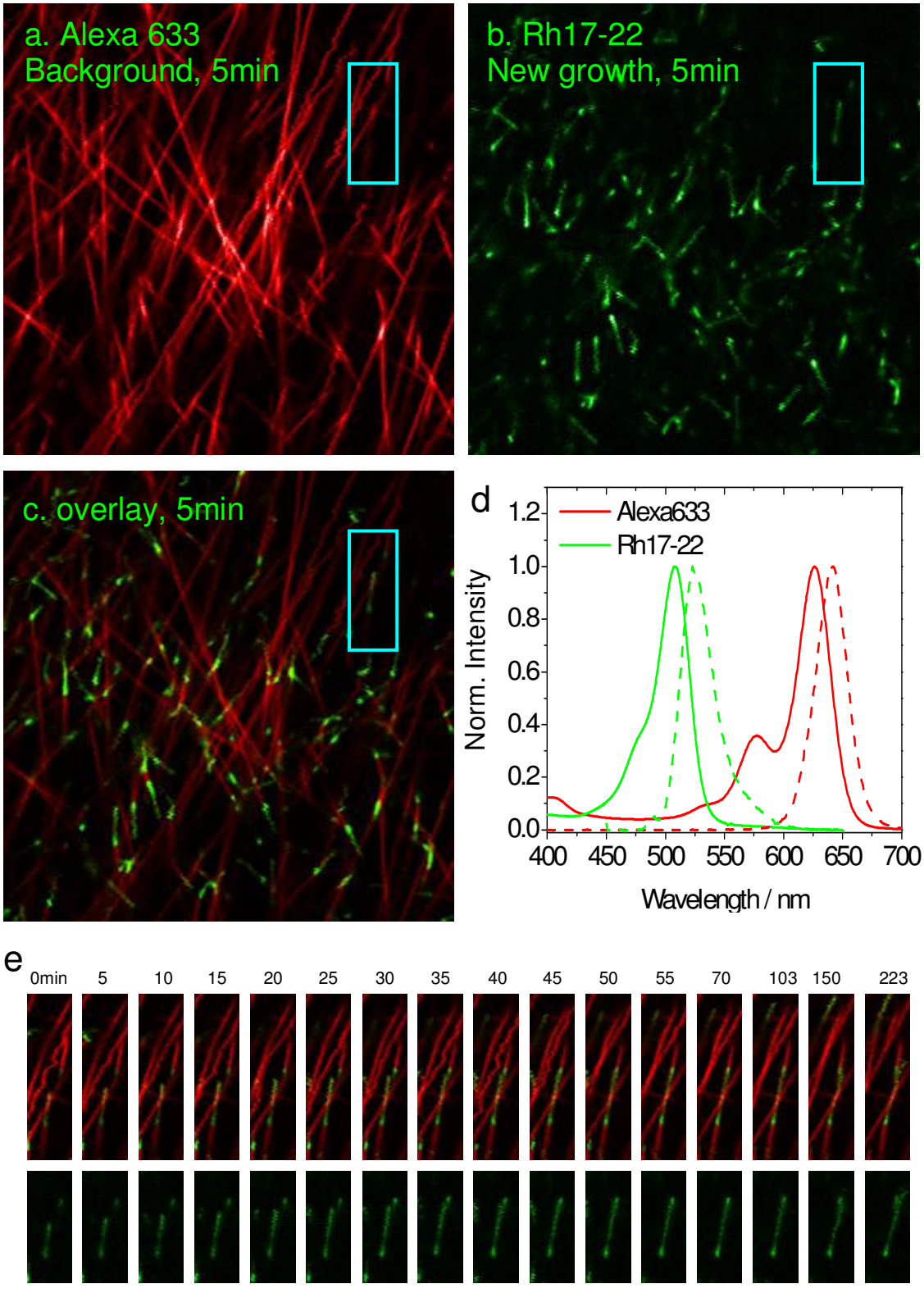
a. Alexa 633
Background, 5min
b. Rh17-22
New growth, 5min
c. overlay, 5min
d
Alexa633
Rh17-22
Norm. Intensity
Wavelength / nm
e
0min
5
10
15
20
25
30
35
40
45
50
55
70
103
150
223

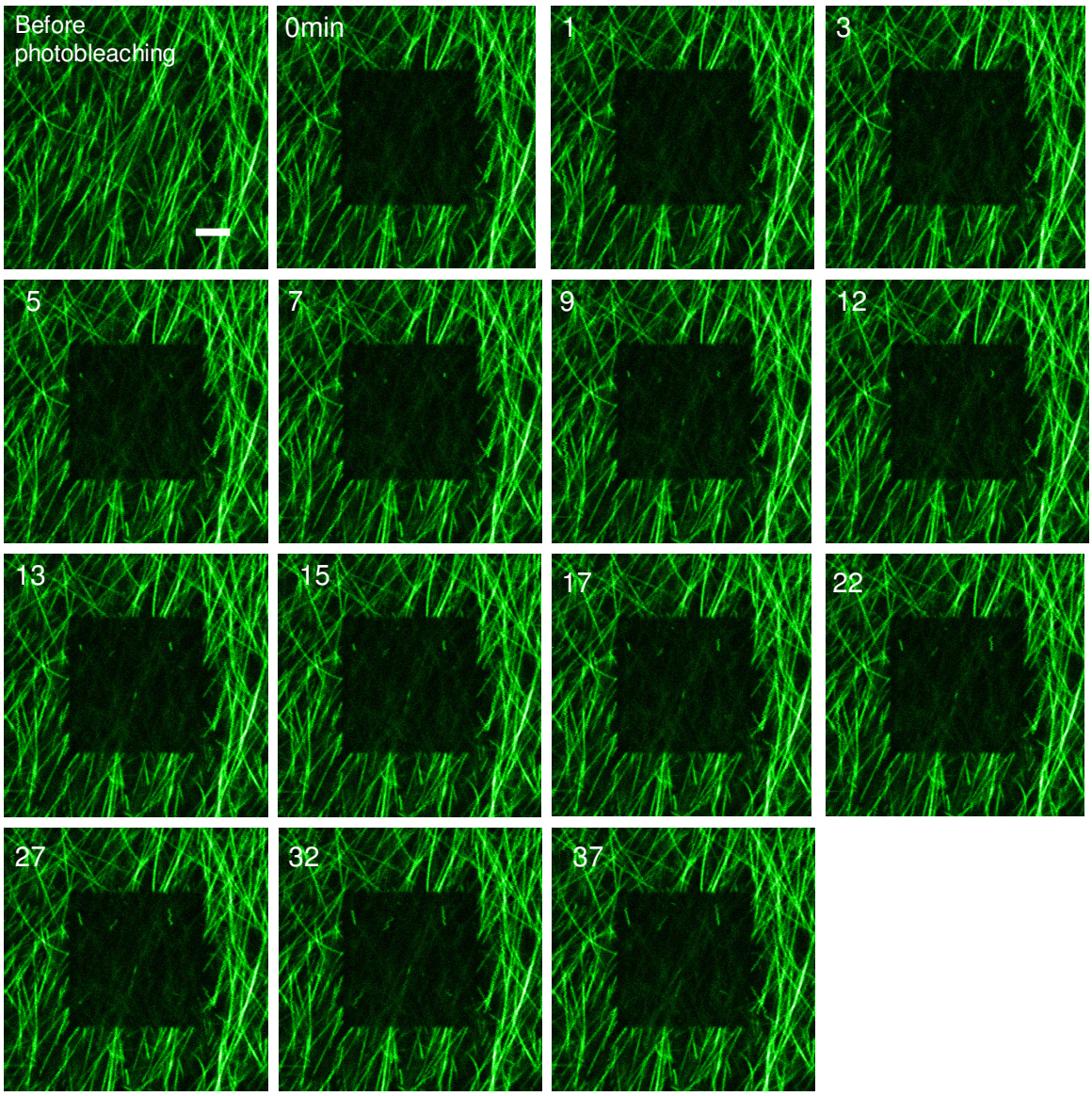

Figure 6.9. New growth observed in fluorescence recovery after photobleaching of mature Aβ(16-22) tubes

The fluorescence recovery was recorded over 40min after the photobleaching. In the photobleached dark region, the new tube growth appeared as the bright fine lines, which is distinct from the bulk fluorescence recovery on the tubes. Scale=5μm.

DISCUSSION

Early kinetic models for amyloid growth argued that individual nucleating events created templates for the addition and conformational induction of new monomers (Jarrett 1993, Haper 1997, Lomakin 1997, Uversky 2004, Yong 2002), and propagation steps were indeed first order in peptides (Esler 2000, Cannon 2004). Further AFM and TEM studies identified particle-like species as possible intermediates (Harper 1997, Stine 2003). Although these micelle-like particles were later implicated in neuronal dysfunction (Lambert 2001, Haass 2007, Walsh 2007, Zhao 2008), many recent studies suggest the particles may be off-pathway intermediates (Baskakov 2002, Modler 2003, Gosal 2005, Kaylor 2005, Necula 2007). The nucleated conformational conversion model (Serio 2000) also implicated intermediate disordered oligomers serving as nucleating centers for the addition of monomers, and/or other oligomers, during propagation. However, the general existence, size, and composition of intermediate oligomeric species, their relationship to protein folding events, and their role in amyloid misfolding remain unclear (Kirkitadze 2001, Baskakov 2002, Souillac 2002, Gorman 2003, Kayed 2003, Gosal 2005, Oddo 2006, Necula 2007). Here, the observed large aggregates of Aβ(16-22), which confirmed to be on the amyloid nucleation pathway, suggests the molten globular states of peptide aggregates possibly initiate the amyloid nucleation.

Even though some amyliodogenic peptides are surface active (Ambroggio 2005, Lin 2007), these aggregates are not micelles or vesicles. The assemblies are far too large for micellular architectures composed of short peptides. Optical dissection shows the aggregates to be homogeneously fluorescent throughout their interior, again inconsistent with vesicle organization. Finally, no evidence for aggregate formation at air/water

interfaces, a critical intermediate for micelle assembly (Chari 2004, O'Driscoll 2005), could be found even with these brightly florescent monomers. Rather, the aggregates emerge randomly by phase separation within the solution.

The energies required to desolvate two peptides in an aqueous environment to form interstrand backbone hydrogen bonds are significant (Rodriguez-Larrea 2006, Daidone 2007). Recent efforts to probe the requirements for secondary protein structure determination in amyloid indeed revealed the critical step of peptide desolvation occurs early ([1]Liang 2008), just as in native protein folding. These quantitative fluorescence microscopy measurements fix an early event in amyloid assembly as a phase transition to micron size assemblies containing as many as billion amyloid monomers. These intermolecular peptide assemblies reorganize dynamically within the aggregate and display properties most like the dehydrated molten globule intermediates in protein folding (Fernandez 2002, Fernandez 2003, Kim 2006, Meijer 2007). Like the molten globule, the nucleation of cross-β amyloid structures occurs predominantly, if not exclusively, within these desolvated peptide aggregates.

For native protein folding, phase separation to a molten globule involves a single polypeptide chain with a homogeneous particle size. These intermolecular molten globule assemblies undergo exchange with free peptide in solution and the sizes of the molten globule assemblies will depend on properties that include the length of the polypeptide, its specific amino acid sequence, and the environmental conditions employed. Moreover, all the molten globule assemblies may not have the same probability of nucleating amyloid assembly, and this probability seems very high for the nucleating core as the Aβ protein ([1]Liang 2008).

Unlike native proteins, nucleation and elongation are distinct processes in amyloid assembly. Elongation is spatially separated from the sites of nucleation within the clusters, and can proceed independently once growth is nucleated. This difference explains the ability to seed amyloid growth by adding pre-nucleated structures to solutions of amyloid forming peptides (Colby 2007, Schilling 2006). Over time, as the amyloids mature, the large clusters disperse. However, within these more mature assemblies, the nanotube ends remain dynamic and at equilibrium with free peptide. Amyloid steady state dynamics may be characteristic in amyloid system, and play an important role in transmissible amyloidosis, such as prion (Surewicz 2006, Surewicz 2007).

Lattice models of similar small amyloidogenic peptides have now captured many features of nucleated growth, templated assembly, and nucleated conformational conversion (Chen 2008), which occur in these intermolecular molten globules. The nucleation mechanism within these aggregates may well explain an outstanding puzzle related to amyloid diseases. Specifically, the critical concentration measured for amyloid formation in vitro typically greatly exceeds the concentrations generally thought to be present in human tissues, leaving unanswered how amyloids grow within human tissue. The amyloid nucleation mechanism presented here with molten globular state, unlike micelle formation, does not require high dissolved protein concentrations, but only that a critical level becomes sequestered within a tissue. The issues of tissue specificity may best be addressed by determining unique features of tissues that facilitate nucleation of toxic amyloid.

CHAPTER 7

POTENTIAL APPLICATION OF AMYLOID NANOTUBES

INTRODUCTION

Amyloid nanotubes formed by Aβ(16-22) congeners have hollow cylindrical shape, and contain the cross-β scaffold. Functional group incorporation is usually the first step in applying nanotubes as optical or electronic materials. In this chapter, I will exploit paracrystalline amyloid self-assembly to construct pigment arrays on Aβ(16-22) nanotube scaffold, and use Förster resonance energy transfer (FRET) measurement (Meer 1994, Towles 2007) to probe the resulting pigment arrangement, which mimics the light harvesting antenna. Secondly, I will investigate the optical signal generated by sulfate induced amyloid nanotube bundles (Lu 2007). The sulfate bundling decreases the lamination distance, and the stacked aromatic rings of phenylalanine residues interact under the applied two photon excitation. In addition, Aβ(16-22) congener tubes produce

second harmonic generation (SHG) (Campagnola 2003, Plotnikov 2006), under the two photon excitation. SHG is a nonlinear optical process that when multiple photons interact with nonlinear materials, new photons are generated with twice the energy, and therefore twice of the frequency and half the wavelength of the initial photons. This chapter mainly provides a few examples of Aβ(16-22) nanotubes as potential nanomaterials.

MATERIALS AND METHODS

Fluorescence Lifetime Imaging

The fluorescence lifetime imaging was measured using the time-correlated single-photon-counting (TCSPC) technique and Becker & Hickl electronics (Peter 2004). The detector was a Hamamatsu H7422-40 PMT (Hamamatsu Photonics, Japan) and a bandpass emission filter HQ530/50 (Chroma Technology) was used for lifetime measurement. The 256×256 pixel images were taken in a 100μs pixel-time scanning mode with a total collection time ranged from 120 to 180s. The fluorescence decay histogram for each pixel was well described by a single-exponential decay. A Levenberg–Marquardt routine for nonlinear fitting is applied to fit a decay curve to the data of this model function in a separate off-line software package SPCImage (Becker & Hickl Gmbh). The lifetime of rhodamine 6G in pure water (lifetime =4.08ns) was measured before each experiment.

Calculation of R_0

Föster radius is calculated through the overlap integral for the donor emission spectrum and the acceptor absorption spectrum. The definition is as below (Meer 1994):

$$R_0 = \sqrt[6]{\frac{8.8\times10^{-5}\kappa^2 Q_D J_{DA}}{n^4}}$$

$$J_{DA} = \int_0^\infty f_D(\lambda)\varepsilon_A(\lambda)\lambda^4 d\lambda$$

κ^2 is the orientation factor. In the calculation, the donor and acceptor are assumed to be randomly rotating dipoles, with the average value of κ^2, 2/3.

Q_D is the quantum yield of the donor, and the value is 0.6.

n is approximate index of refraction of the solution, the value is 1.343.

J_{DA} is the overlap integral of the donor emission spectrum and the acceptor absorption spectrum, and its definition as shown above.

ε_A is the extinction coefficient of the acceptor at each wavelength. The calculation uses a constant value of 150000.

Sulfate Bundling

The tubes were prepared as described in early chapters. The sulfate bundled samples were prepared at room temperature by mixing tubes (2mM) and 18mM sodium sulfate solution (acetonitrile:water (2:3, v:v) with 0.1%TFA) in 1:1 (v:v) ratio. After the mixing, the sulfate bundled samples were let stay overnight to undergo the fluorescence imaging experiments.

Cryo-SEM

At room temperature, 1~2 μL of sample is placed into a gold planchette and plunged into liquid ethane (-183 ^{o}C) to be cryo-immobilized. The vitrified sample is then stored in liquid nitrogen until transfer to the Cryo-stage, which is maintained at between -170 and -190 ^{o}C at this time. The sample is secured in place and the top scrapped off; liquid nitrogen is poured over the sample fracture face; the Cryo-stage is transferred to

the Denton DV602 Chromium coater and evacuated. With a vacuum of 3 to 4×10^{-7} Torr, the temperature is carefully ramped up to -105 ^{o}C. The samples are etched for 15 minutes. The temperature is then dropped to between -170 to -190 ^{o}C, and the vacuum is maintained. The samples are sputter coated with a 2.5 nm layer of Chromium, and then transferred to the Topcon DS130F SEM upper stage for In-Lens imaging at 25kV.

Two Photon Fluorescence Spectroscopy

The two-photon excitation experimental setup is similar to what has been described in the previous chapters. Fluorescence spectra were acquired with Acton Grating Spectrometer, which is coupled with a Back Illuminated CCD (Roper Scientific Inc.) via a fiber optics.

Part I Light Harvesting Antenna on an Amyloid Scaffold

As discribed in previous chapters, Aβ(16-22), the seven-residue amyloid-β segment Ac-KLVFFAE-NH2, self-assembles into soluble amyloid nanotubes in CH_3CN:H_2O (2:3, v:v) with 0.1%TFA (Lu 2003). These Aβ(16-22) nanotubes maintain antiparallel one-residue shifted β-sheet bilayers within a cross-β architecture (Mehta 2008), creating a nanotube surface that positions the peptide termini in a 5Å X 10Å rectangular pattern. Amyloid fibrils are sufficiently robust for functional molecular engineering (Gilead 2005, Hamada 2004, MacPhee 2000, Kodama 2004), and this patterned array across the nanotube surface appeared suitable for light harvesting antenna construction.

Chapter 5 has addressed Rh16-22 can co-assemble with Aβ(16-22) into nanotubes. As amyloids assemble through nucleation-dependent events, peptide co-

assembly can be used to increase the range of accessible structures (Gilead 2005, Hamada 2004). With Aβ(16-22) maintained as the dominant peptide to nucleate tube morphology, for example Aβ(16-22)/Rh16-22 at 250:1 molar ratio in a 1mM total peptide solution in CH_3CN:H_2O (2:3, v:v) with 0.1%TFA, nanotube assemblies are readily observed by TEM. The overall morphology of the co-assemblies appear identical to the Aβ(16-22) nanotubes by TEM and the fluorescence seen by two-photon excitation (Figure 7.1.a, excited at λ_{ex}=780nm) is homogeneously distributed across each nanotube. To test directly for co-assembly, Rh110 alone was shown not to bind to the Aβ(16-22) nanotubes (Figure 7.1.b).

The demonstration of light harvesting by the incorporated Rh16-22 requires energy transfer to adjacent chromophores (Miller 2007, Ma 2008). Taking advantage of the diagnostic Congo Red staining (Elghetany 1989) of amyloid nanotubes (Lu 2003, Mehta 2008), we explored the use of one of Rh110's FRET acceptors (Figure 7.1.c), Alexa 555 (A555), which maintains similar sulfate functionality on a planar aromatic nucleus. When mixed with mature Aβ(16-22) assemblies, A555 indeed homogenously decorated the nanotube structure with no apparent morphological distortion of the architecture (Figure 7.1.e, λ_{ex}=980nm). Likewise, when added to the Aβ(16-22)/Rh16-22 co-assembly, dye binding was also rapid and two photon fluorescence (data not shown) and lifetime imaging under the donor excitation wavelength (λ_{ex}=780nm) (Figure 7.1.f) was consistent with the binding to the intact nanotubes. As control, bound A555 is shown not to be excited efficiently at this wavelength (Figure 7.1.d).

Figure 7.1. Fluorescence imaging of donor and acceptor with Aβ(16-22) nanotubes.

(a) Aβ(16-22):Rh16-22 co-assembly (250:1 molar ratio, and λ_{ex}=780nm)

(b) Aβ(16-22) mature nanotubes with Rh110, (250:1 molar ratio, and λ_{ex}=780nm)

(c) Single-photon absorbance and emission of Rh110 and Alexa 555 in CH_3CN:H_2O (2:3, v:v) with 0.1% TFA

(d) Aβ(16-22) mature nanotubes with A555 (1000:1 molar ratio, λ_{ex}=780nm)

(e) Aβ(16-22) mature nanotubes with A555 (1000:1 molar ratio, λ_{ex}=980nm)

(f) Lifetime Image of Aβ(16-22):Rh16-22 fluorescence nanotubes (250:1 molar ratio, and λ_{ex}=780nm). Image scale=5μm

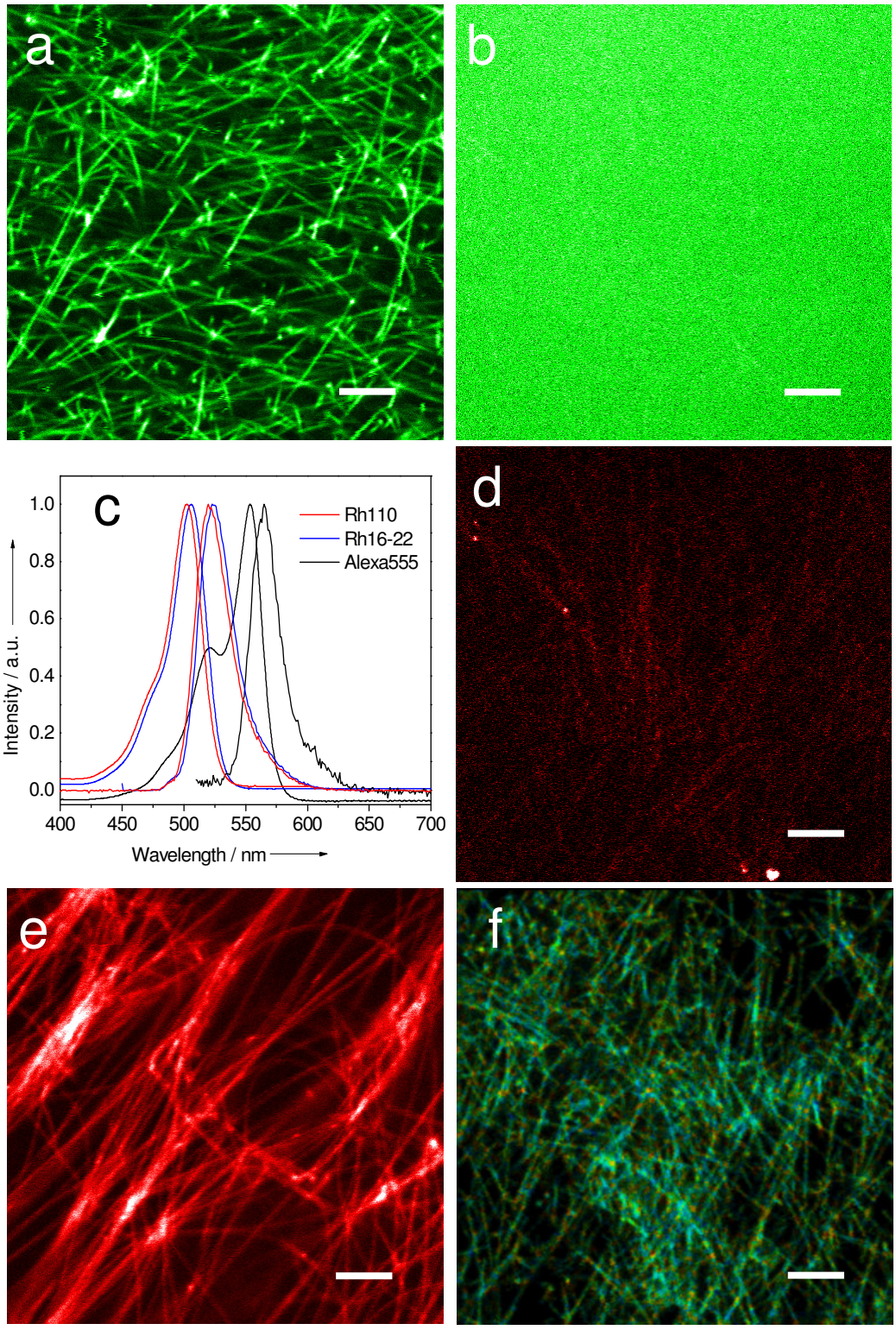
a
b
c
Rh110
Rh16-22
Alexa555
Intensity / a.u.
Wavelength / nm
1.0
0.8
0.6
0.4
0.2
0.0
400
450
500
550
600
650
700
d
e
f

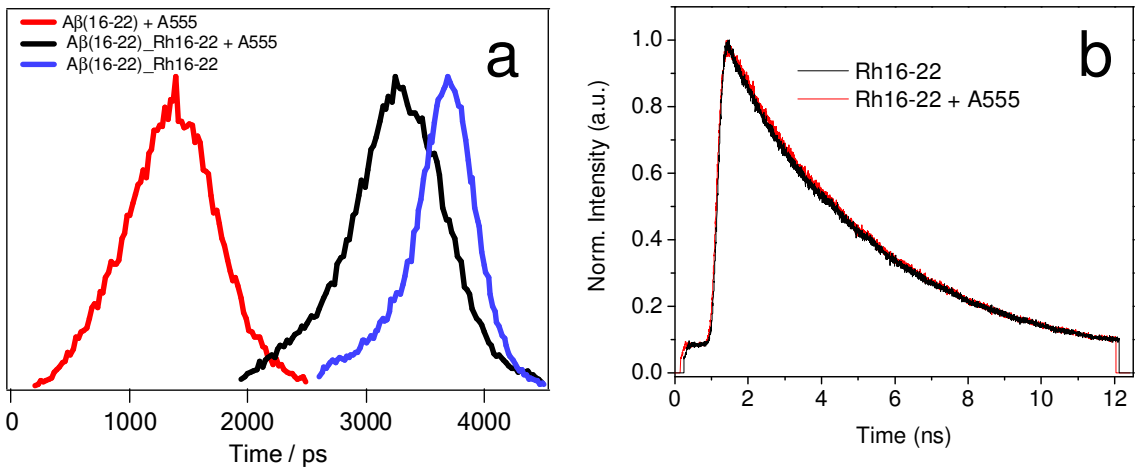

Figure 7.2. FRET lifetime analysis.

(a) Lifetime distribution of A555 (red) with mature Aβ(16-22) nanotubes, and Aβ(16-22):Rh16-22 fluorescence nanotubes in the presence (black) and absence (blue) of A555;

(b) Representative lifetime decays of Rh16-22 and a mixture of Rh16-22 and A555 in the absence of Aβ(16-22) nanotubes in CH_3CN:H_2O (2:3, v:v) with 0.1% TFA

Förster energy transfer efficiency with a single donor and acceptor has been assigned as inversely proportional to the sixth power of their separation (Meer 1994, Towles 2007), and for Rh110 and A555 the assigned Förster radius R_0 is 6.6 nm. However, this single distance model is not sufficient to describe a pattern of multiple donors and acceptors across the 2D surface (Dewey 1980, Corry 2005). Given the initial 250:1 concentration ratio of Aβ(16-22) and Rh16-22, and assuming minimal impact of the attached chromophore on peptide incorporation frequency, every 10 laminates (10nm) of 12 β-strands (12.5nm) should have a single Rh16-22 peptide. When this nanotube pattern is further layered with A555 at a 4X lower concentration,

the approximate spacing between the donor and acceptor is estimated to be on the order of 10nm. When A555 is added to mature co-assembled Aβ(16-22)/Rh16-22 nanotubes to give the A555/Rh16-22/Aβ(16-22) assembly at a 1:4:1000 ration with Aβ(16-22) at 0.5mM, the center of the Rh16-22 lifetime distribution shifts from 3.7 to 3.3ns (Figure 7.2.a). This corresponds to a FRET efficiency of 11%, calculated as 1-τ'/τ, where τ' is the Rh16-22 lifetime in the presence of A555, and τ is its lifetime in the absence (Wallrade 2005). Under these conditions, only minimal direct excitation of the A555 acceptor should occur (Figure 7.1.d) and account for less than 2% of the total signal in the FRET samples. To further rule out the influence of direct acceptor excitation on the measured FRET efficiency, we modeled what the average lifetime would be for the mixture of the two dyes with 2% of the total intensity arising from direct acceptor excitation when fit to a single exponential decay. The average fluorescence lifetime of Rh16-22 in Aβ(16-22) nanotubes is 3.7ns, and the average lifetime of A555 on Aβ(16-22) nanotubes is 1.3ns. For the peak A555 signal at 2% of the Rh110 signal, the lifetime would shift only to 3.6ns, significantly longer that the measured lifetime of 3.3ns. In addition, there is no energy transfer between Rh16-22 and A555 in solution when they are not co-assembled into Aβ(16-22) tubes (Figure 7.2.b). Preliminary experiments suggest indeed that a further increase the FRET efficiency can be achieved by increasing the ratio of the donor along the amyloid scaffold. Taken together, these results are most consistent with the functionalized Rh16-22 peptides being randomly incorporated as the Aβ(16-22) nanotubes assemble and demonstrate the light harvesting ability of this amyloid cross-β scaffold.

This demonstrated ability to assemble strong chromophores across the

paracrystalline amyloid network allows for precise ordering along the inner and outer compartment walls of an all protein nanotube. Given the dimensions of the array, it should now be possible to incorporate further molecular recognition elements, construct higher order arrays (Lu 2007), and even include elements for energy and electron separation reactions. Accordingly, this extension of amyloid self-assembly to more precise supramolecular arrays containing functional pigments provides a critical first step in constructing a self-assembling nanoscale scaffold for new bio-inspired antenna and photosynthetic devices.

Part II Exciton Coupling and Second Harmonic Generation in Amyloid Nanotube Sulfate Bundles

Aβ(16-22) tubes can be bundled in presence of sulfate (Lu 2007), and the bundles adopt macroscale lamellar arrays through protein salting out strategy. Aβ(16-22) congeners, V18I, V18terL, L17Abu, E22I, E22L, and E22V, also can be sulfate bundled, producing white precipitates. However, the macroscale array is not maintained when the tube diameter becomes larger. For example, L17Abu tubes are about 10 times larger than Aβ(16-22) tubes, and L17Abu tubes are deformed in sulfate bundles as shown in Figure 7.3.. Without sulfate addition, L17Abu tubes were not deformed, and have the morphology as cylinders. The Aβ(16-22) congener tubes have positive charges on the surface (Lu 2003), the tube bundles induced by sulfate possibly involve the neutralization of these charges.

Under two-photon excitation, the bundled tubes were observed to have optical signals (Figure 7.4.). In general, these signals were absence when the tubes were not bundled. L17Abu tube bundles however have stronger signals with higher intensity under the same excitation, and these signals are homogeneous distributed within L17Abu tube bundles. Without sulfates, the signals appeared as white dots along L17Abu tubes. For other sulfate bundles, such as V18I, E22V, and E22L, the optical signals are not homogeneously distributed. Their spectra (Figure 7.5.) suggest two types of signals: (i) second harmonic generation which appears at the half of the excitation wavelength, (ii) fluorescence centered at 530nm and 570nm. SHG is a nonlinear optical process, in which photons interact with a non-centrosymmetric material, and induce nonlinear polarization, resulting in the production of a coherent wave at exactly the twice of the incident photon

frequency (Campagnola 2003, Plotnikov 2006). The Aβ16-22) congener tubes are peptide assemblies, contain amino acid chiral centers. SHG observation is consistent with Aβ16-22) congener tubes are non-centrosymmetric materials. However, the fluorescence signals above 500nm are unexpected because the only chromophore within Aβ16-22) congener tubes is the phenylalanine aromatic side chain, although there are billions of them. In addition, the fluorescence signals of Aβ16-22) sulfate bundles are seemed to be excitation wavelength dependent. When the wavelength was increased to 820nm and above, the fluorescence at 570nm got stronger.

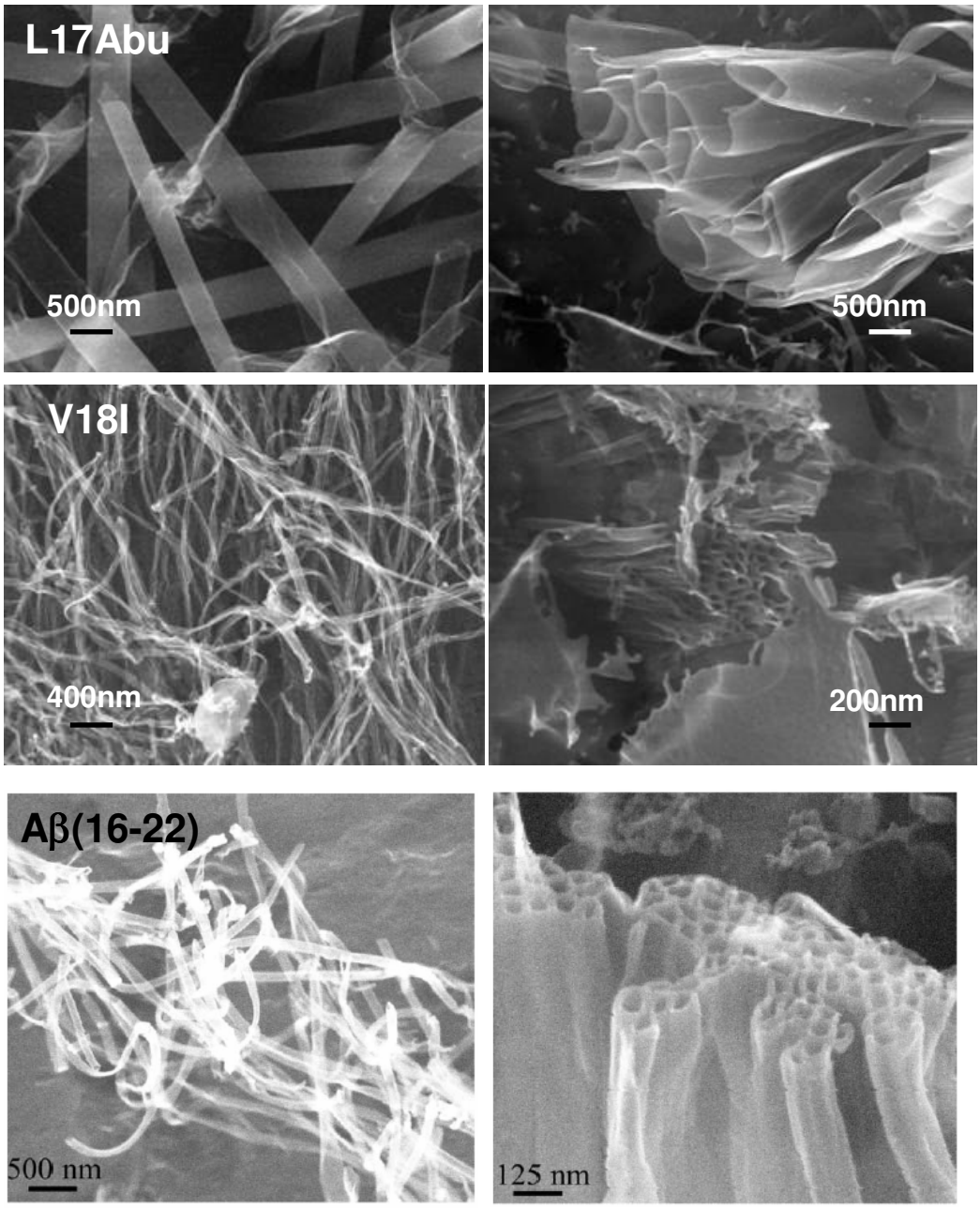

Figure 7.3. Cryo-SEM of sulfate bundled nanotubes

Cryo-SEM images of L17Abu and V18I nanotubes before (left) and after (right) sulfate bundling The bottom panels are the Aβ(16-22) nanotubes before (left) and after (right) sulfate bundling (Lu 2007).

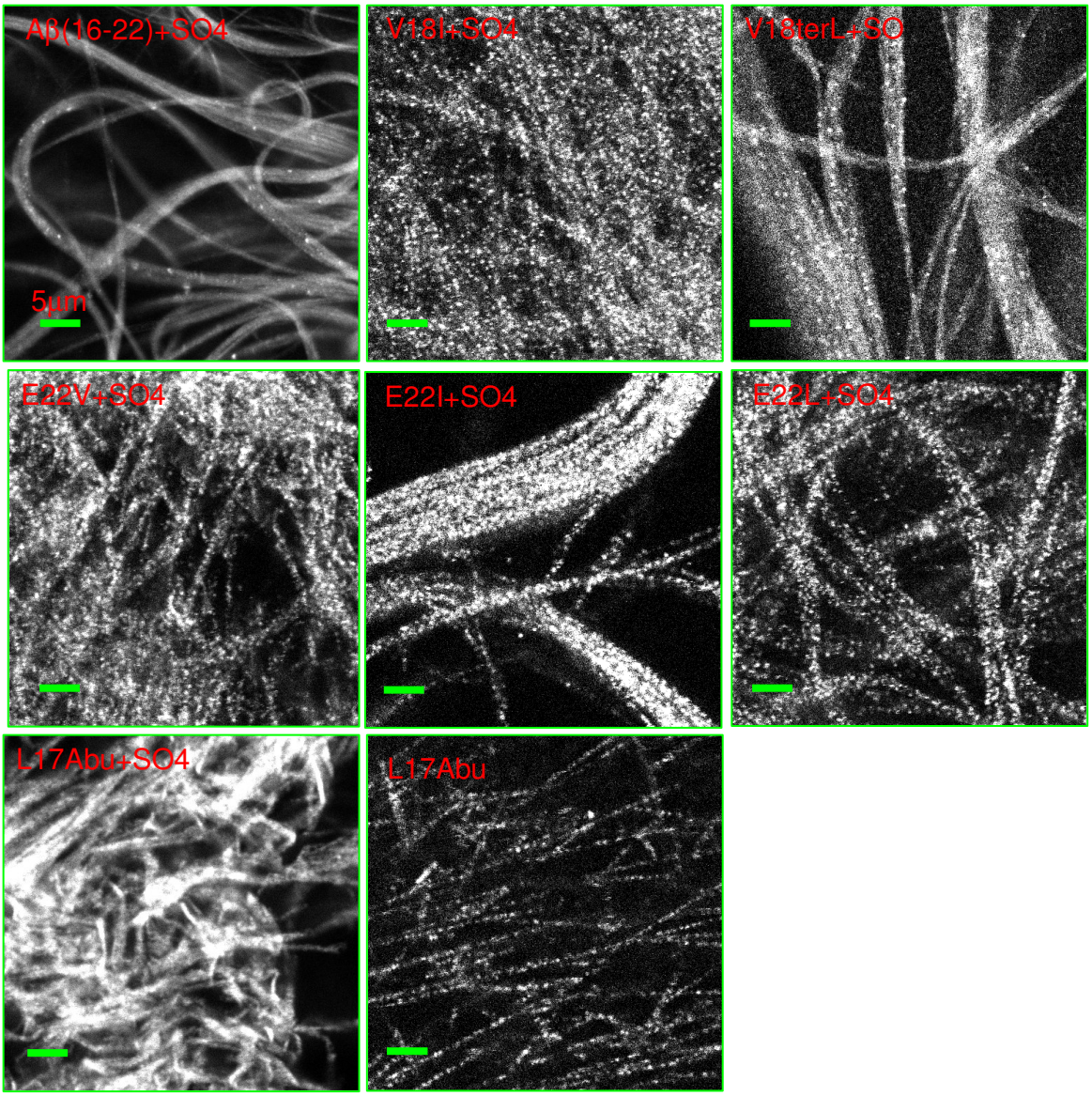

Figure 7.4. Optical signals of sulfate bundled Aβ(16-22) congener tubes under two-photon excitation.

Tube bundle precipitates were produced when Na_2SO_4 (18mM) were added to Aβ16-22) congener tubes (2mM) in 1:1 (v:v) ratio. The optical signals are from these tube bundle precipitates as shown above. In the absence of Na_2SO_4, only L17Abu tubes can generate the optical signals, but with weaker intensity comparing with L17Abu tube sulfate bundles. All the fluorescence images were acquired under 780nm excitation.

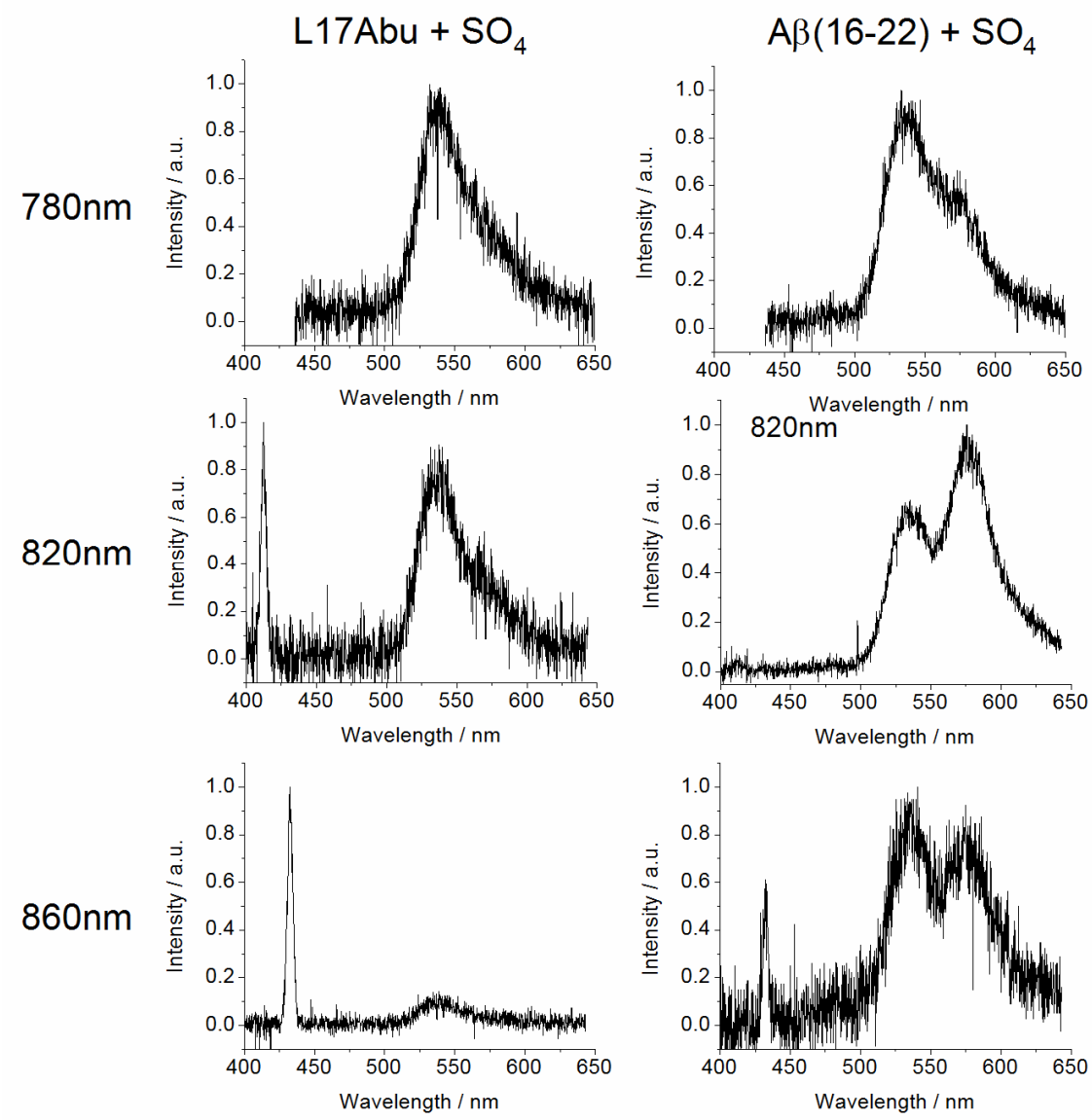

Figure 7.5. Spectra of fluorescence and SHG under two-photon excitation

L17Abu tube sulfate bundles (left) and Aβ16-22) tube sulfate bundles (right). The fluorescence and SHG spectra were acquired under excitation wavelengths, 780nm, 820nm, and 860nm.

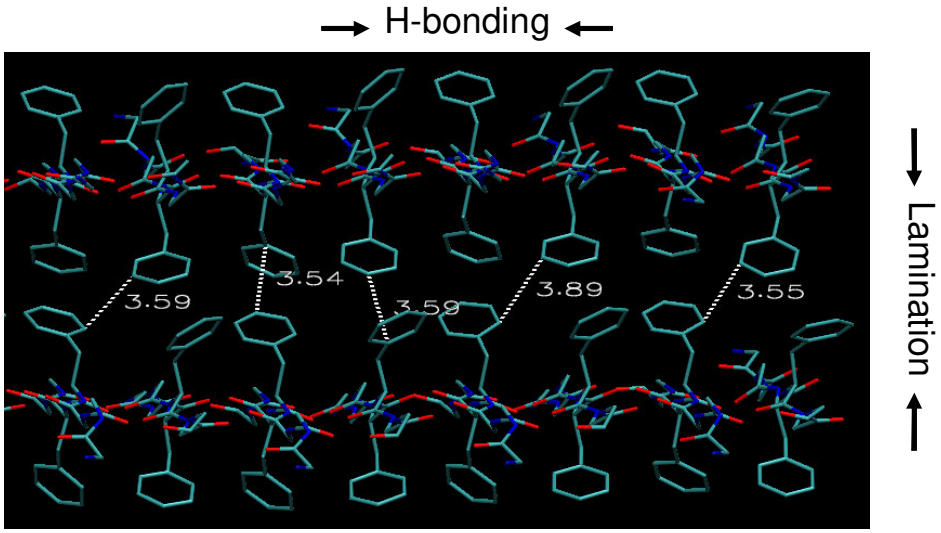

Figure 7.6. Phenylalanine stacking in the amyloid cross-β frame, in which β-strands are ~5Å apart in H-bonding dimension, and are ~10Å apart in the lamination dimension. As labeled above, the distance between adjacent phenylalanine aromatic rings is 3-4Å..

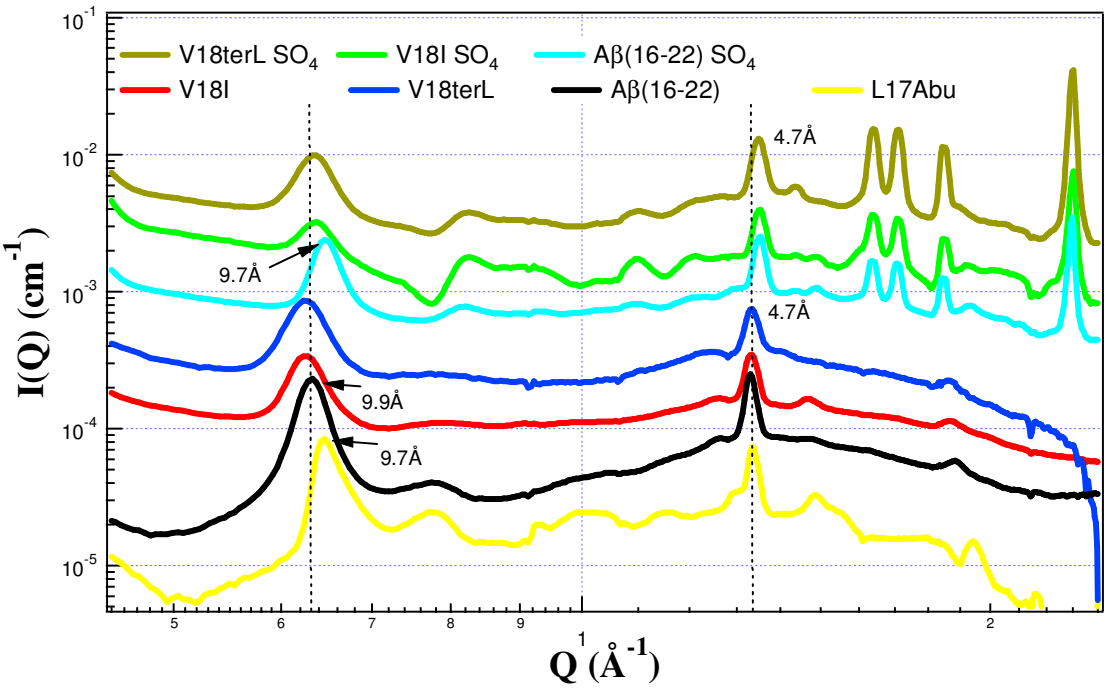

Figure 7.7. WASX of Aβ(16-22) congener tubes in presence and absence of sulfate bundling

The only chromophore in the tube bundles is phenylalanine, but the phenylalanine fluorescence is at 283nm under the UV excitation (265nm). The aromatic side chains of Aβ(16-22) are packed in the network as shown in Figure 7.6., and this phenylalanine side chain network resides within the tubes even without the sulfate bundling. However, except L17Abu, all other congener tubes without sulfate bundling do not produce the fluorescence under two-photon excitation. As shown in Figure 7.7., the sulfate bundling can decrease the lamination distance. For example, Aβ(16-22) bundled tubes have the lamination distance as 9.7Å, which is shorter than the lamination distance, 9.9Å, in absence of sulfate. Among all these Aβ(16-22) congener tubes, L17Abu tubes have the shortest lamination distance, 9.7Å, which is close to the lamination distance of Aβ(16-22) sulfate bundled tubes. The shorter lamination distance may be due to the size of side chains as described in Chapter 4. Abu has 2 carbon atoms in the side chain, which is much smaller than Leu17 (which has 4 carbon atoms in the side chain) in Aβ(16-22). terL in V18terL and Ile in V18I both are larger than V18 in Aβ(16-22), and they both have longer lamination distance (~10.1Å) than Aβ(16-22) tubes (9.9Å), and in the sulfate bundling their lamination distances did not decrease as much as Aβ(16-22) tubes. Therefore, the shorter lamination distance may be the reason that L17Abu tube sulfate bundles have stronger fluorescence signals, even without sulfate bundling. The distance dependence of the fluorescence signal suggests the distance dependence molecular coupling among the phenylalanine aromatic rings. The excitonic coupling can be resulted from direct Coulomb interactions, in which two dipoles are close proximity side by side, and their orientation and intermolecular distance determine dipole-dipole interaction decay, exhibiting chromophore absorption and emission wavelength shift (Freer 1996,

Rist 2002). Within the tubes, the phenylalanine aromatic rings are adjacent in the distance range of 3-4Å. The excitonic coupling can occur in this distance range.

The excitation of these sulfate bundled tubes is under two–photon excitation at 780nm. The energy level of phenylalanine absorption in solution (265nm, 4.68eV) is about three time of the energy of photons provided in excitation (780nm, 1.59eV). Excitonic coupling may occur when chromospheres are close, and their transition dipole moments start interacting with each other. These interactions can alter their absorption and luminescence properties. The phenylalanine networks within Aβ(16-22) congener tubes are continuous, and the transition dipolar coupling can be abundant. It is not quite clear how the phenylalanine electronic levels split under the transition dipolar coupling, but there is great chance the transition dipolar coupling generates lower energy state, and produces a red shift of absorption. This will allow the 780nm two-photon excitation. In addition, when increasing the excitation wavelengths, a red shifted emission appears at 570nm, 2.18eV for Aβ(16-22) tubes. This is consistent with energy level splitting under transition dipolar coupling (Rist 2002). However, this emission is absence for L17Abu tubes over all the applied excitation wavelengths. This indicates the distance sensitivity of these optical interactions.

The optical signals generated by Aβ(16-22) congener tubes are from intrinsic aromatic amino acid packing in their amyloid scaffold. The excitonic coupling among phenylalanine provides another potential of Aβ(16-22) congener tubes to be used in optical devices.

CHAPTER 8

CONCLUSION AND PERSPECTIVES

Protein folding is a basic process of life, by which newly synthetic proteins fold into specific three-dimensional structure with biological functions. The aggregation of misfolded proteins prevents protein functionalism, and can result in fatal diseases. Understanding the mechanism of protein folding, preventing misfolding and aggregation has always been the major focus in biochemistry. Amyloid is characteristic of insoluble fibril protein aggregates, and carries the cross-β spine. The folding process of synthesized amino acid chains into functional three-tensional structures depends on both the intrinsic amino acid sequences and the vacillating cellular environment. The protein or peptide amyloid assembly is also amino acid sequence orientated in a particular condition, especially in the amyloid early nucleation which is viewed as the critical steps in determining amyloid assembly. The energetically favorable state for a given amino acid

chain in a given condition is determined by the binding or packing preference for each amino acid residue, and therefore can determine the protein folding or assembly. Determining the factors which contribute to the polypeptide association is critical to unveil the mechanism of protein folding and assembly.

In this dissertation, a few model systems were generated to determine the factors which contribute to the binding and packing of the amino acid sequences in Aβ(16-22) amyloid assembly. Aβ(16-22) can form soluble amyloid fibers or tubes under distinct conditions. The resulting soluble amyloid makes these model systems easy to handle, and applicable to structural investigation. Congeners of Aβ(16-22) are generated by modifying the L17 and V18 side chains with Leu and Val analogs. The structural changes among these congeners are significant, differing in β-sheet orientation, β-sheet registry, and β-sheet lamination, to give either fiber or tube morphologies. Specific factors have been identified which determine the side chain interactions, and dictate the cross-β arrangement. For example, the preference of side chain cross-strand pairing in adjacent β-strands can shift the β-sheet registry from antiparallel in-register β-sheet to antiparallel one-residue-shifted one. Also, conformational entropy can destabilize the sheet-sheet stacking, and reduce the number of laminants. Finally, the predominant side chain packing can determine the β-strand orientation. Overall, the correlation of the side chain interactions and the backbone H-bonding suggests an early desolvation event in the amyloid assembly. The desolvation event, a critical feature in the hydrophobic collapse, implies that protein misfolding, particularly in aggregated assemblies like the amyloid assembly, follows a similar pathway like protein folding.

In the fluorescence imaging of the co-assembled Aβ(16-22)/Rh17-22 system, large aggregates (2~8μm) containing molten globular properties were observed. The large aggregates do not have amyloid signatures, but Aβ(16-22) tubes can grow from the inside of these aggregates. The nucleation event occurs inside these aggregates, and no traditional oligomerized intermediates are observed during Aβ(16-22) assembly. The oligomer intermediate of amyloid assembly is still under debate for being the on or off pathway species, and their characters in term of size and shape, and roles in amyloid assembly are elusive. While amyloid nucleation produces the first amyloid repeating structural unit, the size or shape of the early polypeptide molten aggregate might not be critical. The early stage of amyloid assembly requires desolvation. The early polypeptide accumulation should be sufficient to drive away water and provide the environment for the amyloid nuclei to form. The formation of large aggregates observed in Aβ(16-22) assembly appears to occur through hydrophobic collapse, and the mechanism of amyloid assembly identified here reveals the common feature of protein folding is shared in amyloid assembly. The trademark difference between the protein folding leading to the cellular functions and the amyloid assembly leading to diseased cell deaths may be the polypeptide accumulation to initiate amyloid assembly, rather than polypeptide single chain evolving in protein folding. This has been recognized in many neurodegenerative diseases that a symptom along with the diseases is over-production of the target proteins. Removing or blocking the protein accumulation can be an option to block the amyloid pathological pathway.

Amyloid cross-β scaffold provides a unique structural frame with controlled molecular interactions to incorporate functional groups. In this dissertation, fluorescence

functional groups were fabricated into Aβ(16-22) nanotubes to mimic light harvesting antenna. Förster energy transfer along the nanotube surface has been demonstrated to self-coded acceptor dyes, confirming a critical first step in constructing a self-assembling nanoscale scaffold for new bio-inspired antenna and photosynthetic devices. Furthermore, the excitonic coupling was observed among the intrinsic aromatic amino acid packing in the sulfate induced Aβ(16-22) congener tube bundles, which provides another advantage of amyloid assembly scaffold to generate optical devises.

REFERENCES

Ambroggio, E. E., Kim, D. H., Separovic, F., Barrow, C. J., Barnham, K. J., Bagatolli, L. A., and Fidelio, G. D. (2005) Surface Behavior and Lipid Interaction of Alzheimer β-Amyloid Peptide 1–42: A Membrane-disrupting Peptide. *Biophys. J. 88*, 2706–2713.

Antzutkin, O. N., Leapman, R. D., Balbach, J. J., and Tycko, R. (2002) Supramolecular Structural Constraints on Alzheimer's β-Amyloid Fibrils from Electron Microscopy and Solid-State Nuclear Magnetic Resonance. *Biochemistry 41*, 15436-15450.

Arora, A., Ha, C., and Park, C. B. (2004) Protein Folding under Extreme Temperatures Insulin Amyloid Fibrillation at above 100°C: New Insights into Protein Folding under Extreme Temperatures. *Protein Sci. 13*, 2429–2436.

Auer, S., Dobson, C. M., and Vendruscolo, M. (2007) Characterization of the Nucleation Barriers for Protein Aggregation and Amyloid Formation. *HFSP J. 1*, 137-146.

Avbelj, F., and Baldwin, R. L. (2002) Role of Backbone Solvation in Determining Thermodynamic β Propensities of the Amino Acids. *Proc. Nat. Acad. Sci. U.S.A. 99*, 1309–1313.

Ban, T., Yamaguchi, K., and Goto, Y. (2006) Direct Observation of Amyloid Fibril Growth, Propagation, and Adaptation. *Acc. Chem. Res. 39*, 663–670.

Baskakov, I. V., Legname, G., Baldwin, M. A., Prusiner, S. B., and Cohen, F. E. (2002) Pathway Complexity of Prion Protein Assembly into Amyloid. *J. Biol. Chem.* 21140-21148.

Benzinger, T. L. S., Gregory, D. M., Burkoth, T. S., Miller-Auer, H., Lynn, D. G., Botto, R. E., and Meredith, S. C. (1998) Propagating Structure of Alzheimer's β-amyloid(10-35) is Parallel β-sheet with Residues in Exact Register *Proc. Natl. Acad. Sci. USA 95*, 13407–13412.

Blaber, M., Zhang, X. J., and Matthews, B. W. (1993) Structural Basis of Amino Acid α-helix Propensity. *Science 260*, 1637–1640.

Blake, C., and Serpell, L. (1996) Synchrotron X-ray Studies Suggest that the Core of the Transthyretin Amyloid Fibril is a Continuous β-sheet helix. *Structure 4*, 989-998.

Bossy-Wetzel, E., Schwarzenbacher, R., and Lipton, S. A. (2004) Moelcular Pathways to Neurodegeneration. *Nat. Med. Neurodegeneration*, S2-S9.

Bowers, K. J., Chow, E., Xu, H., Dror, R. O., Eastwood, M. P., Gregersen, B. A., Klepeis, J. L., Kolossváry, I., Moraes, M. A., Sacerdoti, F. D., Salmon, J. K., Shan, Y., and Shaw, D. E. (2006) Scalable Algorithms for Molecular Dynamics Simulations on Commodity Clusters," in *Proceedings of the ACM/IEEE Conference on Supercomputing (SC06)*, Tampa, Florida.

Buxbaum, J. N. (2003) Diseases of Protein Conformation: What do in vitro Experiments Tell us about in vivo Ddiseases? *Trends Biochem. Sci. 28*, 585-592.

Campagnola, P., and Mohler, W. A. (2003) Nonlinear Optical Spectroscopy And Imaging of Structural Proteins in Living Tissues. *Opt. Photonics News*, 40-45.

Cannon, M. J., Williams, A. D., Wetzel, R., and Myszka, D. G. (2004) Kinetic Analysis of β-amyloid Fbril Elongation. *Anal. Biochem. 328*, 67–75.

Carrotta, R., Carlo, M. D., Manno, M., Montana, G., Picone, P., Romancino, D., and Biagio, P. L. S. (2006) Toxicity of Recombinant ß-amyloid Prefibrillar Oligomers on the Morphogenesis of the Sea Urchin Paracentrotus Lividus. *FASEB J. 20*, 1916-1917.

Chari, K., Seo, Y.-S., and Satija, S. (2004) Competitive Adsorption at the Air−Water Interface from a Self-Assembling Polymer-Surfactant Mixture. *J. Phys. Chem. B 108*, 11442-11446.

Chen, J., Bryngelson, J. D., and Thirumalai, D. (2008) Estimations of the Size of Nucleation Regions in Globular Proteins. *J. Phys. Chem. B 112*, 16115-16120.

Chen, S., Ferrone, F. A., and Wetzel, R. (2002) Huntington's Disease Age-of-onset Linked to Polyglutamine Aggregation Nucleation. *Proc. Natl. Acad. Sci. USA 99*, 11884-11889.

Chou, P. Y., and Fasman, G. D. (1974) Conformational Parameters for Amino Acids in α-helical, β-sheet, and Random Coil Regions Calculated from Proteins. *Biochemistry 13*, 211–222.

Colby, D. W., Zhang, Q., Wang, S., Groth, D., Legname, G., Riesner, D., and Prusiner, S. B. (2007) Prion Detection by an Amyloid Seeding Assay. *Proc. Natl. Acad. Sci. USA 104*, 20914–20919.

Collins, S. R., Douglass, A., Vale, R. D., and Weissman, J. S. (2004) Mechanism of Prion Propagation: Amyloid Growth Occurs by Monomer Addition. *PLoS Biol. 2*, e321-e321.

Come, J. H., Fraser, P. E., and Lansbury, P. T. (1993) A Kinetic Model for Amyloid Formation in the Prion Diseases: Importance of Seeding. *Proc. Natl. Acad. Sci. USA 90*, 5959-5963.

Congdon, E. E., Kim, S., Bonchak, J., Songrug, T., Matzavinos, A., and Kuret, J. (2008) Nucleation-dependent Tau Filament Formation. *J. Biol. Chem. 283*, 13806-13816.

Corry, B., Jayatilaka, D., and Rigbyy, P. (2005) A Flexible Approach to the Calculation of Resonance Energy Transfer Efficiency between Multiple Donors and Acceptors in Complex Geometries. *Biophys. J. 89*, 3822–3836.

Crick, S. L., Jayaraman, M., Frieden, C., Wetzel, R., and Pappu, R. V. (2006) Fluorescence Correlation Spectroscopy Shows that Monomeric Polyglutamine Molecules form Collapsed Structures in Aqueous Solutions. *Proc. Natl. Acad. Sci. USA 103*, 16764–16769

Daidone, I., Ulmschneider, M. B., Nola, A. D., Amadei, A., and Smith, J. C. (2007) Dehydration-driven Solvent Exposure of Hydrophobic Surfaces as a Driving Force in Peptide Folding. *Proc. Natl. Acad. Sci. USA 104*, 15230–15235.

Decatur, S. M. (2006) Elucidation of Residue-Level Structure and Dynamics of Polypeptides via Isotope-Edited Infrared Spectroscopy. *Acc. Chem. Res. 39*, 169-175.

Dewey, T. G., and Hammes, G. G. (1980) Calculation of Fluorescence Resonance Energy Transfer on Surface *Biophys. J. 32* 1023-1036.

Ding, J. W., Yan, X. H., Cao, J. X., Wang, D. L., Tang, Y., and Yang, Q. B. (2003) Curvature and Strain Effects on Electronic Properties of Single-wall Carbon Nanotubes. *J. Phys.: Condens. Matter 15*, L439–L445.

Dinner, A. R., Andrej Sali, Smith, L. J., Dobson, C. M., and Karplus, M. (2000) Understanding Protein Folding via Free-energy Surfaces from Theory and Experiment. *Trends in Biochem. Sci. 25*, 331-339.

Dobson, C. M. (2003) Protein Folding and Misfolding. *Nature 426*, 884-890.

Dobson, C. M. (2004) Experimental Investigation of Pprotein Folding and Misfolding. *Methods 34*, 4-14.

Doig, A. J., and Sternberg, M. J. (1995) Side-chain Conformational Entropy in Protein Folding. *Protein Sci. 4*, 2247-2251.

[1]Dong, J., Lu, K., Lakdawala, A., Mehta, A. K., and Lynn, D. (2006) Controlling Amyloid Growth in Multiple Dimensions. *Amyloid 13*, 206-215.

[2]Dong, J., Shokes, J. E., Scott, R. A., and Lynn, D. G. (2006) Modulating Amyloid Self-Assembly and Fibril Morphology with Zn(II). *J. Am. Chem. Soc. 128*, 3540-3542.

Dzwolak, W., Grudzielanek, S., Smirnovas, V., Ravindra, R., Nicolini, C., Jansen, R., Loksztejn, A., Porowski, S., and Winter, R. (2005) Ethanol-Perturbed Amyloidogenic Self-Assembly of Insulin: Looking for Origins of Amyloid Strains. *Biochemistry 44*, 8948-8958.

Dzwolak, W., Ravindrab, R., and Winter, R. (2004) Hydration and structure-the two sides of the insulin aggregation process. *Phys. Chem. Chem. Phys. 6*, 1938-1943.

Elghetany, M. T., Saleem, A., and Barr, K. (1989) The Congo Red Stain Revisited. *Ann. Clin. Lab. Sci. 19*, 190-195.

Elliott, A., Ambrose, E. J., and Robinson, C. (1950) Chain Configurations in Natured and Denatured Insulin: Evidence from Infra-red Spectra. *Nature 166*, 194-195.

Esler, W. P., Stimson, E. R., Jennings, J. M., Vinters, H. V., Ghilardi, J. R., Lee, J. P., Mantyh, P. W., and Maggio, J. E. (2000) Alzheimer's Disease Amyloid Propagation by a Template-Dependent Dock-Lock Mechanism. *Biochemistry 39*, 6288-6295.

Fandrich, M., Fletcher, M. A., and Dobson, C. M. (2001) Amyloid Ffibrils from Muscle Myoglobin. *Nature 410*, 165-166.

Farber, P. J., and Mittermaier, A. (2008) Side Chain Burial and Hydrophobic Core Packing in Protein Folding Transition States. *Protein Sci. 17*, 644-651.

Fasman, G. D. (1996) Circular Dichroism and the Conformational Analysis of Biomolecules, Plenum Press, New York.

Fernandez, A., Kardos, J., and Goto, Y. (2003) Protein Folding: Could Hydrophobic Collapse be Coupled with Hydrogen-bond Formation? *FEBS Lett. 536*, 187-192.

Fernandez, A., Sosnick, T. R., and Colubri, A. (2002) Dynamics of Hydrogen Bond Desolvation in Protein Folding. *J. Mol. Biol. 321*, 659–675.

Fernandez-Escamilla, A.-M., Rousseau, F., Schymkowitz, J., and Serrano, L. (2004) Prediction of Sequence-dependence and Mutational Effects on the Aggregation of Peptides and Proteins. *Nat. Biotechnol. 22*, 1302-1306.

Freer, A., Prince, S., Sauer, K., Papiz, M., Lawless, A. H., McDermott, G., Cogdell, R., and Isaacs, N. W. (1996) Pigment–pigment Interactions and Energy Transfer in the Antenna Complex of the Photosynthetic Bacterium Rhodopseudomonas Acidophila. *Structure 4*, 449-462.

Freire, F., Fisk, J. D., Peoples, A. J., Ivancic, M., Guzei, I. A., and Gellman, S. H. (2008) Diacid Linkers That Promote Parallel β-Sheet Secondary Structure in Water. *J. Am. Chem. Soc 130*, 7839-7841.

Gailer, C., and Feigel, M. (1997) Is the Parallel or Antiparallel β-sheet More Stable? A Semiempirical Study. *J. Comput. Aided Mol. Des. 11*, 273–277.

Gao, X., and Matsui, H. (2005) Peptide-Based Nanotubes and Their Applications in Bionanotechnology. *Adv. Mater. 17*, 2037-2050.

Gellman, S. H. (1998) Minimal Model Systems for β-sheet Secondary Structure in Proteins. *Curr. Opin. Chem. Biol. 2*, 717-725.

Ghadiri, M. R., Granja, J. R., Milligan, R. A., McRee, D. E., and Khazanovich, N. (1993) Self-assembling Organic Nanotubes Based on a Cyclic Peptide Architecture. *Nature 366*, 324 - 327

Gilead, S., and Gazit, E. (2005) Self-organization of Short Peptide Fragments: From Amyloid Fibrils to Nanoscale Supramolecular Assemblies. *Supermol. Chem. 17*, 87-92.

Gordon, D. J., Balbach, J. J., Tycko, R., and Meredith, S. C. (2004) Increasing the Amphiphilicity of an Amyloidogenic Peptide Changes the β-Sheet Structure in the Fibrils from Antiparallel to Parallel, *Biophys. J. 86*, 428-434.

Gorman, P. M., Yip, C. M., Fraser, P. E., and Chakrabartty, A. (2003) Alternate Aggregation Pathways of the Alzheimer β-Amyloid Peptide: Aβ Association Kinetics at Endosomal pH. *J. Mol. Biol. 325*, 743-757.

Gosal, W. S., Morten, I. J., Hewitt, E. W., Smith, D. A., Thomson, N. H., and Radford, S. E. (2005) Competing Pathways Determine Fibril Morphology in the Self-assembly of β2-Microglobulin into Amyloid. *J. Mol. Biol. 351*, 850-864.

Haass, C., and Selkoe, D. J. (2007) Soluble Protein Oligomers in Neurodegeneration: Lessons from the Alzheimer's Amyloid β-peptide. *Nat Rev Mol Cell Biol. 8*, 101-112.

Habicht, G., Haupt, C., Friedrich, R. P., Hortschansky, P., Sachse, C., Meinhardt, J., Wieligmann, K., Gellermann, G. P., Brodhun, M., Gotz, J., Halbhuber, K.-J., Rocken, C., Horn, U., and Fandrich, a. M. (2007) Directed Selection of a Conformational Antibody Domain that Prevents Mature Amyloid Fibril Formation by Stabilizing Aβ Protofibrils. *Proc. Natl. Acad. Sci. USA 104*, 19232-19237.

Halverson, K. J., Sucholeiki, I., Ashburn, T. T., and Lansbury, P. T. J. (1991) Location of β-Sheet-Forming Sequences in Amyloid Proteins by FTIR. *J. Am. Chem. Soc. 113*, 6701-6703.

Hamada, D., Yanagihara, I., and Tsumoto, K. (2004) Engineering Amyloidogenicity towards the Development of Nanofibrillar Mmaterials. *Trends Biotechnol. 22*, 93-97.

Harper, J. D., and Peter T. Lansbury, J. (1997) Models of Amyloid Seeding in Alzheimer's Disease and Scrapie: Mechanistic Truths and Physiological Consequences of the Time-dependent Solubility of Amyloid Proteins. *Annu. Rev. Biochem. 66*, 386-407.

Haustein, E., and Schwille, P. (2003) Ultrasensitive Investigations of Biological Systems by Fluorescence Correlation Spectroscopy. *Methods 29*, 153–166.

Hendsch, Z. S., and Tidor, B. (1994) Do Salt Bridges Sstabilize Proteins? A Continuum Electrostatic Analysis. *Protein Sci. 3*, 211-226.

Hess, S., Lindquist, S. L., and Scheibel, T. (2007) Alternative Assembly Pathways of the Amyloidogenic Yeast Prion Determinant Sup35–NM. *EMBO Rep. 8*, 1196-1201.

[1]Hiramatsu, H., Goto, Y., Naiki, H., and Kitagawa, T. (2005) Structural Model of the Amyloid Fibril Formed by β2-Microglobulin #21-31Fragment Based on Vibrational Spectroscopy. *J. Am. Chem. Soc 127*, 7988-7989.

[2]Hiramatsu, H., and Kitagawa, T. (2005) FT-IR Approaches on Amyloid Fibril Structure. *Biochim. Biophys. Acta 1753*, 100 – 107.

Holmes, T. C., Lacalle, S. d., Su, X., Liu, G., Rich, A., and Zhang, S. (2000) Extensive Neurite Outgrowth and Active Synapse Formation on Self-assembling Peptide Scaffolds. *Proc. Natl. Acad. Sci. USA 97*, 6728–6733

Honig, B., and Nicholis, A. (1995) Claasical Electrostatics in Biology and Chemistry. *Science 268*, 1144-1149.

Horovitz, A., Matthews, J. M., and Fersht, A. R. (1992) α-Helix Stability in Proteins. II. Factors that Influence Stability at an Internal Position. *J.Mol. Biol. 227*, 560–568.

Hurshman, A. R., White, J. T., Powers, E. T., and Kelly, J. W. (2004) Transthyretin Aggregation under Partially Denaturing Conditions Is a Downhill Polymerization. *Biochemistry 43*, 7365-7381.

Hutchinson, E. G., Sessions, R. B., Thornton, J. M., and Woolfson, D. N. (1998) Determinants of Strand Register in Antiparallel β-sheet of Protein. *Protein Sci. 7*, 2287-2300.

Hwang, W., Zhang, S., Kamm, R. D., and Karplus, M. (2004) Kinetic Control of Dimer Structure Formation in Amyloid Fibrillogenesis. *Proc. Natl. Acad. Sci. USA 101*, 12916–12921.

Iijima, S. (1991) Helical Microtubules of Graphitic Carbon. *Nature 354*, 56 - 58.

Iijima, S., and Ichihashi, T. (1993) Single-shell Carbon Nanotubes of 1-nm Diameter. *Nature 363*, 603 - 605.

Ikebe, J., Kamiya, N., Ito, J.-I., Shindo, H., and Higo, J. (2007) Simulation Study on the Disordered State of an Alzheimer's β Amyloid Peptide Aβ(12–36) in Water Consisting of Random-structural, β-structural, and Helical Clusters. *Protein Sci. 16*, 1596–1608.

Jang, S., and Shin, S. (2008) Computational Study on the Structural Diversity of Amyloid Beta Peptide (Aβ10-35) Oligomers. *J. Phys. Chem. B 112*, 3479-3484.

Jarrett, J. T., and Peter T. Lansbury, J. (1993) Seeding "One-dimensional Crystallization" of Amyloid: A Pathogenic Mechanism in Alzheimer's Disease and Scrapie? . *Cell 73*, 1055-1058

Jones, E. M., and Surewicz, W. K. (2005) Fibril Conformation as the Basis of Species and Strain-Dependent Seeding Specificity of Mammalian Prion Amyloids. *Cell 121*, 63-72.

Juszczyk, P., Kołodziejczyk, A. S., and Grzonka, Z. (2005) Circular Dichroism and Aggregation Studies of Amyloid β (11–28) Fragment and its Variants. *Acta Biochim. Pol. 52*, 425–431.

Kardos, J. z., Yamamoto, K., Hasegawa, K., Naiki, H., and Goto, Y. (2004) Direct Measurement of the Thermodynamic Parameters of Amyloid Formation by Isothermal Titration Calori. *J. Bio. Chem 279*, 55308–55314.

Kayed, R., Bernhagen, J., Greenfield, N., Sweimeh, K., Brunner, H., Voelter, W., and Kapurniotu, A. (1999) Conformational Transitions of Islet Amyloid Polypeptide (IAPP) in Amyloid Formation in vitro. *J. Mol. Biol. 287*, 781-796.

Kayed, R., Head, E., Thompson, J. L., McIntire, T. M., Milton, S. C., Cotman, C. W., and Glabe, C. G. (2003) Common Structure of Soluble Amyloid Oligomers Implies Common Mechanism of Pathogenesis. *Science 300*, 486 - 489.

Kaylor, J., Bodner, N., Edridge, S., Yamin, G., Hong, D.-P., and Fink, A. L. (2005) Characterization of Oligomeric Intermediates in α-Synuclein Fibrillation: FRET Studies of Y125W/Y133F/Y136F α-Synuclein. *J. Mol. Biol. 353*, 357-372.

Khazanovich, N., Granja, J. R., McRee, D. E., Milligan, R. A., and Ghadiri, M. R. (1994) Nanoscale Tubular Ensembles with Specified Internal Diameters. Design of a Self-Assembled Nanotube with a 13-ANG. Pore *J. Am. Chem. Soc. 116*, 6011-6012.

Kim, C. A., and Berg, J. M. (1993) Thermodynamic β-sheet Propensities Measured Using a Zinc-finger Host Peptide. *Nature 362*, 267–270.

Kim, W., and Hecht, M. H. (2006) Generic Hydrophobic Residues Are Sufficient to Promote Aggregation of the Alzheimer's Aβ42 Peptide. *Proc. Natl. Acad. Sci. USA 103*, 15824–15829.

Kirkitadze, M. D., Condron, M. M., and Teplow, D. B. (2001) Identification and Characterization of Key Kinetic Intermediates in Amyloid β-protein Fibrillogenesis. *J. Mol. Biol. 312*, 1103-1119.

Kiuchi, Y., Isobe, Y., Fukushima, K., and Kimura, M. (2002) Disassembly of Amyloid β-Protein Fibril by Basement Membrane Components. *Life Sci. 70*, 2421-2431.

Kodama, H., Matsumura, S., Yamashitaa, T., and Mihara, H. (2004) Construction of a Protein array on Amyloid-like Fibrils Using Co-assembly of Designed Peptides. *Chem. Commun.* 2876-2877.

Kubelka, J., and Keiderling, T. A. (2001) The Anomalous Infrared Amide I Intensity Distribution in ^{13}C Isotopically Labeled Peptide β-sheets Comes from Extended, Multiple-stranded Structures, An ab initio Study. *J. Am. Chem. Soc. 123*, 6142-6150.

Kumar, S., and Nussinov, R. (2002) Close-range Elctrostatic Interactions in Proteins. *ChemBioChem 3*, 604-617.

Laidman, J., Forse, G. J., and Yeates, T. O. (2006) Conformational Change nad Assembly through Edge β Strands in Transthyretin and Other Amyloid Proteins. *Acc. Chem. Res. 39*, 576-583.

Lakdawala, A., Wang, M., Nevins, N., Liotta, D. C., Rusinska-Roszak, D., Lozynski, M., and Snyder, J. P. (2001) Calculated Conformer Eenergies for Organic Molecules with Multiple Polar Functionalities Are Method Dependent: Taxol (case study). *BMC Chem. Biol. 1*, 2.

Lakdawala, A. S., Morgan, D. M., Liotta, D. C., Lynn, D. G., and Snyder, J. P. (2002) Dynamics and Fluidity of Amyloid Fibrils: A Model of Fibrous Protein Aggregates. *J. Am. Chem. Soc. 124*, 15150-15151.

Lambert, M. P., Viola, K. L., Chromy, B. A., Chang, L., Morgan, T. E., Yu, J., Venton, D. L., Krafft, G. A., Finch, C. E., and Klein, W. L. (2001) Vaccination with Soluble Aβ Oligomers Generates Toxicity-neutralizing Antibodies. *J Neurochem. 7*, 595-605.

Lazar, G. A., Desjarlais, J. R., and Handel, T. M. (1997) De novo Design of the Hydrophobic Core of Ubiquitin. *Protein Sci. 6*, 1167-1178.

Lesser, G. J., and Rose, G. D. (1990) Hydrophobicity of Amino Acid Subgroups in Proteins. *PROTEINS: Structure, Function, and Genetics 8*, 6-13.

Li, L.-s., Jiang, H., Messmore, B. W., Bull, S. R., and Stupp, S. I. (2007) A Torsional Strain Mechanism To Tune Pitch in Supramolecular Helices. *Angew. Chem. Int. Ed. 46*, 5873 –5876.

[1]Liang, Y., Guo, P., Pingali, S. V., Pabit, S., Thiyagarajan, P., Berland, K. M., and Lynn, D. G. (2008) Light Harvesting Antenna on an Amyloid Scaffold. *Chem. Commun.* 6522 - 6524.

[2]Liang, Y., Pingali, S. V., Jogalekar, A. S., Snyder, J. P., Thiyagarajan, P., and Lynn, D. G. (2008) Cross-Strand Pairing and Amyloid Assembly. *Biochemistry 47*, 10018-10026.

Lin, J.-M., Lina, T.-L., and Jeng, U.-S. (2007) Time-resolved Grazing-incidence Small-angle X-ray Scattering Studies of Lipid Multibilayers with the Insertion of Amyloid Peptide during the Swelling Process. *J. Appl. Cryst. 40*, s367–s372.

Liu, P., Ni, R., Mehta, A. K., Childers, W. S., Lakdawala, A., Pingali, S. V., Thiyagarajan, P., and Lynn, D. G. (2008) Nucleobase-Directed Amyloid Nanotube Assembly. *J. Am. Chem. Soc. 130*, 16867-16869.

Lomakin, A., Chung, D. S., Benedek, G. B., Kirschner, D. A., and Teplow, D. B. (1996) On the Nucleation and Growth of Amyloid β-protein Fibrils: Detection of Nuclei and Quantitation of Rate Constants. *Proc. Natl. Acad. Sci. USA 93*, 1125–1129.

Lomakin, A., Teplow, D. B., Kirschner, D. A., and Benedek, G. B. (1997) Kinetic Theory of Fibrillogenesis of Amyloid β-protein. *Proc. Natl. Acad. Sci. USA 94*, 7942–7947.

Lu, K. (2006) Discovery of Diverse Peptide Nanotube Architecture from the Self-Assembly of Designed Amyloid-beta Cassettes, in *Chemistry* pp 232, Emory University, Atlanta, Ga.

Lu, K., Guo, L., Mehta, A. K., Childers, W. S., Dublin, S. N., Skanthakumar, S., Conticello, V. P., Thiyagarajan, P., Apkarian, R. P., and Lynn, D. G. (2007) Macroscale Assembly of Peptide Nanotubes. *Chem. Commun.*, 2729 - 2731.

Lu, K., Jacob, J., Thiyagarajan, P., Conticello, V. P., and Lynn, D. (2003) Exploiting Amyloid Fibril Lamination for Nanotube Self-Assembly. *J. Am. Chem. Soc. 125*, 6391-6393.

Lu, M., Hiramatsu, H., Goto, Y., and Kitagawa, T. (2006) Structure of Interacting Segments in the Growing Amyloid Fibril of β2-Microglobulin Probed with IR Spectroscopy. *J. Mol. Biol. 362*, 355–364.

Lundmark, K., Westermark, G. T., Olsen, A., and Westermark, P. (2005) Protein Fibrils in Nature Can Enhance Amyloid Protein, A Amyloidosis in Mice: Cross-seeding as a Disease Mechanism. *Proc. Natl. Acad. Sci. USA 102*, 6098–6102.

Lyu, P. C., Liff, M. I., Marky, L. A., and Kallenbach, N. R. (1990) Side Chain Contributions to the Stability of α-helical Structure in Peptides. *Science 250*, 669–673.

Ma, Y.-Z., Miller, R. A., Fleming, G. R., and Francis, M. B. (2008) Energy Transfer Dynamics in Light-Harvesting Assemblies Templated by the Tobacco Mosaic Virus Coat Protein. *J. Phys. Chem. 112*, 6887-6892.

MacPhee, C. E., and Dobson, C. M. (2000) Formation of Mixed Fibrils Demonstrates the Generic Nature and Potential Utility of Amyloid Nanostructures. *J. Am. Chem. Soc. 122*, 12707-12713.

Makabe, K., McElheny, D., Tereshko, V., Hilyard, A., Gawlak, G., Yan, S., Koide, A., and Koide, S. (2006) Atomic Structures of Peptide Self-assembly Mimics. *Proc. Natl. Acad. Sci. USA 103*, 17753–17758.

Makabe, K., Yan, S., Tereshko, V., Gawlak, G., and Koide, S. (2007) β-Strand Flipping and Slipping Triggered by Turn Replacement Reveal the Opportunistic Nature of β-Strand Pairing. *J. Am. Chem. Soc. 129*, 14661-14669.

Makin, O. S., Sikorski, P., and Serpell, L. C. (2006) Diffraction to Study Protein and Peptide Assemblies. *Curr. Opin. Chem. Biol. 10*, 417–422.

Medina, M. A., and Schwille, P. (2002) Fluorescence Correlation Spectroscopy for the Detection and Study of Single Molecules in Biology. *BioEssays 24*, 758–764.

Meer, B. W. v. d. (1994) Resonance Energy Transfer : Theory and Data, New York : VCH.

Mehta, A. K., Lu, K., Childers, W. S., Liang, Y., Dublin, S. N., Dong, J., Snyder, J. P., Pingali, S. V., Thiyagarajan, P., and Lynn, D. G. (2008) Facial Symmetry in Protein Self-Assembly. *J. Am. Chem. Soc. 130*, 9829–9835.

Meijer, J. T., Roeters, M., Viola, V., Lowik, D. W. P. M., Vriend, G., and Hest, J. C. M. v. (2007) Stabilization of Peptide Fibrils by Hydrophobic Interaction. *Langmuir 23*, 2058-2063.

Melquiond, A., Gelly, J.-C., Mousseau, N., and Derreumaux, P. (2007) Probing Amyloid Fibril Formation of the NFGAIL Peptide by Computer Simulations. *J. Chem. Phys. 126*, 065101(1-7).

Miller, R. A., Presley, A. D., and Francis, M. B. (2007) Self-Assembling Light-Harvesting Systems from Synthetically Modified Tobacco Mosaic Virus Coat Proteins. *J. Am. Chem. Soc. 129*, 3104-3109.

Minor, D. J. J., and Kim, P. S. (1994) Context is a Major Determinant of β-sheet Propensity. *Nature 371*, 264–267.

Modler, A. J., Gast, K., Lutsch, G., and Damaschun, G. (2003) Assembly of Amyloid Protofibrils via Critical Oligomers—A Novel Pathway of Amyloid Formation. *J. Mol. Biol. 325*, 135-148.

Morgan, D. M., Dong, J., Jacob, J., Lu, K., Apkarian, R. P., Thiyagarajan, P., and Lynn, D. G. (2002) Metal Switch for Amyloid Formation: Insight into the Structure of the Nucleus. *J. Am. Chem. Soc. 124*, 12644-12645.

Mukhopadhyay, S., Krishnan, R., Lemke, E. A., Lindquist, S., and Deniz, A. A. (2007) A Natively Unfolded Yeast Prion Monomer Adopts an Ensemble of Collapsed and Rapidly Fluctuating Structures. *Proc. Natl. Acad. Sci. USA 104*, 2649–2654.

Nagy, A., Wu, J., and Berland, K. M. (2005) Observation Volumes and Gamma Factors in Two-Photon Fluorescence Fluctuation Spectroscopy. *Biophys. J. 89*, 2077-2090.

Nakashima, N., Asakuma, S., and Kunitake, T. (1985) Optical Microscopic Study of Helical Superstructures of Chiral Bilayer Membranes. *J. Am. Chem. Soc. 107*, 509-510.

Necula, M., Kayed, R., Milton, S., and Glabe, C. G. (2007) Small Molecule Inhibitors of Aggregation Indicate That Amyloid β Oligomerization and Fibrillization Pathways Are Independent and Distinct. *J. Biol. Chem. 282*, 10311-10324.

Nguyen, H. D., and Hall, C. K. (2004) Molecular Dynamics Simulations of Spontaneous Fibril Formation by Random-coil Peptides. *Proc. Natl. Acad. Sci. USA 101*, 16180–16185.

Nichols, M. R., Moss, M. A., Reed, D. K., Lin, W.-L., Mukhopadhyay, R., Hoh, J. H., and Rosenberry, T. L. (2002) Growth of β-Amyloid(1-40) Protofibrils by Monomer Elongation and Lateral Association. Characterization of Distinct Products by Light Scattering and Atomic Force Microscopy. *Biochemistry 41*, 6115-6127.

O'Neil, K. T., and DeGrado, W. F. (1990) A Thermodynamic Scale for the Helixforming Tendencies of the Commonly Occurring Amino Acids. *Science 250*, 646–651.

Oddo, S., Caccamo, A., Tran, L., Lambert, M. P., Glabe, C. G., Klein, W. L., and LaFerla, F. M. (2006) Temporal Profile of Amyloid-β(Aβ) Oligomerization in an in vivo Model of Alzheimer Disease. *J. Biol. Chem. 281*, 1599-1604.

O'Driscoll, B. M. D., Milsom, E., Fernandez-Martin, C., White, L., Roser, S. J., and Edler, K. J. (2005) Thin Films of Polyethylenimine and Alkyltrimethylammonium Bromides at the Air/Water Interface. *Macromolecules 38*, 8785-8794.

Pace, C. N., Shirley, B. A., Mcnutt, M., and Gajiwala, K. (1996) Forces Contributing to the Conformational Stability of Proteins. *FASEB J. 10*, 75-83.

Padmanabhan, S., Marqusee, S., Ridgeway, T., Laue, T. M., and Baldwin, R. L. (1990) Relative Helix-forming Tendencies of Nonpolar Amino Acids. *Nature 344*, 268–270.

Paul, C., and Axelsen, P. H. (2005) β Sheet Structure in Amyloid β Fibrils and Vibrational Dipolar Coupling. *J. Am. Chem. Soc. 127*, 5754-5755.

Pauling, L., and Corey, R. B. (1951) The Pleated Sheet, a New Layer Configuration of Polypeptide Chains. *Proc. Natl. Acad. Sci. USA 37*, 251-256.

Pavlov, N. A., Cherny, D. I., Heim, G., Jovin, T. M., and Subramaniam, V. (2002) Amyloid Fibrils from the Mammalian Protein Prothymosin alpha. *FEBS Lett. 517*, 37-40.

Penel, S., and Doig, A. J. (2001) Rotamer Strain Energy in Protein Helices - Quantification of a Major Force Opposing Protein Folding. *J. Mol. Biol. 305*, 961-968.

Peter, M., and Ameer-Beg, S. M. (2004) Imaging Molecular Interactions by Multiphoton FLIM. *Biology of the Cell 96*, 231-236.

Petty, S. A., and Decatur, S. M. (2005) Experimental Evidence for the Reorganization of β-Strands within Aggregates of the Aβ(16-22) Peptide. *J. Am. Chem. Soc. 127*, 13488-13489.

Plotnikov, S. V., Millard, A. C., Campagnola, P. J., and Mohler, W. A. (2006) Characterization of the Myosin-Based Source for Second-Harmonic Generation from Muscle Sarcomeres. *Biophys. J. 90*, 693–703.

Poirier, M. A., Li, H., Macosko, J., Cai, S., Amzel, M., and Ross, C. A. (2002) Huntingtin Spheroids and Protofibrils as Precursors in Polyglutamine Fibrilization. *J. Biol. Chem. 277*, 41032–41037.

Quijano, F. A. R., Morrow, D., Wise, B. M., Brancia, F. L., and Goux, W. J. (2006) Prediction of Nucleating Sequences from Amyloidogenic Propensities of Tau-Related Peptides. *Biochemistry 45*, 4638-4652.

Rist, M., Wagenknecht, H.-A., and Fiebig, T. (2002) Exciton and Excimer Formation in DNA at Room Temperature. *ChemPhysChem 3*, 704-707.

Rodriguez-Larrea, D., Ibarra-Molero, B., and Sanchez-Ruiz, J. M. (2006) Energetic and Structural Consequences of Desolvation/Solvation Barriers to Protein Folding/Unfolding Assessed from Experimental Unfolding Rates. *Biophys. J.: Biophys. Lett.* L48-L50.

Rose, G. D., Fleming, P. J., Banavar, J. R., and Maritan, A. (2006) A Backbone-based Theory of Protein Folding. *Proc. Natl. Acad. Sci. USA 103*, 16623–16633.

Ryu, S.-E., Choi, H.-J., Kwon, K.-S., Lee, K. N., and Yu, M.-H. (1996) The Native Strains in the Hydrophobic Core and Flexible Reactive Loop of a Serine Protease Inhibitor: Crystal Structure of an Uncleaved α1-antitrypsin at 2.7Å. *Structure 4*, 1181–1192.

Sabate, R., and Estelrich, J. (2005) Evidence of the Existence of Micelles in the Fibrillogenesis of β-Amyloid Peptide. *J. Phys. Chem. B 109*, 11027-11032.

Santiveri, C. M., Santoro, J., Rico, M., and Jimenez, M. A. (2004) Factors Involved in the Stability of Isolated β-sheets: Turn Sequence, β-sheet Twisting, and Hydrophobic Surface Burial. *Protein Sci. 13*, 1134-1147.

Sawaya, M. R., Sambashivan, S., Nelson, R., Ivanova, M. I., Sievers, S. A., Apostol, M. I., Thompson, M. J., Balbirnie, M., Wiltzius, J. J. W., McFarlane, H. T., Madsen, A., Riekel, C., and Eisenberg, D. (2007) Atomic Structures of Amyloid Cross-β Spines Reveal Varied Steric Zippers. *Nature 447*, 453-457.

Scheibel, T., Parthasarathy, R., Sawicki, G., Lin, X.-M., Jaeger, H., and Lindquist, S. L. (2003) Conducting Nanowires Built by Ccontrolled Self-assembly of Amyloid Fibers and Selective Metal Deposition *Proc. Natl. Acad. Sci. USA 100*, 4527-4532.

Scheiner, S. (2006) Contributions of NH-O and CH-O Hydrogen Bonds to the Stability of β-Sheets inProteins. *J. Phys. Chem. B 110*, 18670-18679.

Schilling, S., Lauber, T., Schaupp, M., Manhart, S., Scheel, E., Bohm, G., and Demuth, H.-U. (2006) On the Seeding and Oligomerization of pGlu-Amyloid Peptides (in vitro). *Biochemistry*, 12393-12399.

Sengupta, P., Garai, K., Sahoo, B., Shi, Y., Callaway, D. J. E., and Maiti, S. (2003) The Amyloid β Peptide (Aβ1-40) Is Thermodynamically Soluble at Physiological Concentrations. *Biochemistry 42*, 10506-10513.

Serio, T. R., Cashikar, A. G., Kowal, A. S., Sawicki, G. J., Moslehi, J. J., Serpell, L., Arnsdorf, M. F., and Lindquist, S. L. (2000) Nucleated Conformational Conversion and the Replication of Conformational Information by a Prion Determinant. *Science 289*, 1317-1321.

Shimizu, T., Masuda, M., and Minamikawa, H. (2005) Supramolecular Nanotube Architectures Based on Amphiphilic Molecules. *Chem. Rev. 105*, 1401-1443.

Shuklov, I. A., Dubrovina, N. V., and Börner, A. (2007) Fluorinated Alcohols as Solvents, Cosolvents and Additives in Homogeneous Catalysis. *Synthesis 19*, 2925–2943.

Sikorski, P., Atkins, E. D. T., and Serpell, L. C. (2003) Structure and Texture of Fibrous Crystals Formed by Alzheimer's Aβ(11–25) Peptide Fragment. *Structure 11*, 915-926.

Smirnovas, V., Winter, R., Funck, T., and Dzwolak, W. (2006) Protein Amyloidogenesis in the Context of Volume Fluctuations: A Case Study on Insulin. *ChemPhysChem 7*, 1046 – 1049.

Smith, C. K., and Regan, L. (1995) Guidelines for Protein Design: The Energetics of beta Sheet Side Chain Interactions. *Science 270*, 980-982.

Souillac, P. O., Uversky, V. N., Millett, I. S., Khurana, R., Doniach, S., and Fink, A. L. (2002) Elucidation of the Molecular Mechanism during the Early Events in Immunoglobulin Light Chain Amyloid Fibrillation. *J. Biol. Chem. 277*, 12666-12679.

Spoel, D. v. d., Lindahl, E., Hess, B., Buuren, A. R. v., Apol, E., Meulenhoff, P. J., Tieleman, D. P., Sijbers, A. L. T. M., Feenstra, K. A., Drunen, R. v., and Berendsen, H. J. C. (2005) Gromacs User Manual version 3.3, www.gromacs.org

Stine, W. B., Dahlgren, K. N., Krafft, G. A., and LaDu, M. J. (2003) In vitro Characterization of Conditions for Amyloid-β Peptide Oligomerization and Fibrillogenesis. *J. Biol. Chem. 278*, 11612–11622.

Sunde, M., Serpell, L. C., Bartlam, M., Fraser, P. E., Pepys, M. B., and Blake, C. C. F. (1997) Common Core Structure of Amyloid Fibrils by Synchrotron X-ray Diffraction. *J. Mol. Biol. 273*, 729-739.

Surewicz, W. K. (2007) Protein Science: Discriminating Taste of Prions. *Nature 447*, 541-542.

Surewicz, W. K., Jones, E. M., and Apetri, A. C. (2006) The Emerging Principles of Mammalian Prion Propagation and Transmissibility Barriers: Insight from Studies in Vitro. *Acc. Chem. Res. 39*, 654–662.

SYBYL 7.3, Tripos International, 1699 South Hanley Rd., St. Louis, Missouri, 63144, USA.

Tjernberg, L. O., Pramanik, A., Bjorling, S., Thyberg, P., Thyberg, J., Nordstedt, C., Berndt, K. D., Terenius, L., and Rigler, R. (1999) Amyloid β-peptide Polymerization Studies Using Fluorescence Correlation Spectroscopy. *Chem. Biol. 6*, 53-62.

Towles, K. B., Brown, A. C., Wrenn, S. P., and Dan, N. (2007) Effect of Membrane Microheterogeneity and Domain Size on Fluorescence Resonance Energy Transfer. *Biophys. J. 93*, 655–667.

Trovato, A., Chiti, F., Maritan, A., and Seno, F. (2006) Insight into the Structure of Amyloid Fibrils from the Analysis of Globular Proteins. *PLoS Comput. Biol. 12*, 1608-1618.

Tycko, R. (2003) Applications of Solid State NMR to the Structural Characterization of Amyloid Fibrils: Methods and Results. *Prog. Nucl. Magn. Reson. Spectrosc. 42*, 53-68.

Tycko, R. (2004) Progress towards a Molecular-level Structural Understanding of Amyloid Fibrils. *Curr. Opin. Struct. Biol. 14*, 96-103.

Urbanc, B., Cruz, L., Ding, F., Sammond, D., Khare, S., Buldyrev, S. V., Stanley, H. E., and Dokholyany, N. V. (2004) Molecular Dynamics Simulation of Amyloid β Dimer Formation. *Biophys. J. 87* 2310–2321.

Uversky, V. N., and Fink, A. L. (2004) Conformational Constraints for Amyloid Fibrillation: the Iimportance of Being Unfolded. *Biochim. Biophys. Acta 1698*, 131– 153.

Ventura, S., Vega, M. C., Lacroix, E., Angrand, I., Spagnolo1, L., and Serrano, L. (2002) Conformational Strain in the Hydrophobic Core and its Inplications for Protein Folding and Design. *Nat. Struct. Biol. 9*, 485 - 493.

Wallrabe, H., and Periasamy, A. (2005) Periasamy A: Imaging Protein Molecules Using FRET and FLIM Microscopy. *Curr. Opin. Biotechnol. 16*, 19-27.

Walsh, D. M., and Selkoe, D. J. (2007) A beta oligomers - a decade of discovery. *J. Neurochem. 101*, 1172-1184.

Westermark, P. (2005) Aspects on Human Amyloid Forms and their Fibril Polypeptides. *FEBS J. 272*, 5942-5949.

Wetzel, R. (2006) Kinetics and Thermodynamics of Amyloid Fibril Assembly. *Acc. Chem. Res. 39*, 671-679.

Wogulis, M., Wright, S., Cunningham, D., Chilcote, T., Powell, K., and Rydel, R. E. (2005) Nucleation-Dependent Polymerization Is an Essential Component of Amyloid-Mediated Neuronal Cell Death. *J. Neurosci. 25*, 1071-1080.

Wojcik, J., Altman, K. H., and Scheraga, H. A. (1990) Helix-coil Stability Constants for the Naturally Occurring Amino Acids in Water. XXIII. Proline Parameters from Random Poly-(hydroxybutylglutamineco-L-proline). *Biopolymers 30*, 121–134.

Wood, S. J., Maleeff, B., Hart, T., and Wetzel, R. (1996) Physical, Morphological and Functional Differences between pH 5.8 and 7.4 Aggregates of the Alzheimer's Amyloid Peptide Aβ. *J. Mol. Biol. 256*, 870–877.

Wouters, M. A., and Curmi, P. M. G. (1995) An Analysis of Side Chain Interactions and Pair Correlations within Antiparallel β-sheets: the Difference between Backbone Hydrogen-bonded and Non-hydrogen-bonded Residue Pairs. *Protein: Structure, Function and Genetics 22*, 119-131.

Yager, P., Schoen, P. E., Davies, C., Price, R., and Singh, A. (1985) Structure of Lipid Tubules Formed from a Polymerizable Lecithin. *Biophys. J. 48*, 899-906.

Yan, S., Gawlak, G., Makabe, K., Tereshko, V., Koide, A., and Koide, S. (2007) Hydrophobic Surface Burial is the Major Stability Determinant of a Flat, Single-Layer β-sheet. *J. Mol. Biol. 368*, 230-243.

Yang, A.-S., and Honig, B. (1995) Free Energy Determinants of Secondary Structure Formation: II. Antiparallel β-Sheets. *J. Mol. Biol. 252*, 366–376.

Yong, W., Lomakin, A., Kirkitadze, M. D., Teplow, D. B., Chen, S.-H., and Benedek, G. B. (2002) Structure Determination of Micelle-like Intermediates in Amyloid β-Protein Fibril Assembly by Using Small Angle Neutron Scattering. *Proc. Natl. Acad. Sci. USA 99*, 150–154.

Yoon, S., and Welsh, W. (2004) Detecting Hidden Sequence Propensity for Amyloid Fibril Formation. *Protein Sci. 13*, 2149–2160.

Zaremba, S. M., and Gregoret, L. M. (1999) Context-dependence of Amino Acid Residue Pairing in Antiparallel β-sheet. *J. Mol. Biol. 291,* 463-479

Zhao, W., Zheng, B., and Haynie, D. T. (2006) A Molecular Dynamics Study of the Physical Basis of Stability of Polypeptide Multilayer Nanofilms. *Langmuir 22*, 6668-6675.

Zhao, W. Q., Felice, F. G. D., Fernandez, S., Chen, H., Lambert, M. P., Quon, M. J., GA, G. A. K., and Klein, W. L. (2008) Amyloid beta Oligomers Induce Impairment of Neuronal Insulin Receptors. *FASEB J. 22*, 246-260.